UNIVERSITÀ
DEGLI STUDI
DI PADOVA

Head Office: Università degli Studi di Padova

Department of Industrial Engineering

Ph.D. COURSE IN: INDUSTRIAL ENGINEERING
CURRICULUM: MECHANICAL ENGINEERING
SERIES XXX

Reference standards and methods for traceable X-ray computed tomography dimensional metrology

Thesis written with the financial contribution of the European Union's Seventh Framework Programme under grant agreement No. 607817, INTERAQCT project

Coordinator: Ch.mo Prof. Paolo Colombo
Supervisor: Ch.mo Prof. Simone Carmignato

Ph.D. student: Petr Hermanek

PREFACE

This thesis was prepared as one of the requirements of the Ph.D. degree.

The Ph.D. project has received funding from the European Union's Seventh Framework Programme under grant agreement No. 607817, INTERAQCT project. The work presented in this thesis was carried out from September 2014 to October 2017 at the Department of Industrial Engineering (Dip. di Ingegneria Industriale, DII) and at the Department of Management and Engineering (Dip. di Tecnica e Gestione dei sistemi industriali, DTG) of the University of Padova, Italy, under the supervision of Prof. Simone Carmignato. A part of the work, in the period from April 2016 to June 2016 (seven weeks in total), was performed at Physikalisch-Technische Bundesanstalt (PTB), Braunschweig, Germany, under the supervision of Dr. Markus Bartscher and Dr. Ulrich Neuschaefer-Rube. Experiments were also performed at Centre of Excellence Telč (CET), Telč, Czech Republic, in April 2017-June 2017 (two weeks) under the supervision of doc. Ing. Michal Vopálenský, Ph.D.

I would like to thank my supervisor for his inspiration to my work, support, and discussions related to metrology and X-ray computed tomography (CT). Special thanks are due to my co-supervisor Prof. Enrico Savio for his valuable tips and advises, and my colleagues at DII, namely to Valentina Aloisi, Filippo Zanini and Jitendra Singh Rathore who carried out their research on CT in the same period, and were always available to help and for discussion. I am also grateful to the staff of DII, especially to Mr. Stefano Girardi, who was always helpful and guided me through many challenges related to precision manufacturing.

Furthermore, I would like to express my gratitude to my colleagues from the INTERAQCT project, especially to Massimiliano Ferrucci for the extensive collaboration, discussions about any possible topic, and his helpfulness, and to Evelina Ametova, Fabricio Borges de Oliveira and Emmanuel Manu Dabankah for their contribution to projects elaborated in collaboration. Prof. Wim Dewulf is also thanked for his significant contribution to the research presented in this thesis.

I would like to thank the staff of Department 3.2 at PTB, namely to Dr. Markus Bartscher and Dr. Ulrich Neuschaefer-Rube for their inspiration and advises to my research activity at PTB and for the hospitality during my stay, and to Dr. Michael Neugebauer, Mrs. Astrid Linkogel, Dipl.-Ing. Dieter Schulz, and Jakob Schlie, M.Sc. for their help related to coordinate measurements. The staff of CET Telč, especially Ing. Ivana Kumpová and doc. Ing. Michal Vopálenský, Ph.D. are thanked for their availability and assistance with CT scanning during my stay at CET, and for discussions regarding CT.

Anton Jansson and Prof. Lars Pejryd from Örebro University are thanked for the collaboration related to Dual-energy CT scanning. I am also grateful to Audrey Somera from ENS Paris-Saclay for her contribution and help with evaluating measurement data.

I would also like to thank my girlfriend Klára, who came with me to Italy and was supporting me for all the three years.

Padova, October 2017

Petr Heřmánek

ABSTRACT

X-ray computed tomography (CT) is an imaging technique, which originally found its application in the medical field and over years of research extended its use to industry, mainly to non-destructive testing. In the last years, CT has been also used as a tool for dimensional metrology, and is considered the third generation of measuring techniques in coordinate metrology, after tactile and optical coordinate measuring systems. The main advantage of CT over other measuring instruments is the fact that both internal and external geometries of the measured workpiece can be visualized as a 3D model, and analyzed without destruction.

CT measurement chain is affected by numerous and often complex influence factors. Furthermore, due to the fact that it is still relatively new technique for coordinate metrology, and because of the lack of research and standardized procedures, CT has not yet reached maturity as a dimensional measurement technology. Sources of CT measurement uncertainty are still not completely understood in some cases and, as a result, achieving CT measurement traceability is difficult.

Traceability of measurements is an important property ensuring that the measurement results are traceable to the SI unit through unbroken chains of calibrations. Reference standards are a typical means to test metrological systems and investigate various factors that influence the measurement results. In this thesis, several standards dedicated to different mainstays towards the establishment of measurement traceability – namely metrological performance verification according to international standards, metrological performance verification of CT specific applications, calibration, and evaluation of measurement uncertainty – were developed. Furthermore, as an output of experience and findings gained during the project, a good practice guide for developing reference standards for CT dimensional metrology was compiled.

The first standard proposed in this Ph.D. work was developed for the evaluation of accuracy of CT porosity measurements and for establishing their metrological traceability. The design of the standard contains hemispherical features resembling artificial internal porosity and its dismountable configuration ensures calibration by different measuring instruments. It was proved that not only the accuracy of CT porosity measurements can be evaluated using this standard, but the accuracy can also be improved by using the artifact. Moreover, a procedure for establishing the traceability of CT porosity measurements obtained from industrial parts was proposed.

Calibration of CT instrument geometry was achieved by using a standard developed during this project, namely the CT calibration tube (CT^2), in combination with the so-called “minimization procedure” used for estimating CT geometrical parameters, and a Monte Carlo method for evaluating the measurement uncertainty. Furthermore, based on results from experimental implementations of the developed standard and method, it was proven that it is possible to align the CT system to its nearly ideal geometry. Moreover, a comprehensive CT instrument geometry alignment method was proposed, which is based on the use of the CT^2 standard, the minimization procedure, and a novel advanced reconstruction algorithm (the so called FlexCT, developed by KU Leuven).

Multi-material aspects of CT dimensional measurements were also addressed in this Ph.D. thesis. A series of reference standards were developed for evaluating the multi-material effects on gap measurements. Different behavior between results obtained on mono- and multi-material samples confirmed the existence of the multi-material influence. Furthermore, an alternative dual-energy CT scanning approach was applied to enhance the measurement results.

CONTENTS

1 INTRODUCTION

This chapter provides an introduction to X-ray computed tomography (CT), its general applications with particular aim at dimensional metrology. Issues with the establishment of metrological traceability are discussed here, after a short overview on CT and its industrial applications, which is summarized in the first section of the chapter. In the second section, the INTERAQCT research project is described, which represents the framework that includes this Ph.D. project as well as other different sub-projects focused on advanced quality control by CT. Finally, the structure of the thesis is presented in the last section of this chapter.

1.1 Short overview on CT and its industrial applications

X-ray computed tomography is an imaging method in which the object is irradiated with X-rays or gamma rays and mathematical algorithms are used to create a cross-sectional image or a sequence of such images [1]. The object and/or the imaging apparatus perform relative rotational and/or translational movements, and a large number of radiographic projections is taken. The projections are subsequently reconstructed using mathematical algorithms to form a slice image of the object; a three-dimensional (3D) volumetric model can be obtained by stacking the reconstructed slices giving a unique opportunity to non-destructively visualize the internal and external features of the object.

CT originally found its application in the medical field as a novel visualization technique due to its advantage over traditional 2D radiographic techniques. The first CT scanner was built in 1969 by Hounsfield, who was eventually awarded a Nobel Prize in Physiology and Medicine. Over following years of technological advancements, CT has been adapted for industrial use; firstly, for material analysis and non-destructive testing [2]. Subsequently, the use of CT was broadened also to dimensional metrology by the introduction of the first metrological CT system in 2005 [2]. Several different constructions of CT instruments were developed; today’s industrial CT systems are based on so called third generation of CT scanners [3]. Typically, cone beam and fan beam CT scanners are applied in industry and metrological laboratories.

Typical applications of CT in non-destructive testing are detection of various flaws such as voids, inclusions, cracks, etc., and analyses of material composition of the investigated part. Since CT is still rather expensive technique, it is usually used for quality control of high-end products in automotive and aerospace industry. These parts are typically produced by novel technologies such as micro-injection molding or additive manufacturing (AM), and contain complex, miniature and often internal features that cannot be analyzed by other instruments in a non-destructive way. Since invasive techniques can cause deflections, relaxing of material and other changes in geometry, CT emerges as a promising solution. Its unique property to analyze both internal and external features without any invasive intervention, and research efforts carried out in CT over last decades, allowed extending its application also to quantitative quality control including dimensional metrology. A summary of typical CT applications is shown in Table 1. It is worth noting that various analyses can be performed simultaneously on the acquired dataset, which is one of the most significant advantages of computed tomography.

Table 1. Overview of main industrial applications of CT

Main industrial applications of CT	
Void/porosity detection and measurements*	Material analysis, e.g. density-based material identification
Detection and measurement* of cracks	Dimensional measurements*
Nominal (CAD)/actual comparison*	Tolerance verification*
Verification of assemblies, e.g. verification of position of individual components, dimensional measurements*	Analysis of fibers in composite materials, i.e. analysis of fiber orientation, measurement of fiber length*
Finite element method simulations	Analysis of wall thickness*
Analysis of foam structures	Reverse engineering*
Detection of material defects, e.g. inclusions	Testing of material properties, e.g. absolute permeability, thermal conductivity, etc.

* Dimensional metrology applications

CT is the only technique for industrial quality control able to measure objects with non-accessible features or multi-material components non-destructively [4]. Furthermore, since quality control of single parts is not sufficient for determining whether an assembly conforms to specifications or not, CT can be used for holistic quality control of assemblies in the assembled state [2]. Given the new opportunities that CT offers to dimensional quality control, CT can be considered a third revolutionary development in coordinate metrology [4]. However, CT is a complex technology, and as such suffers from various errors, many of which have not been thoroughly investigated yet. Furthermore, due to the lack of research and standardized procedures, and because it is a relatively new measurement technique, CT has not yet reached maturity as a measurement tool. A summary of advantages and limitations of CT dimensional metrology are shown in Table 2.

Table 2. Advantages and limitations of CT dimensional metrology. Adapted from [4].

Advantages	Limitations
Non-destructive technology	No international standards available
Possibility to perform different analyses on the same dataset	Various imaging errors (artefacts) that influence measurement accuracy
3D visualization of scanned object	Complex and numerous influence factors
High information density	Limited penetration length with respect to scanned material
Object of any material, color, shape, and surface finish can be scanned. The only limiting material property is its attenuation coefficient.	Reduced measurement capability when scanning multi-material objects
	Establishment of measurement traceability is complex due to a large number of influencing factors

1.2 INTERAQCT project description

The work described in this Ph.D. thesis was carried out under the INTERAQCT project framework. The abbreviation stands for “International Network for the Training of Early stage Researchers on Advanced Quality control by Computed Tomography”. The project started in October 2013 and finished in September 2017. It was funded by the European Commission's 7th Framework Programme FP7-PEOPLE – under grant agreement No. 607817. All academic, industrial (including national metrology institutions), and associated partners of the project are listed in Table 3.

Table 3. Partners of INTERAQCT project.

ACADEMIC PARTNERS	**NATIONAL METROLOGY INSTITUTIONS**
KU Leuven, Belgium	PTB, Germany
Fraunhofer IIS, Germany	NPL, UK
UASUA, Austria	**ASSOCIATED PARTNERS**
University of Padova, Italy	LayerWise, Belgium
DTU, Denmark	Novo Nordisk A/S, Denmark
RWTH Aachen, Germany	Borealis Polyolefine GmbH, Austria
INDUSTRIAL PARTNERS	Eltek S.p.A., Italy
X-TEK Systems Ltd, UK	Argon Measuring Solutions, Belgium
Volume Graphics GmbH, Germany	Nuovo Pignone S.r.l., Italy
Materialise, NV, Belgium	Kiekert AG, Germany

The INTERAQCT project has been conceived as a pan-European industrial-academic initiative that provided the unique and encompassing training environment by bringing together expertise from industry and academia in each of these domains: CT-equipment, CT-software, non-destructive testing (NDT), dimensional metrology, additive manufacturing, micro-manufacturing and composite manufacturing. The aim of the project is to exploit full potential of CT in terms of non-destructive testing and coordinate metrology, particularly focusing on improvement of capabilities in dimensional metrology [5]. Individual goals of the projects are listed below:

1) Develop optimized procedures and algorithms that allow fast, yet accurate CT-voxel model acquisition.
2) Quantify and improve the reliability of CT analysis for dimensional quality control and for material defect analysis.
3) Develop application-oriented CT-procedures for integrated quality control of complex products produced by key emerging manufacturing technologies, hence contributing to the reliability and customer acceptance of these emerging processes.

In order to achieve the objectives described above, the tasks were divided into 13 sub-projects for early stage researchers (ESR) and two for experienced researchers (ER):

- ESR1: Knowledge-based system for fast and accurate determination of CT scanning parameters.

- ESR2: Advanced beam hardening correction for multi-material objects.
- ESR3: Advanced segmentation algorithms.
- ESR4: Systematic approach to CT equipment calibration.
- **ESR5: Calibration objects and methods for ensuring traceable CT metrology.**
- ESR6: Task-specific uncertainty determination for CT metrology.
- ESR7: Acceptance testing of CT equipment.
- ESR8: Probability of detection (PoD) of material defects.
- ESR9: CT-based quality optimization of Selective Laser Sintering.
- ESR10: Dedicated calibration procedures for micro-parts.
- ESR11: CT-based quality optimization of micro injection molding and micro manufacturing processes.
- ESR12: Material defect analysis of composite parts.
- ESR13: Integrated quality control of precision assemblies.
- ER1: CT-based quality control of customized porous structures.
- ER2: Integrated quality control of composite parts.

Several groups, so called "Work packages" (WP), were created in order to create a platform for individual sub-projects that are related to a similar subject. Furthermore, sub-projects within the same WP are interconnected, and several sub-projects outreach from their default WP. A diagram of different WPs, sub-projects and links between them are schematically shown in Figure 1.

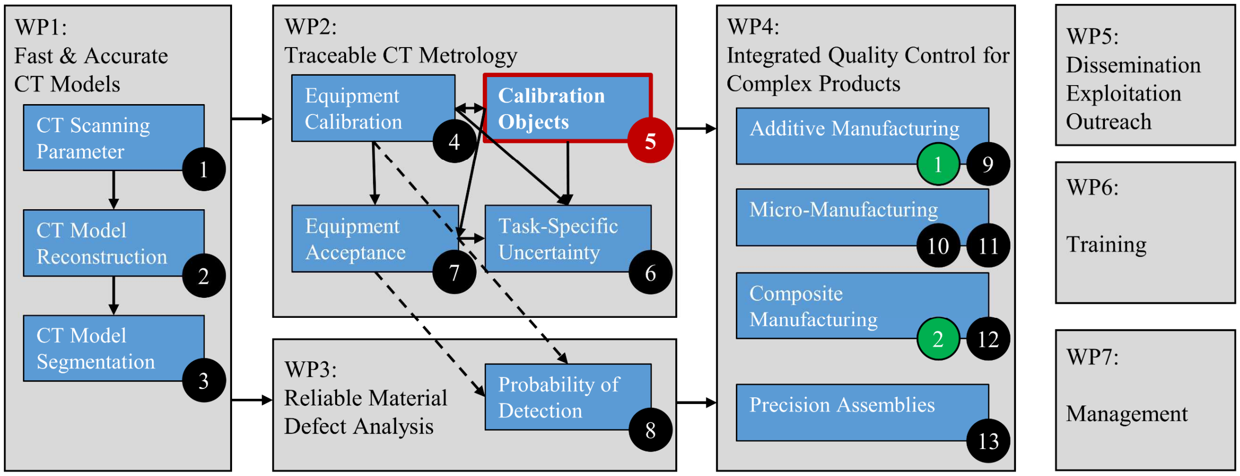

Figure 1. Diagram of INTERAQCT project structure. ESR projects are denoted by dark color, ER projects by bright color. Project No. 5 is the aim of this Ph.D. thesis.

Two projects were assigned to the University of Padova: ESR5 and ESR11. The project aimed at the development of **Calibration objects and methods for ensuring traceable CT metrology (ESR5)** is the subject of this thesis. The main activities of the project comprise development of well-defined reference standards including all development phases starting from material choice, through designing and manufacturing, and calibration in the final step. Subsequently, procedures describing the use of these novel standards towards achieving the traceability of CT dimensional measurements will be proposed.

The term "reference standard" (defined in the International vocabulary of metrology (VIM) [6]) is further in this thesis used as the name for reference objects that in metrology are most often referred to as "artefacts" or "metrological artefacts" [2].

1.3 Project structure

Novel technologies, such as AM and micro-injection molding allow almost unlimited design freedom, and manufacturing of miniature and internal features. These new production opportunities, however, put high demands on quality control. In particular, non-destructive methods are preferred for dimensional measurements, as invasive techniques can cause deformation of material and other effects that can subsequently distort the measurement results. CT as a measuring instrument features great advantages over conventional tactile and optical coordinate measuring systems (CMSs). However, additional challenges in terms of equipment, measurement procedures and data processing come with these new opportunities. In particular, the establishment of metrological traceability is one of major challenges in CT dimensional metrology for several reasons: (i) the complexity of CT measurement process and a large number of influencing factors, the effect of which is in many cases unknown, (ii) lack of international standards, and (iii) lack of research since the technology and its application to dimensional metrology is still relatively new. As a result, CT users are facing difficulties in evaluating measurement uncertainty, a necessary step in establishing measurement traceability, which was proved e.g. in an international inter-laboratory comparison “CT Audit” [7].

Apart from international standards and guidelines, there is also a lack of well-defined reference standards and calibration procedures for the assessment of CT system accuracy and calibration of CT instrument geometry. As a consequence, it is not possible to effectively quantify and correct deterministic errors and establish the traceability of CT dimensional measurements. The lack of standardization subsequently limits the comparability between different CT systems as well as with other coordinate measuring systems [8]. It is also one of the main reasons for limited consideration of CT as a valid measuring technique in industry. Traceability of CT dimensional measurements is essential to make CT comparable to conventional CMSs and to reach the same recognition for coordinate metrology applications.

This Ph.D. thesis proposes novel reference standards and methods towards establishing metrological traceability of CT dimensional measurements. Steps related to the construction of a new reference standard, such as material choice, designing, manufacturing and calibration are also discussed in this work. Furthermore, procedures defining proper use of these standards towards achieving traceable CT dimensional measurements are developed and proposed in this thesis.

Main objectives of this Ph.D. project comprise the development of reference standards/methods for four mainstays of traceability in CT dimensional metrology:

1) Metrological performance verification according to international standards.
2) Metrological performance verification of CT specific applications.
3) Calibration.
4) Evaluation of measurement uncertainty.

Furthermore, a good practice guide is included in this thesis to describe general steps towards developing versatile and efficient reference standards for CT dimensional metrology.

The structure of the thesis is defined as follows:

- **Chapter 2** gives a general overview of CT technology, its principle, and industrial applications. Basics of CT dimensional metrology are explained here, and differences between CT and other CMSs, and their implications to measurement results are discussed.
- **Chapter 3** gives an insight in the state-of-the art of CT dimensional measurements and CT metrological traceability. International CT standardization platform, including standards related to dimensional metrology, is presented here. Major factors that influence CT measurements are identified and presented in this section. Procedure for CT metrological performance verification according to a draft of related ISO standard, as well as methods for task-specific CT instrument calibration as per international standards and guidelines are discussed here. Finally, a thorough overview of existing reference standards for CT dimensional metrology is presented in this chapter.
- **Chapter 4** presents the first reference standard developed during the project aimed at the verification of CT performance in porosity measurements. Individual development phases, i.e. material choice, designing, manufacturing and calibration of the standard are explained in this chapter. The accuracy of CT porosity measurements is evaluated using the newly-developed standard. Furthermore, a procedure to establish traceability of CT porosity measurements is described and demonstrated on an industrial case study. A method for the evaluation of CT porosity measurement uncertainty is described in detail here. Finally, a method to improve CT porosity measurements and to establish the traceability of CT porosity measurements in industry is proposed.
- **Chapter 5** introduces the second reference standard and a method for the calibration of CT system geometry. Similarly to the previous chapter, material choice, designing, manufacturing and calibration phases of the standard development are discussed. Furthermore, so called “minimization” procedure together with a Monte Carlo approach for evaluating the measurement uncertainty are used for the calibration of CT geometrical parameters. The proposed method is verified by a simulation study and experimental results.
- **Chapter 6** describes a reference standard designed for the verification of CT metrological performance in multi-material measurements; in particular, measurements of gaps between different materials are the aim of this chapter. Detailed description of material choice, design of the standard, its manufacturing and calibration is given here. The use of the standard is discussed and multi-material effects on measurement accuracy are presented here. Furthermore, a dual-energy CT approach is introduced in this chapter, and its effects on measurement accuracy and smallest measurable gap are discussed.
- **Chapter 7** summarizes observations and experience obtained during the Ph.D. project in terms of developing new reference standards. The findings are organized in such a way that form a “good practice” guide that guides CT users and researchers through all the stages of new reference standard development, such as material choice, design, manufacturing, calibration, etc.
- **Chapter 8** provides general conclusions derived from the results and achievements of this work. Furthermore, it proposes several procedures that can be directly applied in industry, and gives suggestions for future work as a follow-up to the project.

2 X-RAY COMPUTED TOMOGRAPHY

This chapter gives a brief historical overview of major developments in CT and its evolution from medical to industrial use. Subsequently, a theory about X-ray physics is discussed, followed by the explanation of general CT principle. Major CT industrial applications are discussed including dimensional metrology. Finally, the CT dimensional measurement chain is described, and practical aspects that has to be considered when performing CT dimensional measurements are overviewed. Advantages and disadvantages of CT with respect to conventional CMSs are presented as well as major differences between different techniques.

2.1 Developments of CT

CT is an imaging technique that originally found its application in the medical field as a tool for advanced visualization of human body. The word "tomography" comes from the Greek *tomos* and *graphien* that means *slice* and *write*. CT is based on the acquisition of a large number of radiographic projections that are subsequently reconstructed using mathematical algorithms to form slice images of the scanned object [3]. The stack of reconstructed slices can be then used for 3D visualization of the sample under investigation.

The first step with respect to the development of CT dates back to 1895 when a German physicist Wilhlem Conrad Röntgen discovered X-rays. These newly discovered rays were able to penetrate biological tissue, and found their application in the medical field; the first X-ray image in medicine was taken in 1896. The first prototype of a clinical CT scanner was developed in 1968 by Godfrey Hounsfield, who was eventually awarded the Nobel Prize in Physiology and Medicine in 1979. Hounsfield's CT scanner was officially released in 1971, followed by the first full-body CT scanner in 1975. CT entered industrial application field in 1980 as a tool for non-destructive testing and material analysis. After another ten years of research and improving NDT capabilities of CT, 3D modelling and quantitative analysis became next domains of CT application [9]. First dimensional measurements using CT were performed in 1991, however the accuracy around 0.1 mm was not sufficient compared to conventional CMSs. Real breakthrough in CT dimensional metrology came in 2005 when the first metrological CT system was introduced during the Control fair in Germany [10]. More details about CT history can be found e.g. in [3,11].

The evolution of CT from the discovery of X-rays to the introduction of the first metrological CT system is schematically shown in Figure 2.

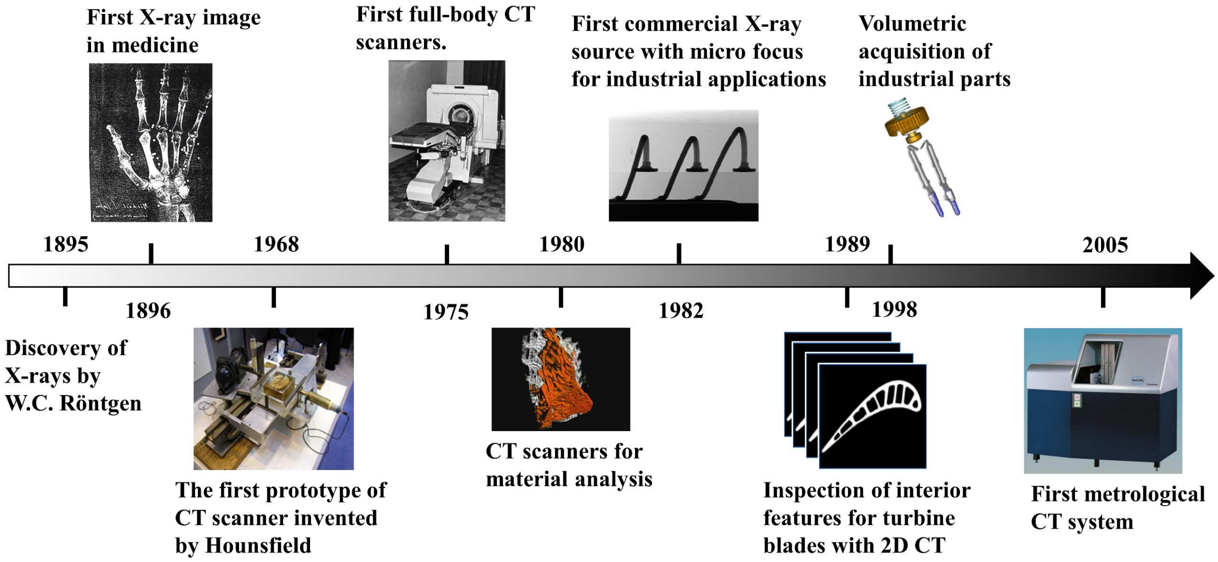

Figure 2. Evolution of X-ray computed tomography. Adapted from [9,10,12–14].

2.2 X-ray physics

This section briefly describes the physical background of X-ray imaging as a first step of the CT scanning chain. Firstly, the X-ray generation is described, followed by the explanation of X-ray attenuation. Finally, the mechanism of X-ray detection is shown.

2.2.1 X-ray generation

X-rays are electromagnetic waves with wavelength ranging from 0.01-10 nm discovered by Wilhelm Conrad Röntgen in 1895. The energy of each X-ray photon is proportional to its frequency according to the following equation:

$$E = h\nu = \frac{hc}{\lambda}, \tag{2.1}$$

where h is Planck's constant (6.63×10^{-34} J·s), c is the speed of light (3×10^{8} m·s^{-1}), and λ is the wavelength of the X-ray. X-rays are classified as soft ($\lambda > 0.1$ nm) and hard ($\lambda < 0.1$ nm) based on their ability to penetrate material. X-rays are generated by means of various sources, such as synchrotrons, linear accelerators, etc. However, X-ray tubes with reflective target are typically used in industrial CT systems, and further explanations will be related to this type of X-ray source.

X-ray tube is composed of two main components – a filament (cathode) and a target (anode) – inserted in an evacuated enclosure (see Figure 3). When the cathode, typically consisting of a thin tungsten wire, is heated, electrons with increased kinetic energy are released from the filament surface. This effect is called the thermionic effect [11]. The target consists of a metal part, typically made of tungsten or molybdenum. The cathode and anode are connected to a high voltage generator. A difference in electric potential between the two electrodes accelerates the electrons generated by thermionic effect towards the target material. The trajectory of accelerated electrons is usually controlled by a focus cap so that they are focused to a small region on the target. The energy of the electrons reaching the target is given by the following formula:

$$E_{electrons} = e\Delta V, \tag{2.2}$$

where e is the electric charge of an electron, equal to 1.6×10^{-19} C, and ΔV is the acceleration voltage between the cathode and anode. The acceleration energy is measured in electron volts (eV). 1 eV is the kinetic energy gained by an electron accelerated by a ΔV of 1 V.

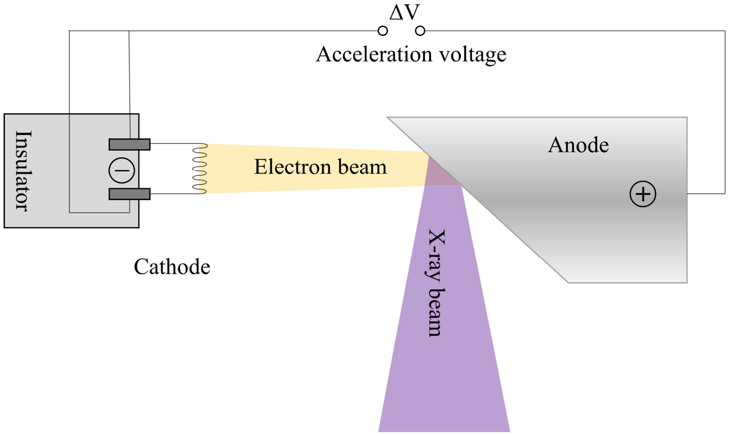

Figure 3. Diagram of main components of X-ray tube. Adapted from [15].

Several interactions occur when the electrons reach the target, resulting in the emission of photons:

1) The electrons penetrating the target material come close to the atom nucleus and are deflected and decelerated by the Coulomb fields. The energy loss caused by the deceleration of electrons results in the generation of X-rays. The term used to describe this phenomenon is *Bremsstrahlung*, which is a contraction of the German words *bremsen* “to brake” and *Strahlung* “radiation” (i.e. “braking radiation”). Since the energy of emitted photons depends on the trajectory of the electron and the proximity to the nucleus, the distribution of energies is continuous (see Figure 4).
2) An incident electron can directly collide with an inner-shell electron and displace it. As a consequence, the atom is ionized and a vacant place is left in the corresponding atom shell. Subsequently, the vacancy is filled with a high-energy electron along with the emission of a photon. Usually, the vacant hole is filled by the electron from the adjacent shell (e.g. if electron from L-shell fills the hole in K-shell, a photon with characteristic energy K_α is radiated). However, the transition from more distant shells can occur resulting in different energies, such as K_β, K_γ, etc. The emission of photons due to the de-excitation of electrons is known as characteristic radiation represented by discrete lines in the X-ray spectrum (see Figure 4).
3) If the electron interacts directly with the nucleus, the entire energy of the electron is transferred to *Bremsstrahlung* with the maximum energy of the X-ray spectrum. However, the probability of this phenomenon is low, as demonstrated by the low intensity of high energy X-rays in Figure 4.

The combination of the three phenomena described above forms so called X-ray spectrum; an example of such spectrum is shown in Figure 4.

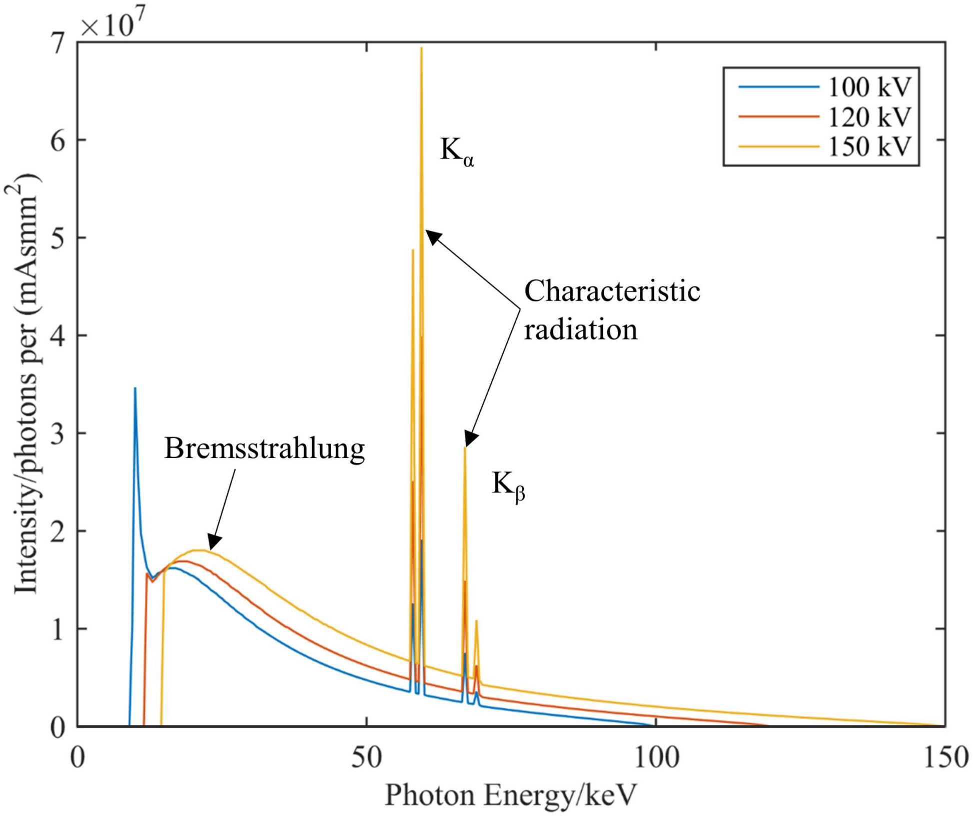

Figure 4. X-ray spectrum at acceleration voltage 100 kV, 120 kV, and 150 kV; the continuous curve represents *bremsstrahlung*, whereas the characteristic radiation is defined by discrete peaks. X-ray spectra were obtained by software SpekCalc [16].

Two main factors that influence the shape of X-ray spectrum and the intensity of X-rays are acceleration voltage and tube current. The acceleration voltage determines both the “quality” and the “quantity” of the X-ray beam. In other words, voltage affects both the energy interval and the amplitude, which can be observed in Figure 4. On the other hand, the tube current generates a linear increase in X-ray intensity, keeping the distribution of X-ray energies unchanged. Therefore, only “quantity” (number of emitted X-ray quanta) can be modified by altering the tube current. The effect of modifying the tube current is shown in Figure 5-a.

The unfiltered X-rays spectrum is composed of photons with a wide range of wavelengths. Low-energy X-rays (soft) are more easily attenuated by matter than those with high energy (hard). As a result, an artefact called beam hardening can be observed in scanned data, affecting the quality of the reconstructed volume. This phenomenon can be partially (or completely) eliminated by applying physical filtering to the X-ray beam. Physical filters are usually in form of a metal sheet (copper, aluminum, tin, etc.) with thickness typically ranging from 0.1 mm to several millimeters. These filters are placed between the X-ray source and the scanned object to harden the X-ray beam. The filtered X-ray spectrum has lower intensity; however, it has higher average energy at the same time. The effect of filtering is shown in Figure 5-b.

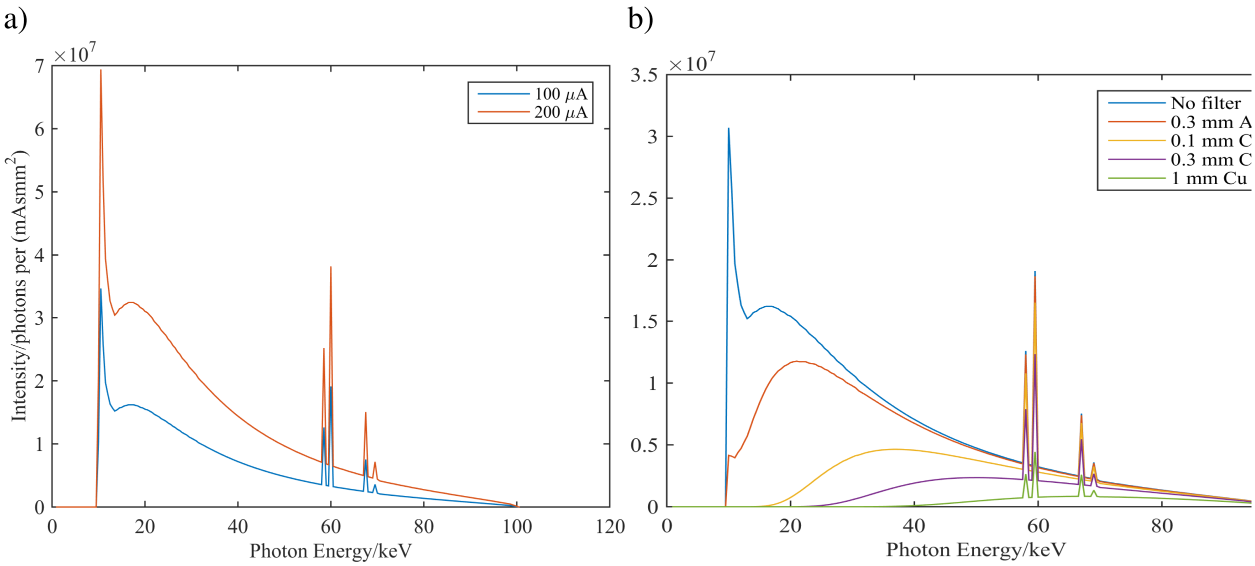

Figure 5. Effects of scanning configuration on X-ray spectra: a) effect of tube current, b) effect of filtering. X-ray spectra were obtained by software SpekCalc [16].

2.2.2 Attenuation of X-rays

After the X-rays are emitted from the source, they are directed towards the workpiece. When X-rays pass through an object, the intensity of the X-ray beam is reduced exponentially due to changes in the number, energy and direction of the incoming photons. This phenomenon is called attenuation and is defined by four different processes [11,17,18]: (i) photoelectric effect μ_{pe}, (ii) Compton scattering μ_{compt}, (iii) Rayleigh/Thomson scattering μ_{ray}, and (iv) pair production μ_{pp}. The total attenuation of X-rays in the penetrated object is determined by the sum of the four contributions:

$$\mu = \mu_{pe} + \mu_{compt} + \mu_{ray} + \mu_{pp}. \tag{2.3}$$

The contribution of individual processes to the total attenuation depends on the energy of the X-rays and the properties of the irradiated material.

The Beer-Lambert law describes the attenuation of X-rays in a material:

$$I(x) = I_0 e^{-\mu x}, \tag{2.4}$$

where I_0 is the incident X-ray intensity, and I is the intensity of X-rays after travelling through a material with attenuation coefficient μ and thickness x. Equation 2.4 works with an assumption that the penetrated material is homogeneous and the beam is monochromatic, which is not realistic in common industrial CT applications. Therefore, in the case of a non-homogeneous workpiece, Equation 2.4 is modified to account for varying attenuation coefficients:

$$I(L) = I_0 e^{-\int_0^L \mu(x) dx}, \tag{2.5}$$

where *μ(x)* is the attenuation coefficient that varies with the penetration depth x, and *L* is the total material thickness. In order to account for the entire spectrum of the X-rays, the Beer-Lambert law is integrated over all photon frequencies:

$$I(L) = \int_0^{E_{max}} I_0(E) e^{-\int_0^L \mu(E,x)dx}\, dE, \tag{2.6}$$

where *E* is the energy of X-rays. However, Equation 2.5 is typically used in practice for simplicity, which is one of the reasons for beam hardening artefacts in CT reconstructions. The process of attenuation is schematically described in Figure 6.

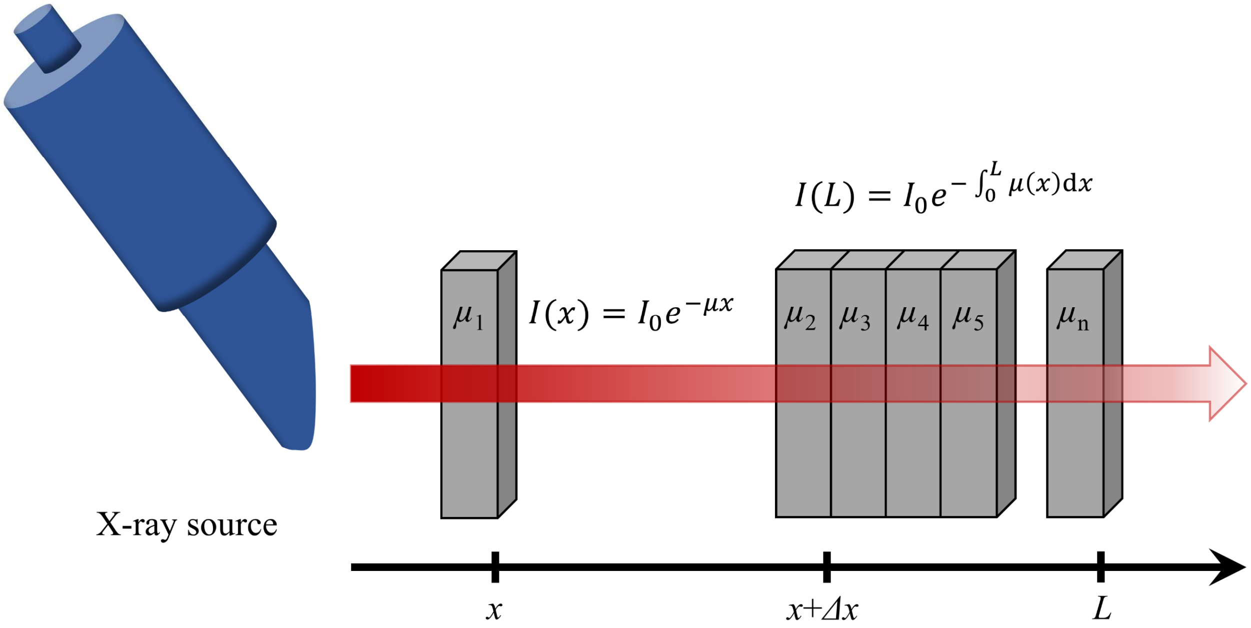

Figure 6. Attenuation of X-rays. Left: attenuation in the case of a homogenous object with an attenuation coefficient μ_1 and thickness *x*. Right: Attenuation for an object composed of different materials with different attenuation coefficients μ_2, μ_3… μ_n.

2.2.3 Detection of X-rays

The X-rays that are not completely attenuated by matter interact with the surface of a detector. The detector surface consists of X-ray sensitive elements, typically scintillators and ionization chambers. These elements emit light when excited by ionizing radiation [3]; the amount of emitted light is ideally proportional to the intensity of incident X-rays. Subsequently, the emitted light in each pixel of the detector is converted into a gray value (GV). Hence, each detector pixel contains the information of the total attenuation of the X-rays along the linear trajectory connecting the source with the corresponding pixel. The information stored in individual pixels form a radiographic image, also called radiograph or projection.

2.3 Principle of X-ray computed tomography

The CT scanning process starts with the acquisition of radiographic projections, described in the previous sections, at multiple object viewing angles. Subsequently, a 3D volumetric model of the workpiece can be generated by applying reconstruction algorithms. The reconstructed volume is composed of 3D pixels, so called voxels. Each voxel is determined by a gray value corresponding to the local attenuation of the material within the measurement volume [19]. The gray value information can be then used for further data post-processing, such as surface determination, and segmentation. A schematic representation of a typical CT scanning procedure is shown in Figure 7.

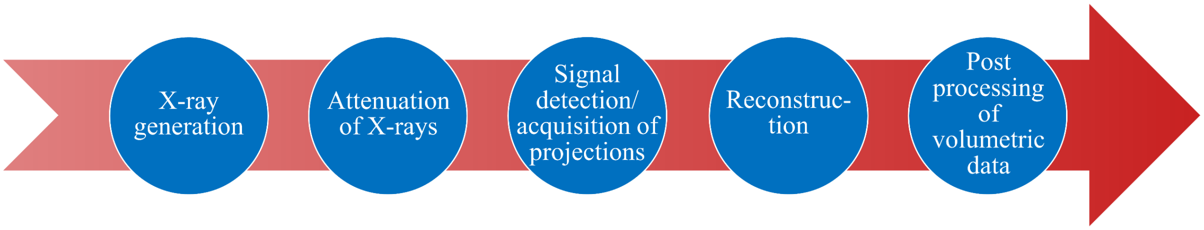

Figure 7. Schematic representation of a typical CT scanning workflow.

The most significant difference between current medical and industrial CT systems is the configuration of the main CT components, i.e. X-ray source, rotary stage and detector. Whereas the X-ray source and the detector rotate around the patient in common medical CT systems, the rotary stage performs the rotary movement in typical industrial CT machines. The reason is twofold: (i) in medical CT, the movement of the patient should be minimized, and (ii) inspection of industrial parts often requires high resolution and accuracy; thus, limiting the motion of the gantry (i.e. X-ray source and detector) is critical with respect to reducing additional error sources. Further details on the principle of CT can be found e.g. in [3,11].

2.3.1 Configuration of CT system

CT acquisition process is based on the concepts of projective geometry, where X-rays are projected from a source onto a detector [19]. Depending on the shape of X-ray beam, two different detector shapes are employed in typical industrial CT systems: (i) flat panel detector for cone-shaped beam (Figure 8-a), and (ii) line detector for fan-shaped beam (Figure 8-b). The configuration with fan beam allows acquisition of individual slices; therefore, in order to image larger volumes, multiple linear slices must be acquired and stitched together. This requires combination of rotational and translational movement of the scanned sample, as well as longer scanning times. Shortfalls of fan-beam can be overcome by the second configuration, i.e. using cone-beam CT systems. In this case, the whole workpiece is imaged in each angular position of the rotary stage; hence, no additional linear translation is necessary. This approach brings significant reduction of required scanning time, however, several problems arise, such as cone beam artefacts, increase of scattered radiation detected on larger detector area, etc.

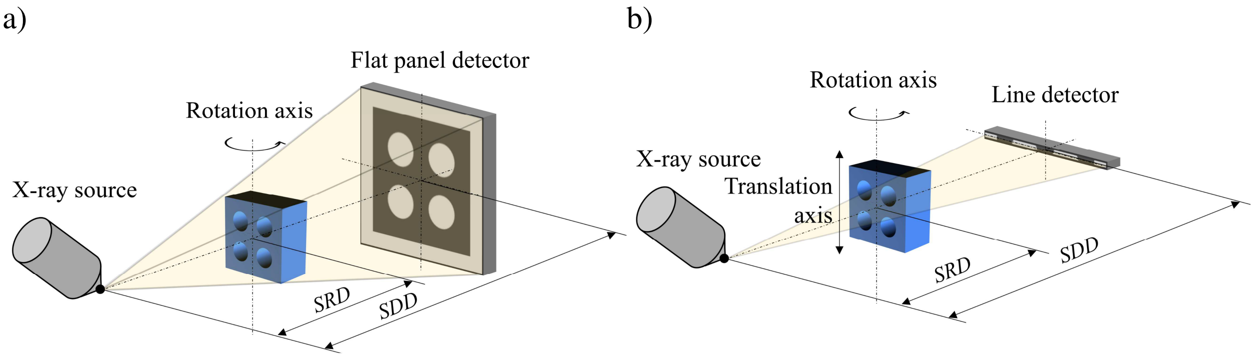

Figure 8. Two common industrial CT configurations: a) cone-beam CT with flat panel detector, b) fan-beam CT with line detector.

This thesis pertains mainly to cone-beam CT systems as they provide advantageous ratio between accuracy and scanning time, and are widely used in industry. Therefore, the acronym CT will be referred to cone-beam systems henceforth in this thesis, unless otherwise specified.

Several parameters, such as tube current and voltage, position and orientation of the object, exposure time, number of projections, etc. must be set prior to scanning. These scanning parameters are determined based on the size and shape of the scanned part, the material of which the workpiece is constructed, and the aim of the CT analysis. In CT dimensional metrology, the parameters are typically optimized in order to achieve the highest resolution possible. One of the major factors that determines the resolution of CT scan is geometrical magnification. Since the X-ray beam is divergent, magnification can be modified by changing the distance of the canned object from the X-ray source. More specifically, by positioning the object closer to the source, higher magnification, and, therefore, higher resolution can be achieved. Another significant aspect that influences the resolution of CT scan is focal spot size. Given the extreme heat load, the electron beam cannot be focused on infinitely small point on the target. As a result, a certain amount of edge blurring is present in the acquired projections depending on the spot size. This so-called penumbra effect is schematically described in Figure 9.

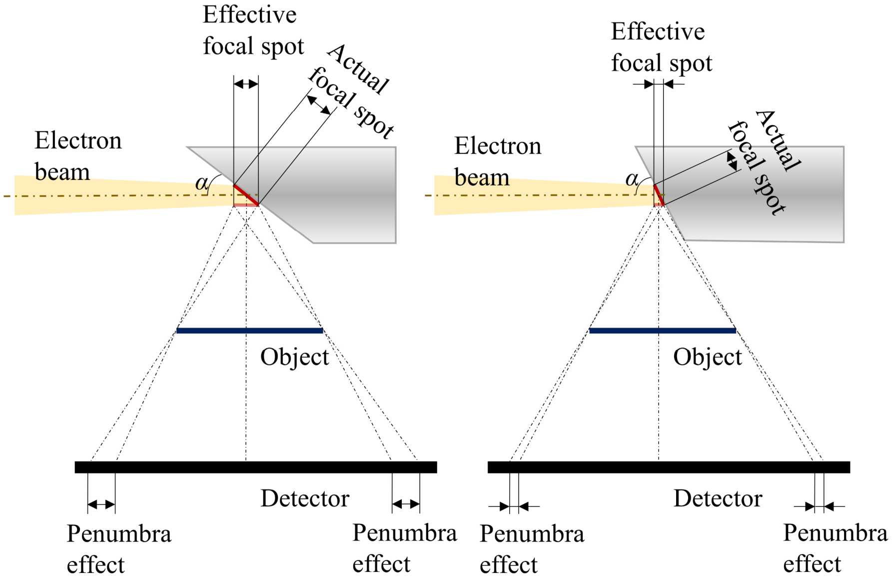

Figure 9. Edge blurring caused by finite focal spot size. The effect of the target angle is demonstrated by two different values of α. Adapted from [15].

Two main factors determine the focal spot size: (i) tube power, which is proportional to the amount of heat transmitted to the target), and (ii) the orientation of the target with respect to the electron beam.

The geometrical magnification M is defined as the ratio between source-to-detector and source-to-rotation-axis distance, denoted in Figure 8 as SDD and SRD, respectively, according to formula:

$$M = \frac{SDD}{SRD}. \tag{2.7}$$

Voxel size (VS) is determined by the magnification M and pixel size p:

$$VS = \frac{p}{M}. \tag{2.8}$$

It should be noted that, due to finite dimensions of the scanned object, different portions of the part are magnified with different magnification depending on their location with respect to the magnification axis (i.e. the line connecting the X-ray source and the detector center). Therefore, only the portion that belongs to the plane defined by the rotation axis and parallel to detector is magnified with factor M. Furthermore, due to the cone-shaped beam and assumptions implemented in reconstruction algorithms, all slices except for the one located in the central plane (i.e. plane orthogonal to the detector and the rotation axis) are affected by beam (Feldkamp) artefacts [20]. These effects are pronounced at the borders of the detector, and for higher magnifications as the object occupies larger X-ray opening angles.

2.3.2 Reconstruction

Reconstruction algorithms are applied on projections acquired in the preceding step according to Figure 7 to obtain a 3D volumetric model of the workpiece. Most common reconstruction methods are based on the “Linear Integral Transformation” described by Johann Radon in 1917 [21], where the absorption of X-rays when passing through a medium with varying linear attenuation coefficient μ is described.

Feldkamp, Davis and Kress developed, based on principles described in Radon’s publication [21], an algorithm to reconstruct a 3D density model from a set of 2D radiographic projections (Feldkamp or FDK method). This algorithm, known as “filtered back projection”, is commonly applied to cone-beam computed tomography systems [22]. As a result of tomographic reconstruction, a 3D volumetric model of the scanned object is obtained. The model is comprised of 3D voxels (volumetric pixels) that represent the gray value corresponding to the local material attenuation at the voxel position within the measurement volume. The principle of reconstruction is schematically explained on an example in Figure 10. In this case, an object composed of 4 × 4 × 4 voxels is imaged at four different angles (i.e. four projections are taken). The two colored voxels represent different attenuation coefficients μ.

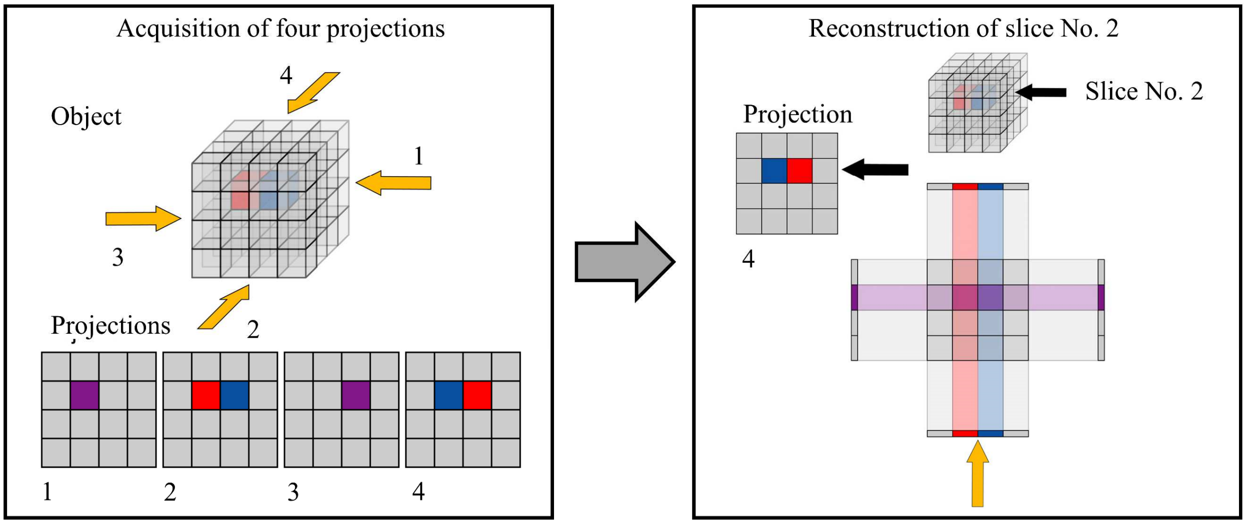

Figure 10. Principle of tomographic reconstruction. Courtesy of GE Sensing & Inspection Technologies GmbH.

2.3.3 Industrial applications of CT

CT provides a holistic volumetric model of the scanned object that can be used for various inspection tasks and dimensional measurements, as well as for reverse engineering applications [4]. The main applications of CT can be found in automotive and aerospace industry for quality control of complex parts. CT is also often used for the inspection of components with internal and micro features produced by promising technologies, such as AM or µ-injection molding. The non-destructive attribute of CT is also utilized in the quality control of assemblies [4].

CT industrial applications can be divided into two different groups: (i) voxel based, qualitative evaluation, and (ii) surface based, quantitative evaluation [4].

Voxel based evaluations can be further divided into [4]:

- Visualization – quality inspection by visualizing e.g. components of assembled workpieces. Typical inspection tasks comprise verification of the interplay or the existence of components, as well as functional analysis of the assembly.
- NDT – CT offers a vast range of NDT applications, such as defect analysis and material characterization. By evaluating CT scanned data, pores, voids, inclusions or cracks can be detected and analyzed, and possible weak spots of the workpiece can be identified. Furthermore, several material characteristics can be inspected; e.g. fiber orientation analysis, density of individual materials in multi-material components, etc. Results of CT NDT can contribute to improving manufacturing processes, such as AM, injection molding, etc.

Surface based evaluations can be further divided into [4]:

- Digitization – a virtual model can be extracted from CT data opening new possibilities in simulations and reverse engineering. The most significant benefit of using CT instead of a simplified CAD models is that manufacturing defects, such as voids, cracks, etc., and actual external and internal geometry of the workpiece are captured in the CT data. This makes simulations (e.g. finite element method) more realistic. Furthermore, the surface of the virtual model can be extracted and used for reverse engineering applications, such as building spare parts, building prototypes, etc.

- Metrology – according to VDI/VDE 2630-1.2 [23], dimensional measurement tasks in industrial CT can be classified into three groups: (i) nominal/actual comparison (either based on nominal or reference geometry), (ii) analysis of size, shape and position tolerances and determination of compensating elements of ruled geometries and free-shape surface, and (iii) wall thickness analysis.

A summary of CT industrial applications, as well as examples of results are shown in Figure 11.

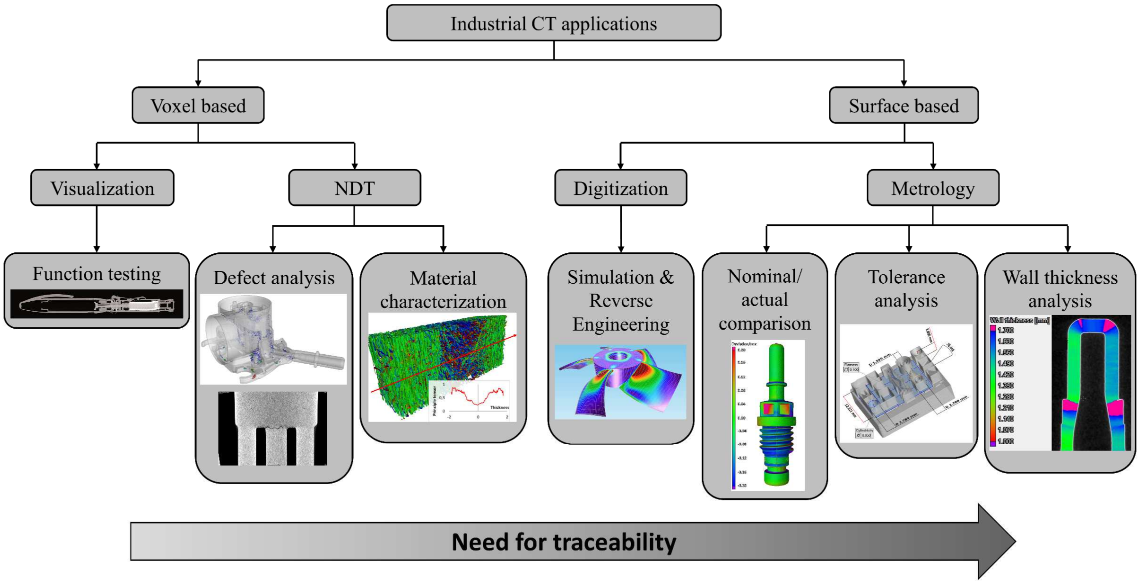

Figure 11. Industrial applications of CT. Adapted from [4].

A thorough review of industrial CT applications can be found in [4].

2.4 CT in dimensional metrology

Dimensional inspection of industrial parts is a critical aspect of quality control. CT offers several advantages over conventional tactile and optical CMSs, such as the possibility to measure inaccessible surfaces without destructing the workpiece. As schematically explained in Figure 11, dimensional metrology is a surface based CT application. Therefore, surface determination is the first step in the CT dimensional measurement chain (see Figure 12).

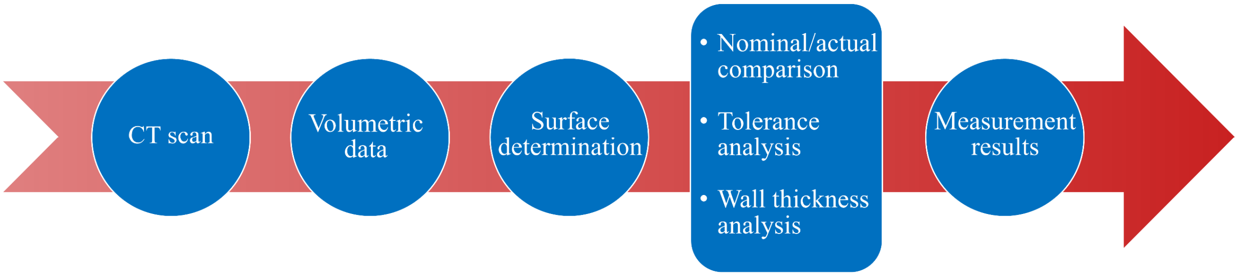

Figure 12. Schematic representation of the CT dimensional measurement chain.

2.4.1 Surface determination

Since individual voxels of measurement volume are determined by gray values that correspond to varying material properties, the edge between two materials can be defined by a transition in gray values. Determination of the threshold value between different materials is a critical aspect in surface extraction and data segmentation. Typically, ISO-50% value, determined as the arithmetic mean value between the background and the material peak, is used for thresholding. The two (or more, depending on the number of materials in the scanned part) peaks can be identified from the histogram of gray values. Currently, there are two common ways to apply the threshold value: (i) globally, and (ii) locally.

Global thresholding is the historically older method, which simply applies the threshold value to the whole dataset. This method, however, requires that the data be homogeneous and without artifacts; otherwise, fluctuations of gray values even within single material can be observed in the analyzed data causing inaccurate surface determination. In practice, however, any real scan suffers to a certain extent from image artifacts, such as beam hardening, scattered radiation or cone beam artifacts. Therefore, local changes in gray values should be considered in order to improve the accuracy of the thresholding. This can be achieved by applying local adaptive thresholding. The method uses a threshold value (e.g. ISO-50%) as a starting point in the first step. In the second step, the algorithm searches for local gradients within the voxel range defined by the user and defines the surface accordingly. The local adaptive method is considered the state-of-the-art concerning surface determination. Comparison between the two different methods can be found e.g. in [22].

2.4.2 Dimensional measurements

CT dimensional measurements are performed on the surface determined in the previous step. VDI/VDE 2630-1.2 [23] defines three different measurement tasks as discussed in Section 2.2.3 and schematically shown in Figure 11.

In the first case, i.e. nominal/actual comparison, the CT data are compared to a reference dataset. The reference can be represented either by a nominal CAD file or another CT dataset. The results are typically represented by a color map of deviations from reference. An example of nominal/actual comparison is shown in Figure 13-a, where a polymer part was measured.

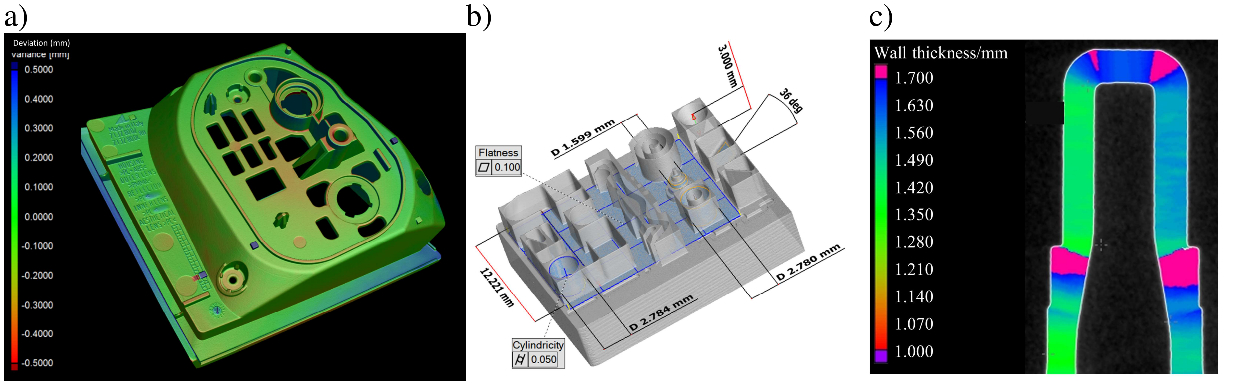

Figure 13. Examples of CT dimensional measurements: a) nominal/actual comparison, b) verification of tolerances, c) wall thickness analysis.

The verification of tolerances is performed on geometric primitives, i.e. spheres, planes, cylinders, etc., fitted on the determined surface. These features are subsequently used for measuring dimensional (e.g. length, diameter) and geometrical (e.g. form error, planarity) characteristics. An example of CT tolerances verification is shown in Figure 13-b.

Wall thickness analysis is used to measure perpendicular distances between opposite surfaces throughout the whole dataset (or a region of interest). As a result, a color map of wall thickness distribution is calculated (see an example of wall thickness analysis in Figure 13-c).

2.4.3 Advantages and limitations of CT dimensional metrology

CT offers several advantages as an alternative measuring instrument to conventional tactile and optical CMSs. The most significant benefit is the fact that CT is so far the only technique that can measure inaccessible surfaces without an invasive intervention. This is in particular important considering the fact that destructive methods can cause relaxing of materials, deflections etc. Another advantage of CT is its unique ability to acquire high-density information of the scanned object that can be used for multiple analyses. In terms of material, the only limit for CT is the attenuation coefficient, whereas tactile and optical CMS have difficulties e.g. when measuring certain materials, and problems with contamination between the probe and the workpiece material can occur. Flexible parts are also not suitable for contact methods, whereas reflexive surfaces and complex 3D features are problematic for optical systems.

However, these advantages are counterbalanced by several shortfalls. The fact that CT is a versatile measurement instrument, complex influencing factors come into the measurement process hindering the evaluation of measurement uncertainty. As a result, the establishment of CT measurement traceability is a challenging task. Furthermore, since CT is still relatively new technique for dimensional metrology, there is a lack of international standards. Another issue pertains to the different nature of the acquisition of measurement points between different CMSs. These differences described e.g. in [24] cause difficulties in comparing data obtained by different techniques. In particular, the point density is significantly different between CT (high density) and tactile CMS (low density). Moreover, surface roughness is captured differently by different techniques causing discrepancy between the measurement results [25].

Advantages and limitations of CT dimensional metrology are summarized in Table 4.

Table 4. Advantages and limitations of CT dimensional metrology. Adapted from [22].

Advantages	Limitations
Non-destructive technique	Complex and numerous influence quantities
Measurements of internal and external geometries	No accepted international test procedures and standards
High information density	Reduced measurement capability due to measurement errors (artefacts)
Multiple analyses on one dataset	Measurement uncertainty often unknown – results not traceable
Possibility to scan any surface, shape, color or material up to a certain attenuation coefficient and thickness penetrable by X- rays	Problems with scanning multi-material objects

3 TRACEABILITY OF CT DIMENSIONAL MEASUREMENTS

This chapter gives a brief introduction about the state-of-the-art of CT dimensional measurements, and discusses the current state of traceability in CT dimensional metrology. Essential requirements and tools for the traceability, as well as major problems related to the establishment of CT measurement traceability are discussed in this chapter. CT standardization platform, and principles defined by standards related to CT dimensional metrology are described here. Subsequently, factors that influence CT measurement accuracy are summarized. Finally, a thorough review of existing reference objects for CT dimensional metrology is given.

3.1 Introduction to CT traceability

In order to bring CT dimensional metrology to the same level of maturity of conventional tactile and optical CMSs, CT measurement results must be traceable to the SI unit (i.e. meter, in the case of dimensional measurements). Metrological traceability is described in VIM [6] as "property of a measurement result whereby the result can be related to a reference through a documented unbroken chain of calibrations, each contributing to the measurement uncertainty". Calibration is, according to VIM [6], defined as "operation that, under specified conditions, in a first step, establishes a relation between the quantity values with measurement uncertainties provided by measurement standards and corresponding indications with associated measurement uncertainties and, in a second step, uses this information to establish a relation for obtaining a measurement result from an indication". The Guide to the Expression of Uncertainty in Measurement (GUM) [26] requires that each source of error be determined and its quantity propagated to uncertainty in the measurement result. This requirement, however, is challenging for CT dimensional measurements for several reasons: (i) CT suffers from complex and numerous influence factors, (ii) many of these influencing factors are not thoroughly studied and quantified yet, which results in difficulties in the evaluation of their contribution to the measurement uncertainty, and (iii) lack of international standards.

The process of achieving metrological traceability in general (i.e. pertaining to all kinds of CMSs, including CT) can be divided into three steps: (i) metrological performance verification according to international standards, (ii) calibration, and (iii) evaluation of measurement uncertainty. An additional step should be defined to cover the versatility of CT instrument: (iv) metrological performance verification of CT specific applications.

A series of international standards ISO 10360 describes procedures for metrological performance verification of tactile and optical CMSs. However, the part related to CT systems is still under development. The only existing reference that describes the application of ISO 10360 for coordinate measuring systems with CT sensors is the German guideline VDI/VDE 2630-1.3 [27]. Due to the numerous and complex CT influencing quantities, a general calibration of CT instrument is not possible. Furthermore, the implementation of GUM [26] method for the evaluation of measurement uncertainty is challenging for the same reason. Therefore, a substitution method based on the use of calibrated workpieces is typically applied to CT measurements. This approach is described in ISO 15530-3 [28] for CMSs in general and in VDI/VDE 2630-2.1 [29] for CT.

The aim of the ongoing research in CT dimensional metrology is to develop an infrastructure of procedures and standards based on the same principles that are applied to conventional tactile and optical CMSs. One of important means to investigate individual CT influencing factors, evaluate the metrological performance of CT, calibrate CT system to specific tasks, and evaluate the measurement uncertainty is the development of dedicated reference standards, which is the aim of this Ph.D. project.

3.2 CT standardization platform

Historically first CT industrial applications are related to NDT; therefore, this field is covered, in terms of standardization, more in detail with respect to CT dimensional metrology. However, the ongoing research in CT resulted in a committee draft of ISO 10360-11 [30] related to acceptance and reverification test for CT, and several guidelines. An overview of existing relevant CT standards and guidelines is presented in Table 5.

Table 5. Summary of relevant international standards and guidelines related to industrial CT.

Standard/guideline	Description
ISO/CD 10360-11	Geometrical Product Specifications (GPS) – Acceptance and reverification tests for coordinate measuring systems (CMS): CMMs using the principle of computed tomography (CT) [30]
VDI/VDE 2630: Computed tomography in dimensional measurement	Part 1.1: Basics and definitions [1]
	Part 1.2 Influencing variables on measurement results and recommendations for computed-tomography dimensional measurements [23]
	Part 1.3 Guideline for the application of DIN EN ISO 10360 for coordinate measuring machines with CT sensors [27]
	Part 1.4: Measurement procedure and comparability [31]
	Part 2.1: Determination of the uncertainty of measurement and test process suitability of coordinate measurements systems with CT sensors [29]
ISO 15708: Non-destructive testing – Radiation methods – Computed tomography	Part 1: Principles [32]
	Part 2: Examination practices [33]
EN 16016 – Non/destructive testing – Radiation method – Computed tomography	Part 1: Terminology [34]
	Part 2: Principle, equipment and samples [35]
	Part 3: Operation and interpretation [36]
	Part 4: Qualification [37]
ASTM E 1441-11	Standard guide for computed tomography (CT) imaging [38]

ASTM E 1695-95	Standard test method for measurement of computed tomography (CT) system performance [39]
ASTM E 1570-11	Standard practice for computed tomographic (CT) system examination [40]
ASTM E 1672-12	Standard guide for computed tomographic (CT) system selection [41]

Substantial research efforts on international standardization level are put into the development of a standard for acceptance and reverification tests for CT, i.e. the standard that will become a part of ISO 10360 series. The committee draft is currently being discussed within the Working Group 10 of the ISO Technical Committee 213; however, it has not concluded its development and, therefore, has not been published yet. The basic idea applied in the ISO/CD 10360-11 [30], as well as in the German guideline VDI/VDE 2630-1.3 [27], is to adapt the knowledge and methods from conventional tactile and optical CMSs to CT. Therefore, several attributes that are evaluated in e.g. ISO 10360-2 [42] (acceptance and reverification tests for tactile CMSs) are also evaluated in the method proposed in ISO/CD 10360-11 [30]; e.g. probing P and length E measurement errors. A short description of the method currently proposed in ISO/CD 10360-11 [30] is given below.

3.2.1 Performance verification according to ISO 10360-11 committee draft

The method is based on repeated measurements of reference standard(s) under specified conditions. Measurement results are subsequently evaluated and compared to Maximum Permissible Errors (MPE). In addition to the probing P and length E errors, attributes related to workpiece material and geometry of the sample should be also evaluated in performance verification of CT systems. Finally, it is suggested to state the metrological structural resolution of the investigated CT system too (optional test in the current version).

Probing characteristics

These errors describe 3D error behavior within a very small measurement volume of the entire CT system. The test provides information how well the system can measure a specific point on the workpiece (a test sphere) surface. Since the magnification at which the object is scanned may affect the measurement errors, at least two different magnifications should be chosen for probing errors testing. These two magnification values M_1, M_2 should cover at least 66% of the magnification range, i.e. $M_2 - M_1 > 0.66 \cdot (M_{\mathrm{max}} - M_{\mathrm{min}})$, where M_{max} and M_{min} are maximum and minimum limiting values of the magnification and $M_2 > M_1$. Following characteristics should be evaluated while testing probing errors of a CT system:

- *Probing form error* $P_{\mathrm{Form.Sph.1x25::CT}}$ – the span of radial deviations of the 25 measurement points from the least-squares fitted sphere. $P_{\mathrm{Form.Sph.1x25::CT}}$ is calculated as the difference between the maximum R_{max} and minimum R_{min} distance of the probing points from the center of the fitted sphere, i.e. $P_{\mathrm{Form.Sph.1x25::CT}} = R_{\mathrm{max}} - R_{\mathrm{min}}$.
- *Probing dispersion error* $P_{\mathrm{Form.Sph.D95\%::CT}}$ – the smallest possible width of all spherical shells that contains 95 % of all data points when fitting a sphere to the measurement data of the test sphere.

- *Probing size error* $P_{\mathrm{Size.Sph.1x25::CT}}$ – the difference between sphere's measured diameter D_a and calibrated value D_r using a least-squares sphere fitted on 25 measurement points. $P_{\mathrm{Form.Sph.1x25::CT}} = D_a – D_r$.
- *Probing size error All* $P_{\mathrm{Size.Sph.All::CT}}$ – the difference between sphere's measured diameter D_a and calibrated value D_r using a least-squares sphere fitted on all measurement points. $P_{\mathrm{Size.Sph.All::CT}} = D_a – D_r$.

Length measurement errors/Basic length measurement errors

The length measurement error describes the 3D error behavior of the CMS in the entire measurement volume. Similarly to the probing errors, this test should be performed in two different magnifications as described earlier in this section. Furthermore, to separate the influence of the penetration length, two types of length measurements are defined: (i) length measurement error $E_{\mathrm{Bi::CT}}$ ($E_{\mathrm{Uni::CT}}$), which requires the metrological characteristic also to cover the case of penetrating a significant amount of material, and (ii) basic length measurement error $E_{\mathrm{Bi.base::CT}}$ ($E_{\mathrm{Uni.base::CT}}$), which does not comprise the penetration of a significant amount of material. Since metrological characteristics can be significantly influenced by the attenuation properties of the scanned material, the standard suggests performing (basic) length measurement errors test on three classes of materials: plastic like materials, aluminum like materials, and steel like materials (as per the version of the committee draft available in August 2017). The discussed standard [30] requires that true bidirectional length measurement errors (i.e. $E_{\mathrm{Bi::CT}}$ and $E_{\mathrm{Bi.base::CT}}$) be tested in order to take into account the local probing error. This is not possible e.g. when measuring sphere center to center distances (SD) where the local probing error is averaged due to the large number of probing points used for fitting the measurement sphere. In the case where only unidirectional (i.e. $E_{\mathrm{Uni::CT}}$ and $E_{\mathrm{Uni.base::CT}}$) measurements are possible, the standard [30] suggests corrective means to ensure comparability with bidirectional measurements. The reference standard should be measured in two different positions and the total number of the length measurements shall be equal or larger than 105 (as defined also in ISO 10360-2 [42]).

The bidirectional test length is calculated from the distance between two measurement points on opposite surfaces. The difference between the measured lengths L_a and the calibrated length L_r of the reference standard, is the length measurement error $E_{\mathrm{Bi::CT}}$/basic length measurement error $E_{\mathrm{Bi.base::CT}}$: The formula is as follows: $E_{\mathrm{Bi::CT}}$ ($E_{\mathrm{Bi.base::CT}}$) $= L_a – L_r$.

Reference standard

Calculation of the probing errors involves spheres or spherical caps or special arrangements of several spheres or spherical caps made of suitable materials.

The reference standards for length measurement errors should be made of a material from the specified material classes. Preferably, it should be possible to perform bidirectional measurements on the workpiece covering short and long penetration lengths through metrologically used features. For this reason, asymmetric objects are suggested by the standard [30]. The measurements can be performed on both internal and external geometries. The calibration uncertainty should be significantly lower than length measurement error MPE, and the roughness *Rz* and form error of measurement features should be lower than 20 % of any probing error MPE. Following types of reference standards are proposed in [30]:

- Hole plate – holes are drilled/milled in a square-shaped outer geometry, and the hole distances are calibrated.
- Sphere/hole plate – A hole plate with a square-shaped outer geometry where each hole is filled symmetrically with a sphere having a diameter of 50%-75% of the diameter of the holes. The sphere distances are calibrated.
- Calotte cube – hemispheres (calottes) are milled into a cube-shaped body, and the calotte distances are calibrated.
- Ball bars / ball rails – a 1D array of spheres mounted on a framework. The sphere distances are calibrated.
- Ball plates / multi-sphere objects – 2D or 3D arrays of spheres. The sphere distances are calibrated.

Metrological structural resolution

The structural (also called spatial) resolution describes the size of the smallest structure that can still be measured dimensionally at a given magnification [27]. Evaluating metrological structural resolution is a critical factor when determining characteristics that specify measuring system accuracy. It shall be stated for CT since e.g. filtering can improve the probing results and decrease the metrological structural resolution at the same time.

However, currently no international standard describes a method for determining the metrological structural resolution; it is still a topic of ongoing research [43,44]. The committee draft of ISO 10360-11 [30] suggests possible methods that are based on procedures described in ISO standards related to optical CMSs and CT (ISO 10360-8 [45], ISO 15708-1 [32], and 15708-2 [33]).

3.2.2 Evaluation of measurement uncertainty

According to GUM [26], uncertainty is a "parameter, associated with the result of a measurement, that characterizes the dispersion of the values that could reasonably be attributed to the measurand". A valid statement of measurement is necessary in order to ensure traceability of measurements. GUM [26] requires that each source of error be determined and its quantity propagated to uncertainty in the measurement result. However, this approach is usually not applicable to CT measurements due to the complex and numerous error sources. Therefore, an alternative approach is commonly applied in determining measurement uncertainty of CT dimensional measurements. Typically, empirical methods are used for determining the uncertainty of CT measurements. These methods are based on the use of calibrated workpieces and are described in ISO 15530-3 [28] for tactile coordinate measuring systems and in VDI/VDE 2630-2.1 [29] specifically for CT systems. Both approaches are based on the same principles with small differences; the method is briefly explained below.

The general aim of methods described in [28,29] is to provide an experimental technique for simplifying the evaluation of measurement uncertainty. The approach is based on measuring calibrated workpieces or measurement standards of similar dimensions and geometry the same way as actual parts. In this way, the individual factors influencing uncertainty are determined mainly by means of measurements. Several steps need to be performed when evaluating the uncertainty according to [28,29]:

1) A workpiece identical to workpiece(s) to be tested should be chosen. If this is not possible, the workpiece should be similar in terms of dimensions, shape and material. Attention must

be payed also to maximum penetration lengths. This workpiece is subsequently calibrated with a CMS ensuring that low measurement uncertainty be achieved.

2) The calibrated workpiece is measured with the CT scanner using the same measurement strategy that is intended to be used on the workpiece to be measured. The measurement should be repeated 20 times under different conditions. ISO 14253-1 [46] suggest using a safety factor in case lower number of repeated measurements is performed. However, this procedure is not recommended for CT systems, where statements based on very low number of measurements appear to be not reliable. The standard uncertainty of measurement u_p is determined as

$$u_p = \sqrt{\frac{1}{n-1} \cdot \sum_{i=1}^{n} (y_i - \bar{y})^2}, \tag{3.1}$$

where n is the number of measurements, y_i is the value indicated by CT and $\bar{y}$ is the mean value of the measurement result.

3) The uncertainty of measurement is calculated using the following equation:

$$U_{MP} = k \cdot \sqrt{u_{cal}^2 + u_{drift}^2 + u_p^2 + u_w^2 + u_b^2}, \tag{3.2}$$

where

U_MP is the expanded uncertainty of measurement of the measurement process,

k is the coverage factor (typically, $k = 2$ is used, which corresponds to a confidence level of 95 %),

u_cal is the standard uncertainty of measurement due to the uncertainty of calibration of the calibrated workpiece calculated from the extended standard uncertainty U_cal stated in the calibration certificate

$$u_{cal} = \frac{U_{cal}}{k}, \tag{3.3}$$

u_drift is the standard uncertainty of measurement due to the change (drift) in workpiece shape since the calibration referred to,

u_p is the standard uncertainty of measurement due to the measurement process,

u_w is the standard uncertainty of measurement due to variations between the calibrated and actual workpiece, e.g. coefficient of thermal expansion, form errors, roughness, elasticity, plasticity, etc.,

u_b is the standard uncertainty of measurement of the correction of the systematic error b between the values y_i indicated by the CT and the calibrated value.

It should be noted that it is recommended to correct known systematic errors b between the mean value of CT measurements and the calibrated value y_cal; $b = \bar{y} - y_\mathrm{cal}$. If the correction is not possible, Equation 3.2 should by modified as follows:

$$U_{MP} = k \cdot \sqrt{u_{cal}^2 + u_{drift}^2 + u_p^2 + u_w^2 + b^2}. \tag{3.4}$$

A complete overview of methods for the evaluation of measurement uncertainty defined by international standards and guidelines is given in the following list:

- GUM [26] method based on the mathematical definition of the measurement model.
- Computer simulation according to GUM Supplement 1 [47].
- Empirical methods based on the determination of measurement uncertainty using calibrated workpieces ISO 15530-3 [28] and VDI/VDE 2630-2.1 [29].
- Uncertainty budget as per ISO/IEC GUIDE 98-3 [48].

3.3 CT influence factors

Influence factors contribute to CT measurement errors and are present in every step of CT measurement chain. The complex nature and large amount of CT influence factors is one of the reasons why achieving the traceability of CT dimensional measurements is a challenging task. Complete understanding, and quantification of individual factors, as well as the investigation of their influence on measurement results are a subject of ongoing research. A complete list of CT influence factors is given in VDI/VDE 2630-1.2 [23]. In this Ph.D. theses, only a short overview of influence factors will be described; a simplified list is shown in Table 6. Further details can be found directly in [20].

Table 6. CT influence factors. Adapted from [22,23]

Category	Influence factor
X-ray source	Spectral characteristics Focal properties Stability
Mechanical axes	Geometrical errors Mechanical stability
Detector	Position and orientation Geometrical distortions Scattering Noise Quantum efficiency Stability
Environment	Temperature Humidity Vibrations
Workpiece	Surface roughness Penetration length X-ray scattering

	Geometry Beam hardening Material composition
Operator settings	Source current and voltage Pre-filtration Detector exposure time Object mounting and orientation Number of projections Magnification
Data processing	Reconstruction Data filtering Threshold determination

3.4 CT reference standards

Reference standards are a typical means to investigate and quantify influence factors, reduce systematic errors, compare different metrological systems, and facilitate achieving traceability of dimensional measurements in general. Compared to optical and tactile CMSs, where suitable reference standards have already been established and partially standardized [2], there is still lack of these objects dedicated to CT. Different reference standards have been proposed for CT, many of which were inspired by corresponding objects designed for conventional CMSs. In this section, an overview of CT related reference standards is presented. The standards are divided into four sections related to four mainstays towards the establishment of CT measurement traceability: (i) metrological performance verification and scale error correction, (ii) metrological performance verification of CT specific applications, (iii) calibration, and (iv) evaluation of measurement uncertainty. It should be noted, however, that most of the objects presented in this chapter are multi-purpose. For this reason, the artifacts are categorized according to their main use.

3.4.1 Metrological performance verification and scale error correction

One of the first steps to accept new measurement technology as a metrological instrument is to verify its metrological performance. Procedures for optical and tactile CMSs are defined by ISO 10360 series, methods of which are based on measuring a calibrated reference standard(s). Working group 10 of the ISO TC 213 is currently working on a part of ISO 10360 related to CMSs with CT sensors (see Section 3.2 for further details). These objects are typically composed of spheres, holes or calottes arranged in a specific pattern [30]. Artifacts presented in this section can be typically used for different applications (besides metrological performance verification), such as scale correction, threshold determination, etc. Therefore, the use of each object presented here is discussed. For better interpretation, the artifacts are further divided into four groups: (i) standards with sphere arrangements, (ii) standards with hole/calotte arrangements, (iii) standards with plane-parallel features, and (iv) other standards.

Standards with sphere arrangements

These objects are the most common in CT dimensional metrology as spheres and distances between them offer several advantages over other geometries; e.g. when fitting spheres, thresholding errors with respect to sphere center identification are averaged over a large number of measurement points. An overview of examples of such artifacts is shown in Figure 14.

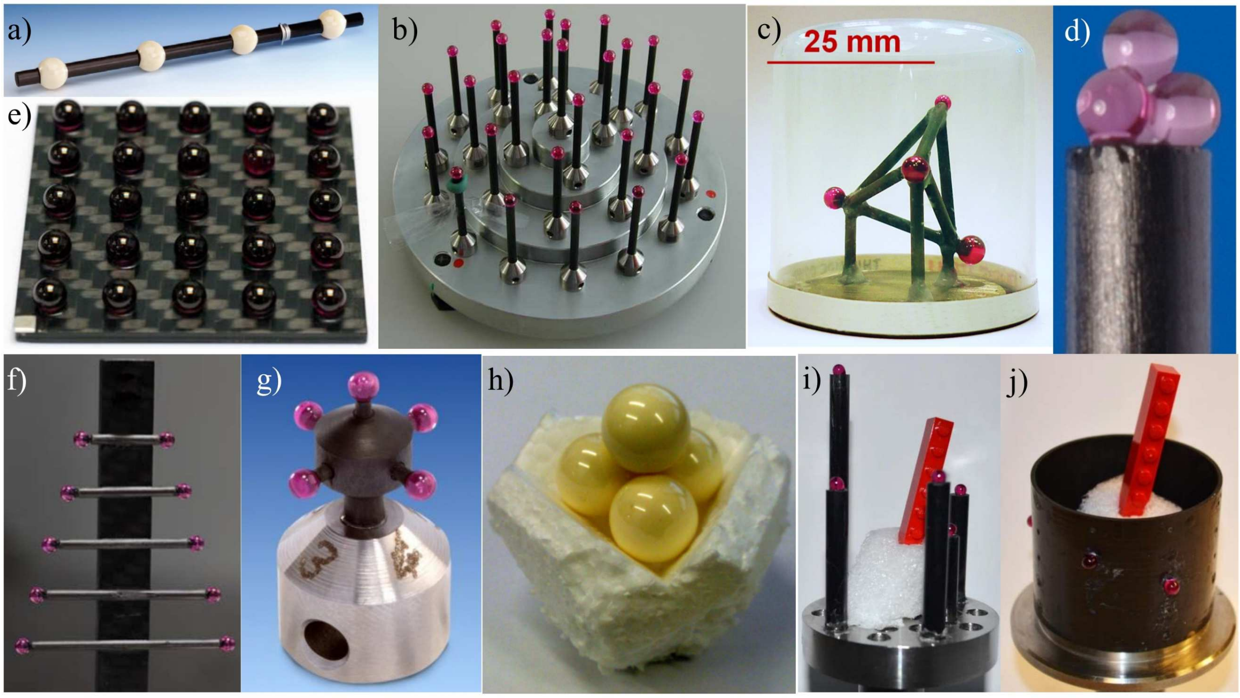

Figure 14. Examples of reference standards with sphere arrangements: a) ball-bar [8], b) 27-sphere gauge [49], c) tetrahedron [7], d) micro tetrahedron [50], e) CT ball plate [22], f) CT tree [22], g) mini probe [50], h) tetrahedral reference standard [51], i) CT crown [52], j) CT tube [53].

Typically, these objects consist of precision spheres with low surface roughness and form error made of different materials (ruby, alumina, zirconia, etc.) attached on a carbon framework. Carbon is preferred over different materials, such as steel, due to its thermal stability and low attenuation coefficient, which ensures that the contrast between spheres and background is not compromised.

One-dimensional sphere arrays, such as ball-bar shown in Figure 14-a [8], can be used for correcting the CT scale factor. However, they are not well-suited for characterizing 3D behavior and performance of the CT system.

Two metrological artifacts, CT ball plate Figure 14-e and CT tree Figure 14-f, were introduced in [22]. The application of both objects in characterizing the performance of CT system was demonstrated according to VDI/VDE 2630-1.3 [27]. Furthermore, both objects can be used for determining measuring errors in the CT volume, and scale correction of CT data. CT ball plate consists of 5 × 5 array of ruby spheres attached on a carbon fiber plate featuring up to 300 sphere distances. CT tree is composed of five ruby ball bars of different length, and one additional sphere. Compared to CT ball plate, CT tree can be used in addition to investigate the tilt of the rotation axis, anisotropies in measurements in vertical direction, etc. Both reference standards were calibrated with low measurement uncertainty using reversal methods [54].

Artifacts in Figure 14-b, c, d, g, h can be used to asses scaling factors, as well as for metrological performance verification as per current version of ISO/CD 10360-11 [30]. The object shown in Figure 14-b is composed of 27 ruby spheres attached on carbon fiber shafts and mounted on a circular table. The shafts feature different heights and are mounted with different distances from the center of the table. This configuration offers a large number of SDs, and mapping of the whole measurement volume at given magnification. Tetrahedron developed at the University of Padova (Figure 14-c) is composed of four ruby spheres of different diameters arranged in a 3D pattern connected by carbon fiber bars. This object was used in an international inter-laboratory comparison CT Audit. Micro tetrahedron (Figure 14-d) and tetrahedral reference standard (Figure 14-h) are composed of four 0.5 mm ruby spheres glued together, and four attached alumina spheres, respectively. Finally, the mini probe (Figure 14-g) consists of five ruby spheres mounted on a carbon framework.

The last two objects shown in Figure 14-i, j were developed at the Technical University of Denmark (DTU). Both artifacts are composed of ruby spheres mounted on a carbon tube and carbon shafts, respectively; the position of individual spheres is calibrated by a tactile coordinate measuring machine (CMM). The objects can be used for the concurrent correction of the scale error; i.e. the objects are scanned together with the investigated part and the scale is corrected based on the measurements performed on the reconstructed volume that contains both the reference and the analyzed object.

Standards with hole/calotte arrangements

Standards with hole/calotte arrangements are inspired by equivalent artifacts that are used by conventional optical and tactile CMSs, i.e. hole plates. Examples of such objects adapted to use by CT systems are shown in Figure 15.

The calotte plate in Figure 15-a consists of 4 × 4 array of Ø 3 mm calottes grinded into a square-shaped geometry made of zerodur (i.e. glass-ceramic material). The distances between the calottes as well as their diameters and form errors were calibrated by a tactile CMS. The calotte cube shown in Figure 15-a was used as one of the items circulated during the CT Audit. The hollow cube is made of titanium and calottes were machined on three of the cube faces. The calottes of Ø 0.8 mm are distributed in 5 × 5 patterns, and the calotte distances as well as calotte diameters and form errors were calibrated by a tactile CMS. The artifacts shown in Figure 15-c, and d represent two types of hole plates. While the plate in Figure 15-c consists of a symmetric 7 × 7 array, the hole plate in Figure 15-d contains holes in a dedicated asymmetric pattern that forms seven different measurement directions (see Figure 15-f). The recommendation given by ISO/CD 10360-11 [30] where asymmetric designs are preferred over those symmetric have been discussed in Section 3.2. The hole plate (Figure 15-d, e) provides, compared to multi-sphere standards, distances between the holes that are distinctly influenced by the surrounding material. The number of measurements and, thus, the amount of time required to perform necessary measurements according to ISO/CD 10360-11 [30] can be significantly reduced by using the hole plate [55].

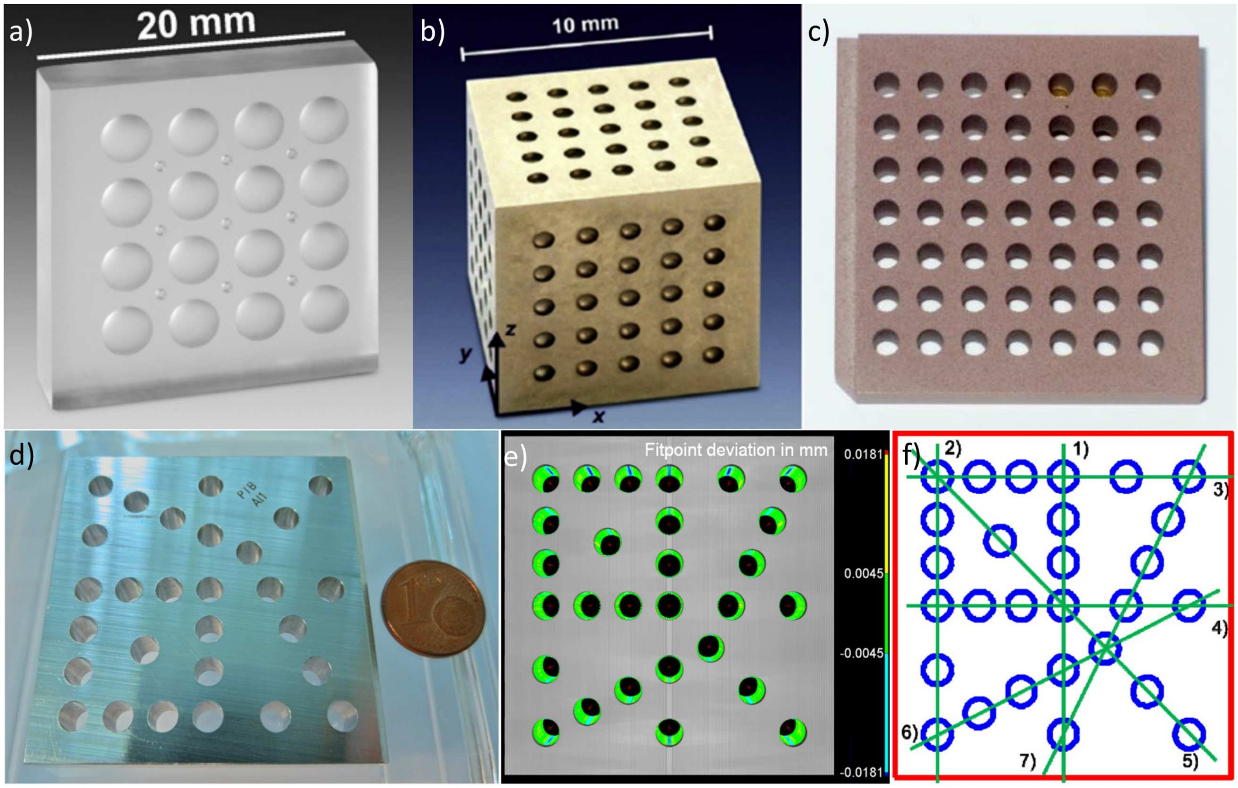

Figure 15. Reference standards with hole/calotte arrangements: a) calotte plate [56], b) calotte cube [56,57], c) 7 × 7 hole plate [57], d) hole plate [55], e) CT measurement of the hole plate [55], f) indication of seven principal measurement directions on the hole plate [55].

Standards with plane-parallel features

Standards with plane-parallel features, such as gauge blocks or step gauges, are widely used for verifying tactile and optical CMSs. However, adopting them directly by CT is not possible due to scanning artefacts, such as beam hardening and cupping effects, resulting in deformed flat surfaces (so called barreling effect as shown in Figure 16-c). One of critical aspects is the material of which the objects is made; i.e. steel or ceramic in the case of tactile and optical CMSs. In the case of CT, polymers or aluminum are more suitable. Standards with plane-parallel features are suitable for performing both uni- and bidirectional point-to-point or face-to-face measurements [2]. Examples of CT reference standards with plane-parallel features are shown in Figure 16.

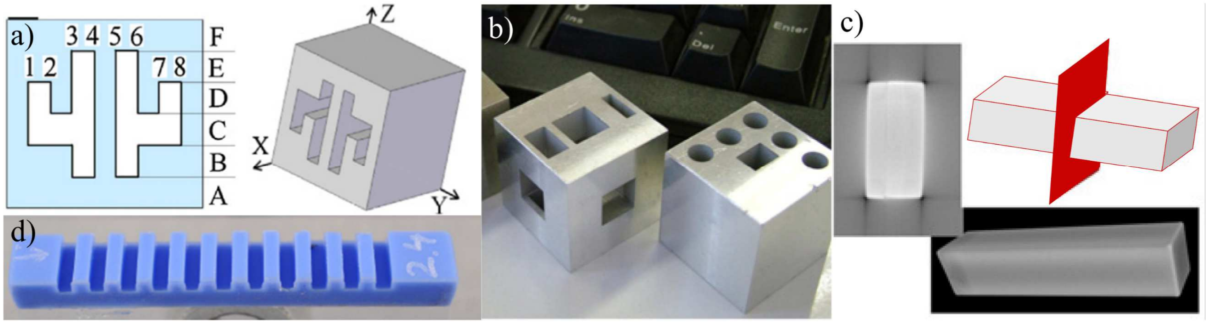

Figure 16. Reference standards with plane-parallel features: a) “cactus” step gauge [58], b) prismatic standards with internal features [2], c) gauge block [2], d) step gauge [59].

Objects with both internal and external plane-parallel features (e.g. artifacts shown in Figure 16-a, b) can be used for investigating both the scale errors and the offset errors (i.e. threshold value and edge detection) [2]. Furthermore, preforming measurements over different wall and air gap thicknesses can allow investigating further effects, such as penetration length influence, etc. The so called "cactus" step gauge (Figure 16-a) is a prismatic part with internal grooves made of aluminum, and developed at KU Leuven. The object is relatively easy to manufacture, thus can be made in different materials to investigate material-specific characteristics. The replica of step gauge shown in Figure 16-d was developed at DTU originally for the performance verification of optical scanners. However, it can also be used for verifying metrological performance of CT systems, as well as for investigating edge detection and thresholding effects. The step gauge can be manufactured in various materials suitable for CT scanning, such as aluminum, titanium, PEEK, PPS, and others [60].

Other standards

In addition to standards categorized earlier in this section, the artifacts with specific features are presented here, and a summary of such objects is shown in Figure 17.

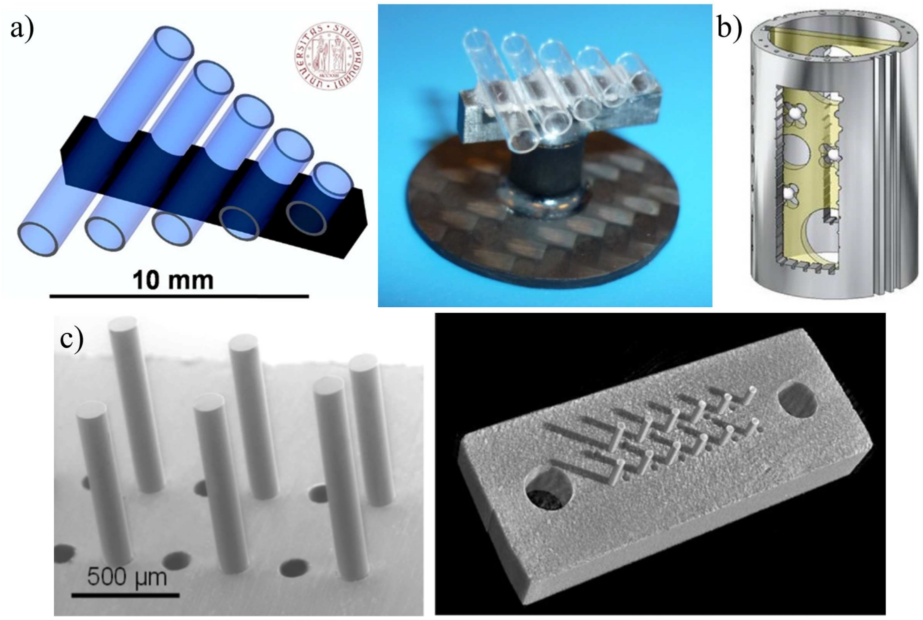

Figure 17. Other standards: a) pan flute gauge [7] (left: schematic CAD representation, right: photo), b) QFM cylinder [7], c) fiber gauge (left: SEM image, right: CT reconstructed 3D image) [61].

The first two objects in Figure 17-a, b were used for inter-laboratory comparison on CT for dimensional metrology CT Audit. Pan flute gauge (Figure 17-a) consists of five borosilicate glass tubes of different length mounted on a carbon fiber support. The object was developed at the University of Padova, and tube lengths, as well as their internal and external diameters were calibrated. It is worth noting that this artifact is suitable for CT metrological performance verification as it allows different uni- and bidirectional length measurements, as well as measurements of internal and external features. QFM cylinder was developed at the University of Erlangen-Nuremberg and is composed of a hollow titanium cylinder with several calottes manufactured on its surface. Two symmetrical breakouts contain several micro structures. Furthermore, a ball plate carrying five sapphire spheres is mounted inside the cylinder. This standard offers variety of different measurements and geometries, such as outer and inner diameter of the cylinder, diameters of calottes and spheres, as well as distances between them, and measurements of the smallest measurable micro structure. Fiber gauge features a regular array of inner and outer micro structures, i.e. cylindrical shafts and holes. The artifact consists of a square-shaped framework with 12 cylindrical holes and 12 glass fibers of a nominal diameter equal to 125 µm; the length of fibers ranges from 350 – 700 µm. The lengths and diameters were calibrated using scanning electron microscopy (SEM) and multisensor CMS equipped with an opto-tactile fiber probe.

In addition to the standards presented in Figure 17, several artifacts were developed to investigate the material effect on CT dimensional measurements. These objects are summarized in Figure 18.

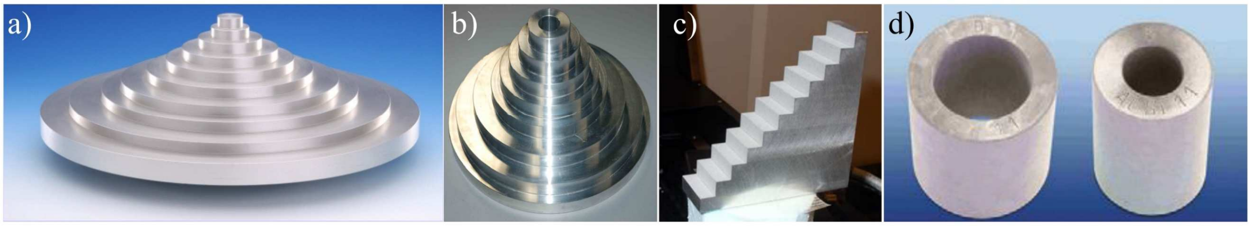

Figure 18. Standards for investigating material-related effects: a) step cylinder without a central hole [50], b) step cylinder with a central hole [62], c) step wedge [22], d) hollow cylinders [50].

Step cylinders without a central hole (Figure 18-a), as well as step wedges (Figure 18-c), can be used for investigating e.g. beam hardening effects, the maximum possible penetrable thickness of a specific material etc. Step cylinders with a central hole (Figure 18-b) can, in addition to the characteristics mentioned above, be used for optimizing the threshold value and correcting the scale error as they involve internal and point-to-point distances. Hollow cylinders (Figure 18-d) can be applied to investigate similar characteristics as step cylinders with a central hole. However, in this case, each hollow cylinder represents only one diameter/thickness combination.

International inter-laboratory comparisons

Typical means to investigate the capabilities of a new measurement technology throughout different laboratories and countries are international inter-laboratory comparisons. So far, four comparisons of CT systems focused on dimensional measurements have been carried out:

1) International comparison of µ-CMMs and µ-CTs
   The comparison was initiated in 2009 by the Swiss Federal Institute for Metrology (METAS) with three other participants: (i) the Dutch National Metrology Institute (VSL), (ii) the National Metrology Institute of Germany (PTB), and (iii) the UK's National Measurement Institute (NPL). Five simple objects were used during the comparison: (i) 85 mm × 85 mm ball plate, (ii) Ø 4 mm sapphire sphere, (iii) Ø 1 mm silicon nitride sphere, (iv) Ø 3 mm × 4.6 mm tungsten carbide ring gauge, and (v) micro tetrahedron composed of four Ø 0.5 mm ruby spheres (see Figure 14-d).
   While all the objects were measured by µ-CMMs, the ball plate due to its dimensions and the ring gauge due to strong beam hardening effects were not scanned by CT [63].
2) International inter-laboratory comparison CT Audit [7]
   The project was organized by the Laboratory of Industrial and Geometrical Metrology at the University of Padova as a round robin format comparison. Several companies, institutions and national measurement institutes in Europe, Asia, and USA participated on

the project [7]. The circulation started in March 2010 and ended in March 2011; the final report was published in January 2012. Four reference standards were measured at each participating institution: (i) CT tetrahedron (Figure 14-c), (ii) pan flute gauge (Figure 17-a), (iii) calotte cube (Figure 15-c), and QFM cylinder (Figure 17-b).

The inter laboratory comparison involved 15 CT systems in total and resulted into several main observations:

a) Most participants were able to perform CT dimensional measurements with sub-voxel accuracy.
b) Measurements of form are more problematic.
c) Most of participants were not able to measure within the specifications of their CT system.
d) The evaluation of measurement uncertainty was problematic for majority of participants.

3) Inter laboratory comparison on Industrial Computed Tomography CIA-CT [64]

The comparison was organized by the Centre for Geometrical Metrology (CGM), Department of Mechanical Engineering of DTU. In total, 27 laboratories from 8 countries participated on the project. Two industrial parts were selected for the comparison: (i) a polymer LEGO brick (Figure 19-a), and (ii) a metallic tubular component from the medical industry (Figure 19-b).

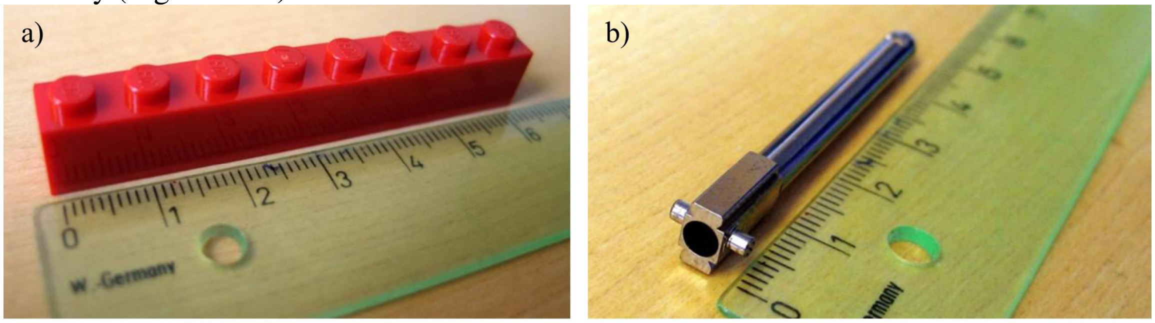

Figure 19. Objects used in the inter-laboratory comparison on Industrial Computed Tomography CIA-CT [64]: a) LEGO brick, b) metallic tubular component from the medical industry.

One set consisting of the two parts was sent to each participant, and the measurements were carried out during January 2013. Reference measurements on each part were performed by the coordinator before and after the objects were measured by a participant. The final report was published in September 2013 resulting into the following conclusions:

a) Roughly half of the participants were able to make a valid statement of measurement uncertainty.
b) Diameters and lengths were measured with relatively low measurement errors.
c) An effect of wall thickness on measurement errors could be identified.
d) Measurements of form were more problematic than size measurements.

4) INTERAQCT Comparison on Assemblies [65]

This inter laboratory comparison was organized by CGM, Department of Mechanical Engineering of DTU, and coordinated by a fellow of the INTERAQCT project. The comparison was focused on multi-material assemblies, and involved 22 laboratories from 7 countries. Both the objects are shown in Figure 20.

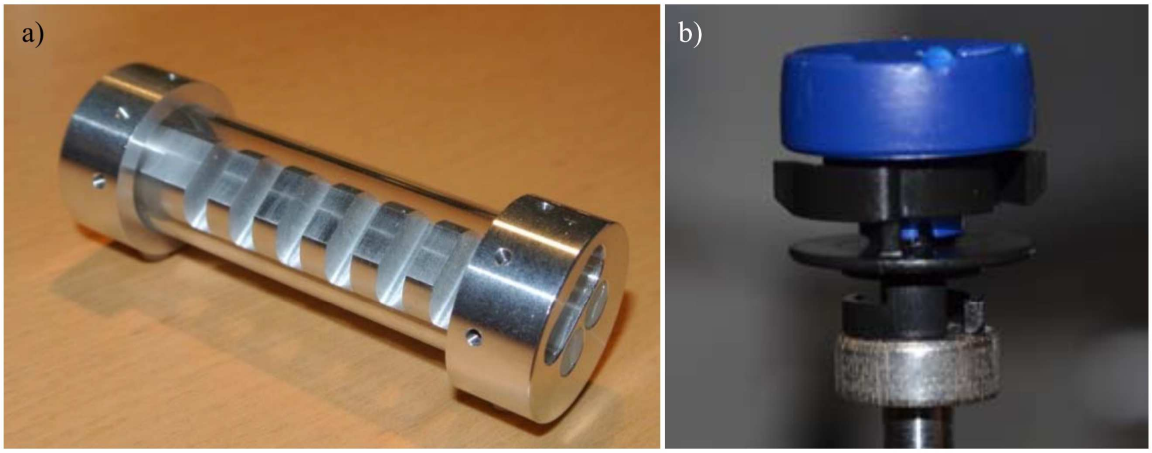

Figure 20. Items used for the INTERAQCT comparison on assemblies [65]: a) aluminum step gauge enclosed in a glass tube, b) industrial polymer assembly.

The first assembly (Figure 20-a) is composed of an aluminum step gauge enclosed in a glass tube housing. This object was manufactured in 22 copies (one copy per participant) and sent over to participants. The technical protocol defined by the coordinator required scanning under two different conditions: (i) "Own choice", where the participant was free to choose all the CT scanning parameters, and (ii) "Fast scan", where the participant was limited by the total scanning time. The first assembly featured several measurands, such as length, form, diameter, etc., including a multi-material distance (i.e. a distance measured between two different materials).

The second assembly was distributed electronically, i.e. participants received four reconstructed data sets with two noise levels instead of a physical object. The scans of the second object were performed by the coordinator. The aim was to investigate the influence of data post-processing on the measurement results.

The measurements on participants' sites were performed in January – August 2016, and the final report was published in November 2016. Main conclusions of the project are:

a) More than half participants were able to make a valid statement of measurement uncertainty while measuring the first assembly.
b) Similar results were achieved when scanning the first assembly under different conditions, i.e. most of participants were able to achieve the same accuracy while reducing the scanning time up to 70 %.
c) Bidirectional measurements were more problematic than the unidirectional ones.
d) Problems with the definition of datum system were observed when analyzing the measurement results performed on the second assembly.

It can be seen from the list above that the CT performance verification is covered relatively well in terms of dedicated reference standards. Furthermore, the choice of the reference standard is already discussed in the committee draft of ISO 10360-11 [30] for acceptance and reverification tests for CMSs with CT sensors. However, except for the last inter-laboratory comparison [65], the objects account only for mono-material effects. Yet, multi-material measurements are an important part of dimensional control of multi-material parts and assemblies. Therefore, investigating the new effects/problems that brings the multi-material aspect of measurements is of high importance. This trend has been also confirmed by recent publications [60,65–69] from researchers participating on the INTERAQCT project that propose new multi-material reference standards (Figure 21) for investigating the multi-material effects on CT dimensional measurements.

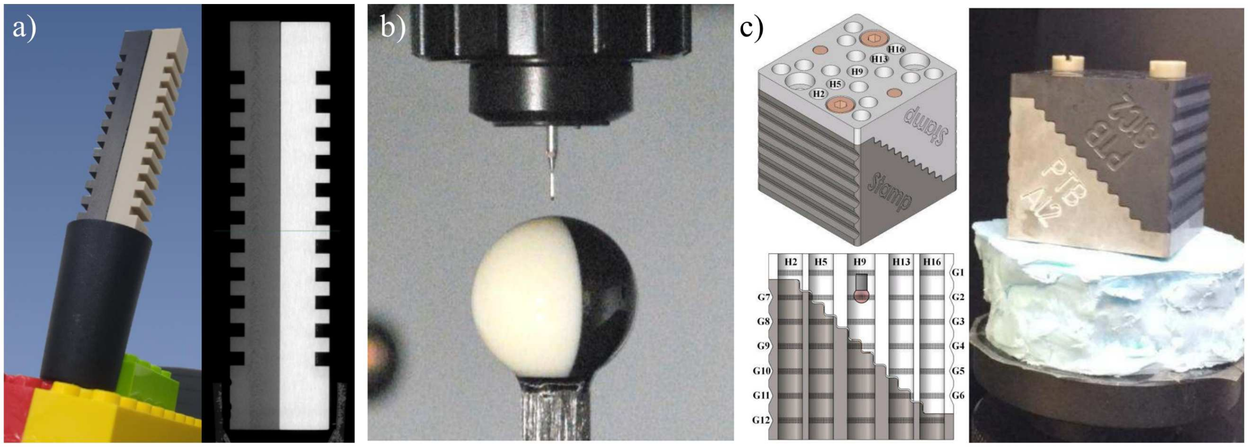

Figure 21. Multi-material reference standards: a) an assembly of multi-material step gauges (left: photo, right: 2D section of CT reconstructed volume) [60], b) multi-material sphere [67], c) multi-material hole cube (MM-HC), (left: schematic CAD representation, right: photo) [68].

The study in [60] aims at the evaluation of performances of different surface determination and segmentation methods on multi-material assemblies. An experimental approach using a set of multi-material reference standards is applied by the authors. The objects (step gauges, see Figure 21-a) are made of three different materials: (i) aluminum, (ii) polyphenylene sulphide (PPS), and (iii) polyetheretherketone (PEEK). The parts were attached together to form three multi-material and three mono-material assemblies; in these configurations, uni- and bidirectional, as well as mono- and multi-material measurements can be performed and investigated so that dense information about individual measurement aspects can be extracted. The methods presented in [67,68] propose procedures for multi-material probing error *P*, and multi-material length measurement error *E* testing as described in ISO/CD 10360-11 [30] for mono-material measurements. Multi-material sphere, as the name suggests, is composed of two hemispheres made of different materials; the authors of [67] selected three different materials: (i) silicon nitride (Si_3N_4), aluminum oxide (Al_2O_3), and lead-free glass N-SF6. Similarly to the previous publication, also here three mono- and three multi-material combinations of hemispheres were manufactured. In [68], a multi-material hole cube concept (MM-HC) is used for defining the procedure for multi-material length measurement error test. The object is composed of two symmetric prismatic parts made of different materials. The object features 17 through holes and 12 *V*-shaped grooves, and was made in three different materials: (i) carbon fiber reinforced silicon carbide SiC (Cesic®), (ii) aluminum, and (iii) titanium. Again, three mono- and three multi-material standards were manufactured. The reference standard allows a whole range of measurement scenarios (further explained in Chapter 6): measurements over different multi-material ratios, in- and inter- material measurements, and mono- and multi-material measurements. Due to the arrangement of holes, uni- and bidirectional measurements can be made in different directions and over different material thickness.

Since the aspects of multi-material measurements have not been comprehensively explored yet, this topic is one of the aims of this Ph.D. thesis, and is discussed in Chapter 6.

3.4.2 Application specific standards

Applications specific standards are objects that are designed either to investigate CT related influencing factors, such as metrological structural resolution, focal spot size, drift, etc., or to investigate CT specific applications, such as nominal/actual comparison, porosity, wall thickness, and fiber orientation analysis. Therefore, this section is divided into two subsections: (i) Reference standards for investigating CT influence factors, and (ii) Reference standards for investigating CT specific applications.

Reference standards for investigating CT influence factors.

Figure 22 shows four different objects that are used for the evaluation of metrological structural resolution. The authors of corresponding publications also propose four different approaches and methods to determine this characteristic.

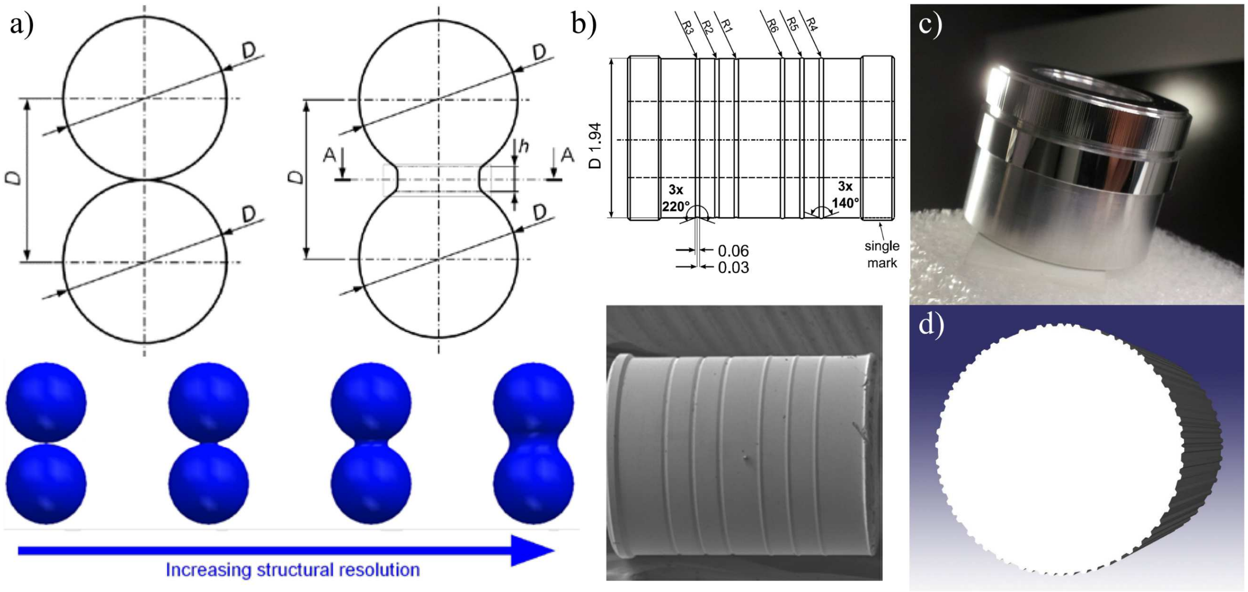

Figure 22. Reference standards for evaluating the metrological structural resolution: a) hourglass standard (top: diagram of the principle of the method, bottom: the effect of increasing structural resolution) [44,70], b) reference standard by PTB (top: CAD drawing of the object, bottom: SEM image of the object) [43], c) Multi-wave standard (MWS) [71], d) Aperiodic Spatial Frequency Standard (ASFS) [72].

VDI/VDE 2630-1.3 [27] defines the structural resolution as the size of the smallest structure that can still be measured within error limits to be specified by the CT system manufacturer. More specifically, it is suggested by [27] to determine the diameter of the smallest sphere measurable within the specified error limits. This approach is, however, not practical in the case when the structural resolution is unknown. Then, a number of spheres must be measured and the procedure becomes time-consuming [70].

The method proposed in [44,70] relies on the use of a reference standard called “hourglass” (Figure 22-a). The artifact was developed at the University of Padova and is composed of two spheres with the same diameter (D) physically touching each other. Due to the finite structural resolution of any CT scan, the region in proximity of the contact point is distorted as shown in the top part of Figure 22-a. The height of the contact zone h, as well as its diameter, increases with increasing structural resolution (see the lower part of Figure 22-a).

Another approach is described in [43], where a method inspired by the curvature transfer function in computer graphics is proposed. The reference standard that is used by the authors of [43] (Figure 22-b) was manufactured at PTB. The object consists of a cylindrical geometry that incorporates three grooves and three flanges. The prototype used in [43] is made of copper coated with an amorphous nickel–phosphor layer. The calibration of the object was performed by atomic force microscopy (AFM).

The object shown in Figure 22-c, so called Multi-wave standard (MWS), consists of an aluminum cylinder with circular multi-wave arrangement and two additional reference surfaces for alignment. The method for determining the metrological structural resolution published by the authors of [71] is based on the frequency response analysis on sinusoidal surfaces.

The authors in [72] use a newly developed reference standard, so called Aperiodic Spatial Frequency Standard (ASFS), shown in Figure 22-d. The method to determine the metrological structural resolution is based on several steps. In a first step, the ASFS is scanned and a surface is determined on the data set. Subsequently, data points along circumferential lines are extracted and a Fourier analysis is performed. Based on further data processing it is possible to derive information about the structural resolution of the CT system.

Another characteristic that can be evaluated by using various reference standards is spatial resolution. Methods applied in determining this factor are related to spatial resolution of the gray scale range of voxels, and should not be mistaken for metrological structural resolution that takes into account the complete CT measurement chain (i.e. threshold determination and surface extraction, filtering and averaging of surface points) [70]. Examples of references standards used for determining the spatial resolution of CT systems are shown in Figure 23.

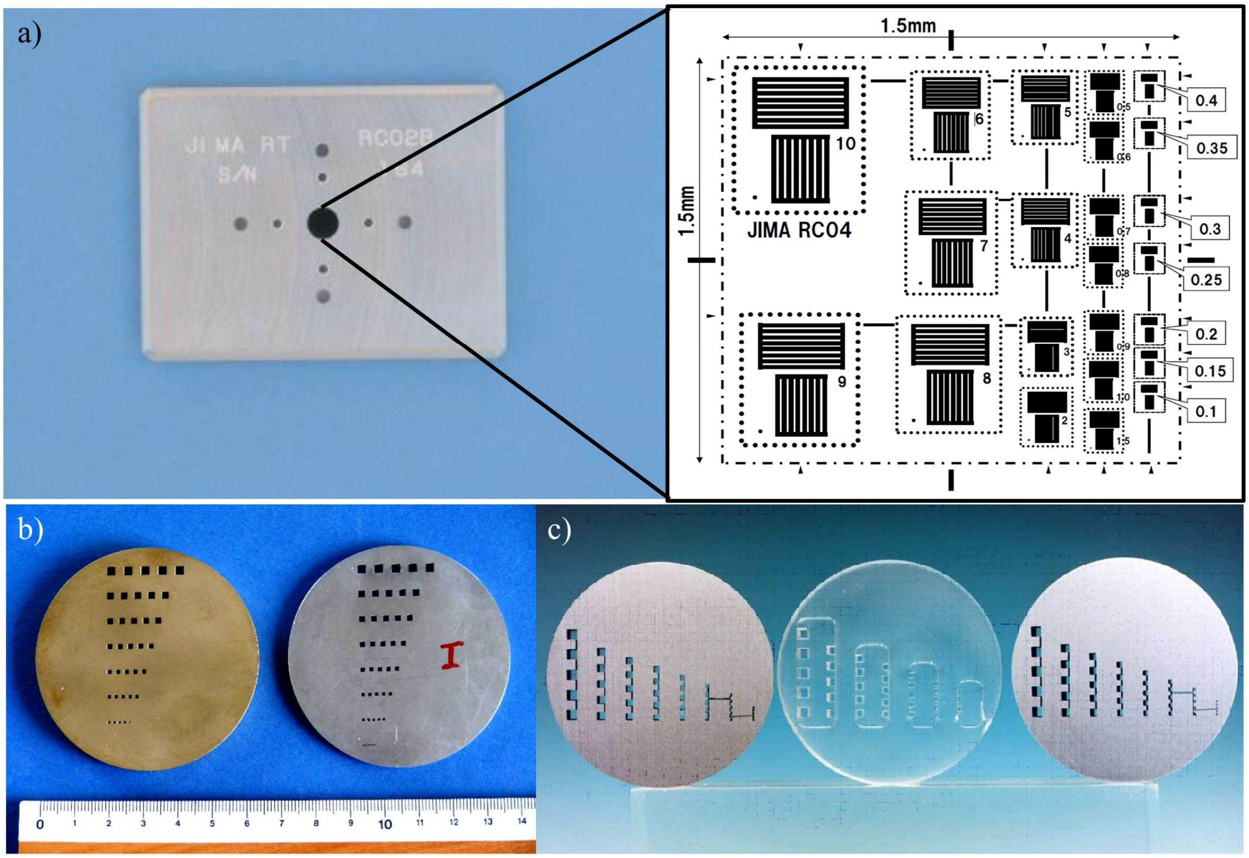

Figure 23. Reference standards for spatial resolution: a) Japan Inspection Instruments Manufacturers' Association (JIMA) resolution chart (left: photo, right: schematic diagram of *T*-shaped line patterns) [73], b), c) line pair gauges [36,74].

JIMA resolution charts (Figure 23-a) provide *T*-shaped line patterns with different line widths. Typical widths range from 0.4 µm to several µm and the method is based on the identification of the pattern where the individual lines can still be recognized. The base of the object is typically made of silicone with a P-SiO_2 or aluminum protection layer. Tungsten or gold are usually used as the absorption material and the gaps are commonly filled with SiO_2.

The spatial resolution can also be determined by calculating the modulation transfer function (MTF). The method is based on analyzing the projection of an edge. ISO 15708-2 [33] uses the edge of a cylinder, whereas e.g. in [75,76] a sharp edge (also called knife-edge) is used.

As an alternative to abovementioned methods, EN 16016-3 [36] suggests the calculation of a contrast factor *R* as a function of the resolution, measured at line-pair structures (Figure 23-b,c). The objects consist of a cylinder in which a square section of 8 rows of 5 holes are machined, spaced at a distance equal to the length of their sides. The objects in Figure 23-c are made of stainless steel, plexiglass, and aluminum, whereas the objects in Figure 23-b used in [74] are made of brass and aluminum.

There are several methods to determine the focal spot size; most of them are based on imaging simple objects composed of a high-absorbing material and a through structure, such as line or hole. The methods are summarized in [77] and use objects shown in Figure 24-a, b, and c.

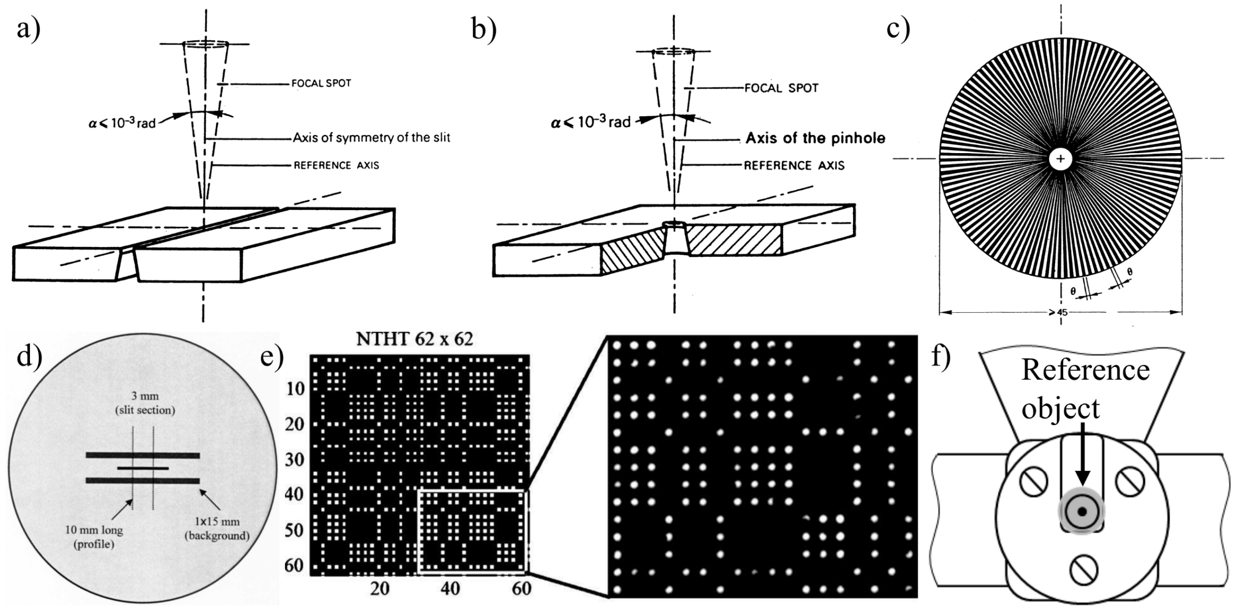

Figure 24. Reference standards for the characterization of the focal spot: a) slit camera, b) pinhole camera, c) star pattern camera [77], d) single slit camera [78], e) 62 × 62 no-two-holes-touching modified uniformly redundant array (NTHT MURA) mask [79], f) object for evaluating the focal spot drift [80].

A slightly modified slit pattern shown in Figure 24-d was used in [78] to investigate the effect of different exposure times on the focal spot size. Another method using a 62 × 62 no-two-holes-touching modified uniformly redundant array (NTHT MURA) mask introduced in Figure 24-e was described in [79]. This coding mask is a type of X-ray and gamma-ray radiation collimator consisting of an array of multiple holes machined in a radiation opaque plate, disposed according to a predetermined spatial arrangement on a two-dimensional grid [79].

Another important factor that affects the accuracy of CT measurement is the stability of the focal spot. Due to a substantial heat load of the X-ray tube and its components, individual parts can dilate, deflect, etc. As a result, the position of the focal spot can change over time, as investigated e.g. in [80]. Most experimental methods that investigate the drift of the focal spot consist of imaging a stationary reference standard (e.g. a metal/ruby sphere [81,82], a hole plate [83] or a cross wire [84]) over a period of time. The authors of [80] designed two simple samples consisting of a small sphere surrounded by X-ray transparent material. The first sample was composed of a steel ball embedded in the center of a polyurethane cylinder, whereas the second consisted of a steel ball attached to a borosilicate glass plate. The design of both objects allowed mounting them directly in the filter holder (Figure 24-f), thereby ensuring their stability.

Reference standards for investigating CT specific applications

CT provides the user with high-density data that can be used for a variety of analyses, such as nominal/actual comparison, porosity analysis, etc. However, this versatility brings further aspects, in terms of measurement accuracy, that must be considered and investigated. In order to evaluate the metrological performance of CT in its specific applications, several standards have been developed.

Nominal/actual comparison [23] is an important tool when measuring e.g. sculptured or freeform surfaces. However, due to the different point density obtained by different CMSs, comparison between different measurement techniques is not a trivial task. A method to fuse data from different CMS sensors was developed in [85] and demonstrated on a cylinder head segment (Figure 25-a) [8].

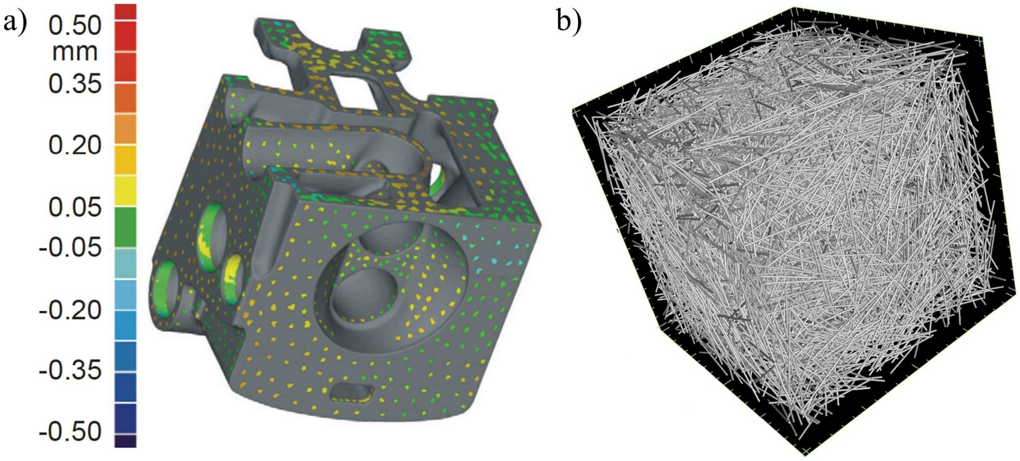

Figure 25. Reference standards for CT specific applications: a) comparison of CMM and CT measurements demonstrated on a cylinder head segment [8], b) simulated dataset with glass fibers [86].

Another unique analysis that can be performed by CT is the non-destructive evaluation of fibers in fiber-reinforced polymers. The importance of evaluating their length and orientation grows with growing demands on composite materials. However, there is currently no method to evaluate the CT accuracy and metrological performance of such analysis. A recent publication [86] introduced an approach to compare CT segmentation techniques for short glass fibers. The authors of [86] used a synthetic reference data set composed of glass fibers shown in Figure 25-b. The aim of their current research is to fully exploit the potential of CT fiber characterization.

In general, achieving traceability in CT specific applications, such as nominal/actual comparison, fiber characterization, or wall thickness analysis is a challenging task. Even though some efforts have been made in this field, there are still many aspects that must be investigated. This applies also to the evaluation of internal porosity/voids, which is one of the most established CT specific applications. Currently, there is no dedicated artifact for evaluating the accuracy and establishing the traceability of CT porosity measurements. Therefore, this topic and related development of the reference standard are addressed in Chapter 4.

3.4.3 Calibration

CT measurement process suffers from a variety of error sources that affect the final measurement accuracy. Due to this fact, and the fact that CT is a multi-purpose tool, a general calibration of CT instrument is not possible. Majority of reference standards developed for CT calibration pertain to the calibration of its geometry. More specifically, to relative position and orientation of its three main components, i.e. X-ray source, rotary stage, and detector. Therefore, in the following section, reference standards dedicated to calibrating the CT instrument geometry are discussed. It should be noted, however, that geometrical calibration alone is not enough to allow a user to determine measurement uncertainty as non-geometrical influence factors exist [19].

Typical algorithms and equations for solving CT system geometry are based on evaluating the position of a projected marker with respect to the modelled, i.e. ideally aligned, case. Therefore, the accurate identification of the marker and its position within the coordinate system is one of the critical aspects in design of a reference standard for characterization of CT instrument geometry. In order to facilitate the recognition of projected markers, the contrast between the framework and the markers must be maximized. For this reason, the components are usually made of materials with significantly different X-ray attenuation coefficients; more specifically, the framework is typically made of a low-attenuation and the markers of a high-attenuation material.

The authors of [87] propose a square plastic plate and four slices of high density material positioned at the vertices of the square (see Figure 26-a). The distance l between the high-density markers is known a priori. CT geometrical parameters are evaluated based on the distortions of the projected square composed of the projected markers. Figure 26-b, c show an example of the aligned and misaligned geometry and its effect on the projected geometry of the reference standard.

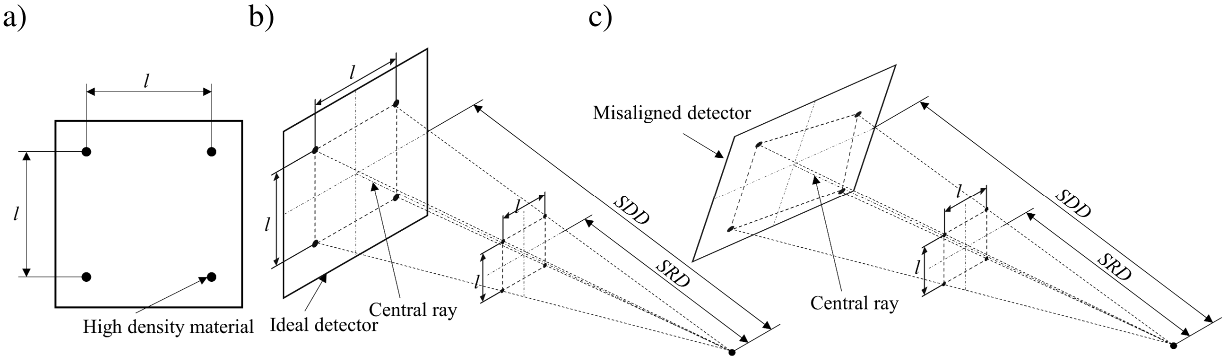

Figure 26. A reference standard used in [87] composed of a plastic square and four slices of high-density material. a) Diagram of the object, b) projection of the high-density features on an ideal detector, c) projection of the high-density features on a misaligned detector.

Another standard (Figure 27-a) proposed in [88] is composed of two steel balls mounted on a plastic plate. The distance between the centers of the spheres is calibrated. The authors of [88] assume the rotation axis to be perfectly aligned and acquire projections of the object from multiple angles. During the rotation of the object, circular trajectories of the two balls are projected on the detector as ellipses (Figure 27-b, c). The CT instrument geometry is solved based on the properties of the projected ellipses. The principle of tracking the circular trajectories is used also in [89] where an object with a number of spheres positioned roughly in a vertical line off the rotation axis is used (example of the standard is in Figure 27-d).

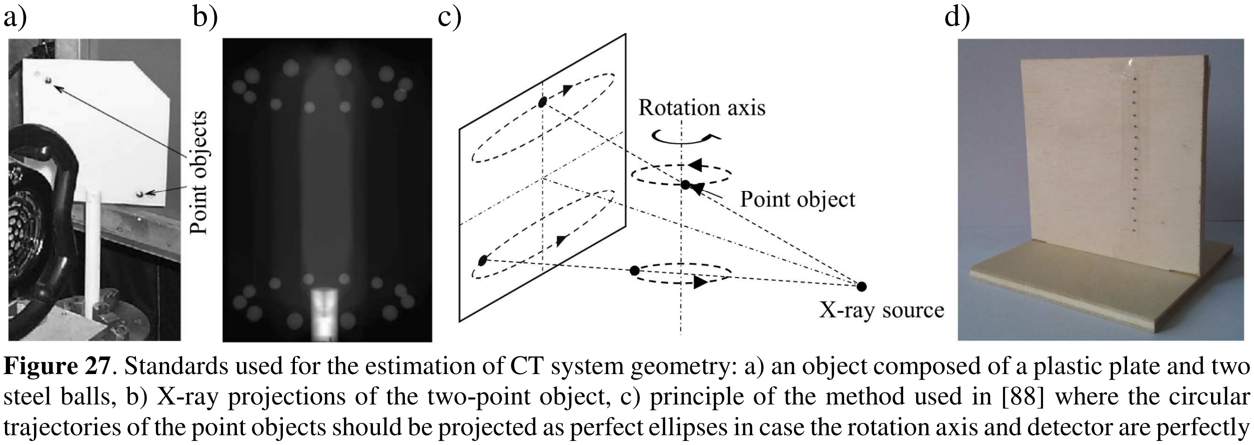

Figure 27. Standards used for the estimation of CT system geometry: a) an object composed of a plastic plate and two steel balls, b) X-ray projections of the two-point object, c) principle of the method used in [88] where the circular trajectories of the point objects should be projected as perfect ellipses in case the rotation axis and detector are perfectly aligned, d) the principle of tracking spheres was applied also in [89] where the object was composed of a number of spheres aligned vertically off the rotation axis.

The authors of [90] and [91] use objects with spherical markers arranged in more complex spatial patterns ensuring higher reliability of the estimation of CT geometrical parameters. The objects shown in Figure 28-a and b are composed of steel balls mounted on a plastic cylindrical framework arranged in circular and helical trajectories, respectively. While the object used in [91] (Figure 28-a) is used in the dynamic mode, i.e. by rotating the object, the artefact applied in [90] is used in the static mode, i.e. without rotational motion, thereby eliminating the errors from instable rotation of the rotary table. Both authors suggest using as high number of spherical markers as possible with respect to avoiding overlaps between projected markers in acquired projections. The minimum number of spheres per circular trajectory, in order to ensure the applicability of algorithms in the static mode, is five [90]. Another aspect, discussed by the authors of [90,91], is the size of the markers that should ensure sufficient number of pixels contained in the projected shadows. To maximize the reliability of the methods, the markers should also be uniformly distributed over the detector.

An interesting study was performed in [92]. The author compares different designs of reference standards applied to estimating the CT geometrical parameters. Furthermore, a new design is proposed in this study – so called candy cane standard (Figure 28-c). The spherical markers in the candy cane standard are arranged on a cylindrical framework in quarter-helical trajectories with relative offset of 90° around the main axis of the cylinder. The design provides improved spatial distribution of the projected markers on the detector when compared to helical trajectories of spheres (Figure 28-b), while at the same time partially eliminates "clustering" of the marker overlaps at the detector edges.

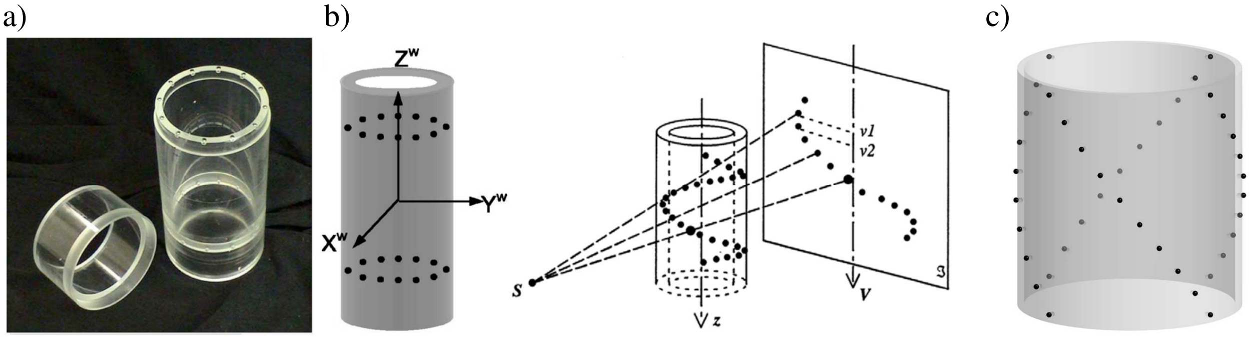

Figure 28. Standards used for the estimation of CT system geometry: a) an object composed of spherical markers arranged in two circular patterns mounted on a plastic cylinder [91], b) an object with spherical markers arranged in a helical trajectory [90], c) candy cane standard [92].

Recent publications [93,94] propose new reference standards for assessing the *SRD* and *SDD* along the whole magnification axis, and for characterizing CT scale and rotary axis errors, respectively. The object in Figure 29-a is composed of three pairs of steel spheres with different diameters for analyses in different magnifications. The printed circuit board (PCB) shown in Figure 29-b and used in [94] represents a planar grid structure with a regular matrix shape. The PCB is made of a high stable polyimide/glass fiber composite. The ring-shaped metal pads are arranged in a 38 × 61 matrix with a 2.54 mm step. They are made of a 35 µm copper layer coated with Au/Ni film ensuring sufficient contrast with respect to substrate material.

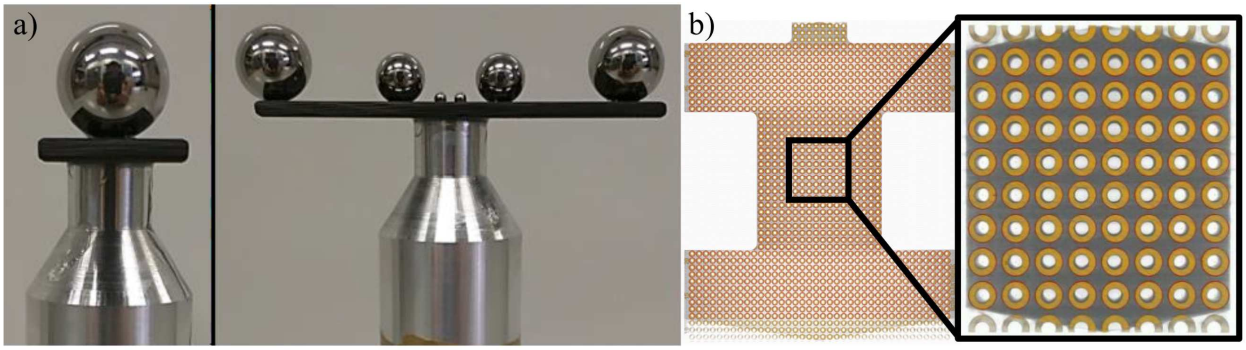

Figure 29. Novel reference standards: a) a standard with three pairs of spheres [93], b) printed circuit board (PCB) [94].

A thorough review of reference standards for the evaluation of CT geometrical parameters can be found in [19]. Although the authors of publications mentioned in this section have either partially or completely solved the geometry of CT instrument, their methods provide estimates of the geometrical parameters but do not provide a metrological approach to the issue of geometrical calibration. More specifically, the measurement of geometrical parameters by comparison to a traceable reference, i.e. calibration, with valid statement of measurement uncertainty has not yet been achieved. Therefore, a reference standard for “real” calibration of CT system geometry and the calibration method are introduced in Chapter 5.

3.4.4 Uncertainty evaluation

The method described in GUM [26] is not suitable for the evaluation of the uncertainty of CT dimensional measurements due to the complex and numerous influence factors in CT. Typically, so called task-specific uncertainty, as defined in ISO 15530-3 [28] and VDI/VDE 2630-2.1 [29], is evaluated instead. Since the method described by the above-mentioned standard and guideline is based on the use of an application-similar calibrated workpiece, it is difficult to define a versatile standard for the evaluation of task-specific uncertainty. Therefore, a few representative examples of the CT uncertainty evaluation process in specific cases are shown here (see examples of standards used for the evaluation of measurement uncertainty in Figure 30).

The authors of [22,95] used three different reference standards in order to investigate the influnce of differentt materials and geometries. The object shown in Figure 30-a is a pipe connector made of an aluminum alloy, whereas the part in Figure 30-b is a micro component used for hearing aid applications (a toggle) made of liquid crystal polymer (LCP). Finally, the part in Figure 30-c is a component of an insulin pen (a component of dose engine) and is made of nickel-coated brass.

CT is the only technique that is able to dimensionaly evaluate internal geometries non-destructively. However, the evaluation of measurement uncertainty according to [28,29] requires that all measurement features be calibrated (e.g. by tactile CMM) and the calibration uncertainty evaluated; this is typically not feasible for internal features. The problem of calibrating non-accessible features was overcome by the authors of [8,96,97], where the application-similar workpiece was cut into parts. The object is shown in Figure 30-d. It is a casted miniaturized single cylinder head made of an aluminum alloy. The part features several properties: (i) it contains both internal and external geometries, (ii) it allows measurements of free form surfaces, (iii) the part can be used for the evaluation of the task-specific uncertainty as it resembles real workpieces, and (iv) the part was sectioned and additional reference features were added for the alignment of measurement data; in particular, spheres were added and cylindrical features were machined in the material.

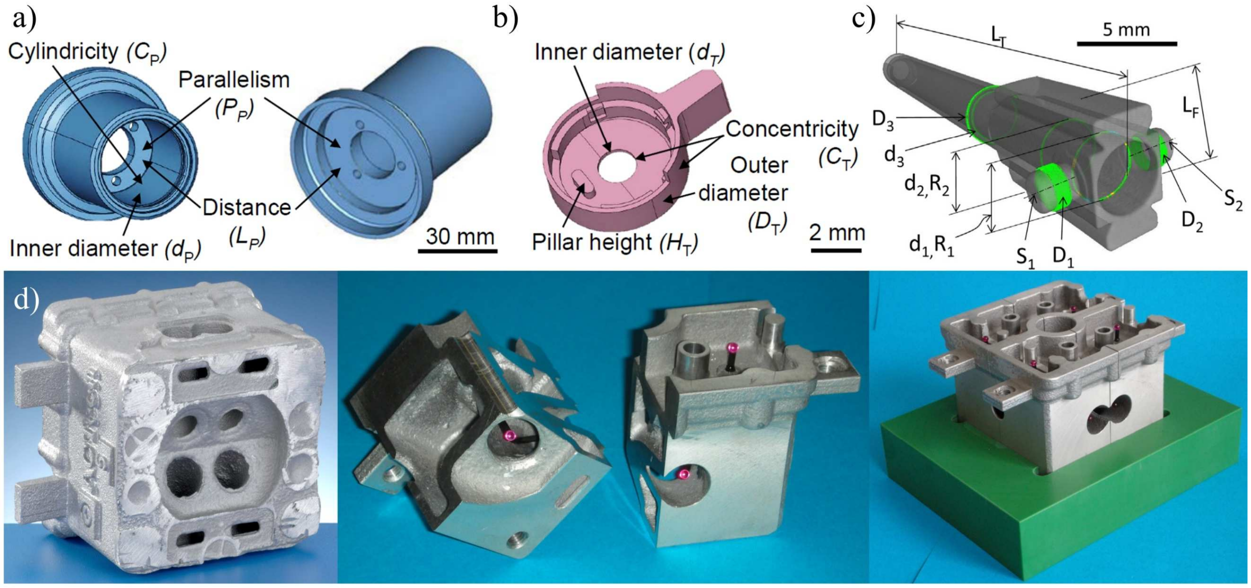

Figure 30. Workpieces used for the evaluation of the task-specific uncertainty: a) pipe connector [22,95] , b) toggle [22,95], c) dose engine [22,95], d) miniaturized cylinder head (left: raw body, middle: two of four segments after mounting reference features, right: four segments mounted together) [96].

The evaluation of task-specific measurement uncertainty will be also demonstrated in the following Chapters (4-6) on specific cases using reference standards developed in this work.

An alternative to the empirical methods [28,29] is the method described in [47] by propagating distributions using a Monte Carlo method. This approach requires thorough knowledge of the measurement chain and the statistical distribution of each influence factor. The uncertainty is evaluated by running a number of simulations, where each influence quantity is varied according to its distribution. The evaluation of measurement uncertainty using a Monte Carlo method will be discussed and applied in Chapter 5

It should be noted that the list of reference standards is not exhaustive. The author selected the most significant and related artifacts for the present Ph.D. thesis.

4 TRACEABILITY AND ACCURACY OF CT POROSITY MEASUREMENTS

CT specific applications were identified in Chapter 3 as one of the fields with a significant lack of reference standards. In particular, internal porosity/voids detection and characterization as one of the most promising CT applications of CT NDT demands a metrological artifact. In this chapter, the importance of internal defects analysis is described and the state-of-the-art with respect to CT porosity measurements is discussed. Subsequently, a new design of the reference standard for CT porosity measurements is proposed and critical aspects regarding development and manufacturing are explained. The calibration procedure and the traceability establishment of CT porosity measurements are described along with the evaluation of measurement uncertainty. Furthermore, the accuracy of CT porosity measurements is evaluated using the newly developed reference standard, and suggestions to improve the accuracy are given. Finally, the method is verified on a case study with an industrial part and a method to improve CT porosity measurements in the industrial environment is proposed.

4.1 Introduction to CT porosity measurements

Manufacturing technologies, such as die casting, additive manufacturing (AM) and injection molding, suffer from various imperfections, one of which is internal porosity [98–105]. The amount of porosity can be reduced by modifying processing parameters [98,106–108], however, its complete elimination is challenging due to technological limits and excessive costs. While a certain level and size of porosity are acceptable in the majority of parts produced by conventional and state-of-the-art technologies, exceeding the required limits can have fatal consequences as the level of porosity inside the product directly influences its mechanical properties [102,103,107,109–112]. It is, therefore, essential to have a reliable instrument that can evaluate these internal defects with high accuracy and documented traceability. Recently released standards and guidelines for the evaluation of internal defects, such as VDG P 201/202 [113,114], underline the abovementioned affirmation.

Several well-established methods have been used for porosity evaluation in industry, one of which is ultrasonic testing, a technique that is widely used in non-destructive inspections for its relative reliability and versatility [115]. Other methods used for the characterization of internal defects are based on: (i) measurement of the sample density, such as Archimedes method and pycnometry, or (ii) direct measurements of pores, such as microscopic analysis of cross-sections and CT [99,116]. The downside of the ultrasonic testing is twofold: it is difficult to extract 3D information about porosity and at the same time the accuracy of the method can be affected by non-homogeneous size and distribution of defects [117,118]. The drawback of density-based methods is too general information that these methods provide, i.e. the total porosity content; recent publications [112,119] proved that this information is not sufficient, and that detailed information about the size, shape and distribution of defects is needed for complete assessment of their effect on mechanical properties. On the contrary, the microscopic analysis provides the information about the size and position of individual defects; however, this information is obtained only on a limited number of cross-sections, thereby introducing significant errors in the case of non-homogeneously distributed defects within the sample. Furthermore, the method is destructive, the preparation of the cross-section is elaborate, time-consuming, and the grinding and polishing of the sample can smear some of the pores or scratch the surface.

CT has emerged as a promising technique for non-destructive testing and dimensional metrology in industry [2,4]. The fact that full 3D information about the external and internal shape, as well as the structure of a sample can be extracted from a CT data set, can overcome most of the drawbacks present in conventional methods for the evaluation of porosity. Although several methods for evaluating the accuracy of CT porosity measurements have been presented in the state-of-the art literature [120,121], none of them have declared full traceability of measurements according to GUM [26], i.e. ensure that the measurement unit be transferred through an unbroken chain of calibrations to the final measurement result including the evaluation of measurement uncertainty.

Achieving traceability of CT dimensional measurements in general is a challenging task because of the complex nature of the CT measurement process chain, and the lack of international standards. Establishing traceability in measurements of internal features including porosity is even more complex as these features are not accessible by conventional measuring instruments and, thus, the calibration is difficult. Furthermore, when it comes to porosity measurements, the typical output is a statement of total porosity content or volume of single defects, i.e. the measurand is volume, which is another challenging task [24].

Recent demands on porosity measurements require a metrological validation method, which is still under development. A reference standard with artificial defects is used in this chapter for the accuracy investigation of porosity measurements by CT. Several reference standards have been used in literature focused on measurements of internal defects. The authors of [120] aimed on material/void segmentation improvement, which is one of the critical points in voids/porosity measurements. A reference standard with micro holes was used in their publication and CT measurements were compared to measurements obtained by microscopy. Nevertheless, the micro holes were accessible from the surface and, therefore, did not simulate real internal defects. Furthermore, the selected measurand was a circle measured in cross-sections, which did not provide any volumetric information about measurements. Jansson et al. [121] designed a reference standard with macro and micro features for a study on additive manufacturing process and CT measurements accuracy. The measurements were performed on both external and internal features. However, the internal features were not measured by any other measuring system than CT as they were enclosed in the material. Therefore, the authors relied on the stability of the manufacturing process.

The reference standard proposed here overcomes the shortfalls of existing above-mentioned artifacts. It contains features resembling internal porosity that were calibrated with documented measurement traceability. In the following sections, the design, manufacturing and calibration of the object is described in detail. Furthermore, the accuracy of CT porosity measurements is evaluated using the object, and suggestions how to improve it are given and applied on a case study. Finally, a method to perform accurate CT porosity measurements in industry is proposed.

4.2 Development of the reference standard

The reference standard was designed taking into account all constrains from both the manufacturing and the application point of view. Three main requirements were defined as follows: (i) artificial defects must be completely internal, (ii) the features must allow calibration by conventional coordinate measuring systems (i.e. the object must be dismountable) and (iii) the material should be widely applied in industry, and at the same time should be suitable for CT scanning and provide sufficient metrological stability.

The standard is made of an aluminum alloy 6005A, which ensures easy penetration by X-rays and at the same time good machinability and metrological stability. Aluminum was chosen also because it is typical of many manufacturing applications (such as casting processes) in which the products are affected by porosity. The dismountable design of the object allows for calibration of the internal artificial defects. These artificial defects are milled as hemispherical calottes into the top plane of inserts, which are then assembled together with the main body of the object to form internal features resembling pores of hemispherical shape.

4.2.1 Design

The geometry of the reference standard is shown in Figure 31. The cylindrical body has a diameter of 15 mm and a height of 23 mm, and contains four holes (Ø 5.1 mm) of different depths for placing cylindrical inserts. The varying depths of the cylindrical openings make the distribution of defects more spread within the object's volume. Hemispherical calottes are milled on the top face of each pin, so that they form artificial internal porosity at the interface between the body and single pins after assembling the object. The diameter of hemispherical features milled into the pins faces ranges from 100 µm to 500 µm. Each pin contains 18 defects, resulting in 72 defects in total. In order to avoid pins from being stuck in the holes and to facilitate fitting at the interface between the hole bottom and pin face, a 0.05 mm gap was left between the components. In each pin, the defects are arranged along two concentric circumferences with diameters 2 mm and 3.5 mm. Furthermore, two additional defects are placed on each pin; the first is placed in the center of a pin and the second (denoted as "Marker" in Figure 31) is located outside the two circumferences and – by breaking the symmetry – ensures unambiguous identification of the defects.

The first prototype of the object suffered from the instability of pins. In order to ensure the stability during the measurement and manipulation with the object, the pins were fixed by four polymer screws. Furthermore, soft rubber washers inserted between the pins and screws ensure uniform distribution of the force produced by the screws.

The stability of the assembly was documented by repeated CT scans, including scans acquired right after the assembly, after two months from the assembly and after disassembling and re-assembling the sample after approximately one year. The average deviations between measurements obtained on individual scans were within the range of repeatability (below 1.5 %) including the measurement of volume *V*, which is the most critical measurand in terms of the stability of the assembly.

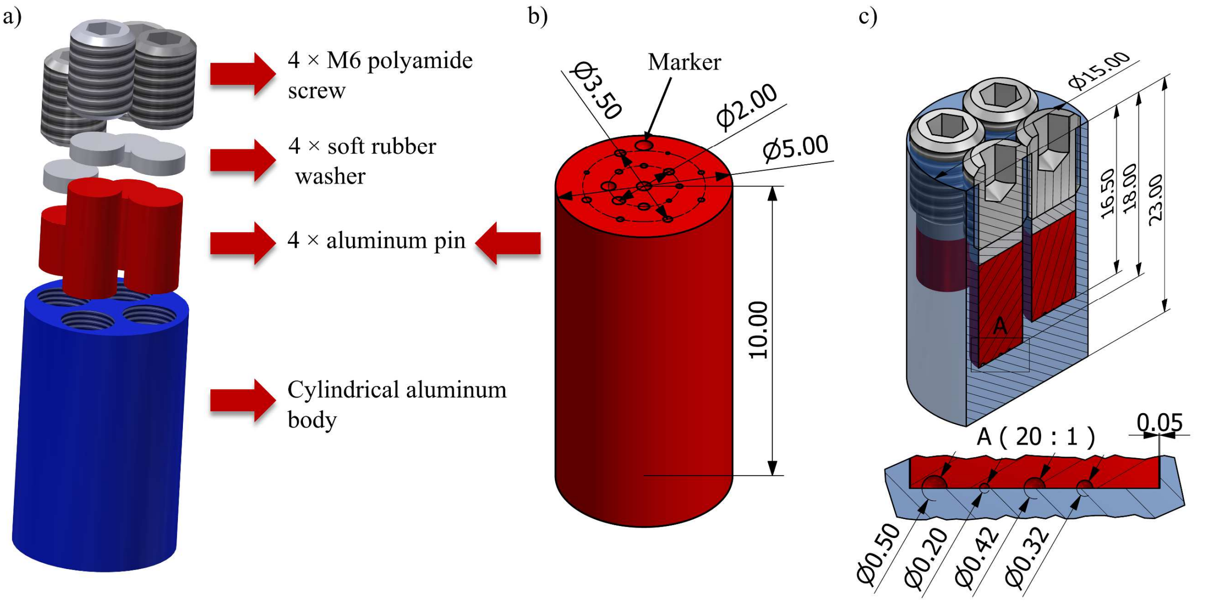

Figure 31. Design of the reference standard: a) 3D view of the components, b) 3D view of a pin including hemispherical calottes, c) general dimensions of the standard (in mm).

4.2.2 Manufacturing

The main parts (cylindrical holes, faces of pins and calottes) were manufactured by an ultra-precision 5 axis machining center (Kugler Micromaster 5X). The machining center was equipped by an aerostatic bearing and micro milling tools of diameters Ø 100 µm and Ø 250 µm. The manufacturing process in case of the first prototype started with finishing of the pin top surface followed by milling of hemispherical calottes. This sequence of machining steps, however, caused burrs on edges of the calottes depicted in Figure 32-a. Even though the height of these burrs was in range of units of µm, the fitting of the hole bottom and the corresponding pin face was not tight enough. Therefore, the new version of the reference standard was manufactured with a reversed order of machining steps. In a first step, the calottes were milled with a machining allowance, and in a second step, this allowance was removed achieving good quality of the top surface and no burrs on calotte edges (Figure 32-b).

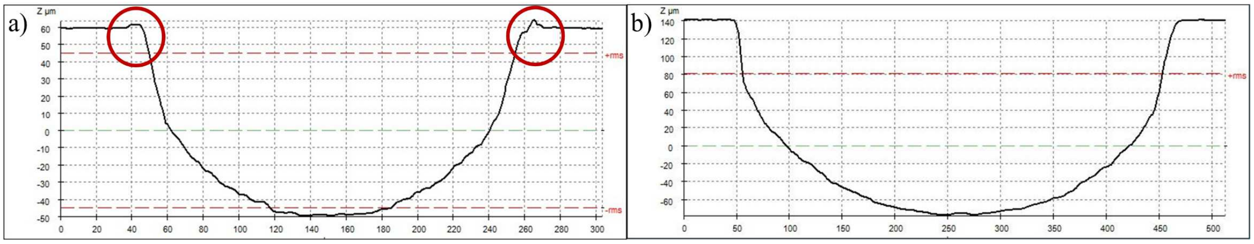

Figure 32. 2D sections through a calotte obtained by 3D optical profiler; a) first prototype design with burrs on the edges, b) second design without burrs

4.3 Calibration

Calibration of the reference standard was performed in several steps that will be described in this section. In the first step, diameter *D*, depth *Z*, and form error *F* of single calottes are measured by a µ-CMM Zeiss F25 following a dedicated probing strategy in order to obtain reliable reference data with low measurement uncertainty. Based on the measured results, volume *V* of single open calottes is calculated. In the following step, the same measurands are evaluated on CT scans of single uncovered pins (i.e. the calottes are not covered by any material in order to resemble the measurement task from the first step) in high resolution. The uncovered calottes are also measured by both 3D optical profilers and the multisensor CMs in order to obtain additional data for further evaluations. Finally, in the third step, the pins are covered by a counterpart with a flat face to form artificial internal porosity, and the above mentioned measurands are evaluated again.

The uncertainty of measurements was evaluated in individual calibration steps using methods adapted from international standards (GUM [26], and ISO 15530-3 [28]), and the German guideline VDI/VDE 2630-2.1 [29]. In order to simplify the task, and reduce time demands and costs of the calibration, a method to transfer the traceability of measurements between calibrated and non-calibrated features within the sample was developed.

4.3.1 Measuring instruments

The traceability of final CT porosity measurements was achieved by a multiple-step calibration procedure using several measuring instruments. The primary calibration that established the traceability of calottes diameter *D* and depth *Z* measurements was carried out at PTB by Dr. Michael Neugebauer using a µ-CMM Zeiss F25. Using a µ-CMM with low maximum permissible error (MPE) ensured low uncertainty of initial measurements, and thus facilitated keeping the uncertainty of final measurement results at minimum. Subsequent measurements were obtained by a multisensor CMS, two different profilers and a metrological CT system. The summary of measuring instruments used for the calibration is shown in Table 7.

Table 7. Measuring instruments used for the calibration of the reference standard**.**

Name	Type	Measurement principle	MPE
Zeiss F25	µ-CMM	Tactile probing	(0.25 + *L*/666) µm, *L* is length in mm
Werth Video Check IP 400	Multisensor CMS	Optical	(1.8+*L*/250) µm, *L* is length in mm
Sensofar Plu Neox	3D optical profiler	Confocal microscopy	N/A
Zygo NewView 8200	3D optical profiler	Confocal microscopy	N/A
Nikon Metrology X-Tek MCT 225	Metrological CT	CT scanning	(9 + *L*/50) µm, *L* is length in mm

CT data from calibration scans was analyzed using software VGStudio MAX 3.0 (Volume Graphics, Germany), and GOM Inspect Professional V8 (GOM, Germany). The latter software was also utilized for evaluating the data obtained from the rest of measuring instruments introduced in Table 7.

4.3.2 µ-CMM measurements

In order to simplify the task, and reduce time demands and costs of the calibration, measurements using the µ-CMM were performed on selected calottes. The method to propagate the uncertainty of calibration measurements to calottes that were not measured by the µ-CMM in the first step is explained in the following sections.

Calottes were measured by probing single points on the surface following a pre-defined pattern. The temperature controlled through the whole measurement was 19.9±0.2 °C. Due to the low coefficient of thermal expansion (CTE) of aluminum and stability of temperature, no temperature-related corrections were applied. The measurement procedure is defined as follows:

1) Coordinate system

   Right-handed Cartesian coordinate system is defined on each of the pins (Figure 33). The origin of the coordinate system is located at the center of Calotte 1 (see Figure 33 for calottes numbering convention) projected onto the top plane of the pin. The *Z*-axis is normal to the top plane of the pin and points away out of it. The *Y*-axis is perpendicular to the *Z*-axis and is defined by the straight line from the center of Sphere 1 to the center of Sphere 18 projected onto the top plane of the pin. The positive *Y*-axis points from the origin towards the center of Sphere 18. The *X*-axis is orthogonal to both the *X*- and *Y*-axes and its positive direction follows the right-hand screw rule.

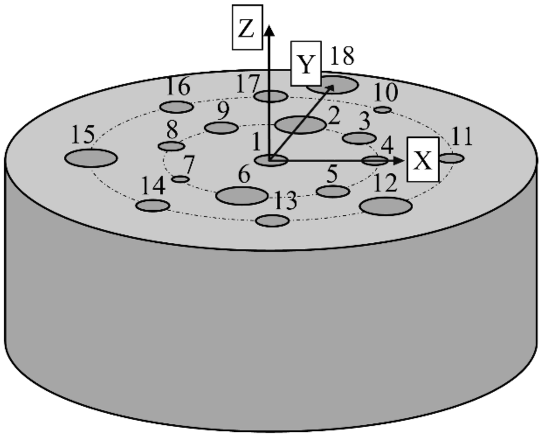

Figure 33. Schematic description of the coordinate system defined on the pin.

2) Probing pattern

   The measurement points were acquired in a pattern schematically shown in Figure 34. The points were probed at different heights along the *Z*-axis, offset by 20 µm from each other (with an initial offset of 10 µm to avoid the edge points), and evenly distributed along the perimeter with a step of 20 µm. In order to map sufficiently the bottom of the calotte, additional points were acquired in a 3 × 3 point grid as shown in the lower part of Figure 34.

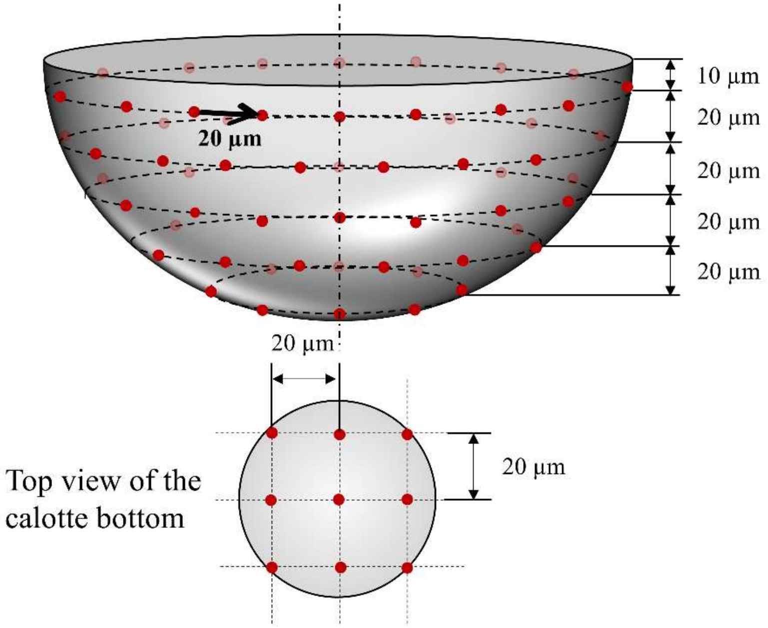

Figure 34. Definition of the probing pattern for the measurement of calottes by µ-CMM. Top: side view of the entire calotte. Bottom: top view of the calotte bottom.

3) Evaluation of results

Least-squares fitting method (Gaussian best fit) was used for the construction of measurement spheres, as well as for the construction of the top plane. Diameter D was evaluated as the diameter of the fitted sphere, and depth Z was measured as the distance between the top plane and the pole of the fitted sphere in the direction of Z-axis. Form error F was calculated as the difference between maximal and minimal distance of the acquired surface points from the center of the fitted sphere.

4) Calculation of calotte volume V

The volume of a calotte, considering the nominal shape, can be calculated according to the formula for calculating the volume of a hemisphere, i.e. $V_{\mathrm{HS}}=1/12\pi D^3$, where D is the diameter of the hemisphere. However, any manufacturing process has its finite precision, and it is not possible to produce perfectly nominal shapes. As a result, the manufactured hemispheres have a certain amount of form error, and the center of fitted sphere does not lie perfectly at the top plane (it typically lies below it). Therefore, the formula for the calculation of hemisphere volume must be corrected in order to reflect this phenomenon.

Simplified schema of the measurement task is shown in Figure 35. The volume of the defect is divided into hemispherical and cylindrical part. The corrected equation is as follows:

$$V = V_{HS} + V_C = \frac{1}{12}\pi D^3 + \frac{1}{4}\pi D^2 H, \qquad (4.1)$$

where V_{HS} is the volume of hemisphere, V_{C} is the volume of cylinder, D is the diameter of the fitted sphere and H is the distance between the sphere center and the top plane.

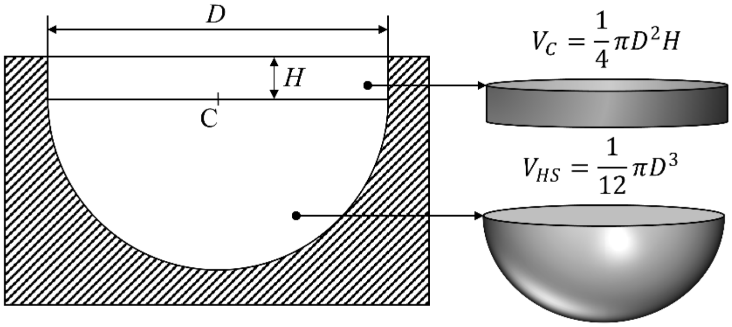

Figure 35. Schematic description of the proposed method for the calculation of a defect volume.

The form of the volume between the hemisphere and the top plane was assumed to be cylindrical. This assumption was verified by the comparison between the calotte diameter measured by the μ-CMM and the diameter of the circle measured in the top plane by the multisensor CMS. The results will be discussed further in this section.

5) Measurement uncertainty

The uncertainty of diameter *D*, depth *Z*, and center-to-plane distance *H* measurements was evaluated at Physikalisch-Technische Bundesanstalt (PTB) where the μ-CMM measurements were performed. The values of expanded uncertainty *U* (with coverage factor *k*=2 that corresponds to a confidence level of 95 %) for *D*, *Z*, and *H* are 1.5 μm, 1 μm, and 1 μm, respectively.

The uncertainty of volume *V* measurements was estimated according to the method described in GUM [26], i.e. by determining each source of error and propagating its quantity to the final measurement uncertainty statement. The error sources considered for the estimation of volume *V* measurement uncertainty, and individual contributions to the uncertainty for one of the calottes are listed in Table 8. It is worth noting that the contribution estimated from repeated measurements by statistical methods (i.e. using Type A evaluation) has been already included in the uncertainty of diameter *D* and center-to-plane distance *H* measurements.

Table 8. Volume *V* measurement error sources and their contribution to the uncertainty of μ-CMM measurements.

Source of error	Standard uncertainty	Contribution to *V* uncertainty/mm^3	Contribution to *V* uncertainty/% of calotte volume
Uncertainty of *D* calibration u_{CD}	0.00075 mm	0.00011	0.52
Uncertainty of *H* calibration u_{CH}	0.00050 mm	0.00005	0.24
Roughness u_R	0.00008 mm^3	0.00008	0.39
Deviation of the top part from cylindrical form u_{TP}	0.00001 mm^3	0.00001	0.06
Form error u_F	negligible	negligible	negligible
Temperature u_T	negligible	negligible	negligible

Values of expanded calibration uncertainties U_{CD} and U_{CH} were provided by PTB, and standard uncertainties u_{CD} and u_{CH} were calculated as the calibrated uncertainty divided by the coverage factor k=2, i.e. $u_{\mathrm{CD}}(u_{\mathrm{CH}})=U_{\mathrm{CD}}(U_{\mathrm{CH}})/2$. Since the calibration uncertainties are given in millimeters and the output quantity is volume given in mm^3, the sensitivity coefficients must be calculated as partial derivatives of the model defined by Equation 4.1. The formulas for the calculation of sensitivity coefficients are defined as follows:

$$\frac{\partial V}{\partial D} = \frac{1}{4}\pi D^2 + \frac{1}{2}\pi DH, \tag{4.2}$$

$$\frac{\partial V}{\partial H} = \frac{1}{4}\pi D^2. \tag{4.3}$$

Due to the morphological filtering of the acquired points caused by a finite diameter of the touch probe, the calotte surface is typically probed on roughness peaks as schematically illustrated in Figure 36. This can result in underestimating the volume of the measured feature as the surface below the peaks remains unmapped. It was therefore necessary to investigate the surface of the calotte by other means.

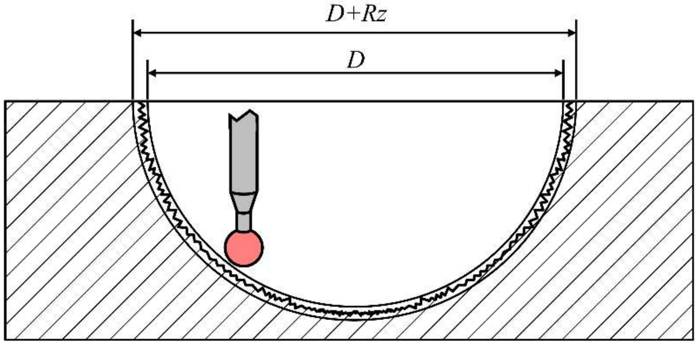

Figure 36. Schematic representation of the influence of roughness on diameter *D* measurements by tactile CMM.

The influence of roughness was estimated based on the measurements obtained by 3D optical profilers. Roughness parameter *Rz* was considered as the attribute that determines the range of measured diameter since it is defined as the sum of height of the largest profile peak and valley within a sampling length [122]. Standard uncertainty related to the roughness of calotte surface was calculated according to equation:

$$u_R = \frac{V_{D+Rz} - V_D}{2\sqrt{3}}, \tag{4.4}$$

where V_D and V_{D+Rz} are volumes of the calotte calculated according to Equation 4.1 using calotte diameter *D* as measured by µ-CMM and diameter *D* extended by the value of *Rz*, respectively. The square root of three represents the approximation by rectangular distribution [123].

The contribution caused by the deviation of the top part from the cylindrical form u_{TP} was estimated based on the measurements by multisensor CMS. Diameters of edge circles D_{C} located at the intersection of a calotte and the top plane (Figure 37) were measured by the optical sensor of the multisensor CMS. Measured diameters D_{C} were compared with diameters *D* obtained by the µ-CMM on the whole calotte surface resulting in a maximum error of 5 μm. Standard uncertainty related to the deviation of the top part from cylindrical form was calculated according to equation:

$$u_{TP} = \frac{V_{CF} - V_C}{2\sqrt{3}}, \tag{4.5}$$

where V_C is the volume of the top cylindrical part of the calotte calculated according to Equation 4.1 and V_{CF} is the volume of a conical frustum representing the case where $D_C > D$. Based on the results obtained by multisensor CMM, and the manufacturing technique (milling), the inverse case is not considered, i.e. $D > D_C$. The volume of the conical frustum was calculated as:

$$V_{CF} = \frac{\pi H}{3}(D^2 + DD_C + D_C^2). \tag{4.6}$$

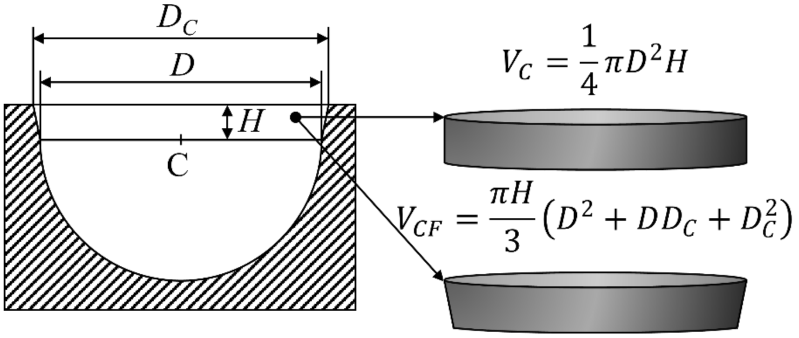

Figure 37. Deviation of the top part of the calotte from the cylindrical form and its influence on diameter *D* and volume *V* measurements.

Standard uncertainty related to form error of calottes u_F was evaluated based on simulations performed on calottes designed in a CAD software with artificial form error ranging from 0-10 μm. The volume of calottes was calculated according to the model defined by Equation 4.1 and compared to the nominal value, resulting in a maximum error of 0.053 %. Contribution of this error to measurement uncertainty calculated following the same principle as described in Equations 4 and 5 was equal to 0.01 %, and thus could be considered negligible. Low influence of form error on the volume measurement can be explained by the fact that the least-squares fitting eliminates the major part of error. Furthermore, form error was already included in the uncertainty budget of diameter *D* measurements.

Measurements of *D* and *H* are influenced by the temperature at which the part is measured, thereby influencing the calculation of volume as well. The error of *D* and *H* measurements caused by temperature was calculated according to equations:

$$\Delta D = D_0 \alpha \theta, \Delta H = H_0 \alpha \theta, \tag{4.7}$$

where D_0 and H_0 are the measured diameter and center-to-plane distance of the calotte, respectively, α is the coefficient of thermal expansion (23×10^{-6} K^{-1} at 20 °C), and θ is the maximum measured deviation of temperature from the 20 °C reference value. The maximum error of volume measurement caused by temperature variation was 0.047 % resulting in standard uncertainty u_T equal to 0.01 % that can be considered negligible.

The values of expanded uncertainty for *D*, *Z* and *V* measurements in the first calibration step are listed in Table 9. Uncertainties of *D* and *Z* measurements are given in µm while the uncertainty of *V* measurement is in % of measured volume. In order to ensure that the uncertainty of volume measurement is not underestimated, the values stated in Table 9 represent the highest uncertainty that was evaluated on selected calottes measured by the µ-CMM.

Table 9. The values of expanded uncertainty for *D*, *Z* and *V* measurements in the first calibration step.

Measurand	**Measurement uncertainty U_{CMM}(k=2)**
Diameter *D*	**1.5 µm**
Depth *Z*	**1 µm**
Volume *V*	**1.3 %**

4.3.3 Measurements of open calottes by CT

While the GUM [26] method was used for the evaluation of measurement uncertainty in the first step, a method adapted from ISO 15530-3 [28] and VDI/VDE 2630-2.1 [29] was used here. Given the measurement task from the first calibration step (i.e. measurements of open porosity) and similarity requirements defined by the above-mentioned standard and guideline, open calottes were measured by CT in order to achieve the traceability of CT measurements. Individual pins were scanned in high resolution 40× (equal to a VS of 5 µm) to minimize systematic errors.

In contrast to the previous step, all 72 calottes were measured here. The measurement features (planes and spheres) for evaluating diameter *D* and depth *Z* of individual calottes were constructed following the same procedure as in the first step, i.e. least-squares fitting. Furthermore, the points close to the edge (10 µm below the top plane similarly to µ-CMM measurements) of the calotte were not considered for the construction of the measurement sphere in order not to bias the results. Since the CT evaluation software has a dedicated module for evaluating the volume of internal porosity, and this module was used also for subsequent calibration and measurements, volume *V* of individual calottes was evaluated using this function. The so-called "*Defect analysis* module" was used applying "Only threshold" algorithm to the dataset, i.e. applying a global threshold value to separate internal porosity from material. In the present case, ISO-50% value was used for thresholding the data, representing the average gray value (GV) between the material and the background peak. Measurement traceability was established through repeated CT measurements of a calotte measured by the µ-CMM in the first step using measurement uncertainties stated in Table 9. Measurement uncertainty was calculated according to the following equation:

$$U = k\sqrt{u_{cal}^2 + u_p^2 + u_w^2 + u_b^2}, \tag{4.8}$$

where:

u_{cal} is the standard uncertainty of measurement due to the uncertainty of calibration of the calibrated feature stated in Table 9, and calculated as $u_{\mathrm{cal}}=U_{\mathrm{CMM}}/2$.

u_{p} is the standard uncertainty of measurement due to the measurement process, i.e. standard deviation of the repeated measurements.

u_w is the standard uncertainty of measurement due to variations in form error and roughness over the measured calottes estimated based on roughness and form errors measured by 3D optical profilers and multisensor CMS following the same principle defined by Equations 4 and 5.

u_b is the standard uncertainty of measurement of the correction of the systematic error *b* between the value indicated by CT and calibrated value containing the standard uncertainty of measurement of CTE. However, as proved in Section 4.3.2, the influence of thermal expansion in temperature controlled environment is negligible given the measurement task.

A summary of error sources, their contribution to the uncertainty, and expanded measurement uncertainty in the second calibration step for all the measurands is shown in Table 10.

Table 10. Error sources, their contribution to the uncertainty, and expanded measurement uncertainty in the second calibration step.

Measurand	u_{cal}	u_p	u_w	***U*(*k*=2)**
Diameter *D*	0.75 µm	0.1 µm	0.5 µm	**1.8 µm**
Depth *Z*	0.5 µm	0.1 µm	0.3 µm	**1.2 µm**
Volume *V*	0.7 %	0.02 %	0.03 %	**1.4 %**

As recommended in both ISO 15530-3 [28] and VDI/VDE 2630-2.1 [29], the systematic error between the value indicated by CT and calibrated value was corrected. Furthermore, in order to verify the procedure proposed here, CT corrected results of *D*, *Z* and *V* measurements obtained on calottes previously calibrated by µ-CMM were compered to µ-CMM calibrated values to check whether they stay within the uncertainty limits.

Different measurement instruments (µ-CMM, CT, 3D optical profiler) use different techniques for the acquisition of measurement points, resulting in point clouds with diverse density. Typically, in the case of single point probing that was used in the first calibration step, CMMs acquire much less measurement points compared to optical techniques. Therefore, also the degree to which the form of the measurement feature (hemisphere, plane) is characterized differs. As a result, the measurement outputs can significantly vary among the used CMSs. In order to exclude these effects, so called patch-based procedure was applied to evaluate CT and 3D optical profiler data, and the results were compared to those obtained by using all acquired points.

The patch-based procedure is schematically explained in Figure 38. Tactile probing was resembled by selecting circular patches with a diameter of 10 µm for the construction of representative points. In order to make sure that the representative points are constructed at the same position where the µ-CMM probed the surface, the coordinates of µ-CMM acquired points were used as the centers of the circular patches. The correct transfer of coordinates was ensured by maintaining the same coordinate system. Representative points were then used for the construction of the measurement sphere. The comparison of results using patch-based procedure and by using all acquired points resulted in deviations below 0.5 µm. Therefore, the effect of different density of measurement points can be considered negligible.

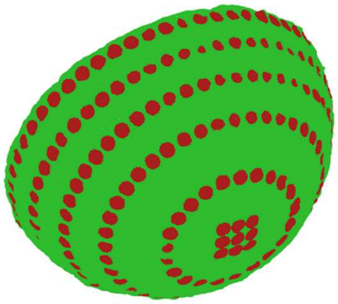

Figure 38. Principle of the patch-based procedure. The circular patches represent the selection of points for the construction of the representative point.

4.3.4 Measurements of closed calottes by CT

Although the traceability of CT porosity measurements has been established in Section 4.3.3, it is valid only for open porosity. It was therefore necessary to perform another calibration step in order to achieve the traceability of closed porosity CT measurements as well.

Given the CT configuration and the need for a high-resolution calibration scan, the pins could not be mounted in the cylindrical body in order to avoid unintentional collision with the X-ray tube. Therefore, the pins were covered by a counterpart with a flat face to form artificial internal porosity and to resemble the final configuration of the reference standard.

Similarly to the previous step, also here the uncertainty of measurements was evaluated according to a method adapted from ISO 15530-3 [28] and VDI/VDE 2630-2.1 [29], using the formula described by Equation 4.8. Given the fact that the configuration was modified by covering the calottes by a counterpart, the contribution of u_w was recalculated according to Equation 4.9 in order to take into account the uncertainty associated with the fitting of the two parts together; more specifically, the variation of fitting tightness over all 72 calottes.

$$u_w = \sqrt{u_{w1}^2 + u_{w2}^2}, \tag{4.9}$$

where u_w1 is identical to u_w used in the second step of the calibration procedure and u_w2 is the contribution to the measurement uncertainty caused by the variation of fitting errors calculated according to the following equation:

$$u_{w2} = \frac{V_R}{2\sqrt{3}}, \tag{4.10}$$

where V_R is the volume of a cylinder with diameter D_C and a height of 1 µm. V_R represents the maximum volume enclosed between the two ideally flat surfaces located above the calotte estimated based on the measurements of form error and roughness on the contact surfaces, i.e. on the faces of the pin and the counterpart. The situation is schematically explained in Figure 39.

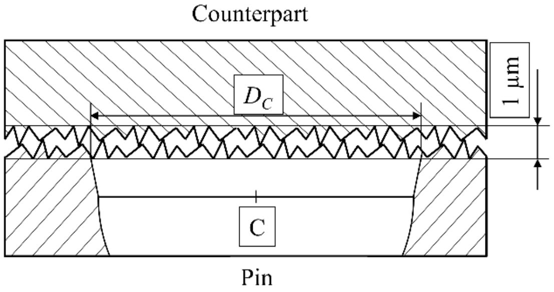

Figure 39. Schematic representation of the fitting of the pin and the counterpart. Microgeometry errors (roughness) of the contact surfaces are magnified in this figure for better visualization.

The measurement task in the case of closed porosity is similar to the open porosity, the only difference is the principle of closing the pores in order to allow the evaluation of their volume. While in the second step, the calottes were closed by the least-squares fitted plane, they were covered by the surface of the counterpart in the present case. Given this different configuration, the top surface closing the calotte has slightly different form and position. This difference caused by finite form error and roughness of the pin and counterpart faces results in variations of the enclosed volume. It is therefore necessary to consider this fact when correcting the systematic error.

The traceability of CT porosity volume measurements was established, and the systematic error between CT and µ-CMM volume measurements was evaluated in the second step of the calibration procedure. Since the difference between the ways of closing the pores explained above is not considered a systematic error, the volume measured in this step was corrected by the systematic error calculated in the previous step. This approach requires that the measurement procedure be similar to the one used in the case of open porosity, i.e. the volume of calotte is evaluated using the *Defect analysis* module.

A summary of error sources, their contribution to the uncertainty, and expanded measurement uncertainty in the third calibration step for all the measurands is shown in Table 11.

Table 11. Error sources, their contribution to the uncertainty, and expanded measurement uncertainty in the third calibration step.

Measurand	u_{cal}	u_{p}	u_{w}	$U(k=2)$
Diameter D	0.75 µm	0.1 µm	0.7 µm	**2.1 µm**
Depth Z	0.5 µm	0.1 µm	0.5 µm	**1.4 µm**
Volume V	0.7 %	0.02 %	0.4 %	**1.6 %**

4.4 Accuracy of CT porosity measurements

The accuracy of CT porosity measurements was evaluated according to several investigations discussed in this section:

1) Influence of CT parameters settings on measurement errors.
2) Repeatability of measurements.
3) Comparison between measurement results obtained from simulated and real CT data sets.
4) Comparison of different evaluation software.

CT datasets for this study were acquired by a metrological CT system, Nikon Metrology X-Tek MCT 225, used at low magnification (18.4×, which corresponds to a voxel size of 11 µm). The maximum permissible error (MPE) of the system is (9 + L/50) µm (where L is length in mm). The data was processed and analyzed using software VGStudio MAX 2.2.6 (Volume Graphics, Germany) except for analyses described in Section 4.4.5, where Volume Player (Fraunhofer EZRT, Germany) and iAnalyse (University of Upper Austria, Austria) software tools were applied.

Each CT dataset was evaluated following the same procedure in order to ensure the consistency of measurement results. The workflow is described as follows:

1) Loading the dataset and determination of surface using the local adaptive method with noise removal to reduce potential noise inside the defects.
2) Alignment of the dataset and segmentation of the volume in order to remove the calotte edge points for the measurement of defects diameter D.
3) Fitting of measuring elements, i.e. least-squares spheres and planes, and measurement of defects diameter D and depth Z.
4) Evaluation of defects volume V using *Defect analysis* module and *Only threshold* algorithm embedded in VGStudio MAX.
5) Exporting the measurement results.

4.4.1 Measurands and measurement strategies

The measurands evaluated in this section are defined in Figure 40: (i) diameter of a defect D, (ii) depth of a defect Z and (iii) volume of a defect V. In an ideal case, the second measurand, Z, would be superfluous as a hemisphere is sufficiently defined by its diameter. However, in a real case where the spheres have a finite form error, centers of spheres in most cases lie under or above the top plane. Defect diameters D were measured on Gaussian best fitted spheres (least-squares method) avoiding edge points which can distort the fitted features. The depth Z was measured as the distance between the top plane and the pole of the least-squares fitted sphere. The least-squares fitting method was applied also for the construction of the top plane; the points for the fitting of the plane were collected inside the defects where the plane can be measured by CT. Volume V was evaluated using the software module Defects analysis in VGStudio MAX (Volume Graphics, Germany.

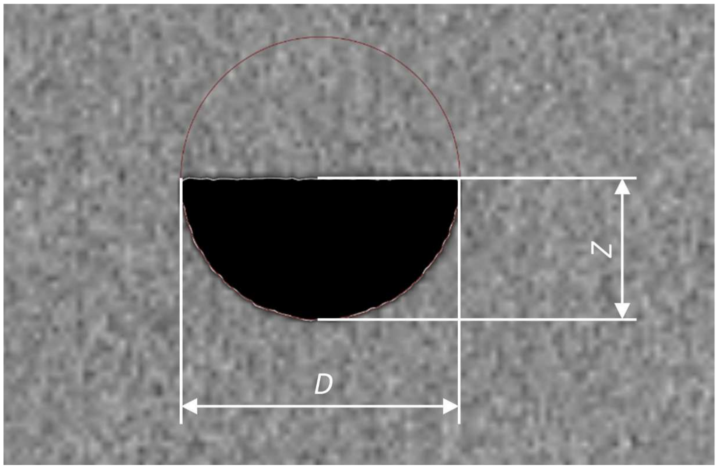

Figure 40. Definition of measurands: defect diameter D and depth Z.

4.4.2 Influence of CT parameters settings on measurement errors

In setting up a CT scan, several factors depending on operator's choice influence final image quality and thus 3D volume dataset itself. Based on preliminary results [124,125], where voltage *U* and current *I* were identified as the most important influencing factors after magnification, four levels of *U* and *I* were chosen and Design of Experiments (DoE) technique was applied to study their influence. Magnification is not considered in this study as its influence was already thoroughly investigated in other studies [117,124,126,127] with conclusion that with higher magnification, higher accuracy is achieved. The scanning parameters are shown in Table 12. The range of parameters was chosen with regards to obtain sufficient power to penetrate the sample with the lowest settings and at the same time not to saturate the detector using the highest settings.

Table 12. Scanning parameters for DoE.

No.	1	2	3	4
Voltage *U*/kV	130	145	160	175
Current *I*/µA	30	35	40	45
Voxel size/µm	10.9			
Exposure time/ms	2829			
Filter	0.25 mm Cu			
Number of projections	1800			

Results of DoE are shown in Figure 41. The analysis was performed for all the 72 defects; however, the plot would be illegible if the complete results were shown. Therefore, simplified charts with four representative examples are plotted in Figure 41; more specifically, one small (Ø 110 µm), two medium (Ø 160 µm and Ø 240 µm) and one large (Ø 400 µm) defect was selected.

a) Diameter measurements (*D*)

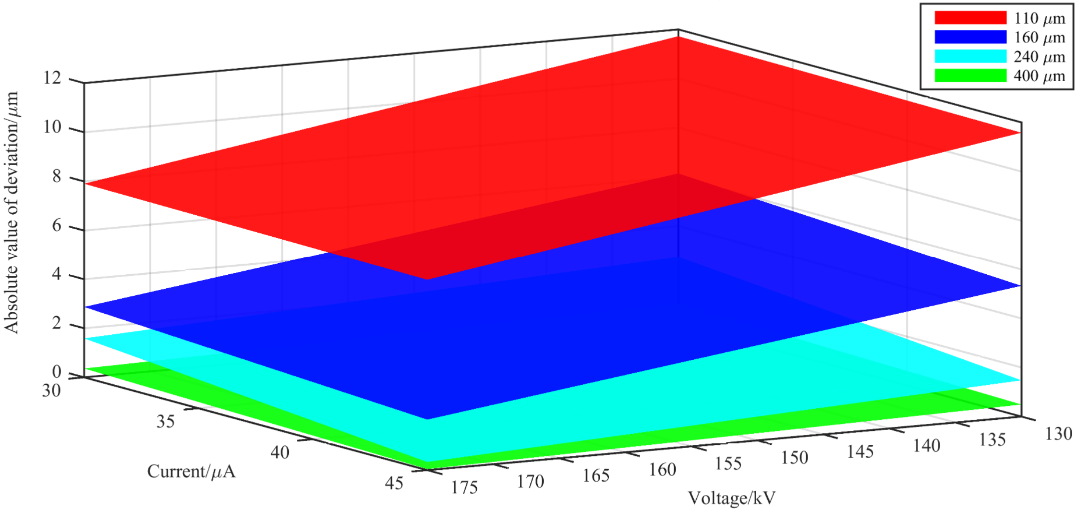

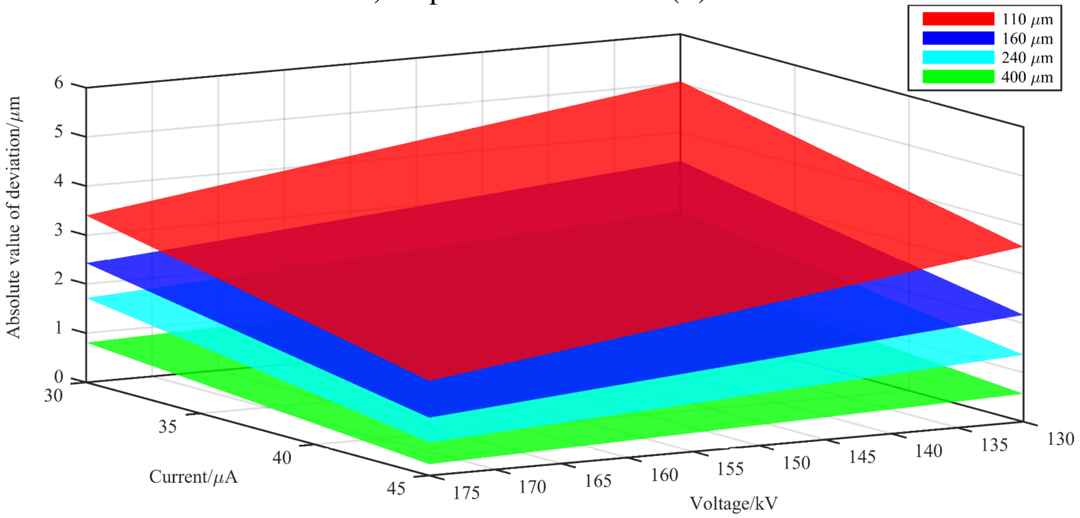
b) Depth measurements (Z)

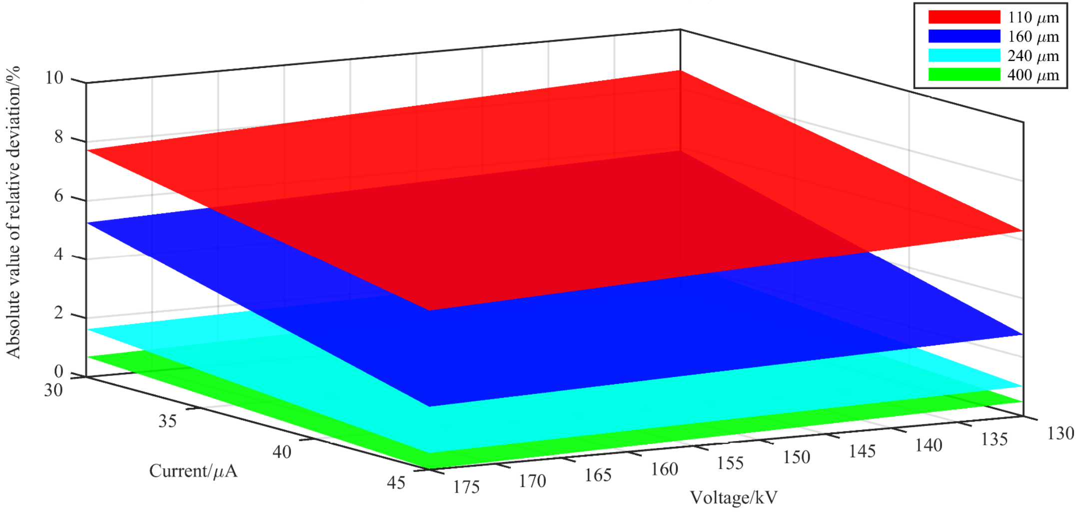
c) Volume measurements (V)

Figure 41. Influence of CT parameters settings on measurement deviations: a) absolute value of D deviations from reference values, b) absolute value of Z deviations from reference values, c) absolute value of relative V deviations from reference values.

Results in Figure 41 show that the higher are the values of voltage and current, the lower are deviations from reference values (obtained by the calibration described in Section 4.3) for all the three characteristics, including volume V. The difference in magnitude between D and Z deviations (difference between Figure 41-a and Figure 41-b) demonstrate that errors are lower for depth measurements than for diameter measurements. Another observation that can be extracted from Figure 41 is that measurements of smaller defects are more problematic (as the deviations are higher for all the three characteristics) than for larger defects. However, apart from D measurements of the smallest defects, the deviations are within ±5 µm, which shows good performance in porosity measurements.

Results plotted in Figure 41 show that the choice of scanning parameters has significant influence on the accuracy of porosity measurements, especially for defects below 160 µm. In fact, in case of the smallest defects, the variation caused by voltage and current settings is approximately 4 µm for D and Z measurements and around 3 % for volume evaluation. The larger are the defects, the lower is the influence of *U* and *I* on measurement errors, as for Ø 400 µm defects the variation is below 1 µm for *D* and *Z* and below 1 % for *V* measurements.

Another proof that higher values of current and voltage have a positive influence on measurement errors can be seen in Figure 42. The chart shows the dependency of the average volume measurement deviations for all 72 defects on *U* and *I* settings. It can be observed that the average deviation decreases from 6.7 % for the lowest settings, down to 2.4 % for the highest settings.
It is worth noting that the scans were performed using low tube power (below 8 W) and, therefore, it was possible to maintain the focal spot size at 3 µm. Hence, by keeping the focal spot size at the lowest level, the effect of investigated parameters (*U*, *I*) was isolated.

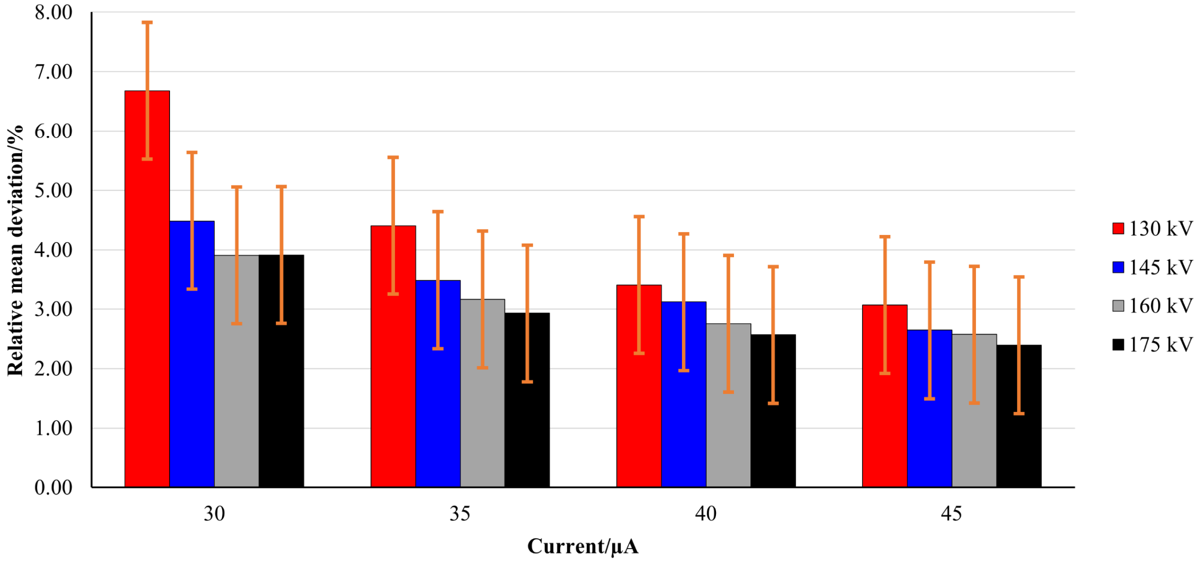

Figure 42. Dependency of relative mean volume deviation on current and voltage settings. Error bars represent mean standard deviation of repeated scans calculated over all 72 defects.

There are two main explanations on why the positive trend of increasing voltage and current on measurement errors was observed:

1) The amount of noise in acquired projections is related to the amount of X-ray radiation, which is directly dependent on the tube current. If all the CT parameters are kept constant, the image noise scales roughly inversely proportional to the square root of the tube current [3,11]; i.e. by increasing the tube current, lower amount of image noise, and thus higher signal-to-noise ratio (SNR) can be achieved.
2) The dependency of conversion rate between the electrons accelerated in an X-ray tube and X-rays is different for current and voltage. While the dependency on current is linear, the generation of X-rays increases squarely with the tube voltage according to the equation $i \propto U^2 Z I$, where i is the X-ray intensity, U and I are the X-ray tube voltage and current, respectively, and Z is the atomic number of the target. In other words, by increasing the tube voltage and, therefore, the energy of X-rays, a square-law X-ray output is generated with only linear increase of the tube power. Because of this behavior, one can achieve lower amount of noise and higher contrast in acquired projections [128].

4.4.3 Repeatability of measurements

During scanning, a CT system is influenced by various factors, such as thermal instability, scattering, focal spot drift, etc. [2], which have impact on the repeatability of CT measurements. These effects directly influence the quality of acquired images and subsequently the reconstructed volume as well. In this study, the stability of the investigated CT system was evaluated based on results from repeated measurements. 12 scans with the same set of CT scanning parameters were acquired during the DoE batch scan described in Section 4.4.2. The optimal scanning conditions resulting in highest measurement accuracy were chosen based on the prior investigation.

Results in Figure 43 show mean deviations for each of the 72 defects supplemented by ± 1 standard deviation.

a)

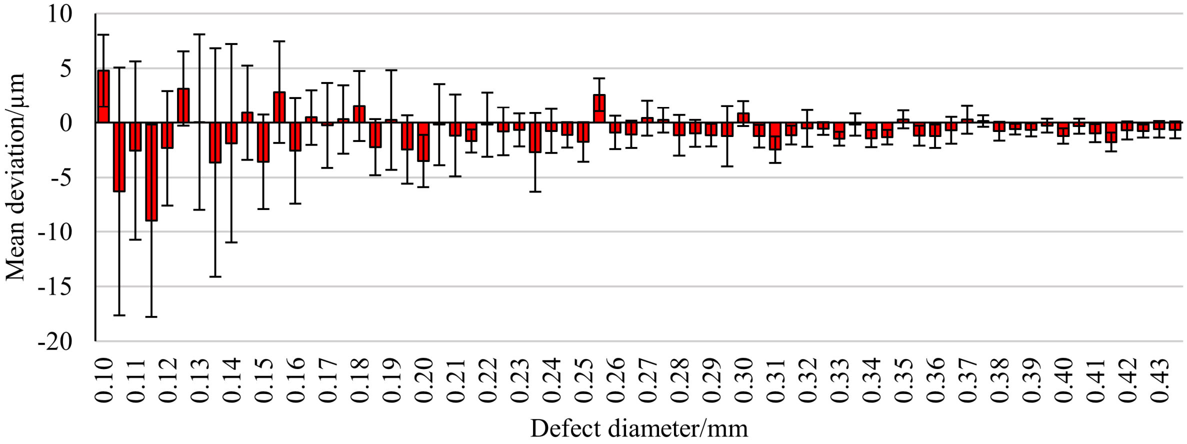

b)

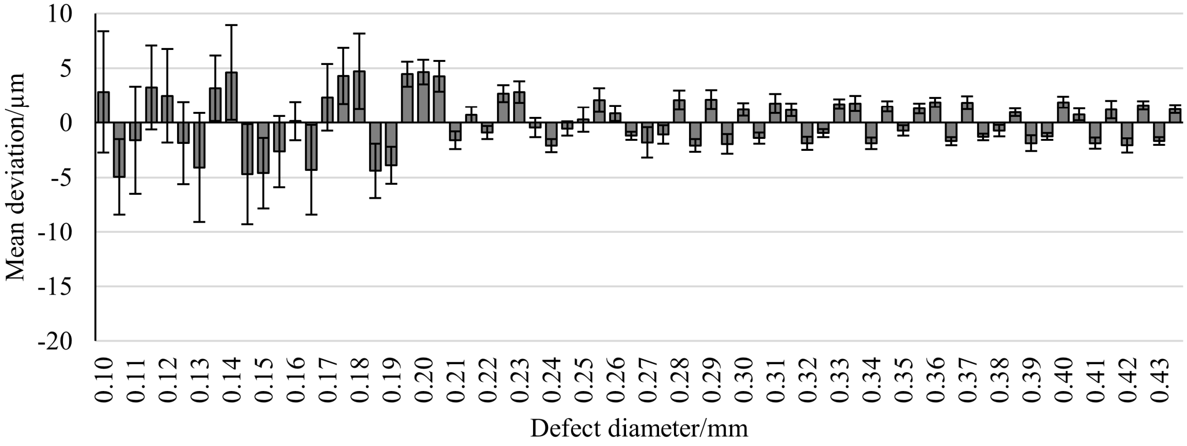

c)

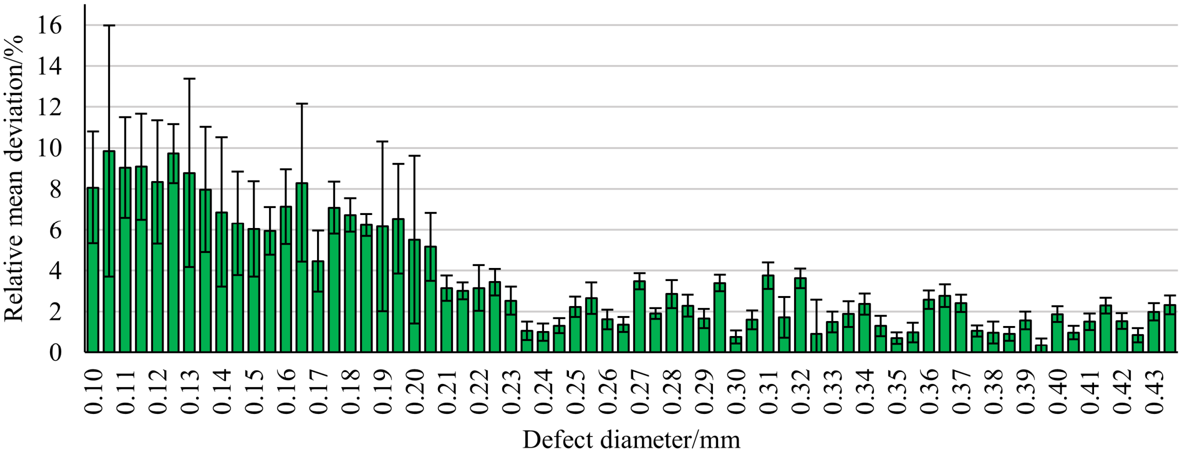

Figure 43. Repeatability of measurements represented by ± 1 standard deviation error bars superimposed onto the histogram of mean value of deviations: a) deviations of diameter *D* measurements, b) deviations of depth *Z* measurements, c) relative deviations of volume *V* measurements.

Values of mean deviation shown in Figure 43-a, b demonstrate good performance of CT in porosity diameter and depth measurements as, apart from 2 cases, the deviation is below ± 5 µm. Nonetheless, measurement errors for smaller defects are higher (close to ± 5 µm) than for larger defects (less than ± 1 µm), which confirms the previous observations; i.e. measurements of smaller defects are more problematic. This trend is confirmed also by values of standard deviation, which ranges from 11 µm for smaller defects, to less than 1 µm for larger defects.

The dependency that can be observed in Figure 43-c shows a positive trend in deviations of volume measurements. In other words, the defects measured in assembled object at lower magnification (voxel size = 11 µm) appear to be larger than at higher magnification (voxel size = 5 µm) where the calibration was performed. This behavior is in agreement with results of relevant publications [117,126,127] and is caused by averaging due to decreasing voxel size, lower sharpness of CT data and decrease of information content with decreasing magnification. Relative deviations of defects below 200 µm are lower than 10 % and lower than 5 % for defects above 200 µm. Hence, also results of volume measurements are in agreement with the observation that measurements of small defects are more problematic.

4.4.4 Comparison between measurement results obtained from simulated and real CT data sets

In addition to real CT scans, numerical simulations with extended range of voltage and current were performed in order to validate the results acquired on the real CT data sets. The CT data were simulated using the software “Analytical RT Inspection Simulation Tool” (aRTist, developed by Bundesanstalt für Materialforschung und -prüfung (BAM), Germany). The simulations were performed using the same parameters as listed in Table 12 supplemented by five additional voltage/current combinations listed in Table 13. In order to isolate the effects of current and voltage, all other parameters were kept unchanged for all the simulation runs. The focal spot size was set to 3 µm, which corresponds to the estimated focal spot size of the real CT scans.

Table 13. Additional current/voltage combinations for CT data simulations

No.	1	2	3	4	5
Voltage/kV	100	130	130	200	250
Current/µA	35	70	100	35	35

The results in Figure 44-a, b, and c show that the effect of voltage and current on the simulated data is similar to the trends observed in real CT datasets; i.e. the higher are the values of U and I, the lower are the measurement errors. Furthermore, similarly to real CT scans, measurements of smaller defects introduce higher measurement errors. Chart in Figure 44-d shows in addition relative mean deviations of volume measurements; i.e. mean measurement errors over all 72 defects for each voltage/current combination. The results confirm previous observations about the positive effect of increasing U and I settings on measurement errors. It must be noted that the magnitude of deviations is lower than that of the real data. This is caused by neglecting in simulated data some of the effects that are actually present in real CT scans, such as geometrical instability of the system, focal spot drift, etc.

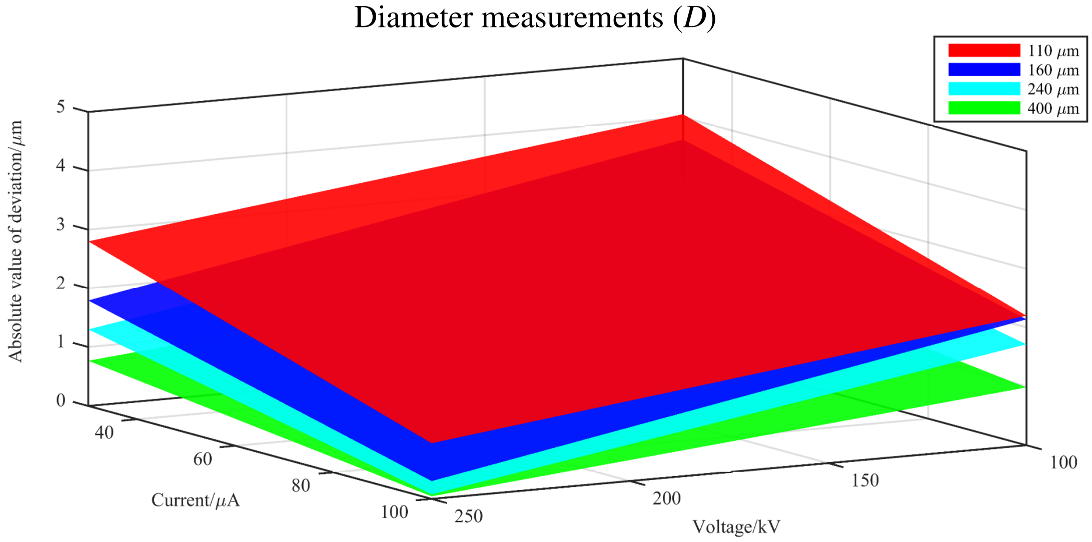

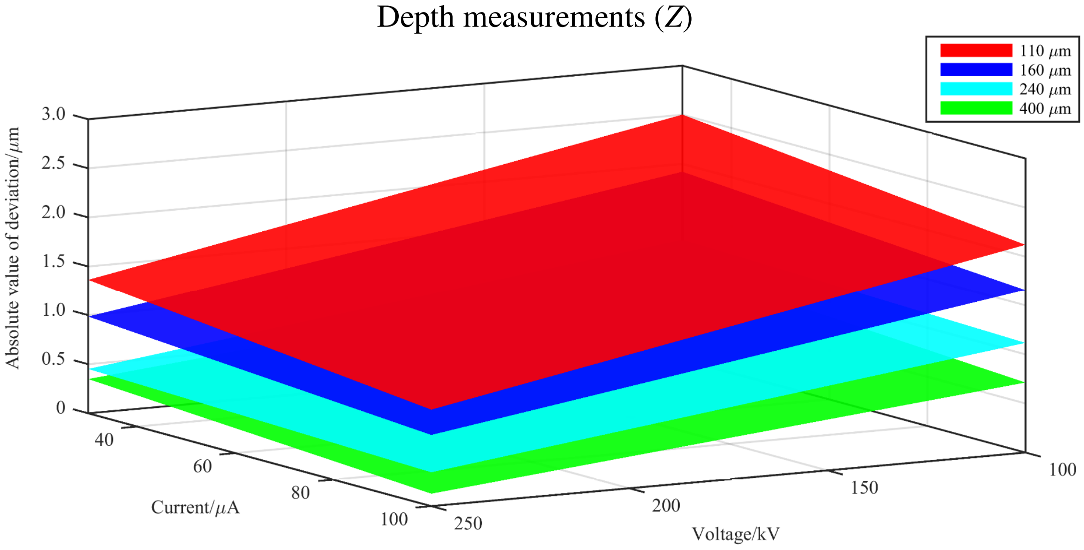

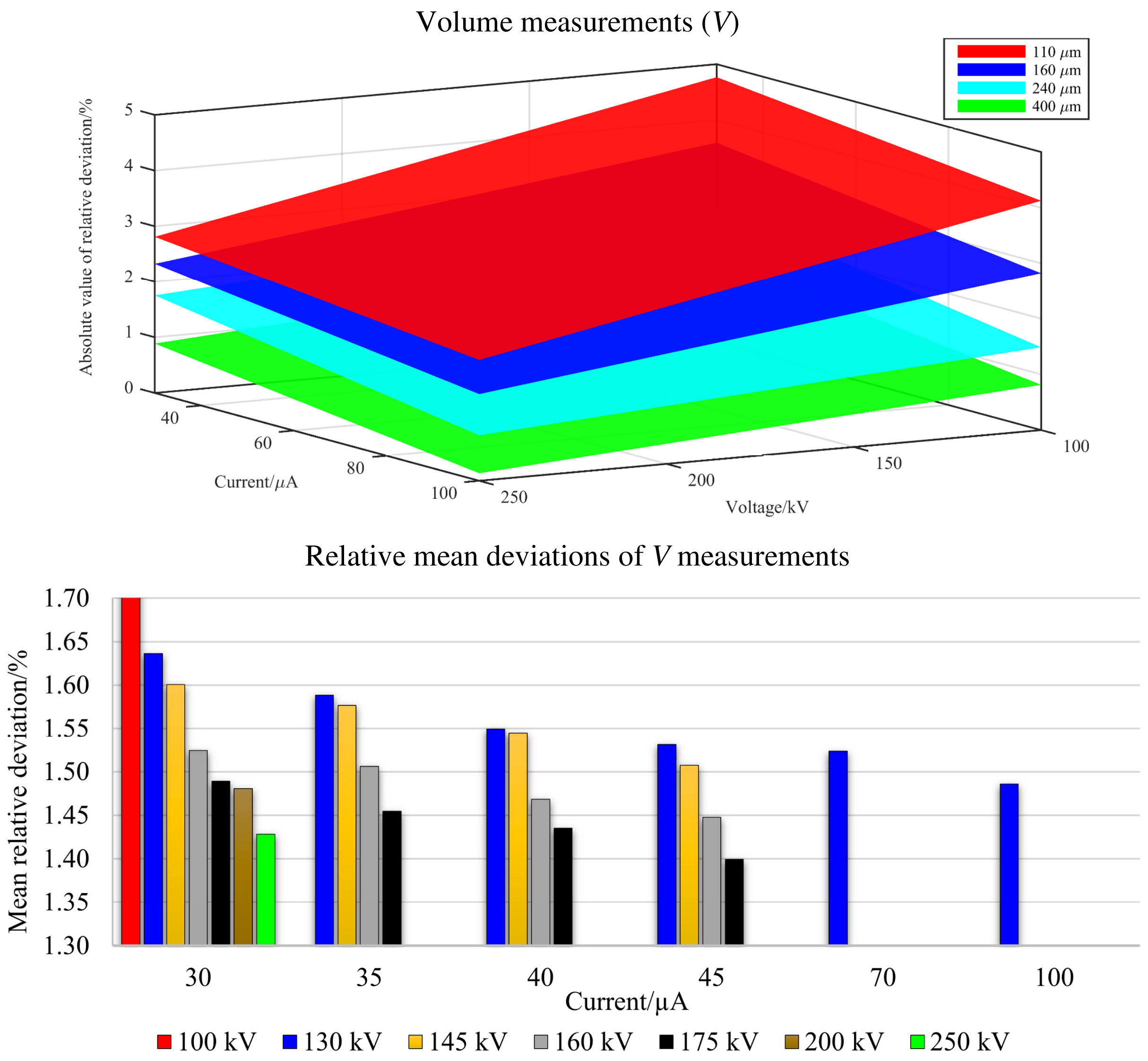

Figure 44. Simulation results: a) influence of CT parameters settings on *D* measurements, b) influence of CT parameters settings on *Z* measurements, c) influence of CT parameters settings on *V* measurements, d) relative mean deviations of *V* measurements related to current and voltage settings.

4.4.5 Comparison of different evaluation software

In previous sections, VGStudio MAX was used for the assessment of internal defects, as it is a well-established software tool in industrial CT applications. However, the increasing importance of the accurate evaluation of internal defects drives the need for new software tools that are being developed. In this section, results of volume measurements from VGStudio MAX are compared to results from Volume Player (developed by Fraunhofer EZRT, Germany) and iAnalyse (developed by the University of Upper Austria). The Only threshold method was applied for all the three software tools with a threshold value obtained by the ISO-50% technique described in Section 2.4.1. The chart in Figure 45 shows that deviations from nominal values are lower for VGStudio MAX than for the other two software tools, while Volume Player and iAnalyse generate exactly the same results. The reason why both the latter software tools demonstrate the same behavior is the fact that they use the same calculation procedure. In a first step, the data is binarized according to the threshold value; i.e. “0” is attributed to the material gray values and “1” is attributed to internal defects (background gray values). In a second step, Connected Component Filter (CCF) is applied for the separation of pores and their labelling [129].

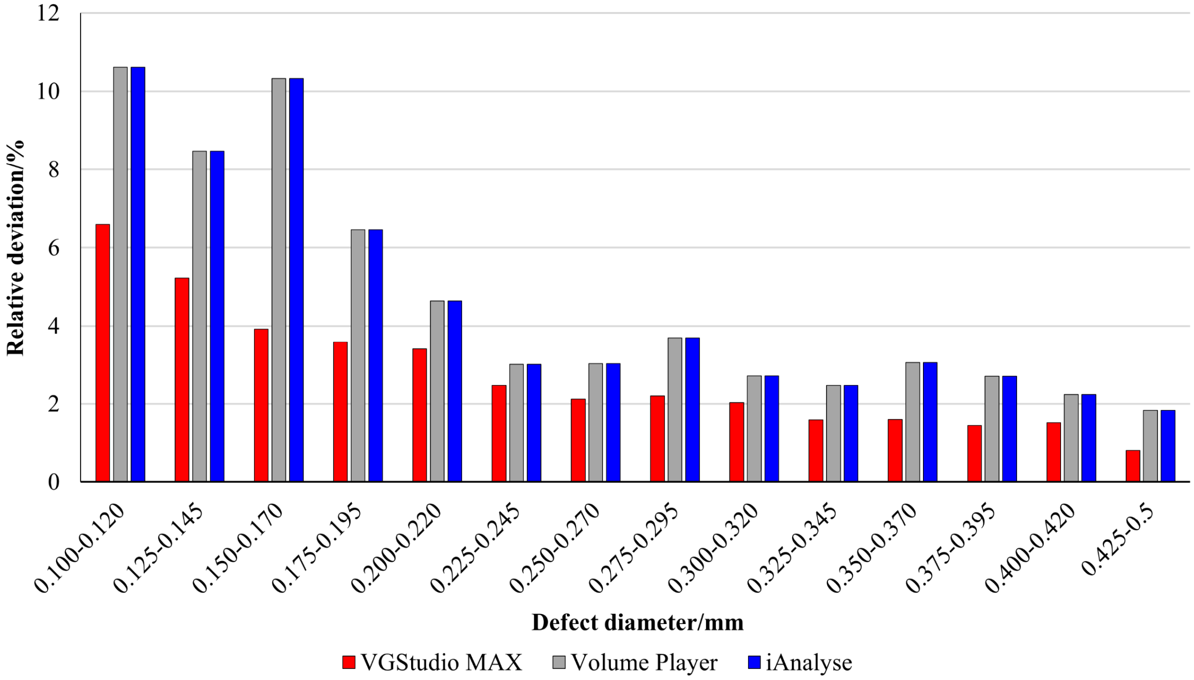

Figure 45. Comparison of three different CT data processing software tools.

4.4.6 Improving porosity measurements by optimizing threshold value

In the previous sections, ISO-50% has been used as a technique for the determination of threshold value that was subsequently used for the determination of surface for diameter *D* and depth *Z* measurements, and as an input for the *Defect analysis* module for the evaluation of defects volume *V*. However, it has been proved that ISO-50% does not necessarily have to be the optimal thresholding technique [130,131]. Therefore, different ISO values were tested in order to investigate their influence on measurement results, and results of this investigation are discussed in this section.

The study was performed for both the calibration and test scans, in higher (40×, VS = 5 µm) and lower (18.4×, VS = 11 µm) magnifications. Nine ISO thresholding levels were used ranging from ISO-10% – ISO-70% with an increment of 10%. Values ISO-25% and ISO-35% were added to the set in order to increase the resolution in the critical range. The specific ISO values were calculated according to the formula ISO-X=$X(GV_{MAT}-GV_{BCKG})+GV_{BCKG}$, where X is the ISO level (in percent), GV_{MAT} is the gray value of material peak and GV_{BCKG} is the gray value of background peak. Each ISO value was then used in the *Defect analysis* module in the evaluation software for evaluating volume *V* of each defect. Similarly, the ISO values were used for the determination of surface using local adaptive thresholding algorithm, and the values of diameter *D* and depth *Z* were evaluated based on measurement features fitted on the defined surface.

Charts shown in Figure 46 represent the comparison of measurement results obtained on selected calottes measured by µ-CMM and CT in high magnification. More specifically, values of *D*, *Z*, and *V* measured on different calottes using different ISO values are plotted in the chart, including µ-CMM values as a reference.

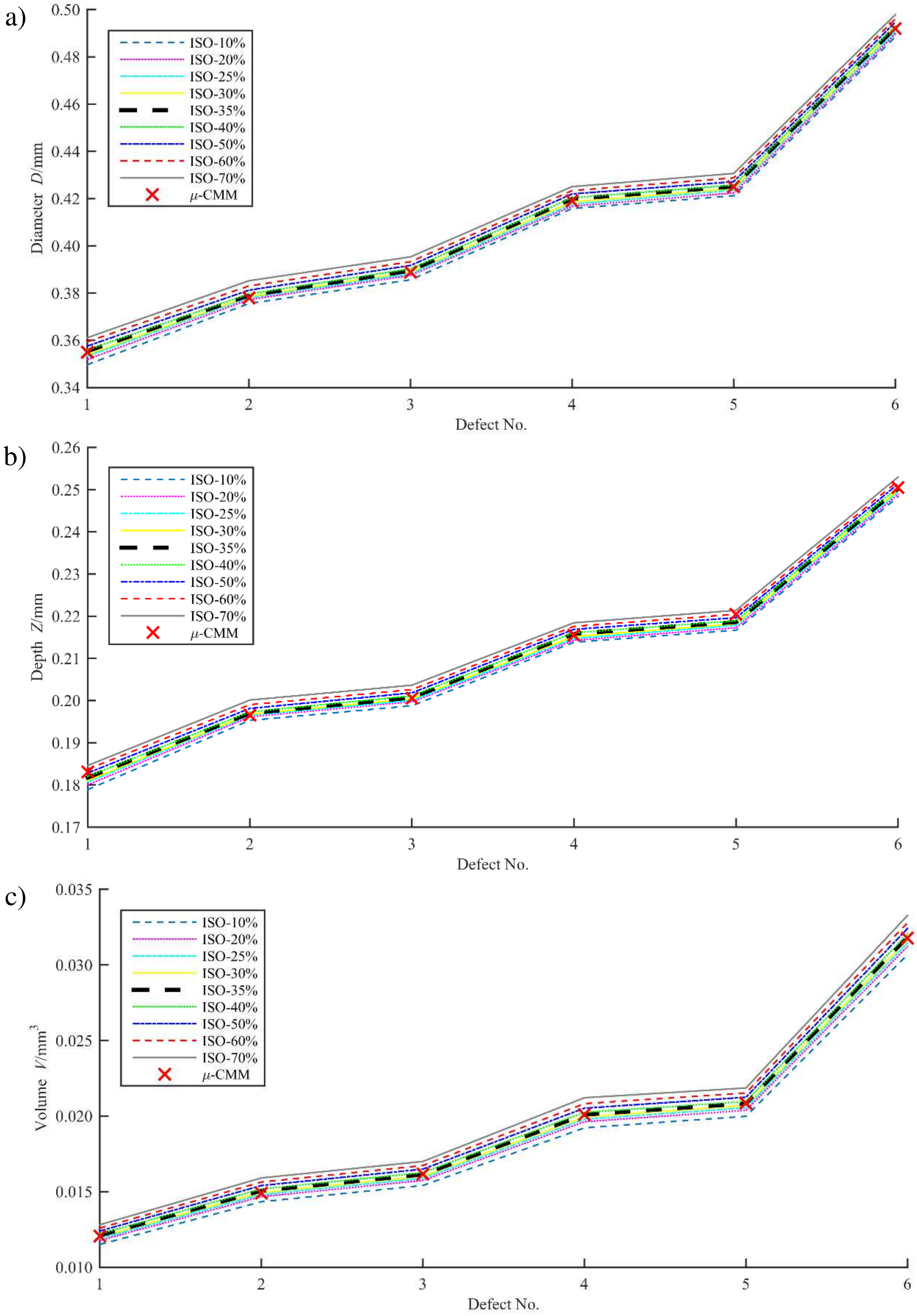

Figure 46. Comparison of µ-CMM and CT measurements in high magnification obtained on selected calottes and using different ISO values; a) diameter *D* measurements, b) depth *Z* measurements, c) volume *V* measurements.

It can be seen from the values plotted in Figure 46 that the results using ISO-35% are matching the reference μ-CMM values in nearly all cases considering different calottes and measurands. The same behavior can be observed also in the results obtained on the scans with low magnification shown in Figure 47. In this case, ISO values calculated the same way as for high magnification scans were applied to scans acquired at low magnification, and measured values of *D*, *Z* and *V* were subsequently compared to calibrated values calculated in Section 4.3. The error between measured and calibrated value was calculated for each individual calotte and measurand at all nine ISO levels. An average error over all 72 calottes was then calculated for each measurand/ISO value combination, and plotted in the chart shown in Figure 47.

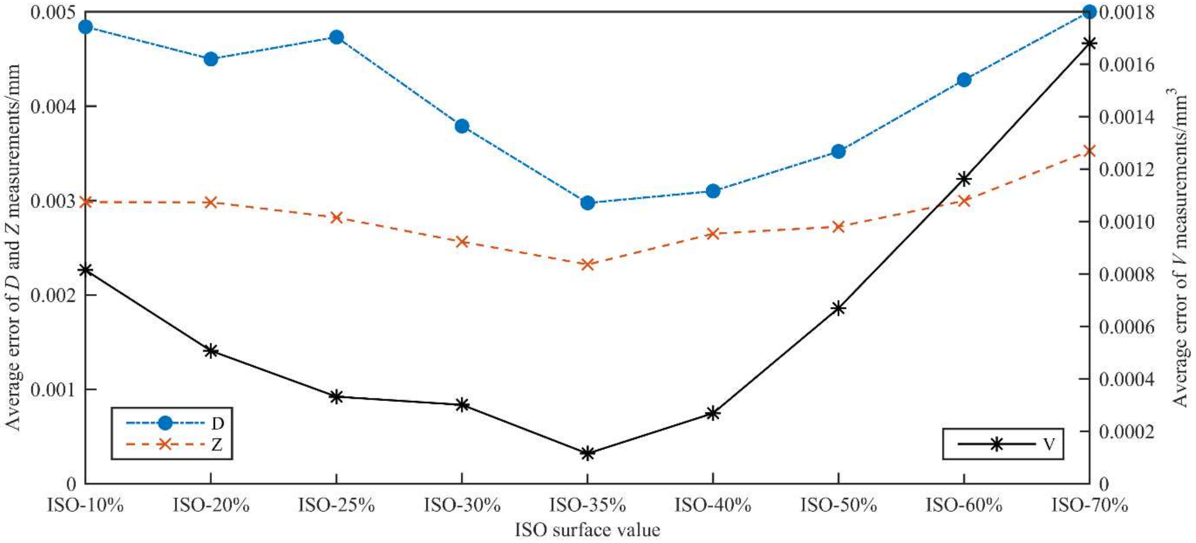

Figure 47. Average error of diameter *D*, depth *Z* and volume *V* measurements calculated as the difference between measurements obtained on CT scans at low magnification using different ISO values and calibrated values.

The results plotted in Figure 47 show that, similarly to high magnification scans, the lowest error is achieved by using ISO-35% value. It can be also seen that while there is no significant difference between ISO-35% and ISO-50% value (the value used by default in the CT evaluation software) for *D* and *Z* measurements, the error of *V* measurements is more than six times higher using the latter ISO value. This discrepancy between the errors observed on different measurands is caused by the fact that while volume *V* was measured using global thresholding, *D* and *Z* were measured on surface defined by local adaptive thresholding that is less sensitive to the initial ISO value.
It can be assumed, based on the observations derived from Figure 46 and Figure 47, that for this special configuration and material, ISO-35% should be used as the preferred ISO value in order to achieve lower measurement errors.

4.5 Case study

A method to achieve the traceability of CT porosity measurements have been described in Section 4.3. It is based on techniques adapted from international standards (GUM [26] and ISO 15530-3 [28]) and the German guideline VDI/VDE 2630-2.1 [29], using the reference standard introduced in this chapter. In this section, a method to achieve traceability of CT porosity measurements is presented and demonstrated on an industrial case study. In accordance with previous sections, methods adapted from ISO 15530-3 [28] and VDI/VDE 2630-2.1 [29] are used here. Furthermore, the calibrated reference standard is used for the optimization of evaluation parameters in order to reduce systematic errors of CT porosity measurements. Finally, a general procedure that can be applied in industry for the improvement of CT porosity measurements is proposed.

4.5.1 Test object

The part (Figure 48) used in this work is a component of a photographic tripod made of aluminum. It was produced during the optimization of manufacturing parameters in high pressure die-casting, and was evaluated as a nonconforming part due to high porosity content, and hence it was scrapped.

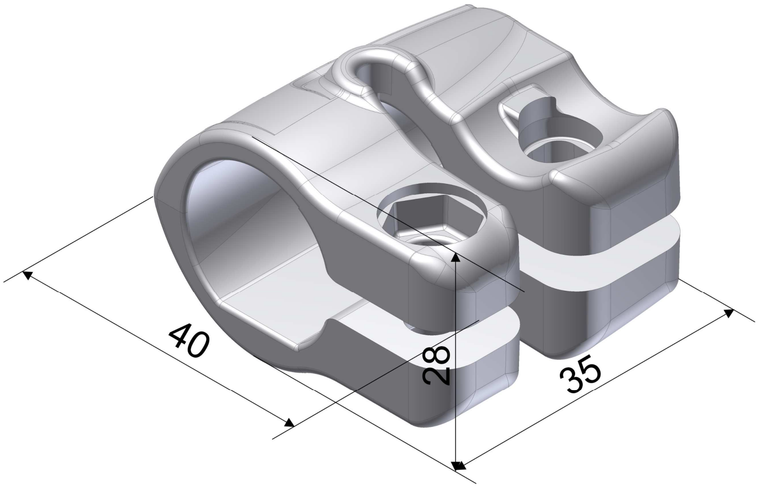

Figure 48. CAD model of the test object with general dimensions in millimeters.

A metrological CT system, Nikon Metrology X-Tek MCT 225, was used for acquiring CT data. The maximum permissible error (MPE) of the system is (9 + L/50) µm (where *L* is length in mm). CT data was processed and evaluated in software VGStudio MAX 3.0 (Volume Graphics, Germany).

4.5.2 Experimental setup

The part under investigation was repeatedly scanned together with the reference standard in 7× magnification (see Figure 49-a), which results in a voxel size of 28 µm. Furthermore, the reference standard was scanned separately (see Figure 49-b) using the same magnification and CT scanning parameters, in order to see the effect of different wall thickness (i.e. different X-ray penetration lengths). The two samples mounted together as well as the reference standard alone were scanned tilted in order to reduce the cone beam artefact [4]. Both the configurations and mounting of the samples on the CT rotary stage are shown in Figure 49.

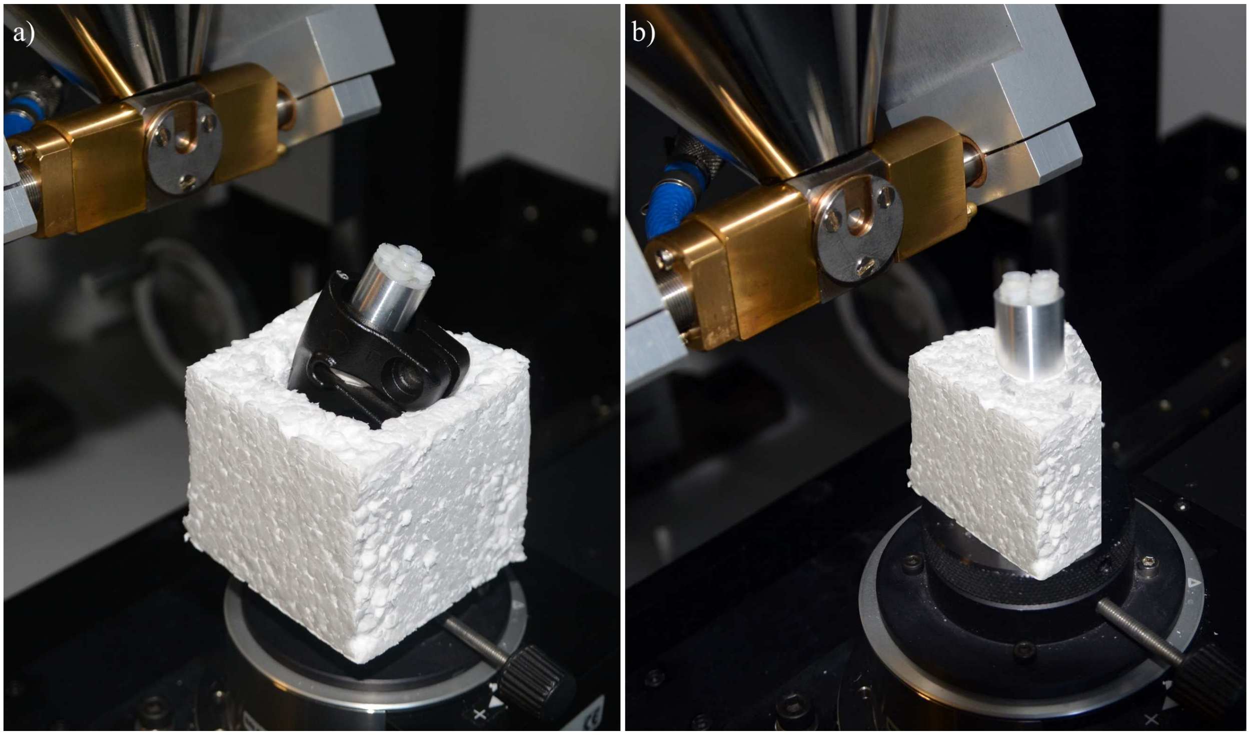

Figure 49. CT scanning configuration: a) reference standard (bright) mounted together with the test object (black), b) reference standard alone.

The CT cabinet is air-conditioned and the temperature was kept within the range 20 ± 0.5 °C during CT measurements. Furthermore, the temperature of the sample and its dimensions were stabilized with enough advance by keeping it inside the CT cabinet overnight before the scan. CT scanning parameters, summarized in Table 14, were optimized in order to obtain best possible contrast-to-noise ratio (CNR) in data and at the same time to reduce possible CT artefacts.

Table 14. CT scanning parameters.

Voltage/kV	Current/µA	Exposure/ms	Voxel size/µm	No. of projections	Filter
210	76	1000	28	2500	0.35 mm Cu

4.5.3 Evaluation methods

Several methods were used for the evaluation of individual CT scans. Similarly to previous sections, VGStudio MAX 3.0 and its *Defect analysis* module were used for the analysis of internal porosity; this module was used throughout this section as it is a typical tool used by industrial users. Since the definition of threshold value is a crucial step in accurate porosity evaluation, as it defines the border between the material and entrapped air inside the pore, its optimization is the focus of this study.

By default, the ISO-50% value (the mean GV between the background and material peak) is used as the input threshold value for the algorithm in the *Defect analysis* module. The algorithm then applies this threshold to the dataset to separate individual pores from material, and to calculate their properties including their volume and total void content in the investigated part.

Procedure for the evaluation of data

As explained in Section 4.5.2, two types of repeated scans were acquired: (i) scans of the test part and reference standard mounted together as shown in Figure 49-a, and (ii) scans of the reference standard alone, as shown in Figure 49-b. In the first configuration, porosity in the workpiece and in the reference standard were analyzed individually. This additional step was introduced in order to facilitate the optimization of threshold value based on an iterative procedure explained further in this section. The second configuration (reference standard only) was added to isolate the influence of thresholding and to evaluate whether it is possible to apply a certain ISO threshold value to evaluate porosity in a specific material independently from the penetration length. The datasets were analyzed following the same procedure:

1) Loading the data in the software.
2) Determination of the surface using automatically calculated ISO-50% threshold value considering gray values from the whole data set; local adaptive thresholding was used for the surface determination.
3) Alignment of the dataset.
4) Defect analysis performed on the reference standard using ISO-50% threshold value.
5) Export of the measurement results.
6) Comparison of the results obtained on the reference standard with calibrated values.
7) Iterative optimization of the threshold value, as explained further in this section.

Optimization of the threshold value

As discussed in [132], ISO-50% does not have to necessarily be the optimal threshold value. This is in particular relevant in cases where the background GV (i.e. the GV representing air) is not homogeneous within the dataset. The variation in background GV can be observed e.g. inside small internal features, where the effect of noise, beam hardening and scattering is intensified, and can result in higher background GV inside these elements with respect to the air surrounding the part. Based on the evaluation of the data obtained in this work, these effects are present also in internal porosity. Therefore, the data were evaluated using an iterative procedure schematically described in Figure 50. In a first step, the data are evaluated using ISO-50% threshold value, and the results obtained on the reference standard are compared to reference values. In a second step, the threshold value is modified based on the deviation of the total void content from the reference. If the total void content evaluated in the first step is too high, the threshold value is shifted towards the material peak (i.e. increased); on the contrary, if the void content is too low, the threshold is decreased. In a third step, the threshold value is modified based on the results obtained using the threshold value determined in the second step, following the same optimization sequence. In a fourth and further steps, the threshold value is modified according to the same procedure as in the second and third step till the deviation between the calibrated and measured total void content fits within $\pm 5\times10^{-5}$ mm^3.

Furthermore, in order to show the influence of non-homogeneity of the background GV within the dataset, the ISO-50% threshold value used in the first step of the iterative procedure was calculated taking into consideration (i) the complete dataset, and (ii) the reference standard region of interest (ROI) only. The ROI was defined so that it contains the material of the reference standard and defects only, thereby eliminating the surrounding air from the calculation of the background GV. Results obtained by using the two different thresholds were subsequently compared to the optimized ones.

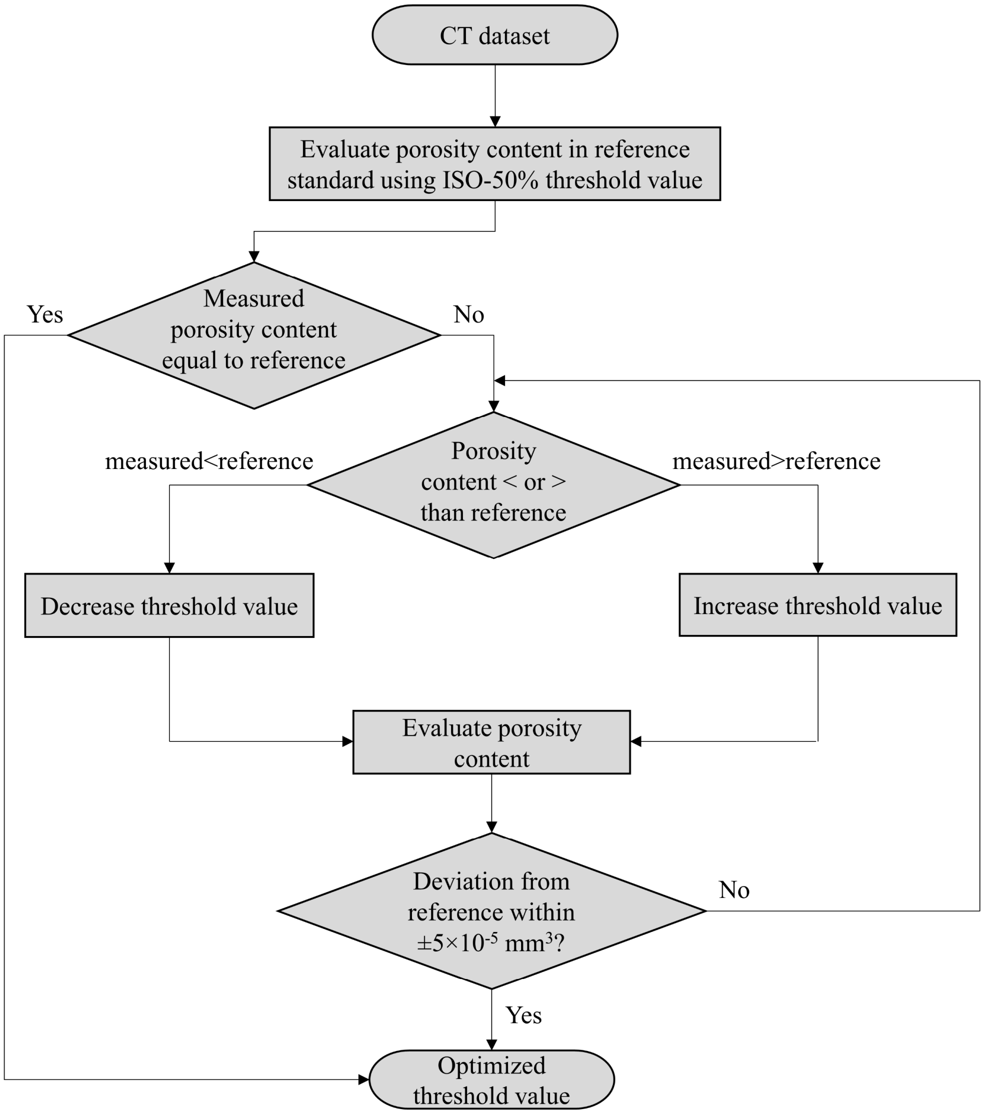

Figure 50. Flowchart of the iterative procedure for the optimization of threshold value.

4.5.4 Results and discussion

The results shown in Figure 51 represent relative measurement errors obtained on the reference standard calculated as the difference between the average measured value (calculated for individual defects using different threshold values), and corresponding calibrated values. The average was evaluated over all repeated measurements for both configurations (both parts together and the reference standard alone). The case where GV of the whole dataset were taken into account for the calculation of the threshold value is denoted as “Complete dataset”, whereas “Reference standard ROI” represents the case where only the GV inside the reference standard ROI were considered. Results using the threshold value determined by the iterative procedure are represented as “Optimized”.

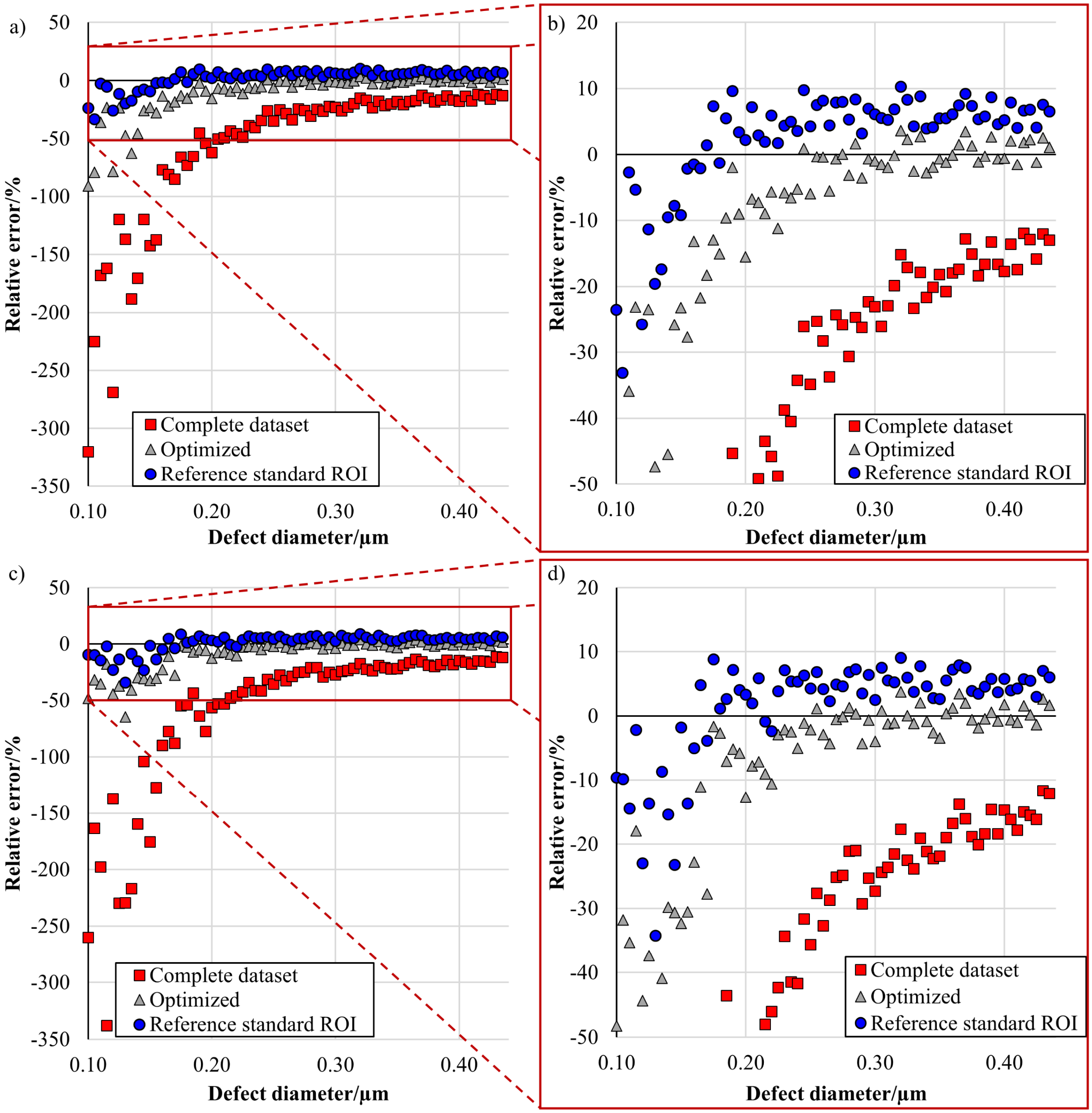

Figure 51. Relative errors of volume measurements evaluated on the reference standard as the difference between the average value from repeated scans (calculated for individual defects), and reference values. a) Results obtained from the reference standard scanned together with the test object; b) a close-up of a) with reduced range on *y*-axis; c) results obtained from the reference standard scanned alone; d) a close-up of c) with reduced range on *y*-axis.

It can be seen from the results plotted in Figure 51 that significantly higher errors are obtained when using the complete dataset for the determination of threshold value (and by subsequent use of this value for the evaluation of porosity) in comparison to the other procedures. More specifically, systematically lower values were obtained by using ISO-50% threshold value evaluated on the whole dataset. On the contrary, "Reference standard ROI" error values are both positive and negative, and the magnitude of error is lower. Whereas the smaller defects were evaluated with relatively high negative errors, the larger defects resulted in low errors with a positive sign. Yet, the error of total void content was higher with respect to "Optimized", where the small defects were slightly underestimated, whereas the errors calculated on large defects were close to zero. Different trends and signs in measurement errors between smaller and larger defects can be better observed in close-ups in Figure 51-b and d. It is worth noting that small defects are evaluated with high relative error in general. This is mainly caused by two reasons: (i) measurements of small defects in general are more challenging as demonstrated also in Section 4.4, and (ii) relatively small absolute error (in mm^3) results in high relative error (in %) in the case of small defects. The second reason is closely related to the resolution of the scan, more specifically to the ratio between the VS and the number of voxels contained in the defect. This effect can be shown on an example where the number of voxels inside the smallest defect (Ø 100 µm) is calculated: given the voxel size (VS=28 µm), a defect of Ø 100 µm is composed of eight voxels. Therefore, an absolute error of one voxel (2×10^{-5} mm^3) results in a relative error of 12.5 %, whereas the same absolute error results in a relative error of 0.07 % in the case of the largest defect (Ø 500 µm).

In order to evaluate the significance of individual defects sizes, the error of total void content calculation was evaluated. The evaluation resulted in errors lower than (i) 5×10^{-5} mm^3 using the optimized threshold, (ii) -0.09 mm^3 using GV of the whole dataset and (iii) 0.04 mm^3 using GV from the reference standard ROI. It can be concluded that while the relative errors of small defects measurements are high, their contribution to the absolute error of total void content evaluation is less significant than the contribution of large defects.

It can be also seen when comparing charts in Figure 51-a, b with charts in Figure 51-c, d that there is no significant difference between the results obtained on the reference standard scanned alone and together with the test part. Therefore, it can be concluded that the differences in penetration length did not affect the results in the present configuration.

The same trends and magnitude of errors as on large defects in the reference standard were observed also on the total void content, both in the test part and in the reference standard. The total void content obtained using threshold calculated from GV of the whole dataset was underestimated with respect to optimized results, whereas the total void content obtained using threshold evaluated on sample/reference standard ROI resulted in an overestimated volume with lower deviation from the optimum. The results from the analysis of total porosity content in both the workpiece and the reference standard supplemented with measurement uncertainty are shown in Figure 52-a, b, respectively. It should be noted that the deviations from the calibrated value in Figure 52-b represent the systematic error of total void content evaluation on the reference standard.

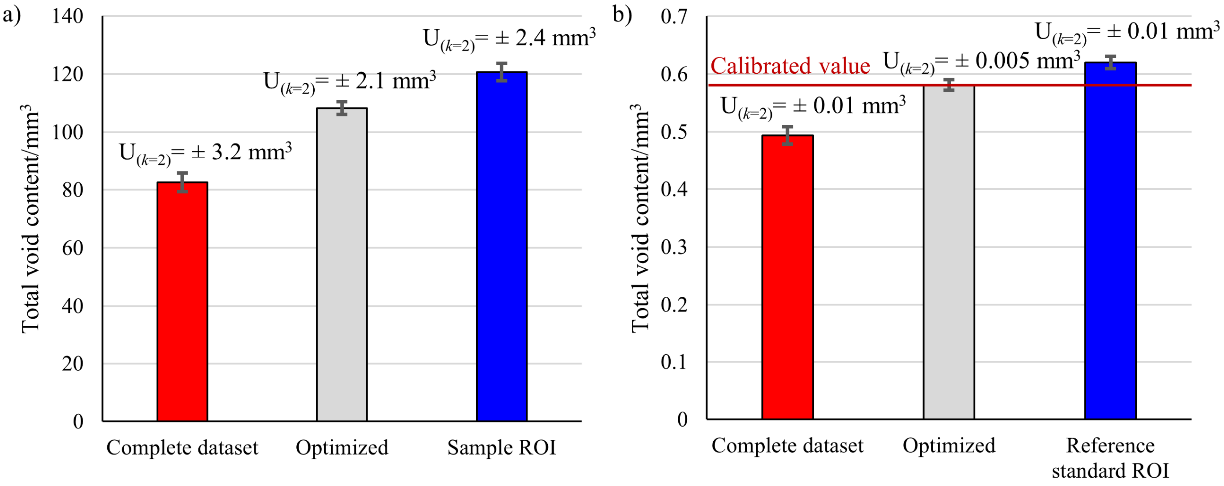

Figure 52. Total void content obtained by using different threshold values: a) total void content in the test object, b) total void content in the reference standard. Error bars represent measurement uncertainty.

The uncertainty of CT porosity measurements was evaluated according to a method adapted from ISO 15530-3 [28] and VDI/VDE 2630-2.1 [29]. The reference standard was repeatedly scanned, as required by the referenced standards and guidelines, alone and together with the test part.

The deviation of total void content evaluated with respect to the optimum obtained on the test part in the case of “Complete dataset” was -25.6 mm^3, whereas it was +12.4 mm^3 using the threshold determined on the sample ROI. The same pattern can be observed in values obtained on the reference standard, where the total volume of defects was calculated with a negative deviation in the case of “Complete dataset” and with a positive deviation in the case of “Reference standard ROI”. The magnitude of measurement uncertainties followed the same trend, i.e. the highest uncertainty was evaluated on “Complete dataset”, the lowest one on “Optimized”, whereas the uncertainty value of “Sample/Reference standard ROI” was between the before-mentioned cases. This can be attributed to the fact that the lowest repeatability was observed in the data obtained using the “Complete dataset” threshold. An example of the defect analysis performed on the test part scanned together with the reference standard is shown in Figure 53.

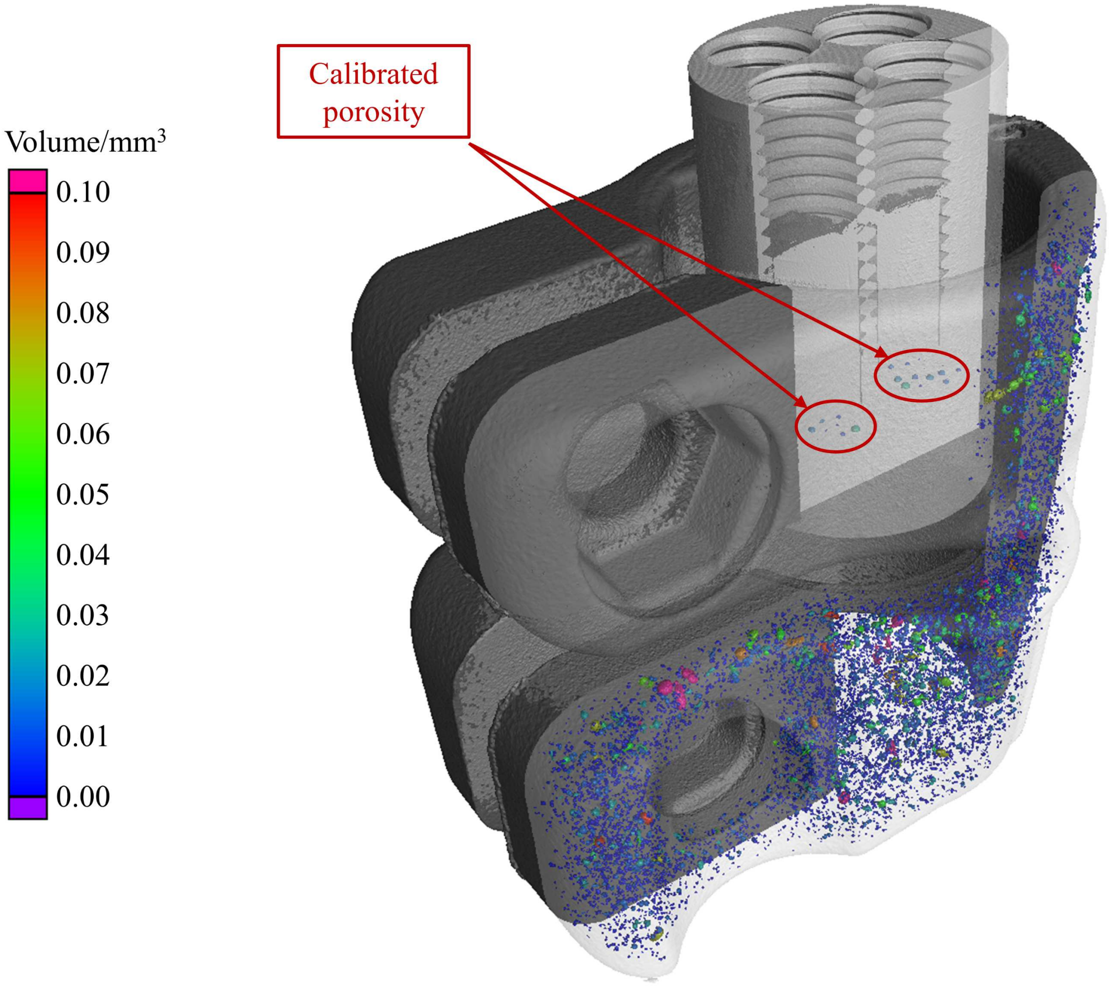

Figure 53. Example of *defect analysis* performed on the test part scanned together with the reference standard. The colors of the two parts were changed in order to reflect the real surface colors, i.e. the test part is black, whereas the reference standard is bright.

It was observed that, whereas the material peak was stable within the dataset (the difference between the peak calculated on the reference standard ROI and on the complete dataset was within ± 100 GV), the background GV was strongly dependent on the evaluated region. This was mainly due to the fact that, while the background surrounding the workpieces was nearly free of noise, the volume entrapped inside the pores was significantly influenced by noise. Furthermore, there was a non-negligible difference in background GV even between small and large defects. Gray values of different ROIs are for better overview shown in Table 15.

Even though both scanned parts are made of aluminum, the material microstructure can cause slight attenuation differences resulting in differences of material GV in the reconstructed volume. In order to make sure that the same threshold value optimized on the reference standard can be used on the investigated sample, the material GV of both were compared. It can be seen from values in Table 15 that the difference is negligible.

It should be noted that the gray values are defined by a GV range instead of a measurement unit. The range in this case is [0,65536], which corresponds to the dynamic range of the 16-bit detector used in this work.

Table 15. Material and background gray values of different ROIs.

	Background GV	Material GV
Complete dataset	9749	23215
Reference standard ROI	14032	23185
Sample ROI	14095	23197
Ø 100 µm defect*	14852	23162
Ø 500 µm defect*	13450	23181

*Defect ROIs were created together with the adjacent material of equal volume.

Given the above-mentioned facts, the proper determination of background is critical when evaluating internal porosity. The global approach, when the global background peak is considered, can significantly bias the results. In fact, gray values of air inside the defects are typically higher than those of air surrounding the part. Therefore, regions inside the internal defects should be selected for determining the background GV in order to reduce errors of CT porosity measurements. This was also proved by results obtained both on the investigated workpiece and on the reference standard; the measurement errors were significantly reduced by calculating the threshold value for subsequent porosity analysis on the sample/reference standard ROI only. However, further optimization is still needed, e.g. by the iterative method using the reference standard proposed in this chapter.

Proposed method for industrial use

The optimization procedure presented in Section 4.5.3 can be easily adapted for the industrial use. A reference standard with calibrated porosity can be scanned either before (maintaining the same scanning conditions as used for the scan of the workpiece) or, more preferably, together with the sample under investigation in a first step. In a second step, the threshold value can be optimized following the iterative procedure schematically explained in Figure 50. In a third step, the optimized threshold is used for the evaluation of internal porosity; individual defects (e.g. the largest voids as they can have critical effects on the part integrity), as well as total void content can be extracted from CT results and further analyzed.

The traceability of CT porosity measurements obtained from the analyzed part is established through the calibrated references standard, and using methods for the evaluation of measurement uncertainty adapted from ISO 15530-3 [28] and VDI/VDE 2630-2.1 [29] following the steps below:

1) Manufacturing of a reference standard made of material similar to the investigated part.
2) Calibration of the reference standard.
3) Repeated scans of the reference standard either alone or together with the analyzed workpiece respecting requirements defined in [28,29].
4) Measurement of the part under investigation (if not scanned already in the previous step).
5) Evaluation of measurement uncertainty according to [28,29].

As explained earlier in this section, it is necessary that the GV of the reference standard material and the investigated sample material be similar to ensure reliable transfer of the threshold value. This requires an individual reference standard for each material in production. Furthermore, not only the threshold transfer requires similar materials but also the standards and guidelines [28,29], from which the uncertainty evaluation method was adapted, define the similarity criteria.

4.6 Conclusions

In the work presented in this chapter, a reference standard with artificial internal defects was developed, calibrated, and applied for thorough evaluation and enhancement of CT internal porosity measurement accuracy including the establishment of measurement traceability, and for an industrial case study.

In particular, this chapter presents a method to establish traceability of internal porosity measurements obtained by coordinate measuring systems with CT sensors. The method is based on a reference standard with artificial porosity calibrated in multiple steps by instruments based on different measuring principles (tactile, optical, CT), and on an approach adapted from international standards and guidelines. A detailed breakdown of individual error sources contributing to measurement uncertainty is described for each calibration step and measurand. The final expanded measurement uncertainties evaluated with a confidence level of 95 % for diameter D, depth Z and volume V of a defect are 2.1 µm, 1.4 µm and 1.6 %, respectively.

The reference standard was subsequently used for the evaluation of accuracy of CT porosity measurements. Several investigations were performed in order to determine the influence of CT parameters settings on measurement errors and the repeatability of measurements. In addition, results from real CT scans were validated by simulations and three different evaluation software tools for CT data processing were compared.

The study on the influence of voltage and current on porosity measurement errors has proven that these factors are important, particularly for small defects. The variation caused by voltage and current was up to 4 µm in the case of diameter and depth measurements and up to 3 % in case of volume measurements. The relationship between tube voltage and current, and deviations in measurements has been determined as follows: the higher the values of tube voltage and current, the lower the observed deviations from reference values. The two main reasons for the improvement in measurements with higher tube voltage and current are: (i) the image noise is approximately inversely proportional to the square root of the tube current, i.e. the image noise decreases with increasing the tube current; (ii) the generation of X-rays increases with the square of the tube voltage, i.e. by increasing voltage, lower noise and better contrast can be achieved in the acquired projections. Nevertheless, it must be noted that, by increasing voltage and current, the tube power increases as well. An increase in tube power can affect the focal spot size, producing a deterioration of the resolution and other image parameters. In this study, the tube power was kept below 8 W, ensuring that the focal spot size was kept at a minimum (3 µm). As a consequence, the effects of tube voltage and current were isolated.

Based on the observed trends, to obtain the best results in evaluation of internal defects by CT, use of high settings of U and I is suggested. Nonetheless, one has to take into account also other boundary conditions such as expected structural resolution, scanning time, etc.

The measurement repeatability was evaluated based on results of 12 different scans, repeated under the same "optimal" conditions. Mean deviations and standard deviations were calculated for the results of the 12 scans. The outputs of this study show that the mean error of diameter and depth measurements can be below 5 µm with standard deviation ranging from 11 µm for the smallest defects to less than 1 μm for the largest ones. As for volume measurements, the relative mean deviation was below 10 % for defects below 200 μm in diameter, while it was below 5% for defects larger than 200 μm in diameter, with standard deviations up to 6 % in the case of smaller defects.

In order to validate the results from real CT scans, simulations with extended range of voltage and current were performed. Comparing the results of simulations with those from real CT scans, it was seen that the trends observed on both data sets have the same tendencies. Yet, the magnitude of deviations was lower in case of simulations because they omit some influencing factors, such as geometrical instability of the system and focal spot drift.

Performance of three different CT evaluation software tools – namely VGStudio MAX, Volume Player and iAnalyse – in determining the volume of internal defects was compared. The outcomes demonstrate that the lowest measurement errors are given by VGStudio MAX. The latter two software tools achieve same results, as expected, because their calculation method is identical.

Results of all performed analyses show that measurements of smaller defects are more problematic, as the errors and standard deviations are constantly higher than for larger defects. Furthermore, the CT measured volume of all 72 defects appears to be higher than reference values. This effect is caused by averaging, lower sharpness of CT data and decrease of information content with decreasing magnification.

The possibility to reduce systematic errors both in calibration and CT porosity measurements in general by optimizing the ISO threshold value used for determining the surface separating the air entrapped inside the defect and material was discussed in this chapter. While the ISO-50% threshold value (the average gray value between the material and the background peak) is used by default, the lowest measurement errors were achieved using ISO-35%, which is subsequently suggested as the optimized value for the present configuration and workpiece material – aluminum.

Section 4.5 gives a guideline on how to establish the traceability of CT porosity measurements obtained on an industrial part. The method is based on the use of the calibrated reference standard and procedures adapted from ISO 15530-3 [28] and VDI/VDE 2630-2.1 [29]. The problem of proper threshold value determination for defect detection and evaluation is discussed; whereas the material gray value is relatively stable within the dataset, the background gray value is strongly dependent on the considered region of interest. This is mainly caused by higher noise inside internal features, especially in those with small volume. It was shown that the background gray value calculated on the whole dataset can result in wrong threshold value determination and subsequently cause significant bias in results.

A procedure for the optimization of threshold value determination in an industrial environment is described in Section 4.5. It is based on initial information of total void content calculated on the reference standard and its comparison with the calibrated value. Based on the deviation, the threshold value is iteratively modified until the error converges to a defined limit. The optimal value is then used for the evaluation of porosity inside the sample under investigation.

Experimental data were evaluated using three different thresholds obtained on: (i) the whole dataset, (ii) sample/reference standard ROI and (iii) optimized value. By using the first threshold, individual defects in the reference standard as well as total void contents were underestimated. On the contrary, in the second case small defects were underestimated, while the larger defects were overestimated (together with total void content). The optimized value resulted in slight underestimation of small defects, whereas the deviation of large defects was kept close to zero; the total void content was optimized to ±5×10^{-5} mm^3 deviation from the reference.

The deviation of total void content with respect to optimum obtained on the investigated part using the first threshold was -25.6 mm^3, whereas it was +12.4 mm^3 using the second threshold. The same pattern was observed in values obtained on the reference standard, where the total volume of defects was calculated with deviation equal to -0.09 mm^3 using the complete dataset and +0.04 mm^3 using the reference standard ROI for threshold calculation. The magnitude of measurement uncertainties followed the same trend, i.e. the highest uncertainty was evaluated using the first threshold, the lowest using the second one, whereas the uncertainty value using the optimized threshold was between the two aforementioned ones. This can be attributed to the fact that the lowest repeatability was observed in the data obtained using the first threshold.

Finally, a method to use the optimization procedure in industry was proposed. A set of reference standards covering the material range in production should be manufactured and calibrated as a first step. Subsequently, these standards can be scanned either before the scan of the investigated part or, more preferably, together with the part. The threshold value can be optimized following the proposed iterative procedure, thereby reducing the systematic errors of CT porosity evaluation. Furthermore, by comparing the measured values obtained from the reference standard to the reference ones (obtained by calibrating the reference standard), and by evaluating the measurement uncertainty according to procedures defined in ISO 15530-3 and VDI/VDE 2630-2.1, the traceability of CT porosity measurements obtained from the investigated part can be achieved.

The investigation presented in this chapter gives a comprehensive overview of CT performance in the evaluation of internal defects and confirms the high potential of CT in this field.

5 CALIBRATION OF CT INSTRUMENT GEOMETRY

This research work was carried out in collaboration with KU Leuven (in particular with Massimiliano Ferrucci and Evelina Ametova, supervised by prof. Wim Dewulf), and can be divided into three main parts: (i) development of a new reference standard, (ii) development of a new calibration method, and (iii) development of an advanced reconstruction algorithm that takes into account the actual CT geometry. Although the individual steps partially overlap, and each step was elaborated in collaboration, the main contribution of the author of this thesis is related to the first part. Therefore, this chapter is mainly focused on the description of the development of the reference standard; the remaining steps are briefly discussed as well; however, further details can be found in corresponding references.

Different methods to assess the CT geometry were discussed in Chapter 3; however, traceability in the parameter measurements has not been achieved yet. In this chapter, a short overview of the current state-of-the-art in the calibration of CT geometrical parameters is given. Subsequently, the development, manufacturing, and calibration of a new reference standard for the calibration of CT instrument geometry is described, and its performance is compared to the state-of-the-art equivalent. Subsequently, the method (i.e. the so-called minimization procedure) to measure the CT instrument geometry is explained, as well as the evaluation of measurement uncertainty by Monte Carlo simulations. The whole calibration procedure is then verified by an experimental study using a custom CT system. Furthermore, an improved reconstruction algorithm is used to correct the CT data based on the information about the actual CT geometry.

5.1 Introduction to CT instrument geometry calibration

One of the essential elements towards the establishment of traceability is the evaluation of measurement uncertainty. According to the GUM [26], identification and quantification of all sources of errors is needed for the complete assessment of measurement uncertainty. The CT measurement process is influenced by many sources of errors, one of which is the alignment of the system geometry [2].

Typically, the geometry of a CT system is defined by the position and orientation of its three main components: X-ray source, rotation axis and detector. The typical configuration of a cone-beam CT system is shown in Figure 54. The CT measurement process is composed of tomographic reconstruction of acquired radiographic projections and data post-processing. The radiographs are usually taken from multiple rotation angles of the sample stage. Each radiograph contains information about X-ray attenuation through the measurement volume. Each pixel of the radiograph provides a measure of the attenuation of X-rays from the X-ray source through the measurement volume and to the corresponding pixel position on the detector. The tomographic reconstruction step then calculates attenuation values for each voxel in the measurement based on the intersections of X-ray trajectories and voxels (3D pixels) within the measurement volume (more details on CT measurement principle are given in Chapter 2).

Accurate reconstruction of the measurement volume relies on accurate spatial knowledge of the X-ray trajectories with respect to the voxel space. Industrial users typically rely on the instrument manufacturers to measure the geometrical alignment of their CT systems and to perform any adjustments. Several methods to estimate the CT instrument geometry have been developed and are discussed in Section 3.4.3. However, calibration of the CT geometrical parameters has not yet been achieved. In this chapter, a reference standard that has been optimized for the purpose of achieving CT geometrical calibration is introduced.

Different methods to estimate geometrical parameters of CT system were developed [88–91,133–135]. Most approaches employ a dedicated reference standard consisting of high-attenuation spherical markers. The coordinates of the sphere centers in a local coordinate frame are known *a priori*. Radiographic projections are acquired for one (static) or more (dynamic) angular positions of the reference standard. CT geometrical parameters are then estimated by comparing the sphere center coordinates to the pixel coordinates of their projections on the detector space. Two methods for estimating the CT geometrical parameters from the observed projection data are direct and iterative [19]. Direct methods are based on solving a discrete set of equations that relate the sphere center coordinates to their projection coordinates. Iterative methods are based on the minimization of error between observed and modelled projections (so called reprojection error). To date, the studies presented in the literature provide estimates of the geometrical parameters but do not provide a metrological approach to the issue of geometrical calibration. More specifically, the measurement of geometrical parameters by comparison to a traceable reference, *i.e.* calibration, with valid statement of measurement uncertainty has not yet been achieved.

The object proposed in this chapter is composed of a cylindrical framework and sphere markers arranged in a dedicated spatial pattern. In order to ensure the metrological traceability of CT instrument geometry assessment, the positions of sphere centers are calibrated by a tactile coordinate measuring machine (CMM). The design of the reference standard is optimized with respect to state-of-the-art equivalents and adapted for both static and dynamic use. The reference standard is applied to measure the geometry of CT systems by minimization, the description of which is given in Section 5.4. The performances of the whole calibration procedure, as well as the performances of the advanced reconstruction algorithms, were evaluated on an experimental study.

5.2 Cone-beam CT instrument geometry definition and CT geometrical parameters

The CT instrument geometry is defined by the relative position and orientation of the three main components: X-ray source, rotation axis and detector [136] as schematically presented in Figure 54. A typical CT system is considered aligned when the following two conditions are met [87]: (i) the line normal to the detector surface at its geometrical center (denoted as the central ray) must pass through the X-ray source and (ii) the rotation axis must be parallel to the detector and projected to the central column of the detector. The detector is considered as a planar area with regularly spaced elements (pixels) of known size and all the components are assumed to be without any temporal error motions, such as drift and vibrations.

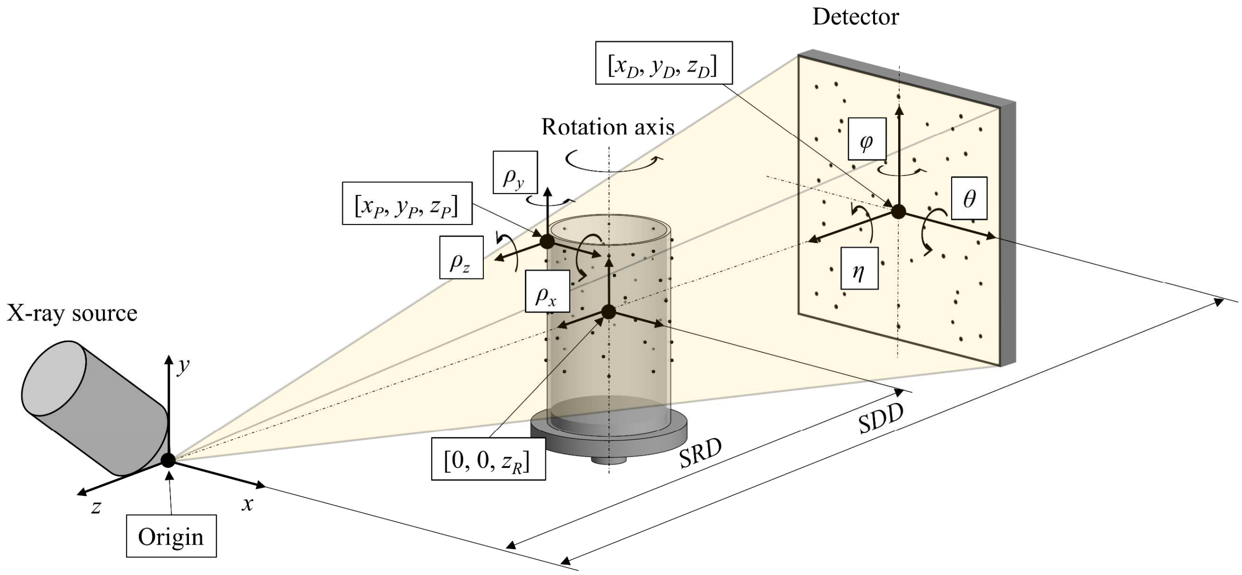

Figure 54. Relative position and orientation of the three main components of a typical cone-beam CT system with flat panel detector. The coordinate system originates in the X-ray source with *x* axis parallel to the detector rows, *y* axis parallel to the detector columns, and *z* axis orthogonal to both *x* and *y* axes.

The parameterization of the CT instrument geometry is schematically shown in Figure 54 and described as follows: a global Cartesian coordinate system is defined with its origin at the source focal spot. The global *y* axis is parallel to the axis of rotation and is positive upwards (against gravity), while the *z* axis is parallel to the line from the source that intersects the axis of rotation orthogonally. The positive *z* axis points away from the axis of rotation and the detector. The *x* axis follows the right-hand screw rule. In an ideally aligned system, the *x* axis is parallel to the detector rows, the *y* axis is parallel to the detector columns, and the *z* axis intersects the detector at its geometrical center. In order to unambiguously describe the calibration task, the relative position and orientation of the reference standard in the global coordinate system must be defined as well.

The geometrical parameters used in this section are summarized in Table 16 and are as follows:

1) The position of the rotation axis is defined by the coordinates of its intersection with the *z* axis (0,0, z_R).
2) The position of the detector center is defined by coordinates x_D, y_D and z_D. The orientation of the detector is given by three extrinsic rotation angles: slant φ about the vertical axis (parallel to the global *y* axis), skew η about the longitudinal axis (parallel to the global *z* axis), and tilt θ about the horizontal axis (parallel to the global *x* axis. The center of rotation is the detector center and the order in which rotations are applied is as follows: (1) φ, (2) η, (3) θ.
3) The position of the reference standard local origin is defined by coordinates x_P, y_P and z_P in the global coordinate frame. The orientation of the local coordinate axes with respect to the global coordinate axes is defined by three extrinsic rotations in the following order: (1) ρ_x, (2) ρ_y, and (3) ρ_z. These parameters are considered nuisance parameters as they do not provide information about the CT instrument geometry; however, they are necessary for the estimation procedure. As such, their values will not be presented in Section 5.5, where performances of the reference standard proposed here and the state-of-the-art equivalent are compared.

Table 16. CT geometrical parameters.

Parameter	**Variables**
Rotation axis position	$0, 0, z_R$
Detector position	x_D, y_D, z_D
Detector orientation	φ, η, θ
Reference standard position	x_P, y_P, z_P
Reference standard orientation	ρ_x, ρ_y, ρ_z

* *SRD* is the source-to-rotation axis distance, see Figure 54.

** *SDD* is the source-to-detector distance, see Figure 54.

5.3 Reference standard

As mentioned in the introduction, a common approach to estimating CT geometrical parameters, irrespective of the method used (direct or iterative), is based on the evaluation of radiographic projections of a dedicated reference standard. Typical reference standards for estimating the CT geometrical parameters consist of several high X-ray absorbing features (see also Section 3.4.3), usually spheres, distributed in a dedicated arrangement.

5.3.1 Design of the reference standard

A critical step in the measurement of CT geometrical parameters is the identification of projected sphere centers in each radiographic image. Accurate identification of the projected sphere centers requires high contrast between spheres and any background in the image. To facilitate the recognition of projected markers, any framework used to hold the spherical markers should be made of a material with X-ray attenuation significantly lower than the attenuation of the spherical markers.

A thorough review of reference standards used in the estimation of CT geometrical parameters is given in Section 3.4.3 and [19]. A notable reference standard is the one proposed in [90], in which twenty four spheres are arranged in two circular trajectories at the axial extremes of a plastic cylinder. The authors of [90] propose a geometrical estimation method based on the acquisition of one projection of the reference standard. More recent reference standards often consist of spherical markers arranged in a helical trajectory along the surface of a cylindrical framework. The author of [92] provides a quantitative comparison of the helical trajectory design to a new design – so called candy cane standard (Figure 55-a). The spherical markers in the candy cane standard are arranged on a cylindrical framework in quarter-helical trajectories with a relative offset of 90° around the main axis of the cylinder. The design provides improved spatial distribution of the projected markers on the detector when compared to helical trajectories of spheres, while at the same time partially eliminates "clustering" of the marker overlaps at the detector edges. Overlapping of spheres in the projection data can significantly impede the accurate measurement of CT geometrical parameters.

While the candy cane standard provides significant improvements, there are still shortcomings in the design. A radiographic projection of the candy cane standard is shown in Figure 55-b. The corresponding density distribution map is shown in Figure 55-c. While there are areas where the point density is high, i.e. markers are clustered (bright regions in Figure 55-c), there are areas where the detector is not covered at all. Thus, the spatial distribution of projected markers can be further optimized – an issue addressed in this study.

Since the minimization method used for solving CT system geometrical parameters is based on analyzing projection data, it is important that the distribution of projected markers be homogeneous in every single radiograph. The density map was therefore generated for one projection using the Parzen-Rosenblatt method [137,138]. Given the fact that the standard is completely symmetrical, it can be assumed that the density map is similar for each projection; the only difference would be in the position of local maxima (bright areas in Figure 55-c).

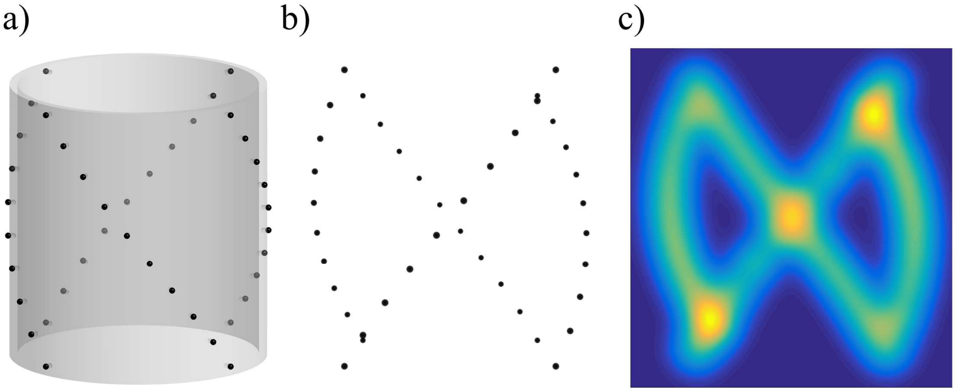

Figure 55. Candy cane standard: (a) CAD model, (b) radiographic projection, (c) density distribution of projected markers.

Overlaps between two or more projected spheres can negatively affect the estimation of geometrical parameters. The object presented in this study is designed to reduce the number of overlaps of projected spheres while also broadening the distribution of projected spheres in the detector field of view. A simulation study was carried out to compare overlaps of the candy cane standard to the overlaps of a series of newly-designed standards consisting of several spatial trajectories of spheres. Scorpius XLab® (Fraunhofer IIS, Germany) was used for generating simulated radiographic data of the various reference standards. The dimensions of the simulated candy cane standard were designed in order to ensure full coverage of the detector while positioned in the half-way along the magnification (*z*) axis of a typical CT system. Given these requirements, the distance between the centers of radially opposed spheres and the vertical distance between the centers of corresponding spheres on both sides of the cylindrical axis were both defined to be 105 mm. The sphere diameter Ø 2.5 mm was chosen for the particular magnification position to ensure that enough detector pixels were contained in the projected shadow of the sphere while at the same time minimizing the number of overlaps between the projected markers. STL files of the other reference standards were created preserving the same overall object dimensions, sphere number and size. Initial simulations indicate that helical trajectories provided the most significant improvements with respect to reducing projected sphere superpositions. As a result, the authors investigated various helical arrangements of spheres. Two parameters were considered in the design of the new standards: (i) number of helices and (ii) number of helical turns along the cylindrical axis. The various designs are summarized in Table 17. Number of helices is limited to 8 and number of turns is limited to 4 as further increments of the parameters result in duplicated designs already constructed by previous combinations. 720 projections were simulated for a full revolution of the reference standards, i.e. 0.5° angular increments between two subsequent projections. The number of overlapping spheres in each of 720 projections was evaluated and the sum of overlaps as a function of helix number and number of turns was calculated.

The effect of modifying the number of helical turns is shown in Figure 56-a, where the number of overlaps against the number of helical turns is plotted. Individual lines in the chart represent different number of helices as defined in Table 17. Varying the number of helical turns had the largest effect on the object with one helix. The number of overlaps for the two and four helix objects varied by 200 and 100, respectively. For the remaining designs, the number of helical turns did not provide significant changes in the number of overlaps. It should be noted that, in the case of two or more helices, the lowest number of overlaps was achieved for a single turn.

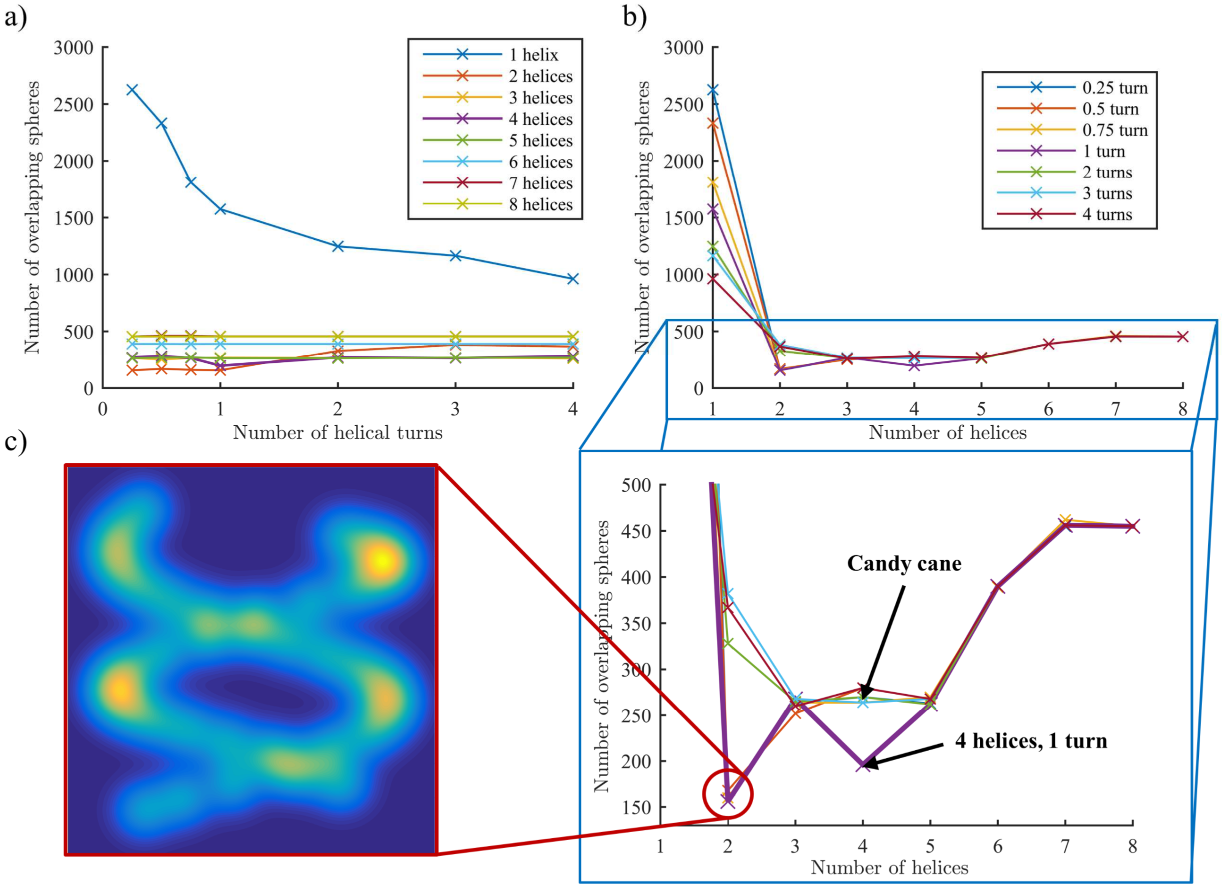

Figure 56. Results from the simulation study, in which the candy cane standard is compared to other helical trajectories of point markers. a) Number of overlapping spheres calculated over 720 projections as a function of the number of helical turns and as a function of number of helices. b) Number of overlapping spheres calculated over 720 projections as a function of the number of helices and as a function of helical turns; a close-up of the plot is provided for the data corresponding to two or more helices. c) Radiographic density map for one projection of the reference standard with two helices and one helical turn.

Table 17. Selected values for the simulated comparison of candy cane standard with newly designed helical trajectories.

Number of helices	Number of helical turns
1	0.25
2	0.5
3	0.75
4	1
5	2
6	3
7	4
8	-

A significant reduction in overlaps is observed for two or more helices, as shown in. Figure 56-b. The minimum number of overlaps with one helix (approximately 1000) is more than double the maxima of the other designs. Additionally, the variation in overlaps for 2-8 helices is below 300. Therefore, the data for one helix was excluded from the close-up in Figure 56-b. Two local minima in number of overlaps were observed for two reference standard designs: two helices with one turn and four helices with one turn. While the design with two helices has the lowest number of overlaps over the whole dataset, the distribution of spherical markers on detector is not uniform. The radiographic density map of the projected markers for one projection of two helices and one turn is shown in Figure 56-c. There are areas on the detector where the projected markers are clustered, as well as areas with low density or complete absence of markers. While the number of overlaps for four helices and one turn is 10 % larger compared to two helices, the distribution of projected markers on the detector is significantly improved, as shown for one projection in Figure 57-c. The small increase in overlaps is dwarfed by the increase in spatial distribution of projected markers; therefore, the design with four helices and one turn (CAD model and a radiographic projection are shown in Figure 57-a and Figure 57-b, respectively) was chosen as a template for the design of the new reference standard presented in this study. Similar data for the state-of-the-art candy cane standard were shown in Figure 55 for comparison. The four helix and one turn design provides a significant improvement in radiographic density and a reduction in the number of overlaps of almost 30 %.

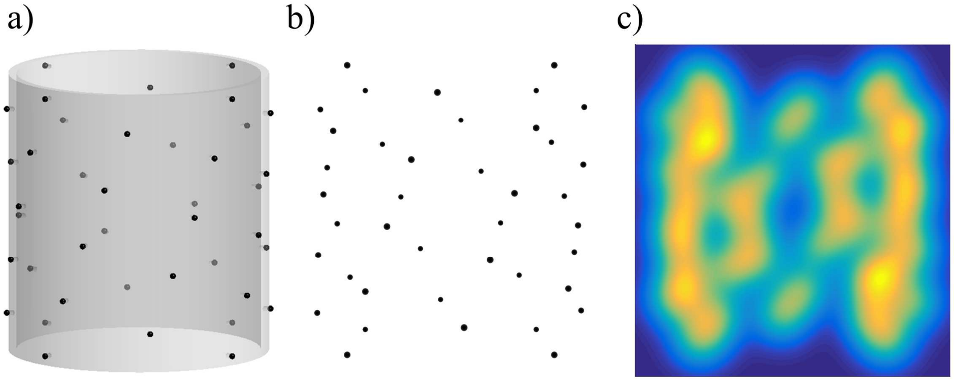

Figure 57. Design with four helices and one helical turn: (a) CAD model, (b) radiographic projection, (c) density distribution of projected markers.

The reference standard developed in this study, named CT Calibration Tube (CT^2), is shown in Figure 58. It is composed of a tube framework with high precision spheres glued on its surface. The materials for the standard were chosen considering the following criteria:

1) High contrast between projected spherical markers and framework.
2) Mechanical stability of reference standard, including low thermal expansion of components and stiffness of the interface between the framework and spheres.
3) Accessibility of sphere surface for coordinate measurements by CMM. At least half of the sphere surface should be accessible by the CMM's touch probe.

In order to achieve high contrast between the projected framework and spheres, the tube framework is made of carbon fibers (attenuation coefficient $\mu = [0.27,1]$ cm^{-1} for photon energy in range [20,200] keV[1] [139]) and sphere markers are made of stainless steel ($\mu = [1.1,195]$ cm^{-1} for photon energy in range [20,200] keV[1] [139]). The attenuation coefficient of the epoxy resin holding the spheres onto the tube framework is negligible ($\mu = [0.12,0.22]$ cm^{-1} for photon energy [20,200] keV[1] [139]). A hollow tube was chosen instead of a solid cylinder to minimize the attenuation of X-rays by the framework.

The thermal stability of the object is ensured by low thermal expansion of all components. The linear expansion coefficient of the carbon fiber material used for the framework is $\mathrm{CTE}_{\mathrm{tube\ framework}} = 0.2\times10^{-6}\ \mathrm{K}^{-1}$. The spheres are made of martensitic hardened stainless steel with linear expansion coefficient of $\mathrm{CTE}_{\mathrm{spheres}} = 10.3\times10^{-6}\ \mathrm{K}^{-1}$. Finally, the two-component epoxy resin has a linear expansion coefficient of $\mathrm{CTE}_{\mathrm{epoxy}} = 16\times10^{-6}\ \mathrm{K}^{-1}$.

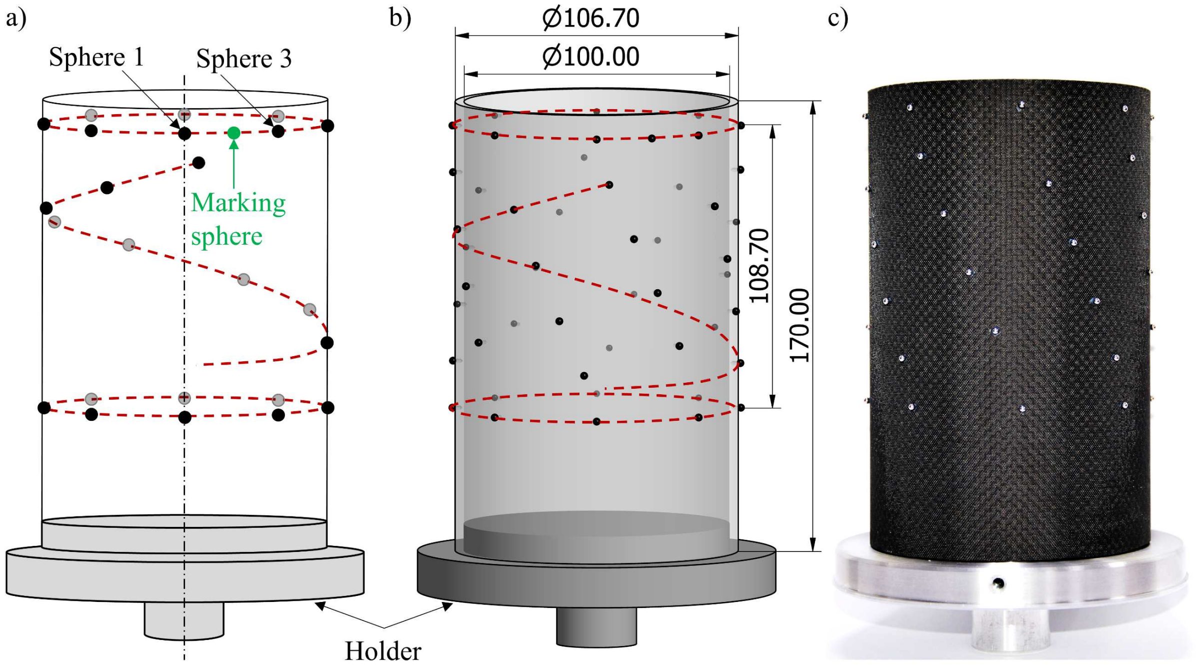

Figure 58. Design of the developed reference standard (CT^2): a) schematic visualization of the circular and helical trajectories (only one out of four helices is shown for improved visualization); b) CAD model of the standard with general dimensions; c) image of the manufactured standard. All dimensions are in millimeters.

---

[1] Typical range of energy spectrum for common industrial CT systems

To ensure high-precision sphere form and size, grade 10 spheres were chosen. For this grade, the variation of sphere diameter and form error is below 0.25 µm, and surface roughness *Ra* below 0.5 µm [140].

The design with four helices and one turn was observed as having the optimal combination of low overlaps and high projected sphere distribution on the detector. This configuration was, therefore, chosen as a base pattern for the design of the optimized reference standard (Figure 58). Each helix is formed by eight spheres evenly distributed along the cylindrical axis. The concept from [90] was also adopted in the new reference standard, allowing static (one projection) determination of CT geometrical parameters. Two circular trajectories each containing eight spheres were added to the upper and lower extremes of the cylindrical framework. The projected circular trajectories are completely free of overlaps and can therefore be used for robust initial estimation of the CT instrument geometry.

Given the cylindrical symmetry of the object, an additional "marking" sphere (see Figure 58-a) was added to the top circular trajectory to ensure unambiguous identification of spheres in the projection data. The CT^2 contains a total number of 49 spheres, including the marker sphere. In the ideal case of infinitesimally small (but still radiographically detectable) point markers, where no overlaps are present, and for a detector with infinite resolution, increasing the number of spheres would improve the accuracy of CT geometrical parameter calibration. In practice, however, the size of the projected spheres on the detector affects the ability to identify the projected sphere centers. If the projected spheres are too small, the error in the determination of sphere center projections will increase as a result of the detector's finite resolution. Given these practical limitations, there exists an optimal number of spheres, after which increasing the number of markers provides negligible improvements on the accuracy of geometrical parameter calibration. This optimal number of spheres was estimated at around 50 in [92], which corresponds to the number of spheres chosen for the object developed for this study. However, it is worth noting that the optimum is valid for present configuration and should be re-evaluated for different combination of materials, magnification, and sphere and object size.

The general dimensions of the CT^2 are shown in Figure 58-b. Typically, the detectors in industrial CT systems are square in shape. To evenly distribute the projected spheres on the detector, the horizontal and vertical extent of the sphere pattern should be equal. The outer diameter of the tube framework is 106.7 mm. The sphere centers are positioned 1 mm above the surface of the tube, resulting in a distance of 108.7 mm between the centers of radially opposed spheres. The vertical distance between the centers of corresponding spheres on both sides of the cylindrical axis is also 108.7 mm. The length along the cylindrical axis of the tube framework was extended to allow a dedicated holder (for inserting into the CT system's rotary stage) to be included while not interfering in the projection data. The diameter of all spheres is 2.5 mm. The selected sphere size ensures that the projected spheres are large enough to overcome pixelization errors in the sphere center determination step, while also reducing overlaps.

5.3.2 Manufacturing of the reference standard

Precise manufacturing is important to achieve the designed spatial distribution of spheres with sufficient accuracy so that additional overlaps are not introduced. The quality of the manufacturing should ensure long-term stability of the sphere center positions. Given the inherent stability of the carbon tube and steel spheres, attention is given to the interface between them. A scheme of the connection is shown in Figure 59. A 2 mm diameter hole was drilled into the outer surface of the tube as a “socket” for each sphere. Drilling into composites is generally a challenging task given the fracturing nature of the material. Therefore, a special diamond coated tool with a 90° tip angle was used. The shape of the tool ensures that single fibers are not pulled out and the external edge of the hole remains smooth. Diamond coating reduce the tool wear as carbon fibers are highly abrasive. The drilling was performed by CNC lathe in order to ensure accurate positioning of the drill bit and, subsequently, the holes.

In selecting the bonding material, the following aspects should be considered: object material(s), intended use of the object, and expected stress. Given the imaging nature of the geometrical calibration procedure, the only expected stress on the reference standard is from vibrations and quivering during the transport and physical contact from CMM calibration measurements of sphere center position. The combination of carbon fiber and stainless steel demands a dedicated adhesive to ensure strong binding. The two-component adhesive Elan-tech® AS 90 with Hardener AW 92 is suitable for this purpose (lap shear strength 31 MPa) and was chosen in the construction of the CT^2.

Calibration of the sphere center position demands that at least half of the sphere’s surface be accessible by the CMM’s contact probe. It is therefore critical when gluing the two components to ensure that no more than half of the sphere’s surface be contaminated by epoxy.

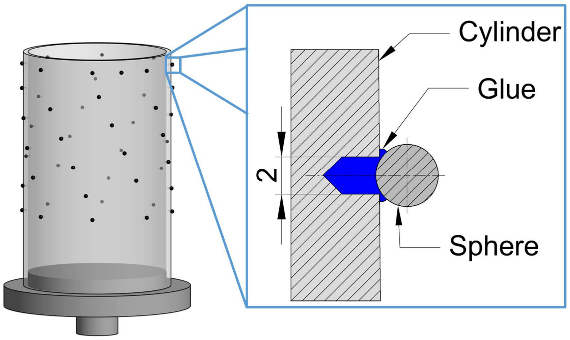

Figure 59. Scheme of the connection between the carbon fiber framework and a sphere.

5.3.3 Calibration of the reference standard

The calibration of the CT^2 consists of measuring the relative coordinate positions of the spheres. This task was performed on a Zeiss Prismo CMM equipped with a rotary table (a diagram of the CMM and the reference coordinate axes are shown in Figure 60-a). The Maximum Permissible Error (MPE) of the CMM is MPE = 2 + L/300 µm, where L is measured length in mm. Probes of 0.5 mm diameter were employed in two styli configurations (see Figure 60-b): (i) a single stylus in -x_{CMM} direction and (ii) a star configuration with four probes in +x_{CMM}, +y_{CMM}, -x_{CMM} and -y_{CMM} direction. Both the CT^2 and the standard for traceability transfer (a ball bar, shown later in this section) were mounted on the rotary table. The measurements were acquired in temperature-controlled environment; the temperature during calibration was within 20 ± 0.5 °C. The coefficients of thermal expansion of the measured components are low; therefore, temperature effects were considered negligible.

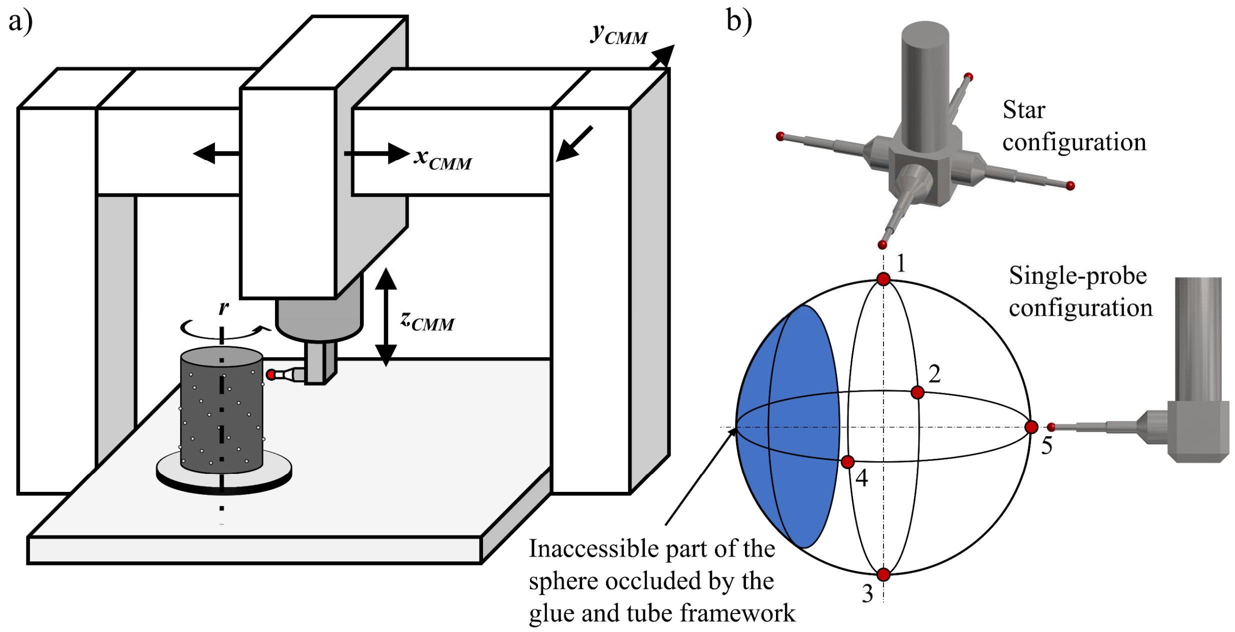

Figure 60. a) Diagram of the CMM system with reference coordinate axes. bb) Two different styli configuration – star and single-probe, and five probing points on the outer sphere surface.

A local right-handed Cartesian coordinate frame is defined for describing the measured positions of the sphere centers (Figure 61). The origin of the coordinate system is located at the center of Sphere 1. The local y_P axis is defined by the straight line from the center of Sphere 1 to the center of Sphere 6. The positive y_P axis points from the origin towards the center of Sphere 6. The x_P axis is perpendicular to the y_P axis and is located in a plane defined by the centers of Sphere 1, Sphere 6 and Sphere 8. The positive x_P axis points in the general direction towards Sphere 2. The z_P axis is orthogonal to both the x_P and y_P axes and its positive direction follows the right-hand screw rule.

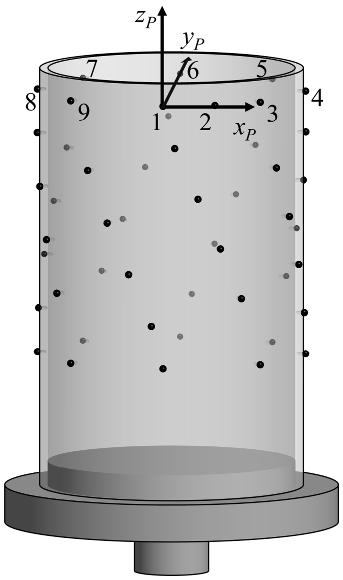

Figure 61. Coordinate system of the CT^2. The origin is placed in Sphere 1.

Method

The calibration procedure used in this work is based on a standard method for calibration of ball and hole plates developed by German Calibration Service (DKD) [141] and applied, for example, in [142] with the use of reversal methods [54]. The procedure is divided into three sequential steps. In a first step, the contribution of the rotary axis error motions to measurement errors is evaluated by applying reversal methods. In a second step, all sphere center coordinates are measured following the same reversal patterns. Finally, in the last step, the traceability of measurements is transferred through reference standard (ball bar) measured in reversal sequence and various orientations. Detailed procedures of each step are described as follows:

1) Rotary axes introduce additional measurement errors. Given the complex spatial arrangement of spheres and limited length of styli (to reduce deflection errors), certain spheres were not accessible by the contact probe without the risk of unintentionally colliding with the object. Therefore, using the rotary table was the only solution for measuring all spheres without the need to reposition the object between measurements. In order to evaluate the effect of the rotary axis on measurement errors, 16 spheres that are accessible without rotating the object were measured using the star styli configuration (Figure 60-b). The reversal procedure described in [141] requires that the measured object be upended such that its z_P axis is pointing downwards. In this new orientation, the opposite sphere surfaces should be measured. However, given that the internal surfaces of the spheres on the CT^2 are inaccessible, the reversal method could not be performed. Instead, the object is rotated four times by 90° about its z_P axis, each time measuring the positions of the 16 sphere centers. The four different positions are shown in Figure 62. For each rotation position of the object, the sphere center coordinates are measured 10 times and the results are averaged. By doing this, errors introduced by probing from different directions and different touch probes are minimized. Additionally, an equivalent to clockwise and counter-clockwise spiral sequence described in [141] is used here: 5 measurements are performed layer-by-layer in counter-clockwise top-down direction and 5 measurements are performed in the reversed sense, i.e. clockwise bottom-up direction (see Figure 63-a, b). Errors due to hysteresis are reduced by the described measurement sequence. The probing strategy shown in Figure 60-b was adapted from [141]; each sphere is probed five times – 4 points are taken at the equator and one at the pole. The low number of probing points is in this case sufficient as the spheres have negligible form error. Evaluation software Zeiss Calypso is used to fit a least-squares sphere to the acquired surface coordinates and extracting the fit sphere center.

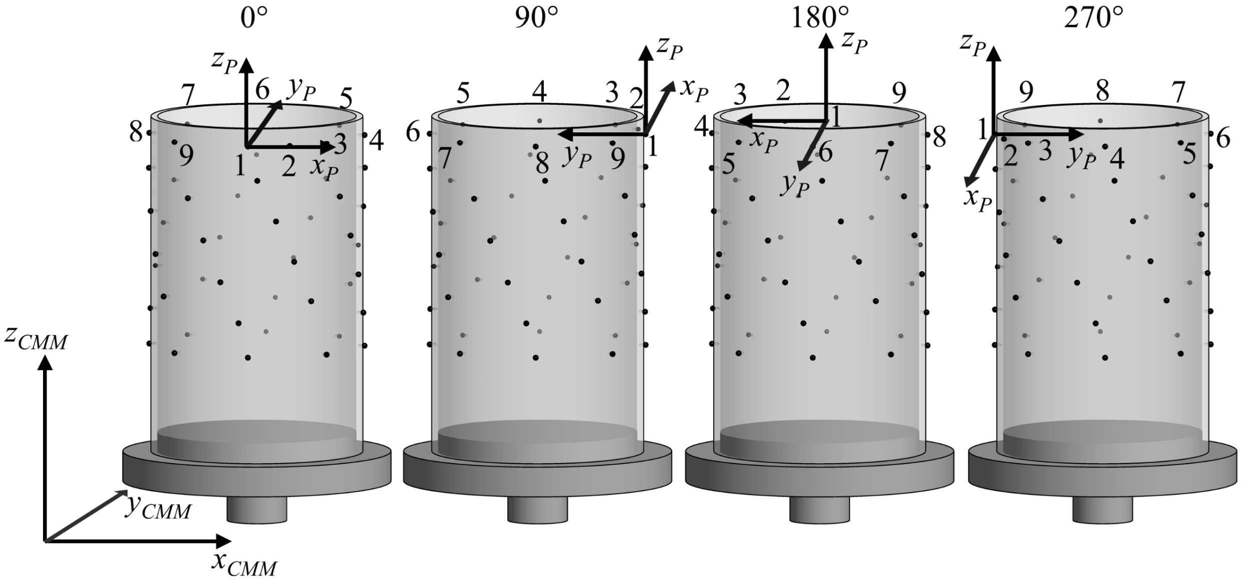

Figure 62. Four different orientations of the CT2 during calibration, each time rotated by 90° about the cylindrical axis.

2) While in the first step the positioning between the spheres was executed by the CMM translation axes only, in the second step, the main movement is performed by the rotary table. The spheres are probed by the single stylus configuration (Figure 60-b). The movement of the CMM x_{CMM}, y_{CMM} and z_{CMM} axes is reduced to a minimum as follows. The stylus is aligned with CMM x_{CMM} axis and translations along x_{CMM} and y_{CMM} are limited to the range necessary to circumscribe the sphere. The range of movement along the z_{CMM} axis is defined by the distance between the top and the bottom spheres for any helical segment. By reducing the translational motion, the errors caused by linear CMM positioning are reduced. The measurement sequence is similar to the sequence from the first step. The object is measured in four different rotational positions (described in Figure 62). For each position, the measurement procedure is repeated 10 times: five measurements are executed top-down and counter-clockwise direction, while the other five measurements are performed in the bottom-up and clockwise direction (see Figure 63-a, b). Measurement results are averaged to minimize the error of the rotation axis. The same five points on the sphere surface (four on the equator and one on the pole) are measured, as shown in Figure 60-b.

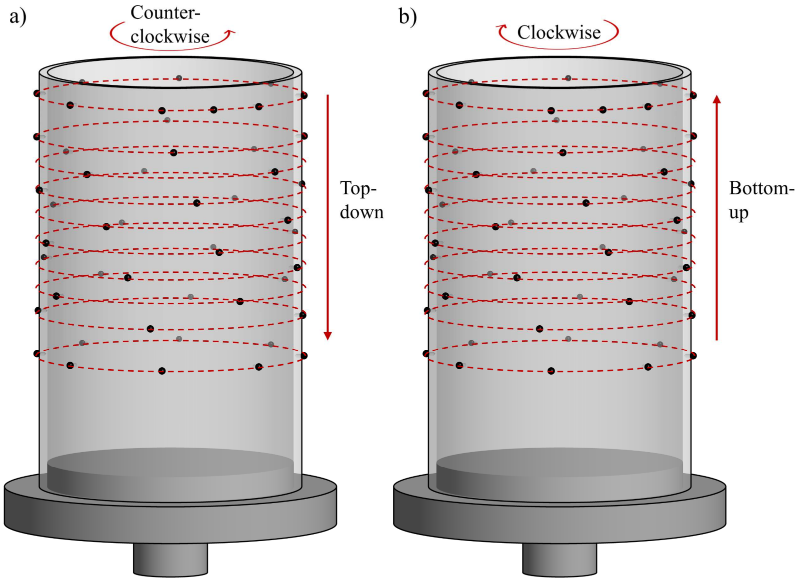

Figure 63. CMM measurement sequence: a) counter-clockwise, top-down measurement sequence; b) clockwise, bottom-up measurement sequence.

3) Traceability in the measured sphere center coordinate points is established by measuring a ball bar (Figure 64-a). Since the spheres on the ball bar, unlike on the object developed in this study, are distributed in one line, the measurement strategy was modified to better resemble the original measurement task. The ball bar is measured in vertical and horizontal positions as shown in Figure 64-b. The same measurement procedure from the second step (in which all 49 spheres were measured), i.e. single probe and rotary stage motion, is used in the measurement of the ball bar.

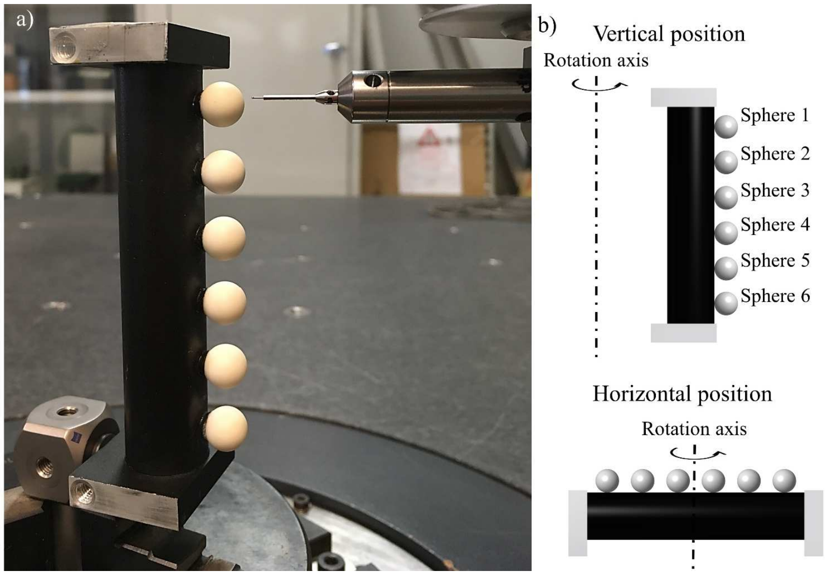

Figure 64. a) Ball bar used for transferring traceability to the measured sphere center coordinates; b) vertical and horizontal orientation of the ball bar.

First, the ball bar is measured in the vertical position. The sample is positioned off the rotary axis such that the balls point in + x_{CMM} direction (Figure 65-a). This orientation of the ball bar is denoted by rotation angle $\alpha = 0°$, with the positive rotation following the right-hand screw rule for the rotary stage axis. Subsequently, the rotary table is rotated to α = +30° and Sphere 1 is measured. The rotary table is rotated by Δα = −12° increments and, at each rotation, the next sphere down is measured, *i.e.* at α = +18° Sphere 2 is measured while at α = +6° Sphere 3 is measured, *etc.* (see Figure 65-b). The entire procedure is repeated five times in this sequence and five times in reversal; *i.e.* starting with the measurement of Sphere 1 at α = -30° rotation and measuring the next sphere down in each subsequent position given by Δα = +12° increments. Similarly to the spheres in the CT^2, five points (four at the equator and one at the pole) are acquired for each sphere.

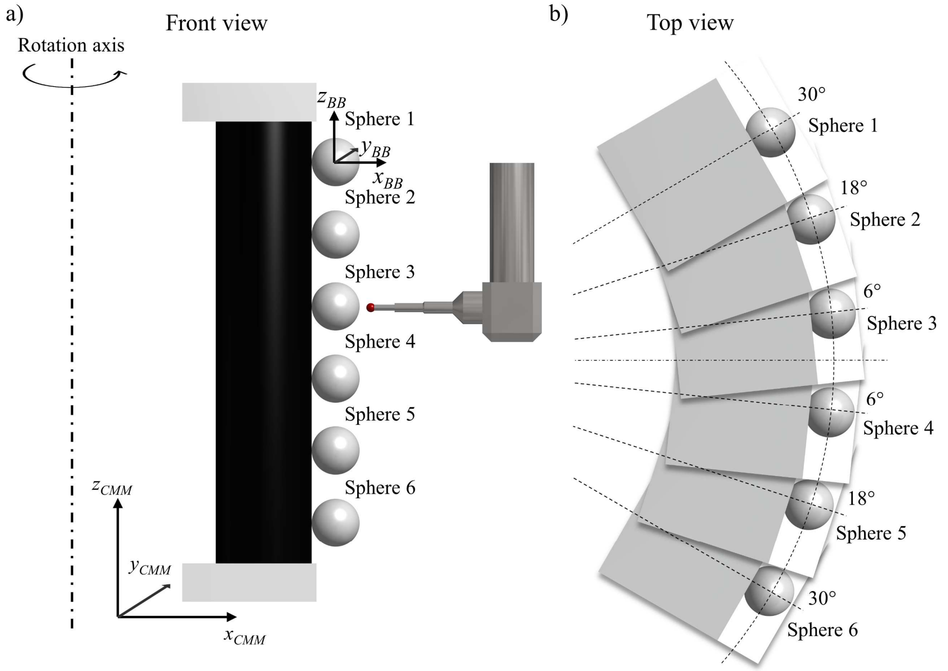

Figure 65. Measurements of the ball bar in vertical position: a) relative position of the ball bar with respect to the CMM coordinate system and rotation axis; b) different angular positions of the ball bar during measurements.

The ball bar is then measured in a horizontal orientation. The sample is positioned such that the length segment between the centers of Spheres 1 and 6 is parallel to the x_{CMM} axis (Figure 66-a). Sphere 1 is measured at this new α = 0° position. The sample is then rotated to α = +90°and Spheres 2 and 3 are measured. Sphere 6 is measured at α = +180° and, finally, Spheres 4 and 5 are measured at α = +270° (see Figure 66-b). Five complete measurement runs are repeated for positive rotation direction and negative rotation direction. Since the relative position of the balls and the touch probe does not allow acquiring the probing points in the same pattern as in the previous steps, the probing strategy was modified. Eight surface points were measured on each sphere, as depicted in Figure 66-c.

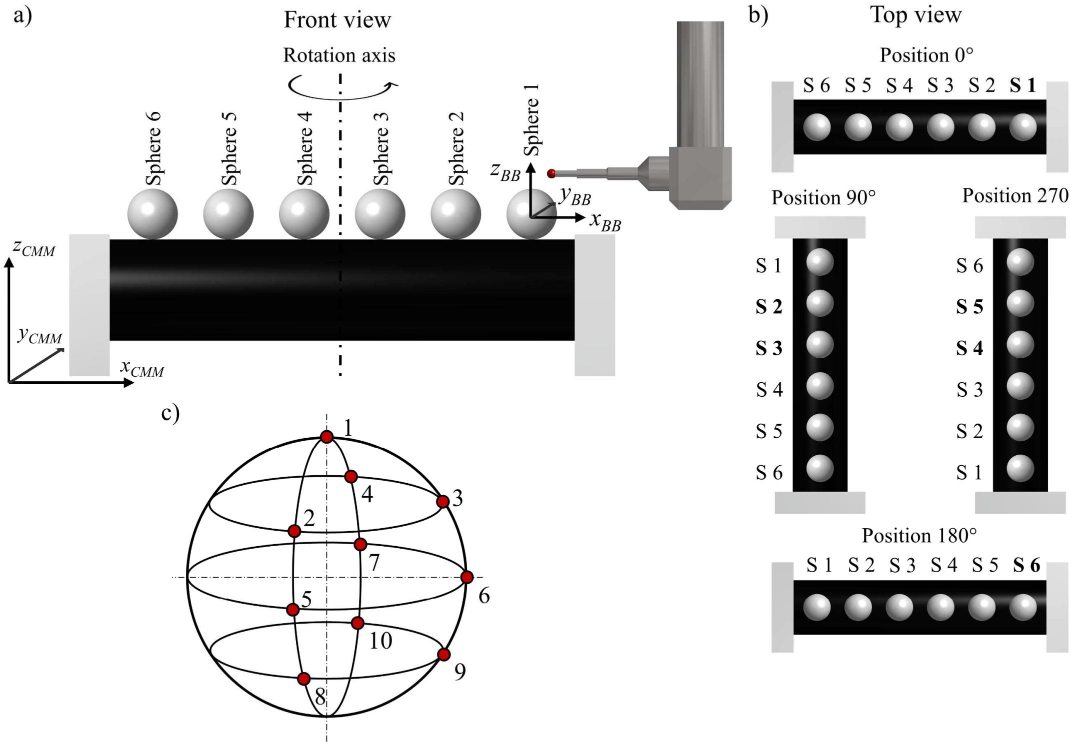

Figure 66. Measurements of the ball bar in horizontal position: a) relative position of the ball bar with respect to the CMM coordinate system and rotation axis; b) different angular positions of the ball bar during measurements. The spheres marked in bold are measured in the corresponding position; c) the pattern of probing points on measured spheres in horizontal position.

The ball bar is measured both horizontally and vertically in four different positions; after performing the above mentioned 10 measurement cycles, the sample is dismounted, rotated by 90° around the x_{CMM} axis, and mounted in the new orientation.

Uncertainty of calibration of sphere center coordinates

Calibration uncertainty was estimated for the position of sphere centers in the coordinate frame defined earlier in this section. A method based on VDI/VDE 2630-2.1 [29] using calibrated workpieces was used in this work. The following factors were considered in evaluating the uncertainty:

(1) Calibration uncertainty of the ball bar u_{cal}, calculated as $u_{\mathrm{cal}}= U_{\mathrm{cal}}/k$, where k is coverage factor (k=2, as stated in the calibration certificate) and U_{cal} is the calibration uncertainty stated in the calibration certificate.

(2) The calibration certificate for the ball bar only provided calibrated values along the x_{CMM} axis coordinate positions of the spheres (with respect to the configuration shown in Figure 66). As a result, it was not possible to calculate and correct for the systematic error for all the three sphere center coordinates. The systematic error between CMM measurements and calibrated ball bar values b was therefore included in the uncertainty budget for the calibration of the CT^2 as suggested in [29]. Measurement bias b was calculated as a maximum measurement error for measurements in horizontal and vertical configuration according to Equation 5.1.

$$b = MAX\{b_{hor}, b_{ver}\}, \tag{5.1}$$

where b_{hor} and b_{ver} denote systematic error in horizontal and vertical orientation, respectively. Systematic errors were evaluated for each sphere separately and the resulting biases b_{hor} and b_{ver} used in Equation 5.1 were calculated as a maximum over all six spheres as shown in Equation 5.2.

$$b_{hor/ver} = MAX\{\overline{y_i} - x_{cal,i}\}, \tag{5.2}$$

where i=1-6 is the number of the sphere, $\overline{y_i}$ is measurement average for all four ball bar positions, and $x_{\mathrm{cal,i}}$ is the calibrated value.

(3) Standard uncertainty of the measurement procedure $\overline{u_p}$ was calculated as an averaged standard uncertainty u_{p} defined in VDI/VDE 2630-2.1 [29] according to Equation 5.3. In other words, $\overline{u_p}$ is calculated as the mean of standard uncertainties u_{p} determined for individual spheres.

$$\overline{u_p} = \frac{\sum_{i=1}^{n} u_{p,i}}{n}, \tag{5.3}$$

where n is the number of spheres and u_{p} defined in following Equation 5.4.

$$u_p = \sqrt{\frac{1}{k-1}\sum_{j=1}^{k}(y_j - \bar{y})^2}, \tag{5.4}$$

where k is the number of measurements (comprising all repetitions in all positions and both the horizontal and vertical orientation) per sphere, y_j is the observed and $\bar{y}$ the average value per sphere.

The final calibration uncertainty is defined by Equation 5.5.

$$U_{k=2} = k\sqrt{u_{cal}^2 + u_p^2 + b^2}, \tag{5.5}$$

where k is coverage factor; for k = 2 a confidence level of 95 % is ensured. The estimated calibration uncertainty and single uncertainty contributions are summarized in Table 18. Since the calibration was performed under controlled conditions, and CMM measurement errors were minimized by using reversal methods and procedures to isolate single error sources (measurements with and without rotating the rotary table), the uncertainty was kept at a minimum. In addition, several tests to optimize the probing force and probing dynamics were performed beforehand. To ensure a reliable estimation of uncertainty in the CT^2 standard, the calibrated ball bar was measured in its horizontal and vertical orientation to resemble the measurement task. Furthermore, the roughness of the spheres on the ball bar was higher than the roughness of the spheres on the CT^2. As a consequence, the procedure for the establishment of measurement traceability was compared to the calibration task even more complex, thereby ensuring reliable estimation of the measurement uncertainty.

Table 18. Summary of the estimated calibration uncertainty contributors and the expanded calibration uncertainty.

Uncertainty contribution	Symbol	Value/µm
Calibrated workpiece	u_{cal}	0.51
Measurement procedure	$\overline{\boldsymbol{u_p}}$	0.33
Systematic error	b	0.85
Expanded uncertainty (*k*=2)	$\boldsymbol{U_{k=2}}$	**2.09**

5.4 Minimization procedure

The CT^2 is designed for measuring the CT instrument geometry by minimization of reprojection errors. The method is based on comparing modelled and observed projections of the reference standard. A ray-tracing model is used to calculate the center projection coordinates for the reference standard with known sphere positions given an initial set of geometrical parameter values. The set of modelled center projection coordinates is compared to the set of observed center projection coordinates from the analysis of the experimentally acquired radiographs. The parameters describing the modelled system are solved by iteratively changing their values until the difference between modelled and observed coordinates, i.e. the reprojection error, is minimized. The sum of the squared residuals of all data points, i.e. total number of spheres multiplied by the total number of projections, is divided by the total number of data points to provide a reprojection error per data point. The resulting set of solved parameters should correspond to the geometry of the system from which the observed data was taken. The MATLAB built-in *fmincon*() for non-linear constrained minimization is applied for this task in conjunction with the MATLAB built-in *GlobalSearch* algorithm for global optimization within a user-specified set of boundary conditions for the geometrical parameters. More details on the minimization procedure and its implementation for the evaluation of CT geometrical parameters are discussed in [143]. The algorithms were developed in collaboration with KU Leuven, namely with Massimiliano Ferrucci and Evelina Ametova.

5.5 Comparison of the CT^2 with a state-of-the-art equivalent

Scans of the CT^2 were simulated in the presence of misalignments of three detector angles θ, φ and η (see Table 19). Gaussian blur (σ = 1 pixel) and Poisson noise were added to the otherwise noiseless and blur-less simulated projections. In the case of well-defined reference standard and minimization procedure, the minimized geometrical parameters should converge to the nominal parameters of the simulated scan.

The minimization procedure was repeated with the state-of-the-art candy cane standard under equivalent nominal scan parameters for comparison. The criteria for the comparison are as follows:

a) Difference between nominal and minimized geometrical parameters.
b) Reprojection error per data point, i.e. the residual average deviation between modelled and observed projected sphere center coordinates after minimization.

The nominal parameters for each simulated acquisition are shown in Table 19. The minimization results (solved parameters) using the CT^2 standard and the candy cane standard are presented in

Table 20 and Table 21, respectively. Deviations between nominal and minimized geometrical parameters using CT^2 and the candy cane standard are shown in Table 22 and Table 23, respectively. Finally, reprojection errors per data point are compared for the CT^2 standard and the candy cane standard in Table 24.

Table 19. Geometrical parameters of the simulated (nominal) system. Values of translation parameters are in millimeters, rotations are in degrees.

		Solved parameters						
		z_R	x_D	y_D	z_D	θ	φ	η
	Ideal	-400.000	0.000	0.000	-1177.000	0.000	0.000	0.000
Simulated misalignments	θ	-400.000	0.000	0.000	-1177.000	2.000	0.000	0.000
	φ	-400.000	0.000	0.000	-1177.000	0.000	2.000	0.000
	η	-400.000	0.000	0.000	-1177.000	0.000	0.000	2.000
	$\theta+\varphi$	-400.000	0.000	0.000	-1177.000	2.000	2.000	0.000
	$\theta+\eta$	-400.000	0.000	0.000	-1177.000	2.000	0.000	2.000
	$\varphi+\eta$	-400.000	0.000	0.000	-1177.000	0.000	2.000	2.000
	$\theta+\varphi+\eta$	-400.000	0.000	0.000	-1177.000	-2.000	-2.000	-2.000

Table 20. Minimized geometrical parameters using CT^2. Values of translation parameters are in millimeters, rotations are in degrees.

		Solved parameters						
		z_R	x_D	y_D	z_D	θ	φ	η
	Ideal	-400.000	0.000	0.000	-1177.000	0.000	0.000	0.000
Simulated misalignments	θ	-399.950	0.000	0.004	-1176.900	1.999	0.000	0.000
	φ	-399.970	0.000	0.000	-1176.900	0.000	2.000	0.000
	η	-399.990	0.000	0.000	-1177.000	0.000	0.000	2.000
	$\theta+\varphi$	-399.970	0.000	-0.001	-1176.900	2.000	2.000	0.000
	$\theta+\eta$	-399.940	0.000	0.001	-1176.800	2.000	0.000	2.000
	$\varphi+\eta$	-399.930	0.000	-0.002	-1176.800	-0.070	2.001	1.999
	$\theta+\varphi+\eta$	-399.950	0.000	0.001	-1176.900	-2.069	-2.001	-1.999

Table 21. Minimized geometrical parameters using the candy cane standard. Values of translation parameters are in millimeters, rotations are in degrees.

		Solved parameters						
		z_R	x_D	y_D	z_D	θ	φ	η
	Ideal	-399.990	0.000	0.000	-1177.000	0.000	0.000	0.000
Simulated misalignments	θ	-399.930	0.000	0.001	-1176.800	1.999	0.000	0.000
	φ	-399.960	0.000	0.000	-1176.900	0.000	2.000	0.000
	η	-400.000	0.000	0.000	-1177.000	0.000	0.000	2.000
	$\theta+\varphi$	-399.940	0.000	-0.001	-1176.800	2.000	2.000	0.000
	$\theta+\eta$	-399.940	0.000	-0.002	-1176.800	2.000	0.000	2.000
	$\varphi+\eta$	-399.940	0.000	-0.002	-1176.800	-0.069	2.001	1.999
	$\theta+\varphi+\eta$	-399.930	0.001	-0.003	-1176.800	-2.070	-2.001	-1.999

Table 22. Absolute deviations between simulated and minimized geometrical parameters using CT^2 standard. Values of translation parameters are in micrometers, rotations are in minutes.

		Solved parameters						
		z_R	x_D	y_D	z_D	θ	φ	η
Simulated misalignments	**Ideal**	0	0.02	0.02	0	0.00	0.01	0.00
	θ	50	0.04	3.71	100	0.04	0.01	0.00
	φ	30	0.25	0.42	100	0.00	0.02	0.00
	η	10	0.10	0.13	0	0.00	0.02	0.00
	$\theta+\varphi$	30	0.41	1.41	100	0.01	0.01	0.00
	$\theta+\eta$	60	0.03	1.25	200	0.02	0.01	0.00
	$\varphi+\eta$	70	0.33	1.56	200	4.17	0.05	0.01
	$\theta+\varphi+\eta$	50	0.35	0.70	100	4.15	0.05	0.07
	Average	**37.5**	**0.19**	**1.15**	**100**	**1.05**	**0.02**	**0.01**

Table 23. Absolute deviations between simulated and minimized geometrical parameters using the candy cane standard. Values of translation parameters are in micrometers, rotations are in minutes.

		Solved parameters						
		z_R	x_D	y_D	z_D	θ	φ	η
Simulated misalignments	**Ideal**	10	0.04	0.29	0	0.00	0.01	0.00
	θ	70	0.03	0.62	200	0.04	0.01	0.00
	φ	40	0.37	0.05	100	0.00	0.00	0.00
	η	0	0.00	0.40	0	0.01	0.00	0.00
	$\theta+\varphi$	60	0.36	1.31	200	0.03	0.01	0.00
	$\theta+\eta$	60	0.07	1.51	200	0.03	0.01	0.00
	$\varphi+\eta$	60	0.35	2.28	200	4.16	0.07	0.07
	$\theta+\varphi+\eta$	70	0.51	3.10	200	4.18	0.04	0.07
	Average	**46.25**	**0.22**	**1.19**	**138**	**1.06**	**0.02**	**0.02**

Table 24. Reprojection error per data point. All values are in pixels.

		Reprojection error	
		CT^2	**Candy cane standard**
Simulated misalignments	**Ideal**	0.015	0.022
	θ	0.016	0.024
	φ	0.016	0.023
	η	0.018	0.022
	$\theta+\varphi$	0.017	0.024
	$\theta+\eta$	0.018	0.021
	$\varphi+\eta$	0.018	0.020
	$\theta+\varphi+\eta$	0.015	0.023
	Average	**0.017**	**0.022**

Simulated results indicate that the solved geometrical parameters for both the candy cane standard and the CT^2 converge to deviations from nominal values within 200 µm for translation parameters and within 5' for rotations. Average deviations in solved values were lower from the CT^2 for six out of seven solved geometrical parameters. The CT^2 outperformed the candy cane standard in solving detector tilt θ and detector skew η, while the average deviation in solving detector slant φ was the same for both standards. Despite the small differences in solved parameter values, both reference standards were successful in solving the geometrical parameters correctly. The data in Table 24 indicate that the reprojection errors from minimization by CT^2 were consistently lower by 12 to 34 % when compared to the reprojection errors from minimization by the candy cane standard.

It could be expected that a significantly lower reprojection error should correspond to lower deviations in the solved parameters from their nominal values; this correlation was not explicitly observed here. The benefits of the CT^2, particularly with respect to the eliminated full sphere overlaps and reduction in partial sphere overlaps when compared to the candy cane standard are, however, critical for the experimental implementation of CT^2 for geometrical calibration of CT systems.

5.6 Monte Carlo method for geometrical calibration

Calibration of CT geometrical parameters as defined in VIM [6] (see also Section 3.1), has not been demonstrated yet. Although several standards have been used in estimation methods discussed in Section 3.4.3, the application of a reference standard with one or more traceable dimensional features has not been shown. This shortfall was overcome by the artifact presented here, since the traceable measurement of the features (i.e. spheres) was demonstrated in Section 5.3.3.

In this section, a Monte Carlo style method for uncertainty assessment of the geometrical parameters solved by minimization is proposed. Monte Carlo methods are based on the observed distribution in the output of a measurement model given a variation in the model inputs for a typically large number of repeat measurements, i.e. often on the order of 10^6. The values assigned to the input variables for each repeat measurement are randomly sampled from a probability distribution proportional to the uncertainty in the respective input. The distribution of the repeatedly solved parameters is taken as a measure of the uncertainty in their estimates, which are typically given by the mean value of the solved values. A more detailed explanation of the Monte Carlo method for assessing uncertainty is provided in [47].

Uncertainty in the input quantities, namely sphere center coordinates (calculated in Section 5.3.3) and center projection coordinates (evaluated in Section 5.6.2), will result in uncertainty of the solved geometrical parameters. To consider these effects, the minimization procedure is repeated several thousand times, each time randomly varying the values of the input quantities from a probability distribution corresponding to the uncertainty in the varied parameter. This Monte Carlo method generates a distribution of solved geometrical parameters. The $k = 2$ uncertainty interval for each solved parameter is given by the upper and lower boundaries (UB and LB, respectively) corresponding to an interval including 95 % of the solved values. A diagram of the Monte Carlo method for geometrical calibration by minimization is shown in Figure 67.

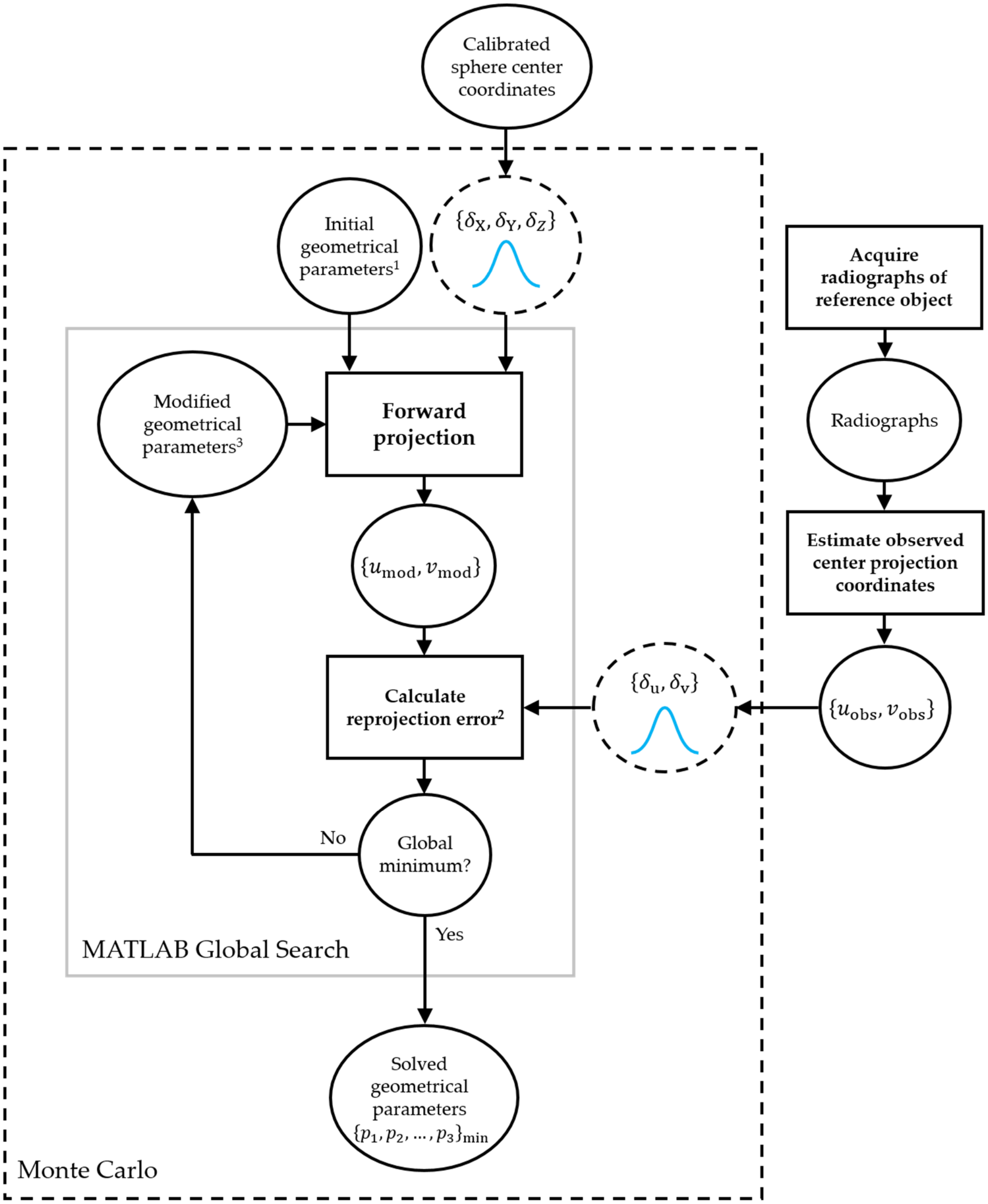

[1] Global search will run the minimization for various initial points within parameter bounds specified by the user.

[2] Defined as the sum of the squared residuals between corresponding modelled and observed center projection coordinates.

[3] The direction in which to modify the parameter values is determined by evaluating the gradients at the current values. In this implementation, the solver fmincon (constrained nonlinear multivariate minimization) is used.

Figure 67. Diagram of Monte Carlo method for geometrical calibration by minimization. δ_X, δ_Y and δ_Z, are the uncertainties of corresponding sphere center coordinates, u_{mod} and v_{mod} are the modelled center projection coordinates, u_{obs} and v_{obs} are the observed center projection coordinates, and δ_u and δ_v are the errors in observed center projection coordinates. Courtesy of Mr. Massimiliano Ferrucci, KU Leuven.

The work related to the Monte Carlo method was developed in collaboration with Massimiliano Ferrucci (KU Leuven, Belgium).

5.6.1 Simulation of radiographic data acquisition

In order to test the performance and robustness of the minimization procedure and the Monte Carlo method, a set of simulations in the presence of various geometrical misalignments of the reference standard, the rotary stage and detector were performed. The simulated data sets were obtained by Scorpius XLab® (Fraunhofer IIS, Germany). The nominal and perturbed geometrical parameters are shown in Table 25 and Table 26. When performing minimization, the initial parameter values were set to their nominal values.

Table 25. Simulated values for instrument geometrical parameters.

		Parameter						
		x_{D} **/mm**	y_{D} **/mm**	z_{D} **/mm**	z_{R} **/mm**	$\boldsymbol{\theta}$ **/°**	$\boldsymbol{\varphi}$ **/°**	$\boldsymbol{\eta}$ **/°**
	Nominal	0	0	-1177	-400	0	0	0
Simulation	1	1.2589	-1.3695	-1175.4426	-402.5449	-0.6756	-0.0989	-0.7867
	2	1.6232	1.8824	-1181.6429	-402.6763	0.5886	-0.8324	0.9238
	3	-1.4921	1.8287	-1173.5087	-399.8152	-0.3776	-0.5420	-0.9907
	4	1.6535	-0.0585	-1172.6601	-398.3250	0.0571	0.8267	0.5498
	5	0.5294	1.2011	-1175.2126	-397.3959	-0.6687	-0.6952	0.6346
	6	-1.6098	-1.4325	-1174.4226	-402.2206	0.2040	0.6516	0.7374
	7	-0.8860	-0.3130	-1174.5687	-399.5871	-0.4741	0.0767	-0.8311
	8	0.1875	1.6629	-1178.0777	-400.1837	0.3082	0.9923	-0.2004
	9	1.8300	1.1688	-1175.4452	-402.9286	0.3784	-0.8436	-0.4803
	10	1.8596	1.8380	-1180.2881	-400.9773	0.4963	-0.1146	0.6001

Table 26. Simulated values for reference standard geometrical parameters.

		Parameter					
		x_{P} **/mm**	y_{P} **/mm**	z_{P} **/mm**	$\boldsymbol{\rho}_{\mathbf{x}}$ **/°**	$\boldsymbol{\rho}_{\mathbf{y}}$ **/°**	$\boldsymbol{\rho}_{\mathbf{z}}$ **/°**
	Nominal	0	0	-400	0	0	0
Simulation	1	1.0051	1.3629	-400.5934	0.4121	-0.1225	-0.4479
	2	-0.9796	-0.9829	-398.6767	-0.9363	-0.2369	0.3594
	3	0.0238	1.2571	-399.6589	-0.4462	0.5310	0.3102
	4	0.7963	-1.0259	-399.8011	-0.9077	0.5904	-0.6748
	5	1.5636	1.7171	-398.3312	-0.8057	-0.6263	-0.7620
	6	1.8372	-0.6001	-400.8566	0.6469	-0.0205	-0.0033
	7	0.1889	-1.2136	-398.9712	0.3897	-0.1088	0.9195
	8	-1.4455	-0.9957	-398.9851	-0.3658	0.2926	-0.3192
	9	-1.4028	0.4642	-400.4782	0.9004	0.4187	0.1705
	10	-0.9700	-0.1068	-399.7287	-0.9311	0.5094	-0.5524

Furthermore, for each simulation, the actual sphere center coordinates in the local coordinate frame were perturbed from their nominal values. Perturbations of single coordinates were randomly sampled from the nominal distributions defined by the calibration uncertainty evaluated in Section 5.3.3. In order to take into consideration rotary stage error motions, random perturbations to the sphere center coordinates as a function of rotary stage position were applied. All error motions are randomly sampled along a uniform distribution symmetrical about zero. The distribution intervals for rotary stage error motions correspond to the specification value to which each error motion is tested as indicated in the control report for a Newport RVS80CC rotary stage, employed in a Nikon 225 kV CT system. Finally, noise and blur were added using built-in MATLAB functions after simulation but prior to the center projection estimation step to resemble these effects present in real scanning tasks.

5.6.2 Error in observed center projection coordinates

The pixel coordinates assigned to each center projection deviate from the actual center projection position as a result of errors introduced by image blur, noise, rotary stage error motions, and the image processing step (explained in [143]). The magnitude of errors was evaluated as a difference between the observed center projection coordinates u_{obs} and v_{obs}, and the exact center projection coordinates u_{exact} and v_{exact} calculated by performing forward projection on the known geometrical parameters of the simulation. The errors in the estimated center projection coordinates δu_{obs} and δv_{obs} followed a normal distribution for all simulated data sets (histograms of center projection errors from Simulation 1 are shown in Figure 68 as an example). Therefore, random perturbations in the input center projection coordinates (as schematically described in Figure 67) are sampled from normal distributions with the same standard deviations as evaluated on the simulated data.

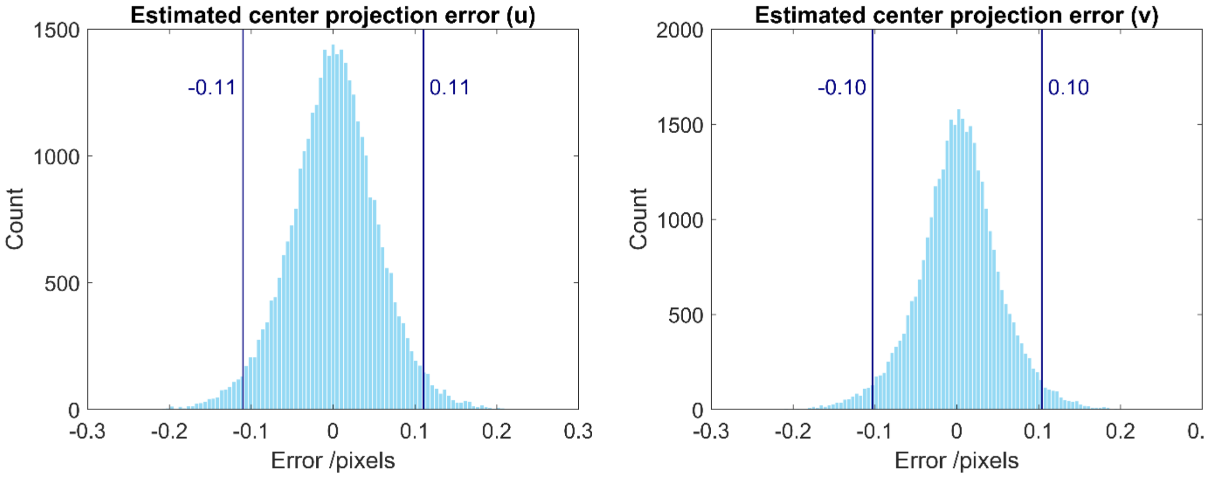

Figure 68. Histograms of errors in the estimated center projection coordinates for Simulation 1.

5.6.3 Monte Carlo calibration results

The Monte Carlo geometrical calibration by minimization was performed for all 10 simulations. In this section, simplified results are shown on the example of Simulation 1. Solved parameters as well as the deviation of the solved parameter mean from the actual value are shown in Table 27-Table 30. The nature of the statistical distributions was similar with all the simulated data sets, i.e.

the solved parameters followed a normal (Gaussian) distribution. Therefore, the results in Table 27-Table 30 are supplemented with the lower and upper error boundaries (LB and UB, respectively) corresponding to 95 % of the solved parameter values for the simulated data set. Furthermore, for better visualization of the results, deviation histograms are shown in Figure 69 for instrument geometrical parameters and Figure 70 for reference standard geometrical parameters.

Table 27. Solved instrument geometrical parameters and lower (LB) and upper (UB) boundaries for 95 % of solved data point distribution.

Solved parameters	x_D **/mm**	y_D **/mm**	z_D **/mm**	θ **/°**	φ **/°**	η **/°**	z_R **/mm**
Mean	1.2590	-1.3711	-1175.3260	-0.6751	-0.0987	-0.7867	-402.5022
LB	1.2587	-1.3726	-1175.3838	-0.6771	-0.0997	-0.7868	-402.5215
UB	1.2592	-1.3696	-1175.2730	-0.6732	-0.0978	-0.7866	-402.4844

Table 28. Solved reference standard geometrical parameters and lower (LB) and upper (UB) boundaries for 95% of solved data point distribution.

Solved parameters	x_P **/mm**	y_P **/mm**	z_P **/mm**	ρ_x **/°**	ρ_y **/°**	ρ_z **/°**
Mean	1.0051	1.3625	-400.5507	0.412208	-0.1227	-0.4479
LB	1.0049	1.3619	-400.5700	0.411984	-0.1229	-0.4481
UB	1.0053	1.3631	-400.5329	0.412436	-0.1225	-0.4477

Table 29. Mean deviation of solved instrument geometrical parameters and lower (LB) and upper (UB) boundaries for 95 % of solved data point distribution.

Deviations	x_D **/mm**	y_D **/mm**	z_D **/mm**	θ**/°**	φ**/°**	η**/°**	z_R **/mm**
Mean	-2.90E-05	-1.12E-03	1.17E-01	4.70E-04	1.71E-04	-1.40E-05	4.28E-02
LB	-2.85E-04	-2.64E-03	5.92E-02	-1.45E-03	-7.84E-04	-9.10E-05	2.35E-02
UB	2.31E-04	4.43E-04	1.70E-01	2.44E-03	1.13E-03	6.20E-05	6.06E-02

Table 30. Mean deviation of reference standard geometrical parameters and lower (LB) and upper (UB) boundaries for 95 % of solved data point distribution.

Deviations	x_P **/mm**	y_P **/mm**	z_P **/mm**	ρ_x **/°**	ρ_y **/°**	ρ_z **/°**
Mean	-2.30E-05	-3.98E-04	4.27E-02	1.08E-04	-1.55E-04	-2.00E-06
LB	-2.16E-04	-9.56E-04	2.34E-02	-1.16E-04	-3.54E-04	-2.24E-04
UB	1.67E-04	1.70E-04	6.05E-02	3.36E-04	4.70E-05	2.22E-04

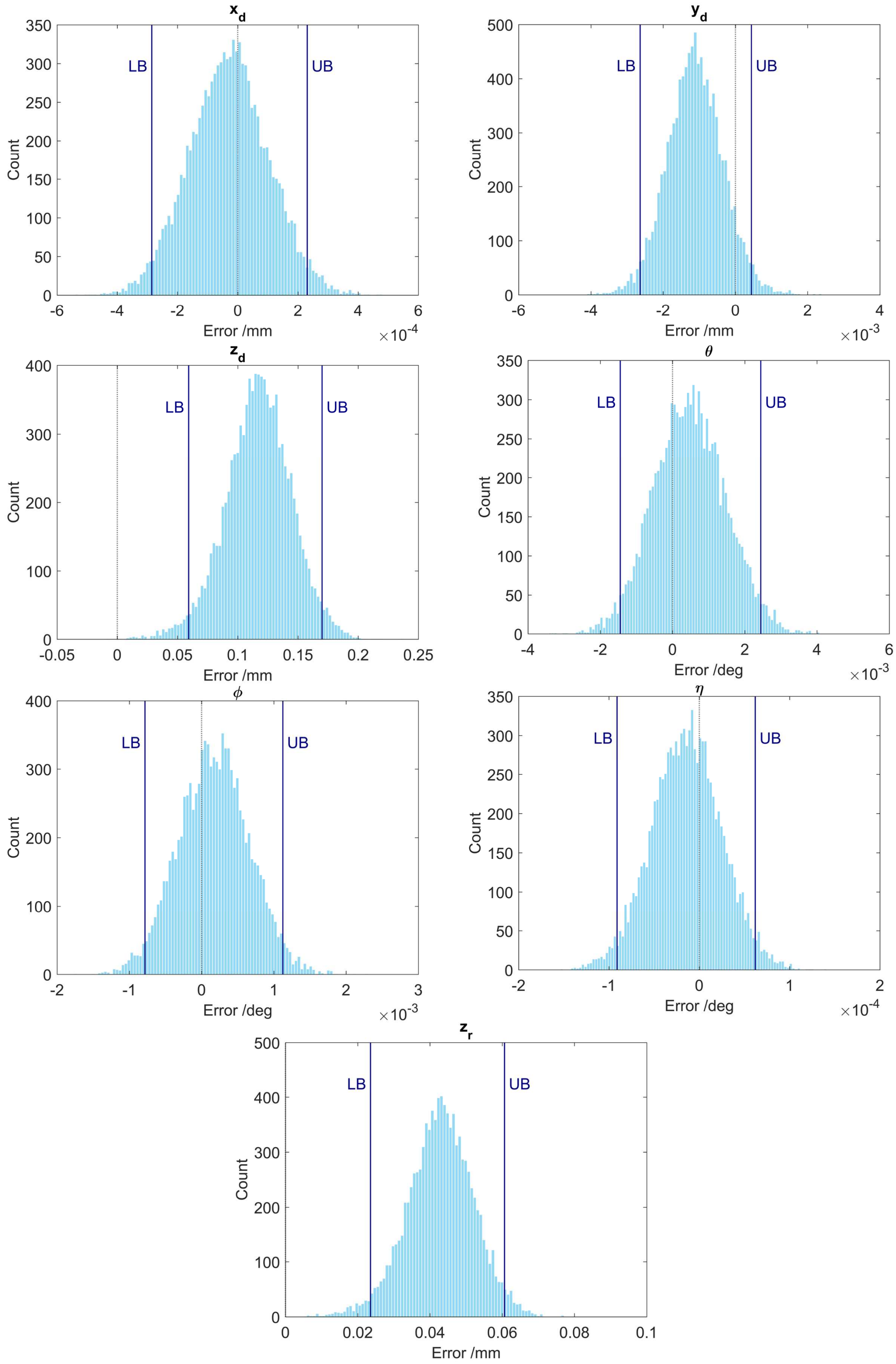

Figure 69. Distribution of solved instrument geometrical parameters from 10,000 repeated minimizations in the presence of perturbed input quantities. The dotted line corresponds to the actual simulated value for the respective parameter, while the solid lines enclose 95 % of the solved data points.

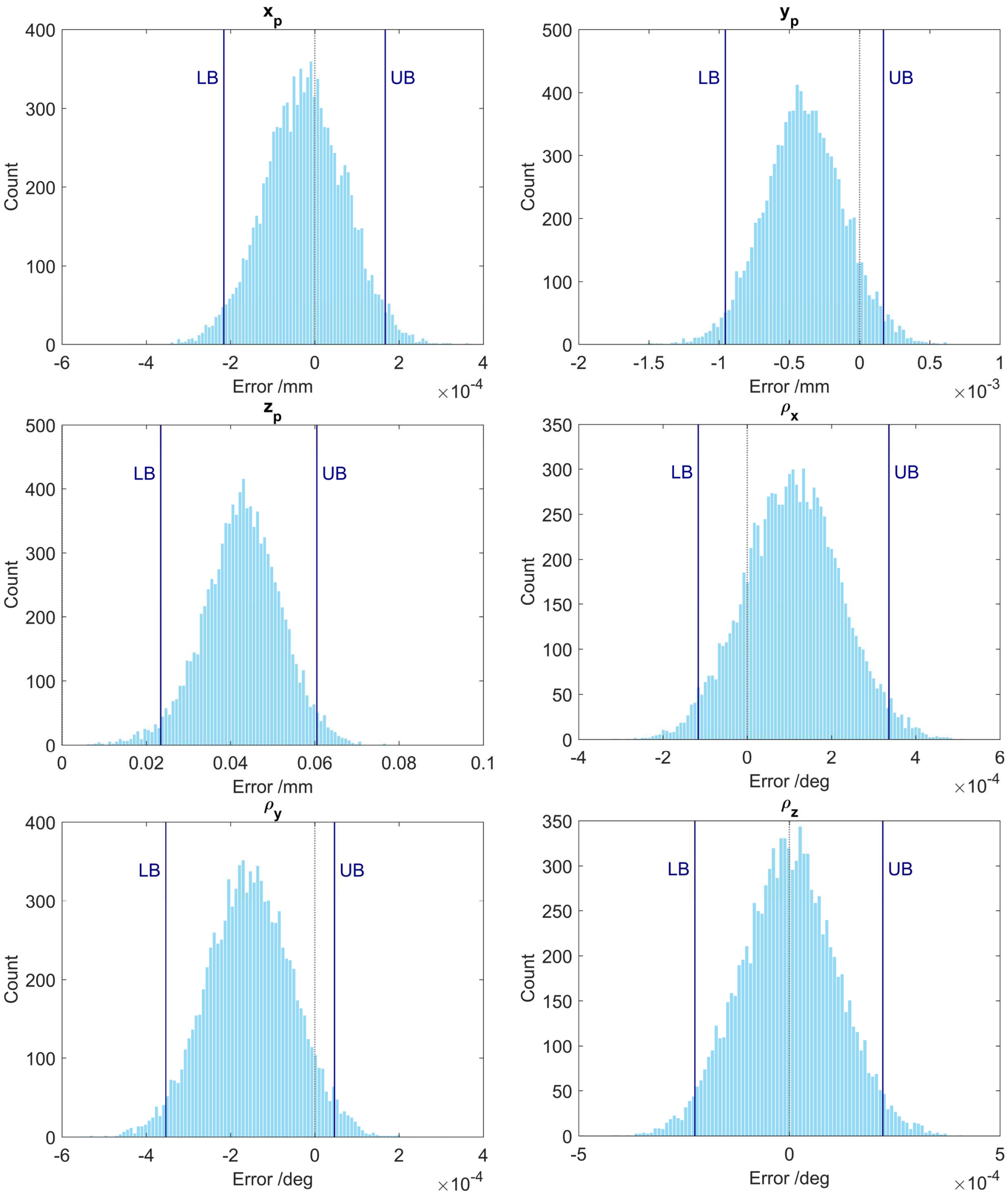

Figure 70. Distribution of solved reference standard geometrical parameters from 10,000 repeated minimizations in the presence of perturbed input quantities. The dotted line corresponds to the actual simulated value for the respective parameter, while the solid lines enclose 95 % of the solved data points.

The Monte Carlo procedure can be considered successful in calibrating the CT geometrical parameters when the actual parameter values are contained within the 95 % (k = 2) confidence interval of the solved parameter distribution. This was shown to be the case for most of the parameters, except for the *z* coordinate positions of rotary stage, reference standard, and detector. This behavior is related to the coupling between these particular parameters.

5.7 Experimental validation

In order to validate the method described in the previous sections of this chapter, experiments were performed on a custom CT system at the Centre of Excellence Telč (Telč, Czech Republic). The experimental study can be divided into two phases: (i) physical modifications to the CT system geometry, and (ii) software correction of the CT system misaligned geometry. In the first phase, preliminary tests were performed in order to analyze several practical aspects related to the acquisition of radiographic projections (i.e. the scanning method – continuous or stepped scanning) and the number of acquired projections during the 360° rotation of the object. Subsequently, several misalignments to the detector were applied and the geometrical parameters were evaluated by the minimization procedure for each of these misalignments. Finally, the CT system was physically aligned to nearly ideal geometry according to the parameters solved by the minimization. The performance of the alignment procedure was evaluated by measuring sphere center to center distances (SD) on the reconstructed volume, and comparing them to the reference values (calculated from the results obtained during the calibration explained in Section 5.3.3). In the second phase, the so-called FlexCT reconstruction algorithm (KU Leuven, Belgium) was used to reconstruct individual datasets representing different detector misalignments acquired in the first phase. The performance of FlexCT was evaluated, similarly to the first phase, based on the deviation between measured and reference SD.

5.7.1 Physical modifications of the CT system geometry

The experiments were performed at Centre of Excellence Telč (CET) using a non-metrological custom CT system. The system is shown in Figure 71; it is also called “Twinned Orthogonal Adjustable Tomograph” (TORATOM) [144] and combines two X-ray source-detector pairs in an orthogonal arrangement.

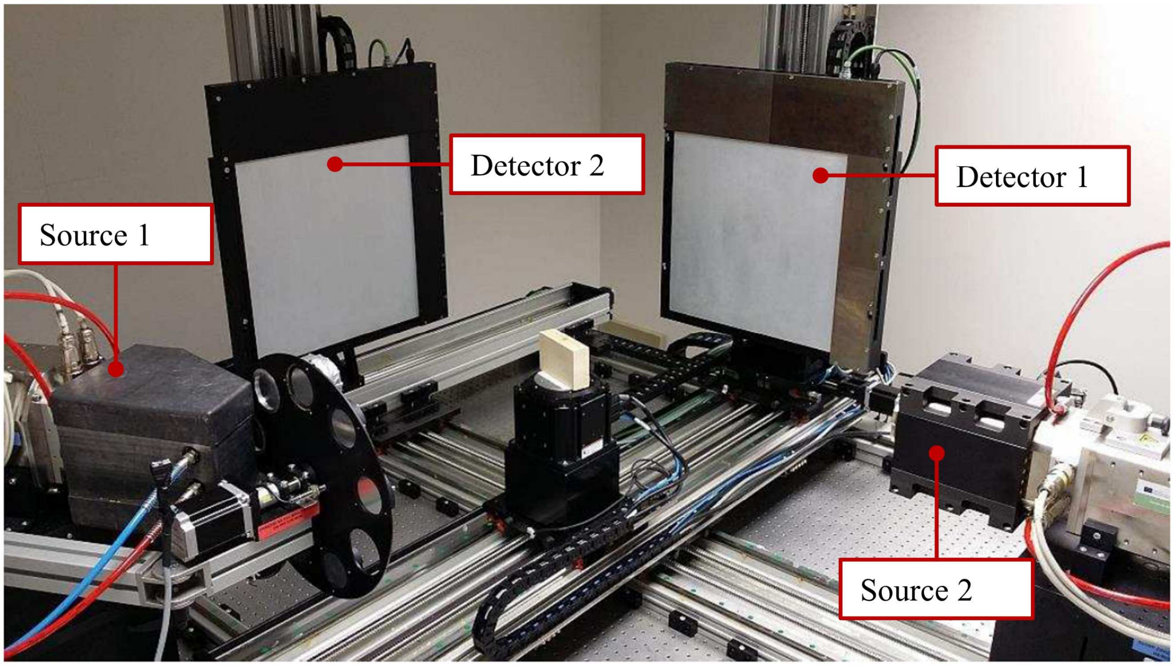

Figure 71. Twinned Orthogonal Adjustable Tomograph (TORATOM) [145].

The main parts of the assembly are arranged in two cross-oriented scanning pairs with shared rotational stage and are mounted on a complex 16-axis CNC positioning system. The scanned samples are placed on a high-precision air bearing rotary stage ABRT-150 (Aerotech, USA). The positioning of the device is performed by linear motion guides, ball screws with zero backlash and stepper motors [145].

The configuration used for the study presented in this section consists of a reflection X-ray tube XWT-240-SE (X-ray Worx, Germany) and a large area flat panel detector XRD1622 (PerkinElmer, USA) with active area 4096 × 4096 mm, resolution 2048 × 2048 px (equal to 200 µm pixel size) and minimum full-scale integration time 1000 ms.

Scanning parameters and procedure

Prior to changing the alignment of the detector, several practical considerations related to scanning parameters were evaluated: (i) X-ray source parameters (i.e. voltage and current), (ii) exposure time, (iii) number of projections, and (iv) scanning approach, i.e. continuous or stepped scanning.

In order to maximize the contrast and keep the focal spot reasonably small, 100 kV and 380 µA were selected as the values of the tube voltage and current, respectively. Since the detector allows acquiring images with a fixed integration time, i.e. 1000 ms, this value was used for scanning in this work.

An initial study was performed to evaluate the effect of the number of projections and the scanning approach on the radiographic data and minimization results. The CT^2 standard was scanned using both the continuous and stepped scanning, and three different numbers of projections, 720, 1440 and 2880, were acquired per scanning method; six scans were obtained in total. It is worth noting that since the detector acquires radiographic images continuously (i.e. one image per 1000 ms), the rotation speed of the rotary stage is inversely proportional to the number of projections. In other words, if one wants to acquire 2880 projections during 360° rotation (i.e. one projection per 0.125°), the speed must be set to 0.125 °/s, whereas it must be 0.5 °/s when acquiring 720 projections (i.e. one projection per 0.5°). Image blurring is inherent to continuous scanning since the acquisition is carried out during the continuous rotation of the sample. However, increasing the speed of rotation results in an increased blur. This effect can be observed in Figure 72 where three cropped projected spheres acquired at different rotation speeds are shown.

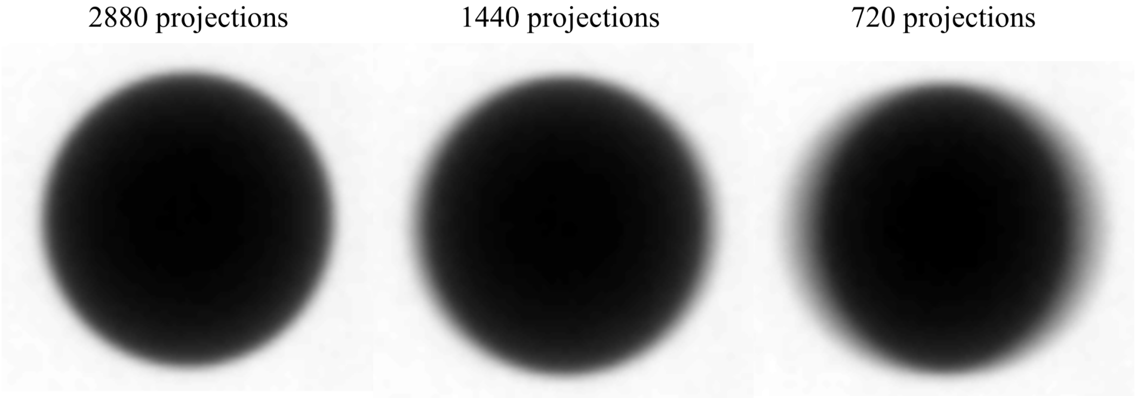

Figure 72. The effect of different number of projections (rotation speed increases from left to right) on the image blurring when scanning continuously.

Furthermore, continuous rotation resulted in clear systematic errors along the horizontal direction of center projection estimates (*u* coordinate) as demonstrated in histograms shown in Figure 73. Since this systematic behavior was not observed along the vertical direction (*v* coordinate) of center projection estimates, the errors can be attributed to the scanning strategy, i.e. continuous rotation.

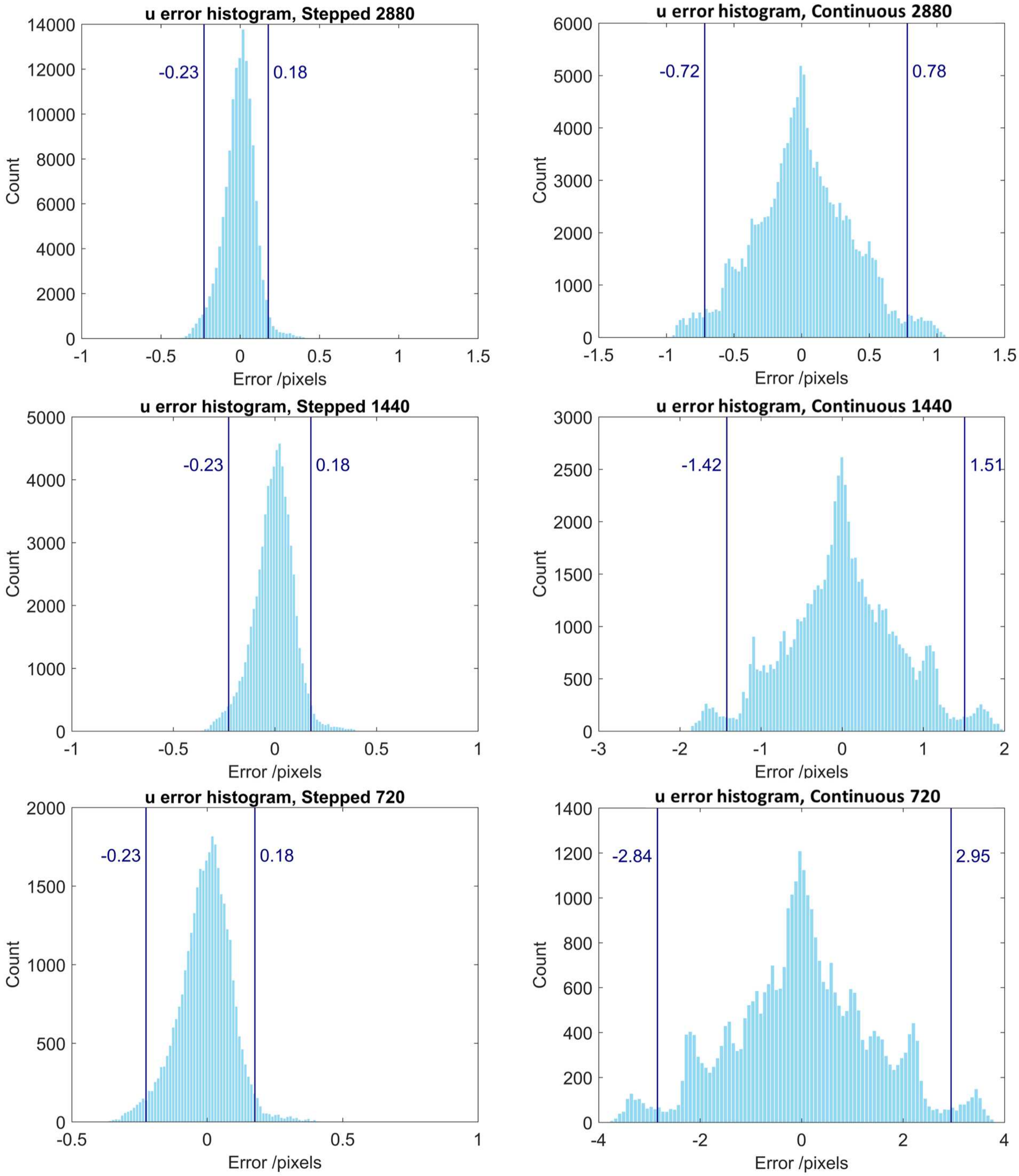

Figure 73. Histograms of errors in the estimation of sphere center projections (*u* coordinate) for different scanning strategies and number of projections.

Based on the above-mentioned observations, continuous scanning was not considered for further use. The effect of different number of projections acquired by stepped scanning was evaluated by comparing minimization results. It was found that the difference in solved parameters and residual reprojection error was very small between using 2800, 1440, and 720 radiographs (see the results in Table 31). Therefore, in order to reduce the time demands, 720 stepped radiographs were chosen as the optimized number of projections for the minimization procedure.

Table 31. Minimization results for different scanning modes and number of projections.

Mode	**#Proj.**	x_{D} **/mm**	y_{D} **/mm**	z_{D} **/mm**	z_{R} **/mm**	θ **/°**	φ **/°**	η **/°**
Stepped	720	0.048	-0.449	-1214.573	-400.964	0.240	0.071	-0.107
	1440	0.048	-0.448	-1214.593	-400.970	0.240	0.071	-0.107
	2880	0.048	-0.448	-1214.562	-400.960	0.240	0.071	-0.107
Continuous	720	0.072	-0.450	-1214.646	-400.983	0.239	0.077	-0.118
	1440	0.063	-0.455	-1214.596	-400.974	0.241	0.077	-0.113
	2880	0.073	-0.458	-1214.541	-400.955	0.241	0.074	-0.110

The summary of scanning parameters used throughout this section is presented in Table 32.

Table 32. Scanning parameters.

Parameter	**Value**
Acceleration voltage	100 kV
Tube current	380 μA
Exposure time	1000 ms
Number of projections	720 (from 0° to 359.5° in increments of 0.5°)
Scanning mode	Stepped

Modifications to the detector orientation

The computer-controlled positioning was used for placing the reference standard in the CT field of view, so that its projection covered completely the detector area, and the rotary stage was used for rotating the object during CT scanning. While the in-plane rotation of the detector (η) can be controlled by a stepper motor, the system does not have motorized units for changing the other two detector angles (φ and θ). Therefore, in order to change the slant and tilt of the detector, an alternative approach was applied; metal washers of a specific thickness were placed between the detector frame and the detector at a certain distance from the detector's pivot point to change the detector orientation by a specific angle. An example of modifying the detector orientation (angle θ) is shown in Figure 74.

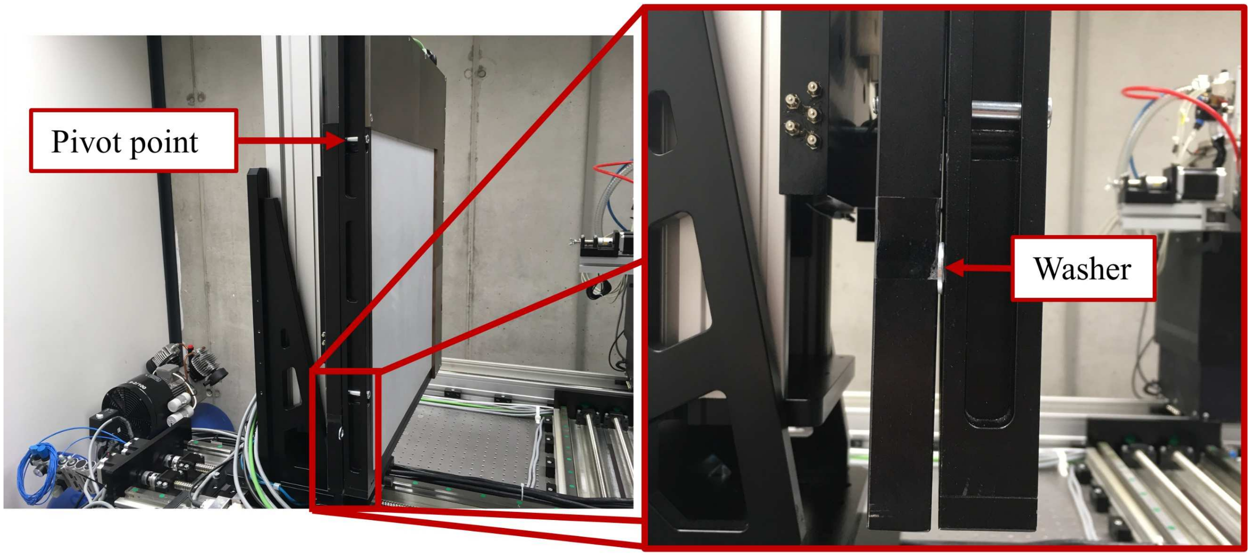

Figure 74. Modification of the detector orientation by inserting metal washers.

After placing the sample to its scanning position (i.e. the position where the projection of the CT^2 standard covers the whole detector area), a standard procedure developed by CET was applied to calculate *SRD* and *SDD*. From that point, the position of the rotary stage was kept fixed throughout the experiments in order to avoid introducing additional positioning errors. The effect of different detector misalignments, as well as the accuracy of the final physical alignment were evaluated based on measurements of SDs performed on the reconstructed datasets. In order to ensure the robustness of the evaluation and to eliminate any correlation effects, another reference standard, CT tree (see Figure 14-f), was scanned and measured in each detector orientation as well. The list and values of detector misalignments applied in this study is shown in Table 33.

Table 33. List and values of applied detector misalignments.

	Parameters		
Misalignment	***θ*/°**	***φ*/°**	***η*/°**
θ	0.1		
	-0.5		
φ		0.1	
		-0.5	
η			0.1
			-0.5
θ*+*φ	0.24	-0.5	
θ*+*η	0.24		0.5
φ*+*η		-0.5	0.24
θ*+*φ*+*η	0.24	-0.5	0.24

Single steps of the workflow applied in this experimental study are described as follows:

1) Positioning of the CT^2 standard.
2) Evaluation of *SRD* and *SDD* by the CET procedure.

3) Modification of the detector alignment.
4) Scan of the CT^2 standard.
5) Scan of the CT tree.
6) Evaluation of geometrical parameters by minimization.
7) Performing steps 3-6 for all the detector misalignments summarized in Table 33.

Furthermore, after applying different misalignments, the detector was aligned according to the parameters evaluated by the minimization. The effects of physically aligning detector will be discussed further in this section.

Evaluation of the data

The effects of various detector misalignments and reconstruction techniques, as well as the accuracy of the physical alignment, were evaluated based on the comparison of the calibrated and measured SDs obtained on the reconstructed data sets. SDs between Sphere 1 and all remaining spheres (i.e. distances between Spheres 1-3, 1-4, …, 1-49) were measured on the CT^2 standard. The reference values were obtained from the calibration presented in Section 5.3.3. On the CT tree, distances between five pairs of spheres were measured as described in [22], where also the reference values can be found.

Data sets acquired with various detector misalignments, as well as with the physically aligned system were reconstructed using VGStudio MAX. Commercial reconstruction software, including VGStudio MAX, offers the possibility to correct x_D and η, however, it fails in correcting other detector misalignments. Yet, VGStudio MAX correction of x_D and η was found unstable when reconstructing the CT tree that occupies just a small portion of the measurement volume. The effect of incorrectly calculated x_D and η values can be observed in Figure 76, where errors in SD measurements obtained from datasets acquired with detector misaligned by η = -0.5° and reconstructed with following corrections are shown: (i) CT^2 and CT tree reconstructed with corrections calculated by VG on related CT dataset (denoted as “VG corrected”), (ii) CT^2 and CT tree reconstructed without any VG correction (denoted as “without VG correction), and (iii) CT tree reconstructed with corrections calculated by VG on the CT^2 dataset (denoted as “VG corrected with CT^2 parameters”). It can be seen that while correcting the CT^2 standard reconstruction by VG, significant reduction of measurement errors can be achieved, this effect cannot be observed on the CT tree dataset. In fact, the errors on CT tree data set reconstructed using VG correction are similar to the data set not corrected at all (only the trend differs). However, when correcting the CT tree reconstruction with x_D and η values calculated on the CT^2 dataset, the measurement errors are reduced to the same magnitude as in the CT^2 standard case. Since the correction of reconstruction by VG was proved unreliable, no software corrections were applied to the datasets discussed further in this section.

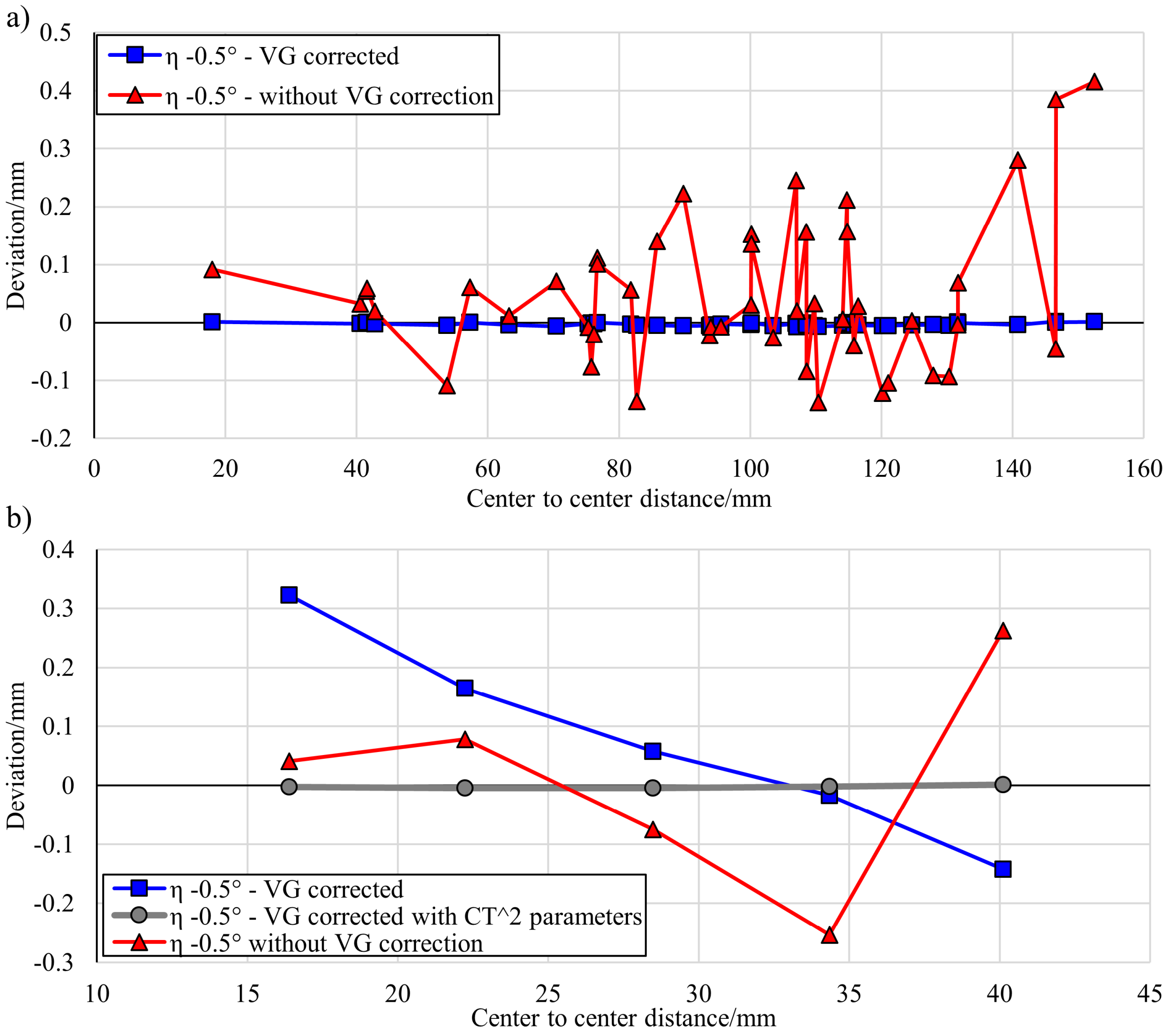

Figure 75. Comparison of the effects of correcting the reconstruction by VGStudio MAX: a) results obtained on CT^2, b) results obtained on CT tree. Reconstructions with corrections calculated by VG on related CT dataset are denoted as “VG corrected”, reconstructions without any VG correction are denoted as “without VG correction, and CT tree reconstructions with corrections calculated by VG on CT^2 dataset are denoted as “VG corrected with CT^2 parameters”.

The data sets were reconstructed using VS calculated according to the CET standard procedure, and based on the z_R and z_D parameters evaluated by minimization procedure. Clear systematic behavior was observed in data with CET calculated VS indicating scale errors. This effect was observed in all data sets acquired at different detector orientations; an example of results obtained both on the CT^2 standard and the CT tree using the two different voxel sizes with the system in its original alignment (i.e. before applying any modifications to the detector position and orientation) is shown in Figure 76. The results in Figure 76 show that by using minimization evaluated VS, scaling errors can be corrected as the increasing trend of errors observed in the data with CET calculated VS was eliminated.

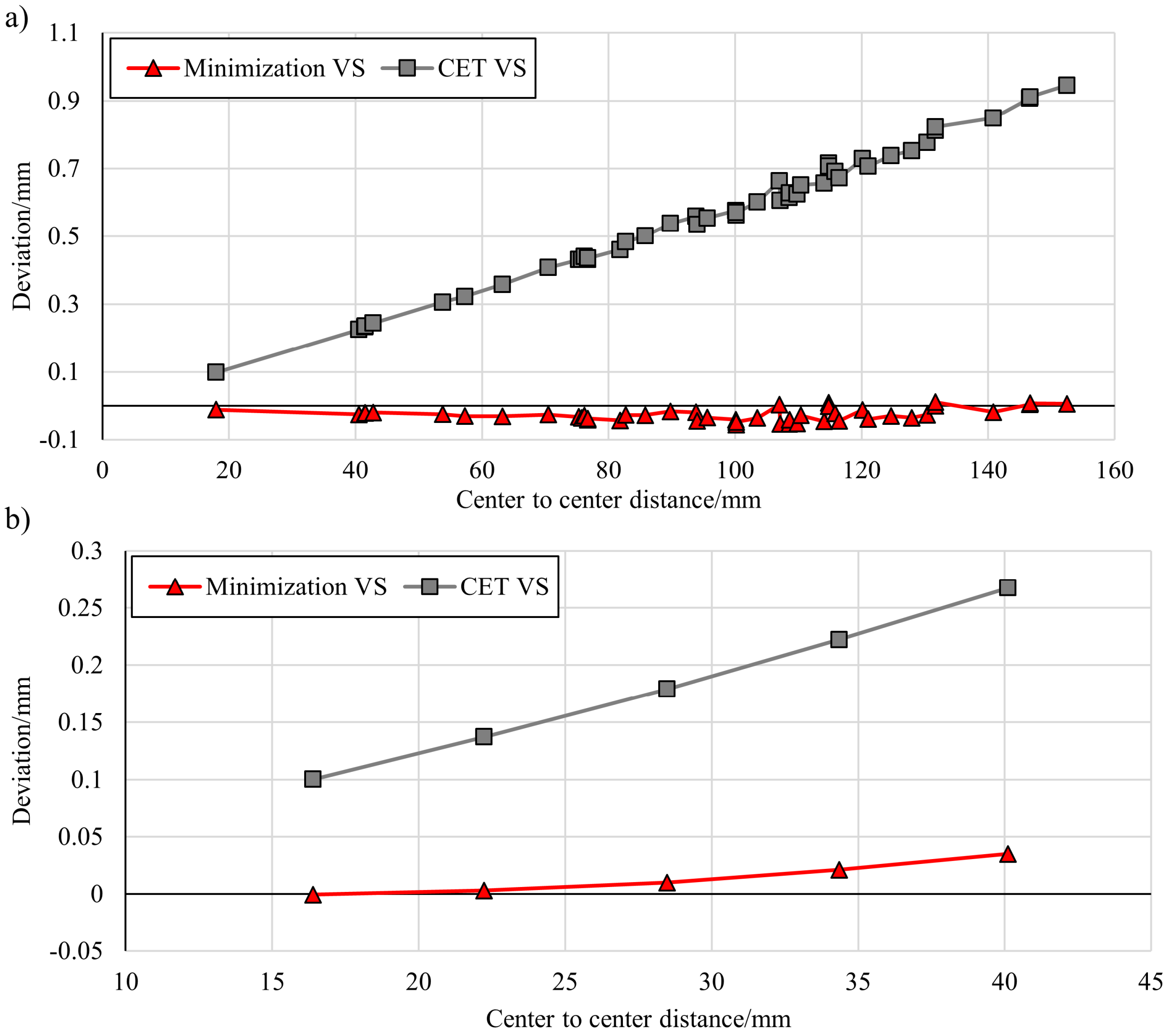

Figure 76. The effect of different VS: a) results obtained on the CT^2 standard, b) results obtained on the CT tree.

After applying various misalignments to the detector, an attempt to align the CT system to its ideal geometry was performed. The procedure involved several iterative steps; in each of the steps, the orientation and position of the detector was modified according to the minimization procedure results. After each modification of the detector alignment, the CT^2 standard was scanned again, and the CT system geometry was solved by minimization to evaluate the residual errors, and to iteratively minimize the misalignments of the geometry. The final geometrical parameters of the "physically aligned" system are shown in Table 34.

Table 34. Geometrical parameters of the "physically aligned" system.

x_D /mm	y_D /mm	z_D /mm	θ/°	φ/°	η/°
0.0276	0.0388	-1211.2929	0.0175	-0.0142	-0.0106

It can be seen that it was possible to align the system to nearly ideal geometry as the angular detector misalignments are below 0.02° and the x and y detector position is misaligned from zero by 0.03 and 0.04 mm, respectively. The effect of physically aligning the CT system can be observed on the significant reduction of SD measurement errors shown in Figure 77 for both the

CT^2 standard and the CT tree. The charts in Figure 77 show the comparison of the CT system in its original alignment and physically aligned CT system according to the minimization procedure.

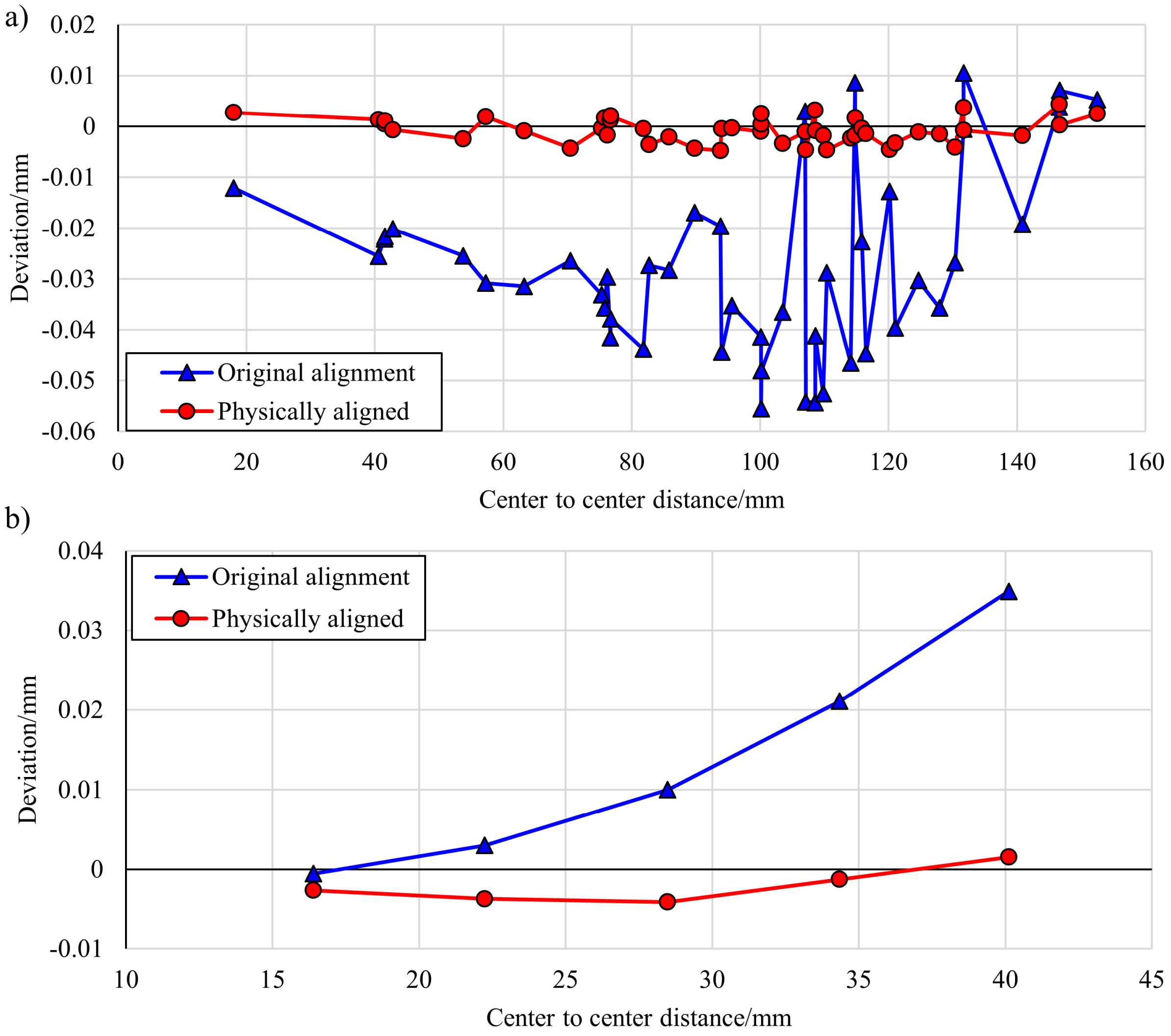

Figure 77. Comparison of SD measurement errors obtained on physically and originally aligned CT system: a) CT^2 standard results, b) CT tree results.

The average absolute errors calculated over all measured SDs on the physically aligned system was 2 µm for both the CT^2 and CT tree standards.

It was possible to minimize the sphere center to center measurement errors by physically aligning the CT system geometry. This proves not only that the minimization was solving the CT instrument geometry correctly, but also the ability to change the alignment of the detector in a controlled way. The ability to control the alignment of the detector is also demonstrated by the results presented in Table 35, where relative errors between the rotation that was applied to the detector and the difference in the related angular parameter calculated by minimization are shown. The highest errors are below 0.025°, which shows good fit between the desired and actual change of the detector alignment.

Table 35. Rotations applied to the detector and changes in the related angular parameter calculated by minimization together with the relative error.

Misalignment	Applied rotation/°	Calculated rotation/°	Relative error/°
θ	0.1	0.1231	**0.0231**
	-0.5	-0.4943	**0.0057**
φ	0.1	0.1082	**0.0082**
	-0.5	-0.4867	**0.0133**
η	0.1	0.0989	**-0.0011**
	-0.5	-0.5004	**-0.0004**
θ/φ	0.24/-0.5	0.2167/-0.4785	**-0.0233/0.0215**
θ/η	0.24/0.5	0.2433/0.4985	**0.0033/-0.0015**
φ/η	-0.5/0.24	-0.4894/0.2463	**0.0106/0.0063**
$\theta/\varphi/\eta$	0.24/-0.5/0.24	0.2172/-0.4784/0.2318	**-0.0228/0.0216/-0.0082**

5.7.2 Software correction of the CT system misaligned geometry

In order to evaluate whether the procedure proposed here can capture the detector misalignments defined in Table 33, the datasets were reconstructed by an advanced reconstruction algorithm, so called “FlexCT” (developed by Evelina Ametova, KU Leuven, Belgium). FlexCT[2] is a modified FDK algorithm adapted to work with misaligned CT systems. The algorithm uses the geometrical parameters evaluated by the minimization procedure for redefining both the preprocessing of radiographs and the imaging geometry in the back-projection step to correct the reconstruction.

After reconstructing individual data sets by FlexCT, sphere center to center distances were subsequently measured on the reconstructed volumes and compared to the reference. Since it was proved in Section 5.7.1 that the results obtained on CT tree follow the same trends as those obtained on the CT^2 standard, and this applies also to FlexCT reconstructed results, only results obtained on the CT^2 standard will be discussed in this section.

Results in Figure 78 show the comparison of SD measurement errors obtained on the VG reconstructed datasets (without any correction) and FlexCT reconstructed datasets. An individual chart was constructed for each detector misalignment.

---

[2] FlexCT was developed by Evelina Ametova from KU Leuven, therefore, the principle of the algorithm is not explained in this Ph.D. thesis in detail.

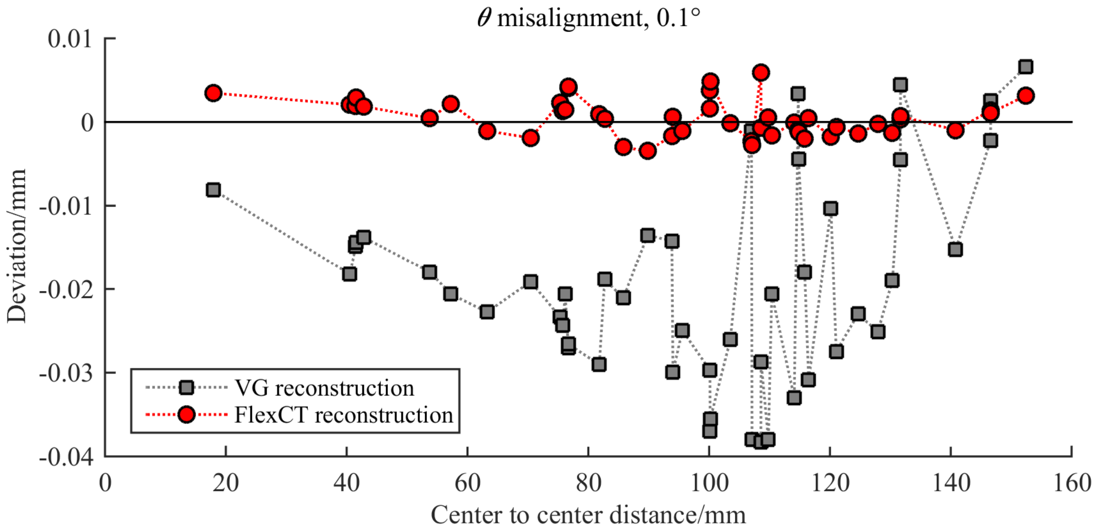
θ misalignment, 0.1°
Deviation/mm
0.01
0
-0.01
-0.02
-0.03
-0.04
0
20
40
60
80
100
120
140
160
Center to center distance/mm
VG reconstruction
FlexCT reconstruction

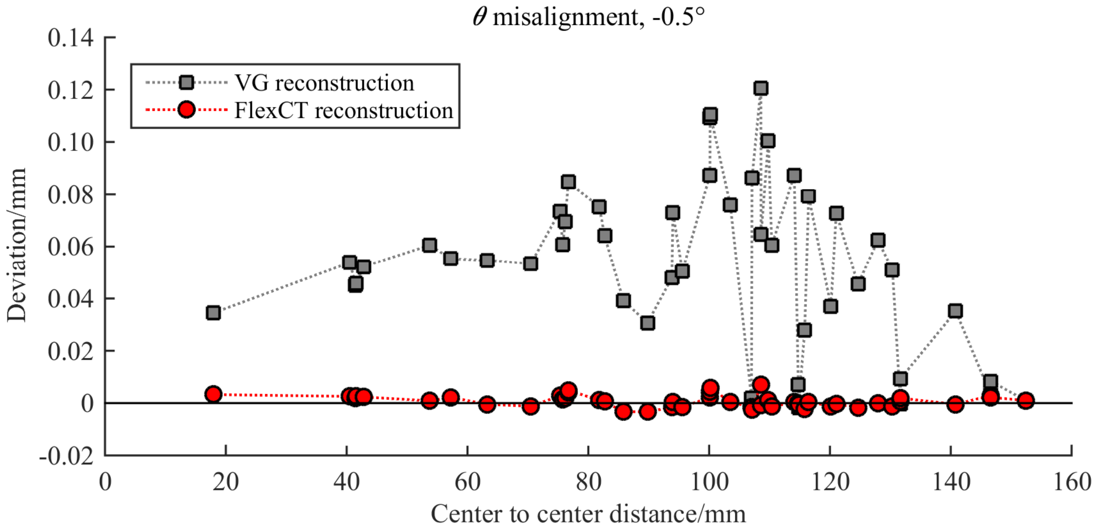
θ misalignment, -0.5°
Deviation/mm
0.14
0.12
0.10
0.08
0.06
0.04
0.02
0
-0.02
0
20
40
60
80
100
120
140
160
Center to center distance/mm
VG reconstruction
FlexCT reconstruction

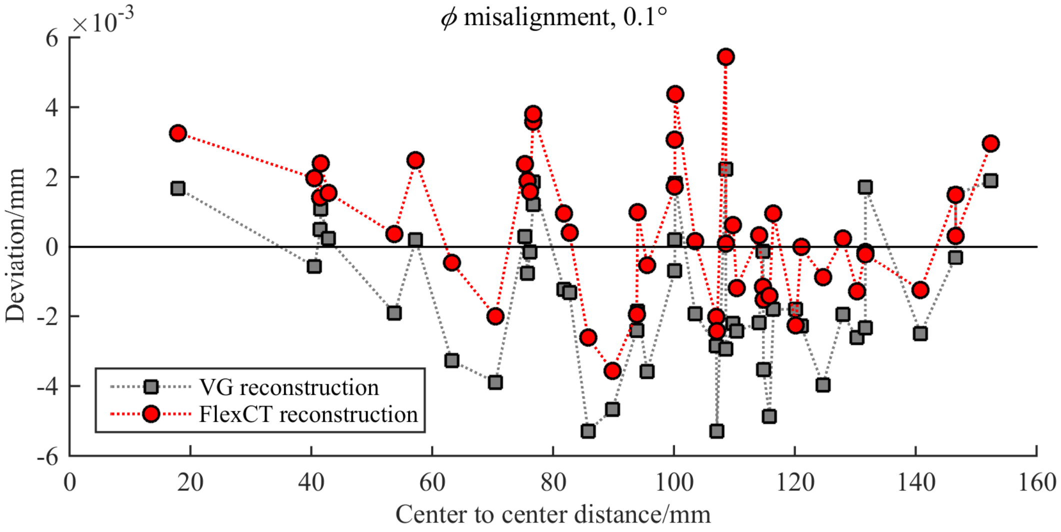
×10^-3
ϕ misalignment, 0.1°
Deviation/mm
6
4
2
0
-2
-4
-6
0
20
40
60
80
100
120
140
160
Center to center distance/mm
VG reconstruction
FlexCT reconstruction

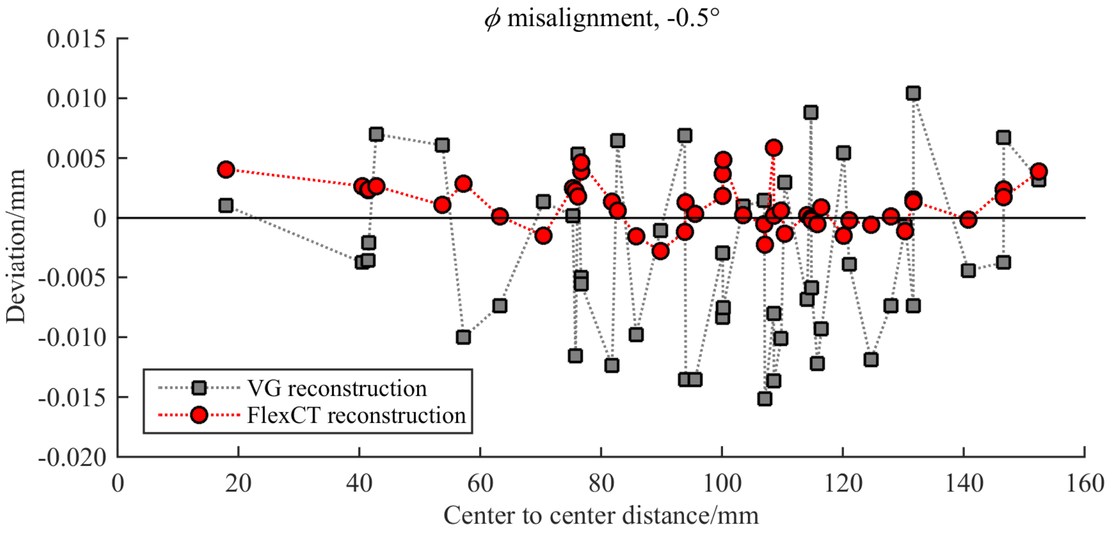
ϕ misalignment, -0.5°
Deviation/mm
0.015
0.010
0.005
0
-0.005
-0.010
-0.015
-0.020
VG reconstruction
FlexCT reconstruction
0
20
40
60
80
100
120
140
160
Center to center distance/mm

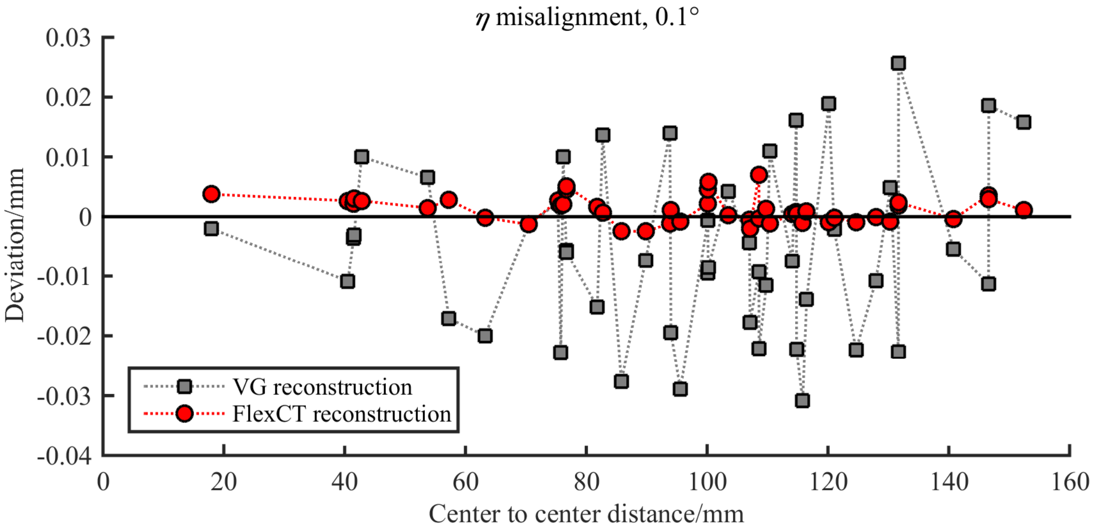
η misalignment, 0.1°
Deviation/mm
0.03
0.02
0.01
0
-0.01
-0.02
-0.03
-0.04
VG reconstruction
FlexCT reconstruction
0
20
40
60
80
100
120
140
160
Center to center distance/mm

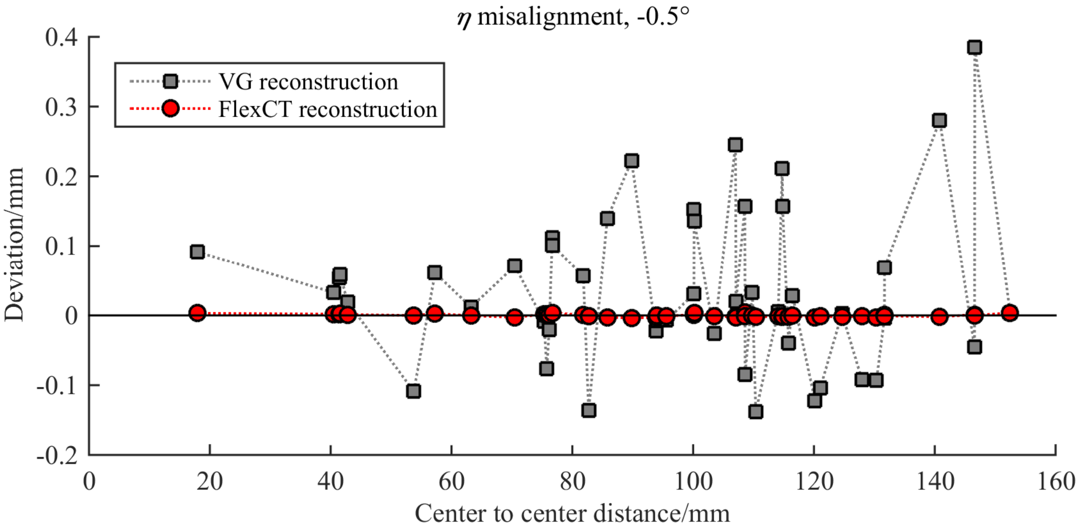
η misalignment, -0.5°
Deviation/mm
0.4
0.3
0.2
0.1
0
-0.1
-0.2
VG reconstruction
FlexCT reconstruction
0
20
40
60
80
100
120
140
160
Center to center distance/mm

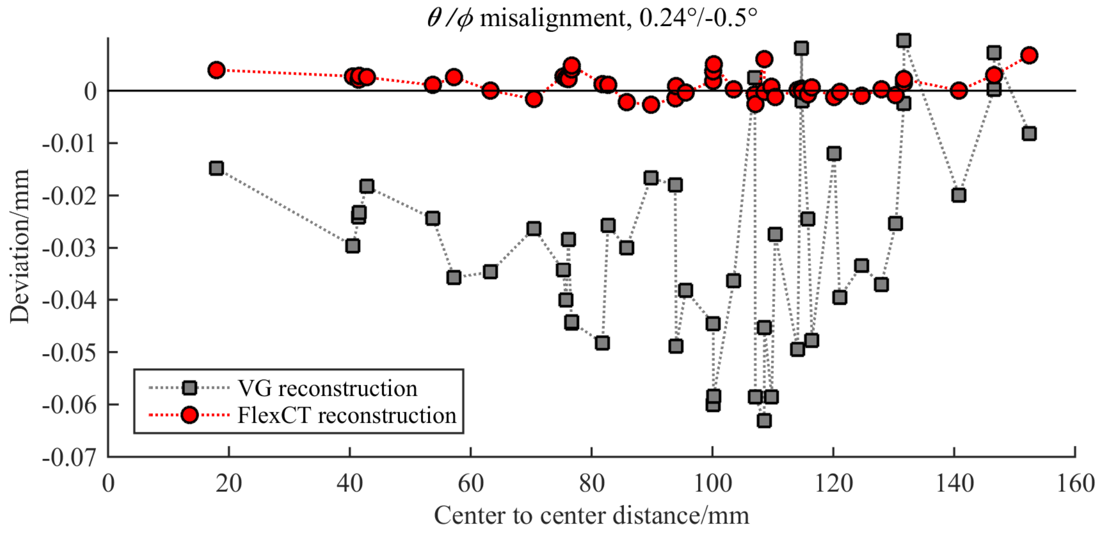
θ / ϕ misalignment, 0.24°/-0.5°
Deviation/mm
0
-0.01
-0.02
-0.03
-0.04
-0.05
-0.06
-0.07
VG reconstruction
FlexCT reconstruction
0
20
40
60
80
100
120
140
160
Center to center distance/mm

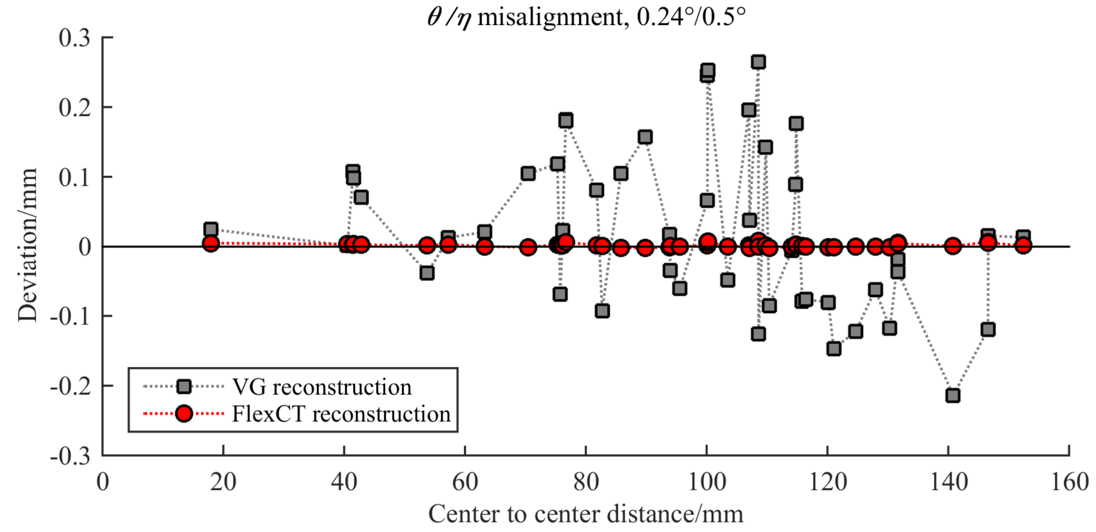
θ / η misalignment, 0.24°/0.5°
Deviation/mm
0.3
0.2
0.1
0
-0.1
-0.2
-0.3
VG reconstruction
FlexCT reconstruction
0
20
40
60
80
100
120
140
160
Center to center distance/mm

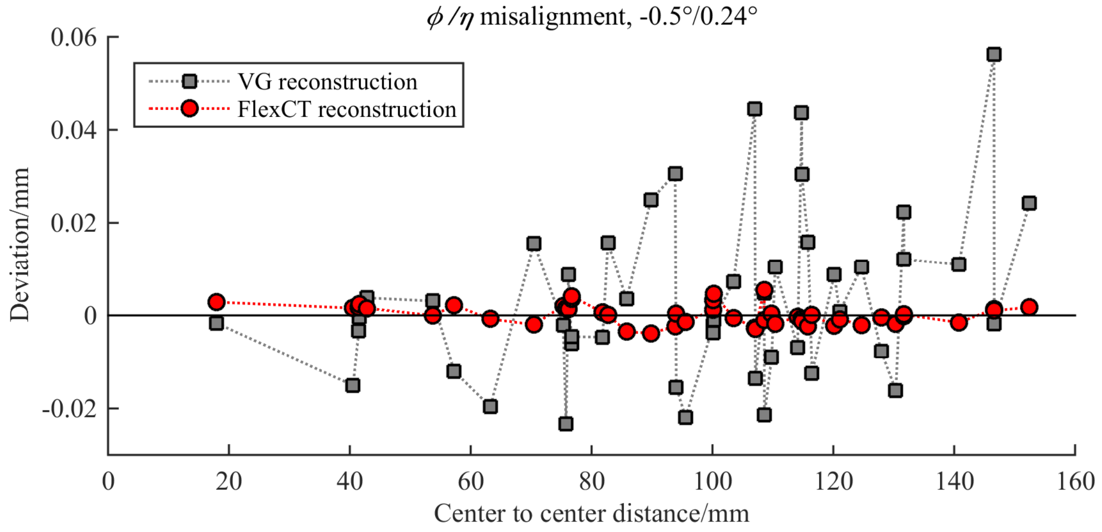
ϕ / η misalignment, -0.5°/0.24°
Deviation/mm
0.06
0.04
0.02
0
-0.02
VG reconstruction
FlexCT reconstruction
0
20
40
60
80
100
120
140
160
Center to center distance/mm

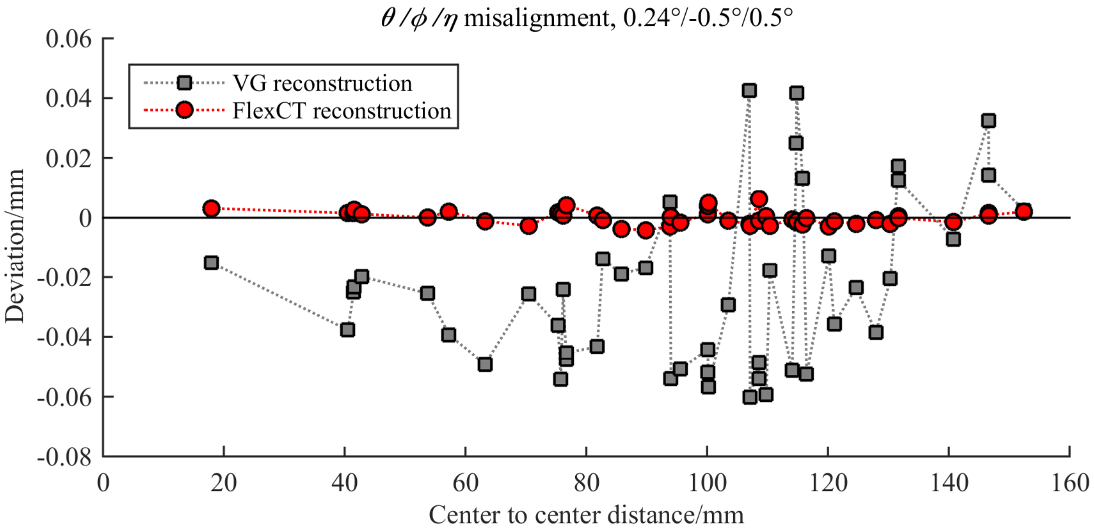

Figure 78. SD measurement errors obtained on VG and FlexCT reconstructed datasets with different detector misalignments.

The results in Figure 78 show that independently from the misaligned angle and the magnitude of the applied rotation, SD measurement errors obtained on the data sets reconstructed by FlexCT were systematically lower than those reconstructed by VGStudio MAX. It is worth noting that measurement errors were kept within ± 5 µm (except for a few outliers). This confirms the excellent performance of the minimization procedure in combination with the advanced reconstruction algorithm FlexCT. Additional results that represent the comparison of the two different ways to align the CT system geometry described in this chapter, i.e. the physical and software alignment, are shown in Figure 79; SD measurement errors obtained on the physically aligned dataset are plotted against the FlexCT reconstructed data set (the data set acquired with the originally aligned system was chosen for the comparison).

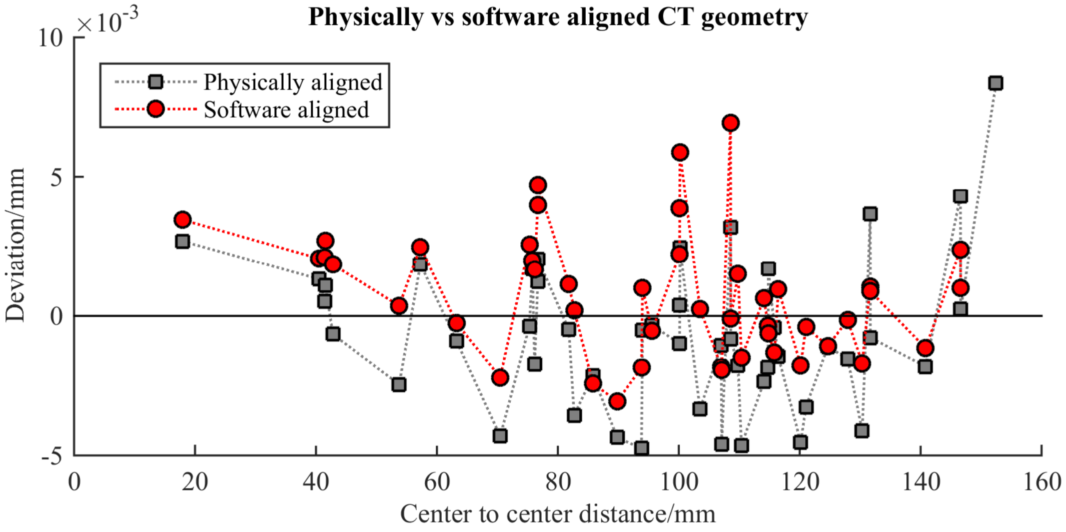

Figure 79. Comparison of the physical and software CT system geometry alignment.

It can be seen from the results that by applying both alignment methods, the SD measurement errors can be significantly reduced. More specifically, the absolute average error calculated over all SDs was equal to 2.1 µm and 1.8 µm for the physical and software alignment, respectively; i.e. by applying the FlexCT reconstruction, slightly lower measurement errors can be achieved.

The outputs of the study presented in this chapter demonstrate that the procedure proposed here outperforms commercial reconstruction software that can typically correct only x_D and η detector misalignments; it was proved that the method proposed in this study can be applied for aligning the complete CT system geometry. Furthermore, the evaluation of CT geometrical parameters by minimization and using the CT^2 standard is, unlike typical commercial software used for correcting detector misalignments, robust and is not affected by dimensions of the scanned object. The complete set of tools presented in this chapter (i.e. the CT^2 standard, the minimization procedure and FlexCT) can be used for a holistic alignment of CT system geometry. A "rough" alignment can be carried out by physically aligning the system applying the iterative procedure explained in Section 5.7.1 in a first step. In a second step, FlexCT algorithm together with residual misalignments calculated by minimization can be used for a "fine" correction of the reconstructed volume. Furthermore, the calibration of CT system geometry as per VIM [6] definition can be achieved by applying the Monte Carlo method proposed in Section 5.6

5.8 Conclusions

An optimized reference standard (CT^2) for the calibration of CT system geometry was developed in this study. The object is composed of 49 steel spheres mounted on a carbon fiber cylinder. The spheres are distributed in four helical trajectories offset by 90° from each other about the cylinder axis, and two circular trajectories at the upper and lower extremes of the cylinder. The design of CT^2 is optimized with respect to state-of-the-art equivalents and adapted for both static (i.e. projections are acquired in one angular position of the object) and dynamic (i.e. projections are acquired in multiple angular position of the object) use. The optimized arrangement of spheres provides improved distribution of projected markers on radiographic images when compared to the state-of-the-art standard. Furthermore, the number of overlapping sphere projections was reduced by almost 30 %; further reduction of overlaps (theoretically to zero) would result in reduction of data points (i.e. spheres and/or radiographic positions), and thus was not considered in this work.

The standard was calibrated by a tactile CMM. The calibration procedure is based on a standard method for calibration of ball and hole plates developed by German Calibration Service (DKD). The procedure is divided into three sequential steps: (i) evaluation of the contribution of the rotary axis error motions to measurement errors by applying reversal methods, (ii) measurement of all sphere center coordinates using the same reversal patterns, and (iii) measurement traceability transfer through a reference standard (ball bar) measured in reversal sequence and at various orientations. The robust calibration procedure ensures that the calibration uncertainty is sufficiently low that its contribution to the uncertainty of estimated geometrical parameters is minimized.

A method for solving CT system geometry by minimization was developed in a collaborative work with KU Leuven. The method is based on determining geometrical parameters by minimizing the difference between observed and modelled projection data of the reference standard, so called reprojection error. Practical considerations are provided in [143] for the analysis of radiographic data and for the robust implementation of the minimization technique. Furthermore, to satisfy the requirements given by the definition of the term “calibration” as per VIM [6], a Monte-Carlo approach was implemented to assess uncertainty in the measured geometrical parameters.

The Monte Carlo procedure was successful in calibrating most of the parameters, except for the z coordinate positions of the rotary stage, reference standard and detector. This behavior is related to the coupling between these particular parameters.

The performance of the proposed reference standard was evaluated on simulated datasets and the results were compared to the same results using the state-of-the-art equivalent. Scans of CT^2 with the presence of misalignments of three detector angles were simulated. The CT geometrical parameters were estimated by the minimization procedure. The results show strong agreement between simulated (nominal) and minimized geometrical parameters; most of the parameters were estimated with deviation lower than 1 % from nominal. Furthermore, six out of seven solved geometrical parameters using CT^2 were estimated with lower deviations compared to the state-of-the-art equivalent. Similarly, the reprojection error per data point was consistently lower for the CT^2, which ensures robust estimation of geometrical parameters. The improvement in reprojection errors, together with the reduction of projected sphere overlaps, are important aspects for the experimental implementation of CT^2 for geometrical calibration of CT systems.

In order to validate the method described in this chapter, experiments were performed on a custom CT system in two phases: (i) physical modifications to the CT system geometry, and (ii) software correction of the CT system misaligned geometry. In the first phase, practical aspects, such as the scanning parameters and the scanning method were discussed. Subsequently, several misalignments were applied to the detector and the geometrical parameters were evaluated by the minimization procedure for each of these misalignments. Finally, the CT system geometry was physically aligned to its nearly ideal geometry. The performance of the alignment procedure was evaluated by measuring sphere center to center distances (SDs) on the reconstructed volume, and comparing them to the reference values. Several observations were made based on the results: (i) typical commercial reconstruction software can correct the horizontal detector offset and the detector in-plane rotation error, and fails in correcting geometrical misalignments. Furthermore, the correction method was proved unstable especially for the CT tree (i.e. a standard, projection of which covers a small portion of the detector area). On the contrary, the method proposed here is independent from the scanned object geometry and dimensions; (ii) the standard procedure for calculating the voxel size applied by the CT system owner resulted in systematic errors of SD measurements, whereas the procedure proposed here was able to correct these errors; (iii) it was possible to align the CT system to its nearly ideal geometry, which was validated by significantly reducing SD measurement errors. Furthermore, different modifications were applied to the detector orientation. Subsequent evaluation of the effects by evaluating the geometrical parameters of the CT system with modified alignment proved that the modifications to the CT system alignment were applied in a controlled way; i.e. the applied misalignment was in agreement with the misalignment calculated after the minimization procedure. As a result, it was proven that by the proposed procedure it is possible not only to align the CT system, but also to control various modifications of its geometry.

In the second phase, the so-called FlexCT algorithm was used for software-based correction of reconstructions of individual datasets representing different detector misalignments acquired in the first phase. The performance of FlexCT was, similarly to the first phase, evaluated based on the evaluation of SD measurement errors. The results from the second phase show that by reconstructing the data sets by FlexCT, SD measurement errors were reduced with respect to those reconstructed by VGStudio MAX independently from the misaligned angle and the magnitude of the applied rotation; the errors stayed within ± 5 µm (except for a few outliers), which confirms excellent performance of the minimization procedure in combination with the FlexCT reconstruction.

The outputs of the comparison between physical and software alignments showed that the software one results in slightly lower SD measurement errors. Given this fact, a holistic CT system geometry alignment procedure – using the complete set of tools presented in this chapter (i.e. the CT^2 standard, the minimization procedure and FlexCT) – was proposed: an iterative physical “rough” alignment is made in the first step, and the FlexCT algorithm along with residual misalignments calculated by minimization are used for the “fine” correction of the reconstructed volume.

6 MULTI-MATERIAL GAP MEASUREMENTS

Multi-material aspects are an important factor influencing CT dimensional measurements. However, methods described in international standards and guidelines [27,30] typically account for mono-material effects only. Furthermore, the reference standards, use of which is suggested by the cited standards and guidelines, are mono-material as well. Recent publications [60,67,68] deal with CT multi-material effects and suggest several multi-material reference standards. In this chapter, a set of multi-material reference standards for gap measurements is developed. After describing possible multi-material scenarios that can occur in typical CT measurement tasks, the focus on the multi-material gap measurements is explained. Subsequently, design, manufacturing and calibration of the standards are described and an experimental study is presented. The experimental results are then discussed. Finally, a dual-energy CT method is applied for possible improvement of multi-material gap measurement results, and its benefits and shortfalls are explained.

6.1 Introduction to multi-material measurements

Metrological performance verification is one of the important steps towards recognizing a novel measurement technique a reliable instrument for dimensional metrology. A common way to assess the performance of a CMS is through well-defined reference standards. Several reference standards [2,7,8,22,55] have been developed and used by the CT metrology research community and industry. Many of these objects were inspired by the reference standards used by traditional CMSs. The measurands are frequently unidirectional point-to-point distances, e.g. sphere center to center distances that are not affected by the surface determination (threshold value) process, and partially beam hardening effects, which are material dependent. Yet material influence on CT measurements is one of the key aspects of CT dimensional metrology. Several investigations have been performed and a number of objects have been developed in this field; the so-called “cactus step-gauge” [58] (Figure 16-a), for example, was used to investigate material-dependent thresholding and the effects of material thickness. The authors of [146] used hole plates (Figure 15-d) and step cylinders (Figure 18-b) to investigate material influences in dimensional CT. Furthermore, step cylinders can also be used for the evaluation of material-specific attenuation and penetration thickness [2]. The above-mentioned publications, however, accounted for the material influences in mono-material samples. In fact, the possibility of performing measurements over different materials is of increasing importance due to the appropriate applications in the dimensional control of multi-material assemblies and multi-material components (e.g. molded polymer parts with metallic inserts).

To date, procedures available for metrological performance verification of CT systems defined in VDI/VDE 2630-1.3 [27] and in the committee draft of ISO 10360-11 [30] account for single material effects and suggest using reference standards composed of one material. However, as discussed in Section 3.4.1, CT multi-material measurements bring new effects that need to be considered. As a result, several recent publications deal with defining a multi-material probing

[67] and length measurement [68] error test for the acceptance testing of dimensional CT systems, and for inspecting the influence of the multi-material aspect on CT measurement results [60].

There are several specific scenarios that occur in multi-material measurement tasks (on overview is shown in Figure 80), possibly creating new measurement errors in comparison to the mono-material case. Furthermore, as the mono-material measurements are the most researched case, they are presented here as well to provide a complete overview:

- The measured features in a mono-material scenario are defined within a single material over an air/material interface. For instance, this type of measurement is represented in industry by measurements of the pitch between holes. Several objects were proposed for investigating the mono/material effects, e.g. the "cactus step-gauge" presented in [58] or the hole plates used in [146].
- Inter-material measurements are defined as measurements carried out over an interface of two and more materials. A typical case of an inter-material scenario is the dimensional control of multi-material assembly.
- The measurands in the case of in-material measurements are defined within the base material with the presence of other material(s) that disturb(s) the measurement task. This configuration is typical, for example, of the quality control of electric plugs in the automotive industry, where metal pins are over molded by plastic (base) material.
- Finally, the gap scenario shown is defined as the measurement of a distance between two different parts over a gap filled either with air, liquid or vacuum. A real case of this kind of measurement can be found, for instance, in the verification of fitting tolerances, where a tolerance with clearance may be required.

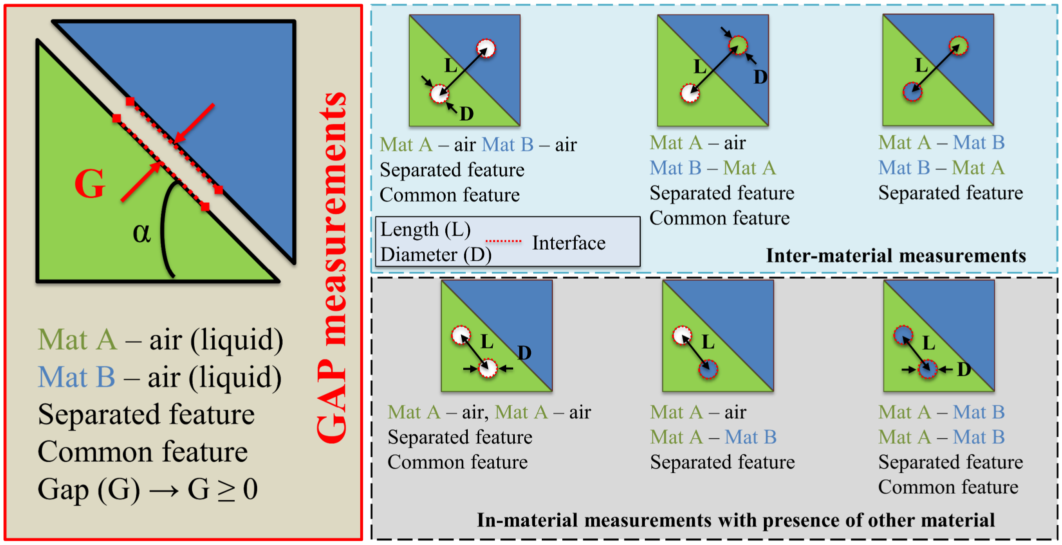

Figure 80. Diagram of possible multi-material measurement scenarios (courtesy of PTB).

In order to thoroughly investigate single effects of each scenario, it is necessary to isolate different configurations (or at least group them in several sub-groups) and analyze them individually. As a general approach, it was decided to proceed systematically from the cases that are most frequent in industry. While multi-material scenarios including inter-material, in-material and mono-material measurements for testing length measurement errors (*E*-test) and probing error tests (*P*-test) are addressed in recent publications [67,68], this chapter is aimed at the multi-material gap case. More specifically, the configurations with micro-gaps that tackle the CT limits are discussed here.

Two of the critical steps of multi-material measurements performed on CT data are proper surface determination and the separation of different materials. Several methods are described in the relevant literature [60,62,147–150]. Thus, in this work, several approaches of surface determination and data segmentation were adapted and applied to evaluate the acquired datasets in order to gain a comprehensive overview of measurement errors and CT performance in multi-material gap measurements.

6.2 Multi-material gap test for CT

Computed tomography measurements in general are affected by various influencing factors (discussed e.g. in [15] and Section 3.3). One of the critical aspects, in terms of measurement errors, is the structural resolution that, according to [16], describes the size of the smallest structure that can still be measured dimensionally; i.e. the smallest measurable gap between two materials in the present case. The aim of the multi-material gap test described in this chapter is to investigate the limits of CT in gap measurements and to analyze the multi-material influence on the measurement results.

A typical way to test the performance of a CT system is through a well-defined reference standard. In order to address the specific case discussed in this chapter, the following requirements for the reference standard were defined:

1) Material requirements:
    a. The selected materials should represent different multi-material scenarios in terms of different attenuation coefficient ratios; i.e. at least one material pairing should represent the case of two materials with close attenuation coefficients and one should represent the case of materials with rather different attenuation coefficients.
    b. The materials should be chosen with respect to sufficient dimensional stability and a low coefficient of thermal expansion (CTE), if possible.
    c. The attenuation coefficients of the selected materials should be adequate for common CT systems in terms of penetrability of the workpieces by X-rays.
    d. The materials should ensure simple and precise manufacturing, also taking manufacturing costs into consideration. The latter requirement is particularly important for the possible dissemination and use of the reference standard in industry.
2) Design requirements:
    a. Gaps should be in the range of below one voxel size to several voxel sizes in order to have a comprehensive overview of different gap sizes. In the best case, the gap should be continuous in order to investigate the smallest measurable gap.
    b. In-material and inter-material measurements in multi-material scenarios should be present.
    c. Mono-material scenarios should be included in the test.
    d. Calibration of all measurement features should be possible by conventional techniques, preferably tactile CMS.

3) Other requirements:
    a. Analysis of relative effects and/or comparison with reference values should be possible.
    b. It should be possible to reveal multi-material-related effects using the reference standard.
    c. The reference standard design and testing application should allow the achievement of a sufficiently low test value uncertainty according to ISO 14253-5 [151] (i.e. enabling multi-material effects statements).

6.3 Reference standard

In order to meet all the requirements described in Section 6.2, a series of reference standards was designed by the University of Padova and PTB (Dr. Markus Bartscher and Fabricio Borges de Oliveira) and manufactured at PTB. Since the beginning of the collaboration, the idea was to create a symmetrical configuration so as not to introduce further variables such as the influence of different material thicknesses and other effects resulting from a non-symmetrical design. Furthermore, in order to reach sufficient resolution/voxel size (VS), the size of the object was limited.

6.3.1 Design

The first proposed design study of the multi-material gap standard is shown in Figure 81-a. It is composed of two parts of identical shape featuring several gaps of different dimensions. The standard can be disassembled and the single features of each component can be calibrated in order to provide reliable reference data. Once the standard is assembled, the reference features defining the measurement coordinate system are remeasured in the assembled state, thereby defining the relative orientation of single parts. The shortcoming of this design is that the two parts are fixed by two screws that may cause deflection of the material and possible instability over time as the material relaxes. Furthermore, the steps proposed in this design represent just discrete values of measurement gaps and, thus, it would be difficult to find the real limit of CT, i.e. the smallest measurable gap.

The design was therefore modified and the final version of the reference standard is presented in Figure 81-b. Similarly to the first version, the object is composed of two identical parts. In the final version, however, the step concept was supplemented by a tempered plane featuring a continuous gap. The main advantage of having both types of gap features is that the single steps define a good reference as the measurement (probing) points can be distributed over a plane and, thus, potential errors can be averaged and minimized. On the other hand, the minimum distance between the two tempered planes is theoretically zero, which gives the user the opportunity to evaluate the smallest measurable gap for the given CT configuration. The second most significant improvement compared to the previous version is the fixing system. The screws from the first concept were replaced by two centering pins made of a polymer (PEEK) that does not introduce any further stress to the parts. Additionally, the chosen material does not disturb CT data as its attenuation coefficient is negligible compared to the materials used for the construction of the multi-material components. After clamping and centering the single parts, the stable position is finally ensured by gluing the components together.

In order to satisfy the material requirements defined in Section 6.2, the bodies of the reference standard were manufactured in three different materials: (i) aluminum, (ii) titanium and (iii) carbon-fiber reinforced silicon carbide (also called SiC or Cesic®). The composition and properties of the materials are shown in Table 36. The standards were manufactured in all combinations, also including mono-material configurations, thereby resulting in six reference standards. By choosing this set of materials, several multi-material scenarios were created. The Al/SiC combination represents the case where the attenuation coefficients are in close proximity, thereby creating a task where separating the single materials is challenging. On the other hand, a Ti/Al or a SiC/Ti combination represents the situation where the contrast between the low-attenuating material and the background is highly affected by the high-attenuating one (Ti). Furthermore, in order to clearly distinguish between mono- and multi-material effects, mono-material reference standards (Ti/Ti, Al/Al, SiC/SiC) were manufactured as well.

Table 36. Properties of materials selected for the manufacturing of multi-material reference standards.

Material	Composition/ Commercial name	Density/g·cm^{-3}	CTE/10^{-6}·K^{-1}	Attenuation coefficient @200 kV, 1 mm Cu filter/mm^{-1}
Aluminum	AlMg4.5Mn0.7	2.66	23.3	0.049
Carbon-fiber reinforced silicon carbide (SiC)	Cesic®	2.65-2.70	2.09	0.053
Titanium	Ti6Al4V	4.42	8.6	0.134

All the materials used for the gap standards were machined by high-precision electrical discharge machining (EDM), providing smooth surfaces with low form deviations (flatness of the measured planes was measured below 2 µm), being adequate for this investigation. Although Cesic® is a ceramic compound, high-precision electrical discharge machining-based techniques are applicable for this material due to its sufficient electrical conductivity. This propriety of Cesic® has shown significant advantage over other considered materials, as all the chosen materials are conductive, and thus might be manufactured using the same manufacturing technology (i.e. similar manufacturing quality was obtained). On the other hand, Cesic® as a carbon-fiber reinforced silicon carbide is not completely homogenous; however, for the used magnification no significant effect of the non-homogeneity on the measurements was expected. Besides this, ceramics are in general fragile materials and they should be manufactured and handled carefully.

The general dimensions of the reference standard are shown in Figure 81-b. The highest achievable resolution in voxel size (VS) concerning the size of the object is roughly 20 µm. Taking into consideration the design requirements from Section 6.2, where gaps ranging from below one VS to several VS were demanded, the steps ranging from 10 µm (roughly half of the VS) to 1000 µm were designed. Furthermore, the tempered plane represents a continuous gap ranging from 500 µm to theoretically 0 µm. In order to facilitate the calibration and to ensure the unambiguous alignment of the workpiece during the calibration and CT measurements of the object, several reference features were defined on the object (see the features highlighted by a red star in Figure 81-b). The reference features also include the two biggest gaps (500 µm and 1000 µm) that are accessible in both the dismounted and the mounted state, and thus can be used for the correction of the gap measurements that cannot be performed by the tactile CMM in the assembled state.

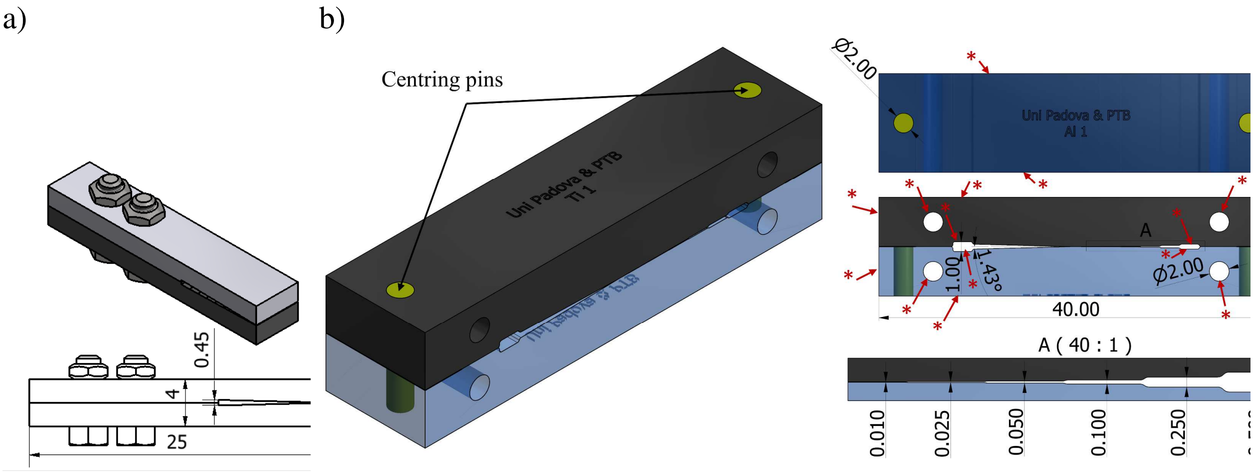

Figure 81. Different versions of the multi-material gap standard: a) rejected first design version with general dimensions, b) accepted second design version with general dimensions and highlighted reference features shown by a red star (*). All dimensions are in millimeters.

6.3.2 Calibration

Reference measurements of the multi-material gap standards were performed using a high-precision tactile micro-CMM Zeiss F25 with the maximum permissible error (MPE) equal to (0.25 + L/666) µm (where L is the measured length in mm). The measurements were performed at PTB by Dr. Michael Neugebauer. A complete calibration could not be performed in the assembled state as it would be impossible to measure the smallest gaps (the size goes down to 0 µm) with the used touch probe with a diameter of 120 µm (see the measurement configuration in Figure 82). It was therefore necessary to follow an alternative calibration procedure composed of measurements in the mounted and dismounted state and subsequent correction of reference values described by the following four steps:

1) Reference measurements of all the steps and the tempered plane on part 1 in the dismounted state.
2) Reference measurements of all the steps and the tempered plane on part 2 in the dismounted state.
3) Assembly and fixation of the two parts, and subsequent reference measurements of the features that are accessible by the tactile probe in the mounted state.
4) Calculation of the non-accessible features using the results from steps 1, 2 and 3.

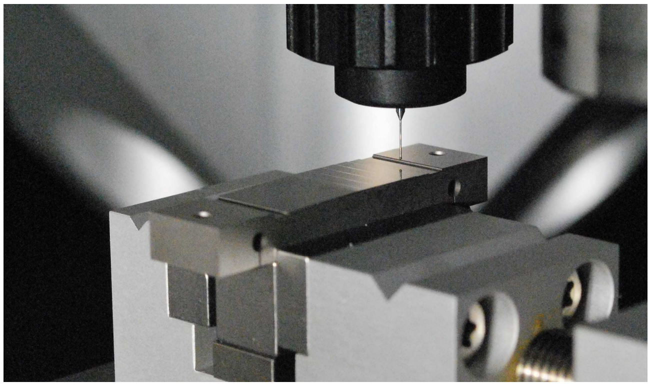

Figure 82. Configuration of the micro-CMS when measuring individual parts of the reference standard (courtesy of PTB).

All the steps and the tempered planes, as well as the contact planes, were measured in steps 1 and 2 of the reference measurements. The position, flatness deviation and tilt of the planes were measured too.

In the third step, the largest accessible gaps, i.e. 500 µm and 1000 µm, were measured. The remaining non-accessible gaps were evaluated based on a linear correction coefficient. This coefficient was calculated from the difference between the measurements of the largest gaps (500 µm and 1000 µm) in the mounted and dismounted state.

It should be noted that the gaps of 500 µm and 1000 µm are positioned at the opposite ends of the workpiece. This ensures a reliable correction of the calculated values for the remaining steps as the correction coefficient was approximated over the distance between the largest gaps.

6.4 Experimental study

In order to evaluate the possible application and capability of the reference standards for the testing of CT performance in multi-material gap measurements, experiments were performed in this study. The experiments were also performed with the aim to validate the proposed multi-material test procedure, and reveal possible flaws and further aspects that need to be improved.

6.4.1 Experimental set-up

The measurements for the purpose of this study were performed on five out of six standards. The missing assembly (Ti/SiC) was broken in the final phase of the manufacturing process and shall be analyzed in future research. The set of workpieces therefore includes three mono-material (Al/Al, Ti/Ti and SiC/SiC) and two multi-material (Ti/Al, Al/SiC) assemblies. Although one material combination is missing, both multi-material scenarios with low and high differences of attenuation coefficients are included. Furthermore, the mono-material combinations are used as a reference to isolate the multi-material effect on measurement results.

Computed tomography scans were acquired on a metrological CT system (Nikon MCT225) with the unidirectional center-to-center sphere distance MPE equal to $(9 + L/50)$ µm (where L is length in mm). The samples were scanned tilted by about 30° with respect to the rotary axis in vertical orientation (see Figure 83-a). The scale of the system is periodically corrected in order to minimize residual systematic scaling error. The errors caused by temperature were not considered as the CT cabinet is air-conditioned and the temperature during the scans was maintained within the range of 20±0.5 °C. Furthermore, the samples were placed into the cabinet with enough advance time to equalize the material and ambient temperature and stabilize the dimensions.

The CT scanning parameters were optimized in order to obtain the best possible results, minimizing CT artefacts, beam hardening in particular, and maximizing the contrast-to-noise ratio (CNR). CNRs were calculated according to Equation 6.1:

$$CNR = (\mu_m - \mu_b)/\sigma_b, \tag{6.1}$$

where μ_m and μ_b are the mean gray values (GV) of the material and background, respectively, and σ_b is the standard deviation of the background GV. The values of μ_m were calculated based on the regions of interest (ROI) defined in the material (lower or top), and the values of μ_b and σ_b based on the ROI inside the two biggest gaps as shown in Figure 83-b. The CNR values and CT scanning parameters are reported in Table 37. It is worth noting that the CNR of the Al part of the Ti/Al assembly is more than 4 times lower than for the other parts. Given the low CNR, problems with defining the surface on the Al part can be expected that will subsequently influence also the measurement results.

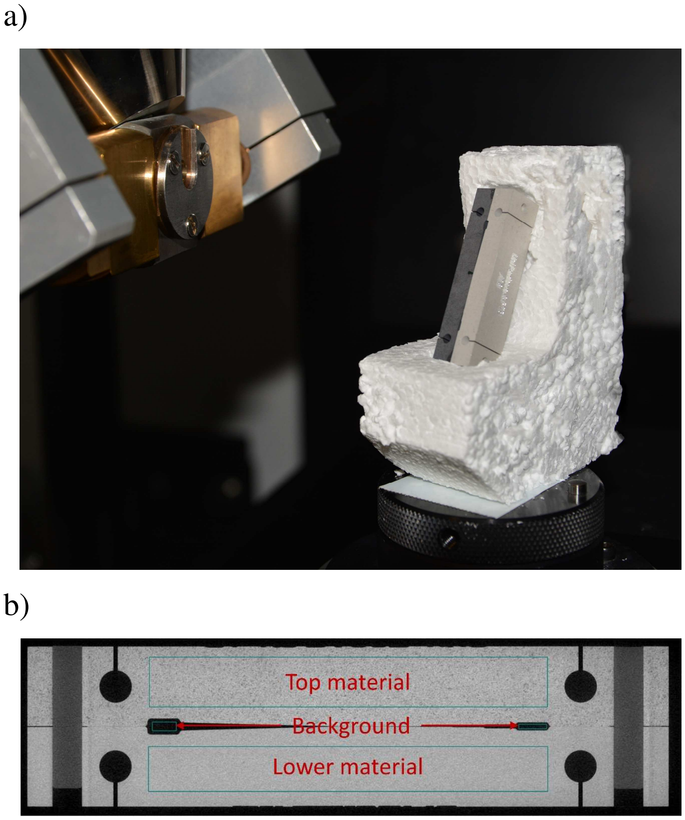

Figure 83. a) Orientation and position of the reference standard during scanning, b) definition of regions selected for the calculation of CNRs.

Table 37. CNRs and scanning parameters for the five scanned samples.

Assembly name lower part/top part	CNR lower part*	CNR top part*	Voltage /kV	Current /µA	Exposure time/ms	Filter	No. of projections
Al/Al	13.6	13.5	220	50	2000	0.5 mm Cu	2000
SiC/SiC	14.0	14.0	220	50	2000	0.5 mm Cu	2000
Ti/Ti	11.2	11.2	220	50	2898	0.75 mm Cu	2000
Al/SiC	13.8	13.4	220	50	2000	0.5 mm Cu	2000
Ti/Al	12.9	**3.0**	220	50	2898	0.75 mm Cu	2000

* lower part stands for the part that is in the first place of the assembly name

6.4.2 Evaluation methods

In order to investigate the effects of multi-material measurements, as well as the effects of different approaches to data post-processing, the acquired data were evaluated using different procedures. The results obtained by these techniques were then compared to the reference CMS values and the trends of the measurement errors were analyzed.

To ensure the full comparability and consistency of the results, the same procedures concerning the definition of measurement features, data alignment, etc. were used regardless of whether the sample was mono- or multi-material. The common measurement procedure is defined by the following steps:

1) Determination of the surface on the lower part.
2) Alignment of the dataset to the lower part using three reference planes (front, lower and left) as shown in Figure 84-a.
3) Duplication of the volume, so that the alignment and the defined reference features are preserved for future re-alignment.
4) Determination of the surface on the top part.
5) Alignment of the dataset to the top part using three reference planes (front, lower and left) as shown in Figure 84-b.
6) Creation of the measurement elements on both volumes.
7) Re-alignment of the copied volume to the lower part using the three copied reference planes (front, lower and left) as shown in Figure 84-a.
8) Export of z coordinates of the measurement elements and calculation of defined gaps.

The gaps were measured as the distance between two opposite points defined on the surfaces of the corresponding steps/tempered planes at certain x coordinates on both halves of the object (see Figure 85-a, b). Slightly different approaches were applied to measurements of single steps and the continuous gap created by the tempered planes.

The points in the case of steps were constructed using a patch-based strategy. This strategy is based on the collection of *a priori* defined fitting points forming a 1×2 mm grid including 55 points (see Figure 85-c). A representative point defined as a center of mass of the fitted points is used for the final evaluation.

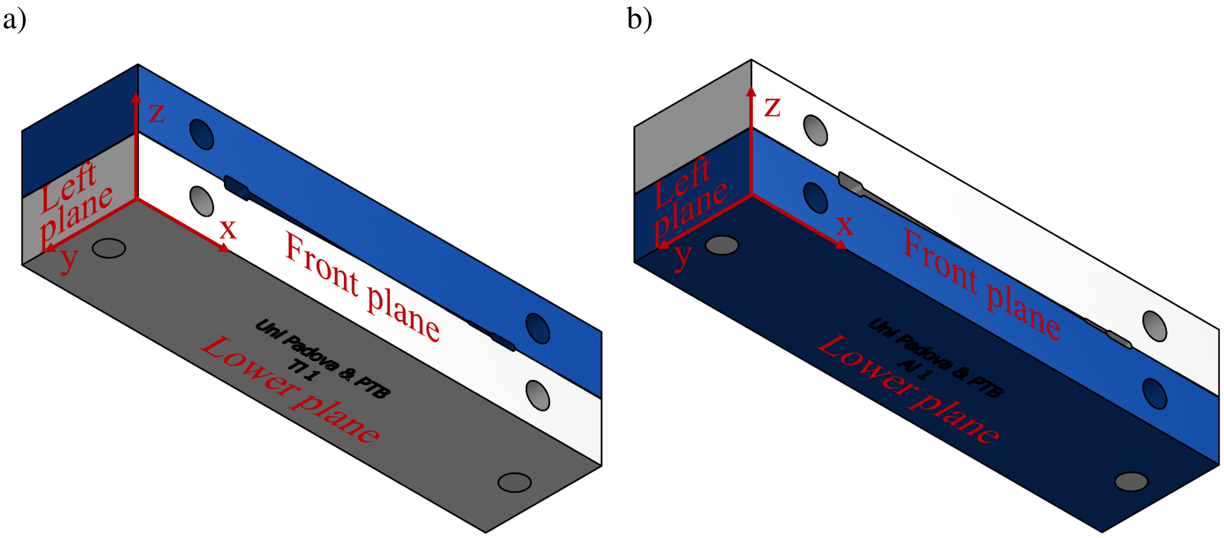

Figure 84. Different alignments for the evaluation of CT data: a) alignment to the lower part, b) alignment to the top part.

A similar patch-based approach is used for constructing the representative points on the tempered planes. In this case, a line-shaped patch constructed by 40 points fitted over a length of 2 mm instead of a grid is used for defining the representative point (see Figure 85-d). The lines are constructed in certain *x* coordinates, thereby defining corresponding gap sizes.

Each gap is measured in three positions, close to the edges and in the center of the part as shown in Figure 85-c, d, and the calculated value is averaged in order to minimize systematic errors. The patch-based approach was applied in order to minimize the influence of noise in the data and to improve the comparability of the CT and CMM results.

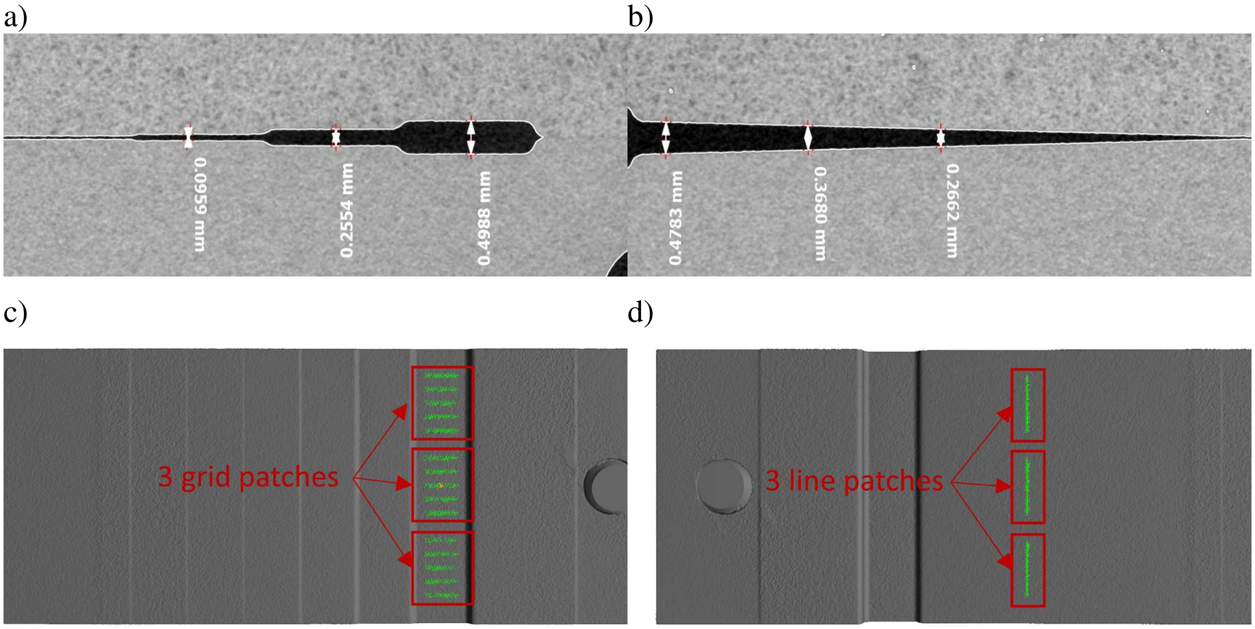

Figure 85. Description of the measurement procedure: a) two-point measurement of the gap between two steps, and b) between two tempered planes. Principle of the patch-based construction of measurement points: c) grid-shaped patches on steps, d) line-shaped patches on tempered planes.

In order to fit the measurement elements, a surface on the acquired CT dataset must be defined. The surface determination procedures used in this experimental study are listed in the four paragraphs below.

1) *Histogram-based surface determination with global thresholding (denoted as "Hist")*
   This method is the simplest way to define a surface on any dataset and is usually applied as a first choice. It is based on applying a global threshold taking into consideration the complete dataset. The threshold is defined differently for mono- and multi-material samples.
   - For mono-material samples, the arithmetic mean value between the background and the material peak (so called ISO-50% value) is calculated and used as the threshold value (see Figure 86-a). The mean is calculated automatically by the evaluation software.
   - For multi-material samples, since in this case the GV histograms consist of two (or more) material peaks (as shown in Figure 86-b, c), different surface determinations for low- and high-attenuation materials must be performed. Hence, a two-step procedure is applied: (i) the surface of the low-attenuating material is defined the same way as described in the mono-material case, i.e. by defining the global threshold in the automatic mode (Figure 86-b); (ii) the surface on the high-attenuating material is defined on the copied volume. In this case, the background line remains at the same place as for the low-attenuating material; the material line, however, is dragged towards the second material peak (Figure 86-c). The shortfall of this procedure is that it requires that the two material peaks be clearly separated; i.e. the attenuation coefficients of the two (or more) materials differ sufficiently. This condition was not satisfied in the case of the Al/SiC sample, where the difference between the attenuation coefficients is too small, and it was not possible to distinguish between the two material peaks. Therefore, the multi-material procedure was applied only for the Ti/Al combination, whereas the surface on the Al/SiC assembly was defined according to the mono-material scheme.
2) *Histogram-based surface determination with local adaptive thresholding (denoted as "Hist-adv")*
   The local adaptive thresholding methods are considered as the state of the art for surface determination. The threshold value, e.g. defined by the ISO-50% calculation described above, is used as a starting point. The algorithm subsequently searches for local gradients within the voxel range defined by the user and defines the surface accordingly.
   The starting threshold value in the present case is calculated the same way as described above (i.e. *Hist* procedure) for mono- and multi-material samples. The search distance for local gradients is set to four voxels.
3) *ROI-based surface determination with global thresholding (denoted as "ROI")*
   The surface is determined for the lower and top part separately for all five samples (i.e. including the mono-material ones); the threshold values are calculated based on ROIs defined in Figure 83-b, and are applied globally (i.e. without the local adaptive algorithm). Two different surfaces are defined even on the mono-material samples in case non-homogeneities are present in the material or the reconstructed data set.
4) *ROI-based based surface determination with local adaptive thresholding (denoted as "ROI-adv")*
   The surface is determined on both parts of the assembly the same way as in the ROI case. However, local adaptive thresholding is applied here.

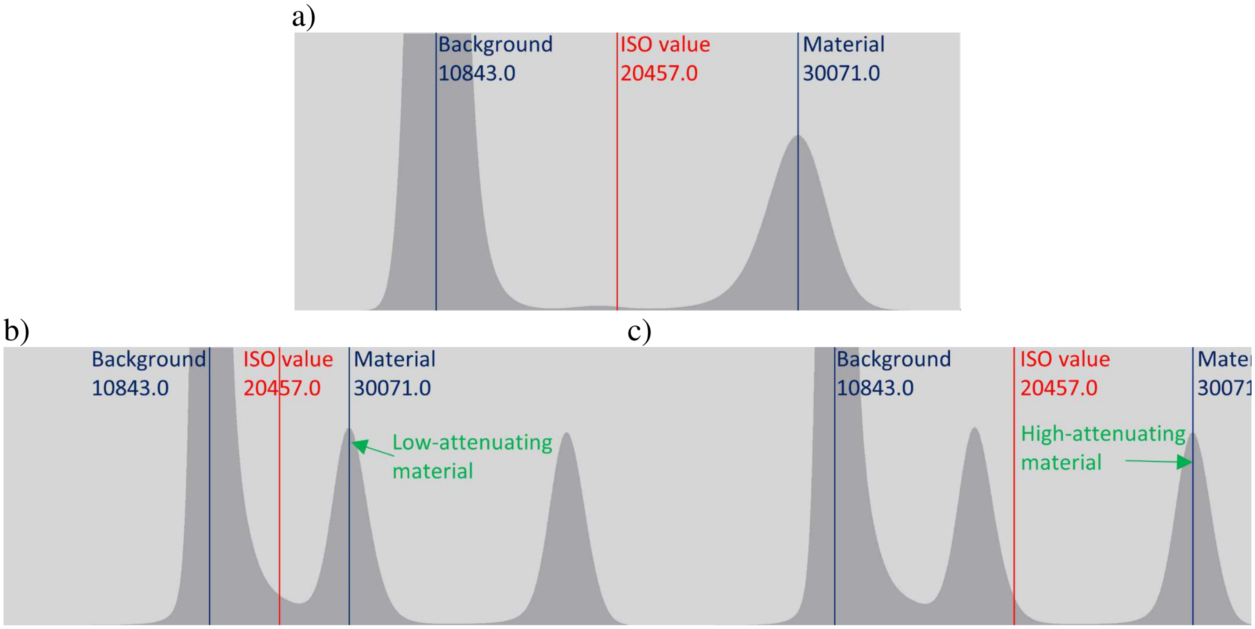

Figure 86. Histogram-based definition of the surface threshold value: a) mono-material case with automatic calculation of ISO-50% threshold value, b) multi-material sample with the automatic selection of low-attenuating material peak, and c) histogram of a multi-material sample, where the material line was dragged towards the high-attenuating material peak.

6.4.3 Results

The five mono- and multi-material standards were scanned and the datasets were analyzed following the procedures described in Section 6.4.2. The measured gaps were subsequently compared to the reference values provided by the tactile micro-CMM. In order to evaluate the performance of different surface determination techniques, and evaluate potential multi-material effects on measurement results, a separate chart showing measurement errors for each evaluation procedure was created. The results can be seen in Figure 87. The number of plotted points is not consistent over all diagrams; this is due to the fact that, for certain combinations of assemblies and measurement procedures, it was not possible to fit measurement features due to the missing surface. Furthermore, only results obtained on the tempered planes are shown as they provide continuous information of the observed trends; the steps provide the same trends, however they represent only discrete values and do not provide additional data.

Several trends can be observed in the charts from Figure 87:

1) The improving effect of local thresholding can be clearly seen when comparing charts in in Figure 87-a and Figure 87-c with charts in Figure 87-b and Figure 87-d. In general, measurement errors using global thresholding are systematically higher compared to local adaptive thresholding even for mono-material standards (including the Al/SiC combination). Furthermore, the curve of the Ti/Al standard using the *Hist* procedure is offset by another 20 µm (i.e. one voxel size) with respect to the other curves. It is also worth noting that the smallest measurable gap is systematically larger using global thresholding, especially in the Ti/Al case. Thus, one can significantly improve the results by using the local adaptive method and reduce the measurement error difference between multi- and mono-material samples.

2) Focusing on mono-material samples, a relation between attenuation coefficients and measurement errors can be observed. It seems that the higher the attenuation coefficient is (in this case Ti has the highest), the higher the measurement errors are. This is especially relevant for the cases where global thresholding was used, as the measurement errors were the highest for titanium samples and the lowest for aluminum or Al/SiC samples.
3) Measurements on the sample composed of parts with the highest difference of attenuation coefficients (Ti/Al) result in the highest measurement errors both for the global and local thresholding. Furthermore, the trends in measurement errors are different between the Ti/Al and other samples. This shows a clear multi-material effect on gap measurement results. The only exception is the *ROI-adv* case, where the measurement errors obtained on the Ti/Al and Ti/Ti sample were similar.
4) The minimum measurable gap in terms of existing surfaces for constructing measurement features (i.e. not with respect to the MPE) is systematically higher in the case of global thresholding and the Ti/Al sample. More specifically, when using local adaptive thresholding, it was possible to fit and measure gaps down to 20 µm (roughly one voxel size) for certain samples, which was also the limit for global thresholding. The limit for the Ti/Al sample was higher; 82.5 µm (four times the voxel size) for both thresholding methods.

a) Hist

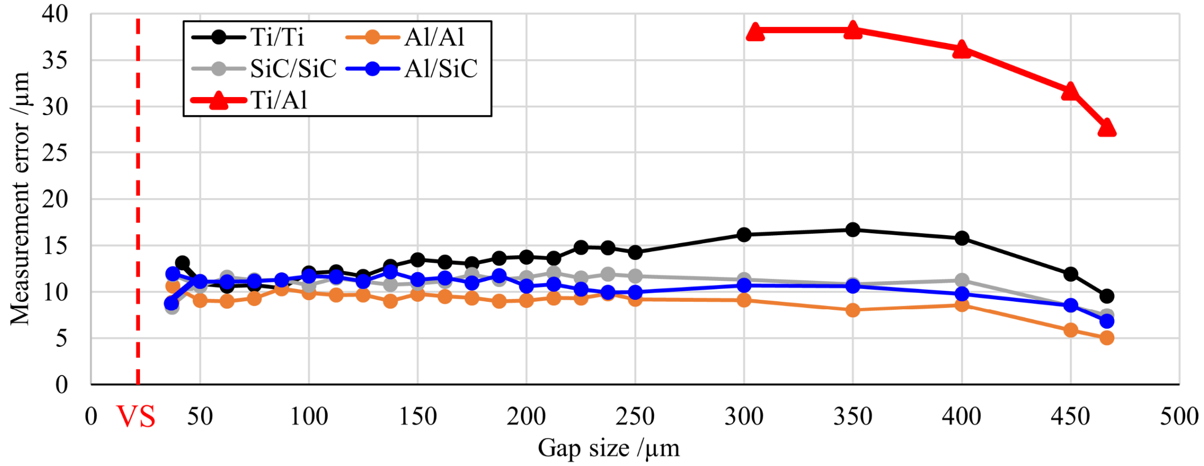

b) Hist-adv

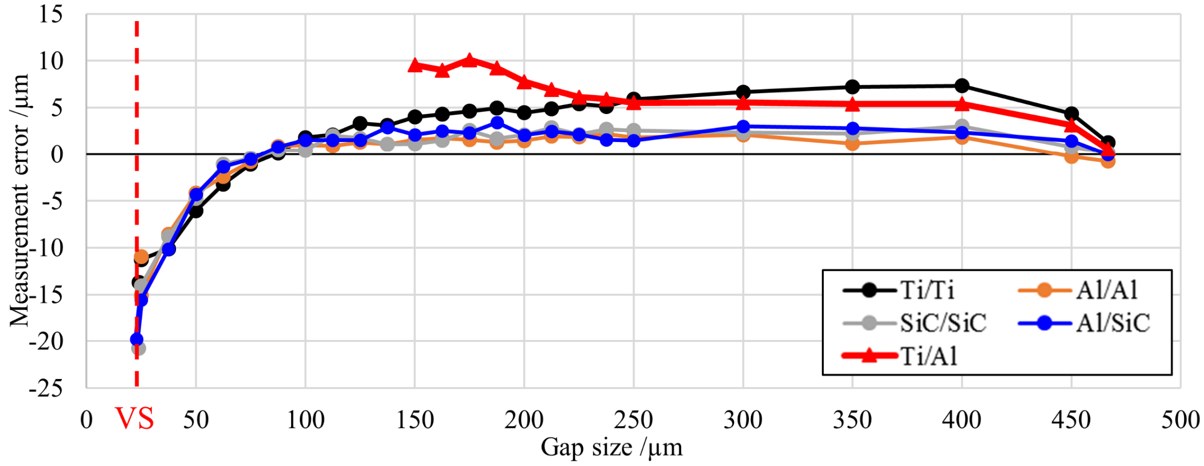

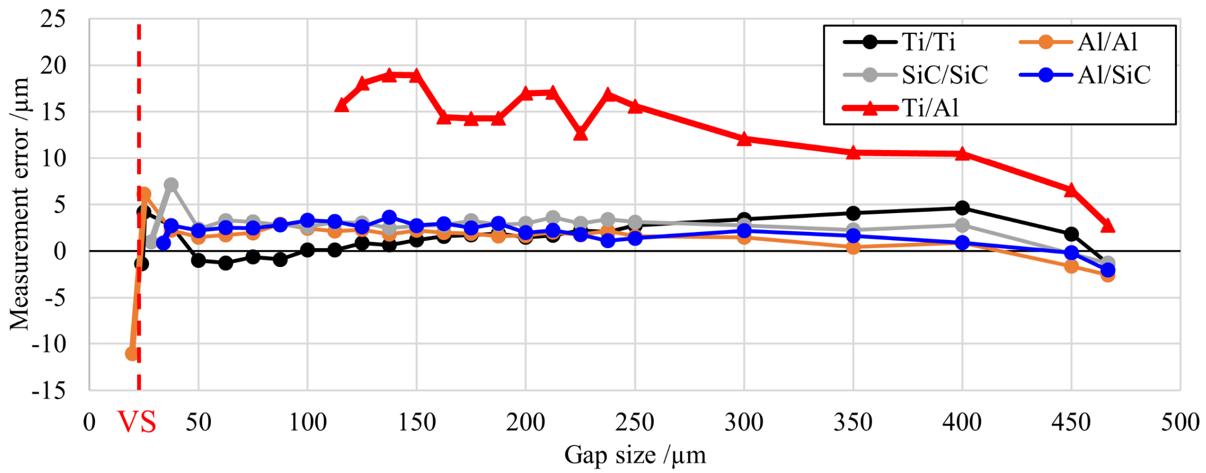
c) ROI

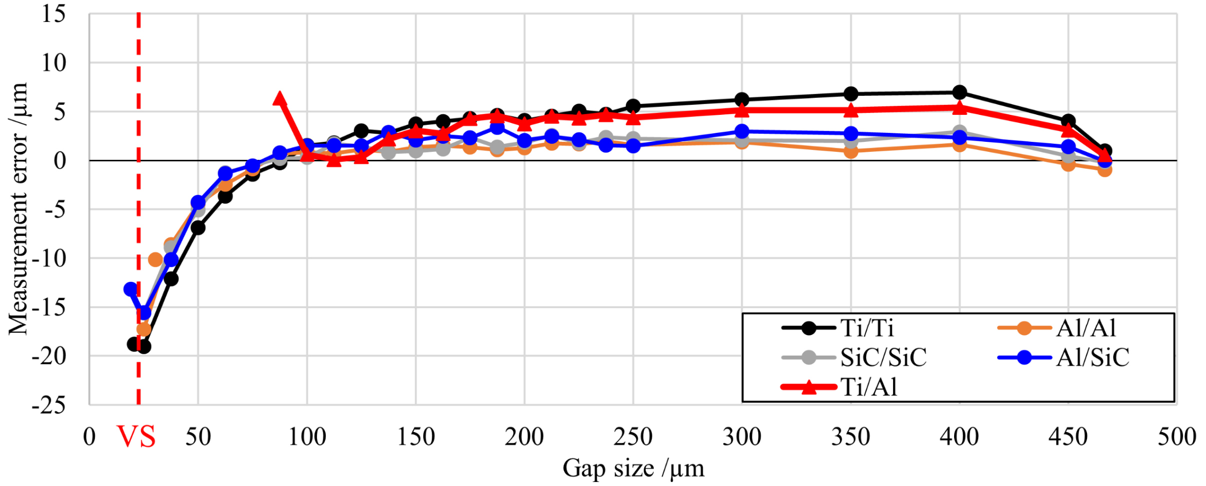
d) ROI-adv

Figure 87. Results of CT measurements performed on gaps formed by two opposite tilted planes. The vertical dashed line represents one voxel size.

The charts are supplemented by Table 38 and Figure 88 where the values of minimum measurable gap are summarized. The minimum measurable gap was evaluated as the smallest gap where the two tempered surfaces are not in contact yet.

Table 38. Smallest measurable gap for different samples and surface determination procedures.

Sample	**Surface determination procedure**							
	Hist		**Hist-adv**		**ROI**		**ROI-adv**	
	Gap/µm	**Error/µm**	**Gap/µm**	**Error/µm**	**Gap/µm**	**Error/µm**	**Gap/µm**	**Error/µm**
Ti/Ti	44.2	13.1	26.3	-13.7	26.3	-1.4	23.0	-18.8
Al/Al	38.3	8.9	26.4	-11.0	20.9	-11.1	31.4	-10.2
SiC/SiC	38.6	8.3	25.3	-20.8	29.7	1.0	21.8	-28.3
Ti/Al	**306.2**	**38.0**	**144.6**	**35.1**	**116.5**	**15.8**	**82.5**	**-26.9**
Al/SiC	37.7	8.8	23.6	-19.8	34.8	0.9	20.0	-13.2

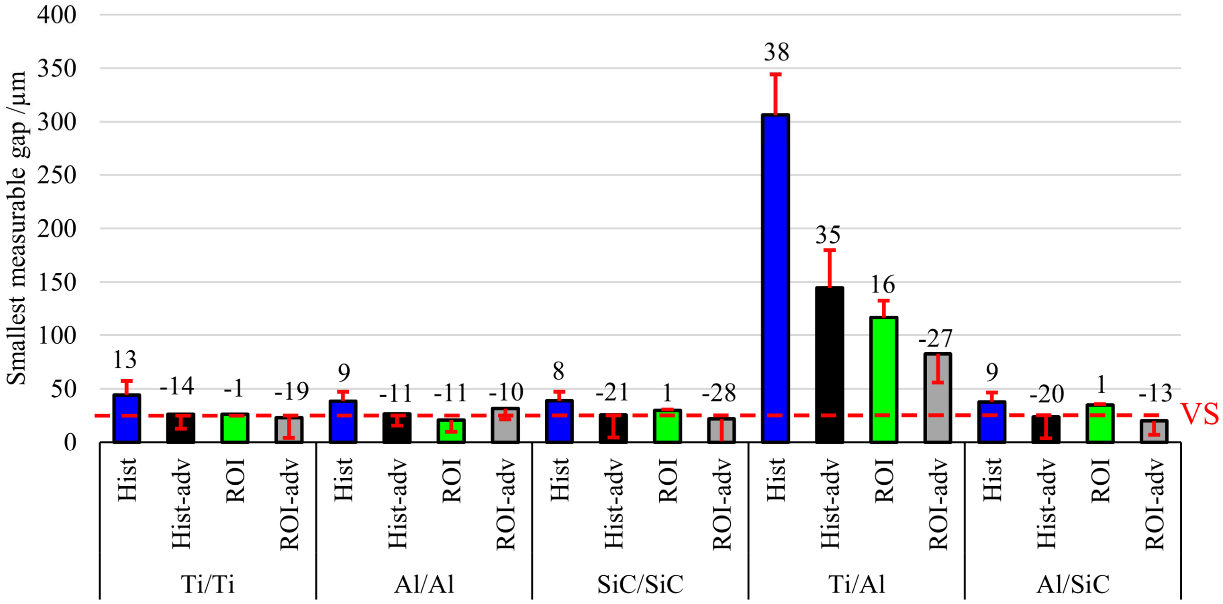

Figure 88. Smallest measurable gap where the two tempered surfaces are not in contact yet. The horizontal axis of the chart represents different surface determination procedures and samples. The error bars show the measurement errors with which the related gap was measured. The dashed horizontal line denotes one voxel size.

Since the two opposite tempered planes represent a continuous feature, i.e. a gap with a certain size range that goes down to zero, the reference standard proposed here could be also applied for evaluating the metrological structural resolution in the multi-material measurement scenario. The concept is similar to the one presented in [44,70], where two spheres in contact (i.e. the distance between the components is theoretically zero as well) are used.

In order to investigate the multi-material influence on unidirectional mono-material measurements, an additional study was performed. The height difference between the reference step and the tempered plane at certain *x* coordinates (corresponding to those used for gap measurements) *S* was measured and compared to reference (see Figure 89). Hence, in this case the measurand is not defined between different parts and materials; it is defined as a distance measured on a mono-material component with a presence of a counterpart made of the same (mono-material samples) or different (multi-material samples) material.

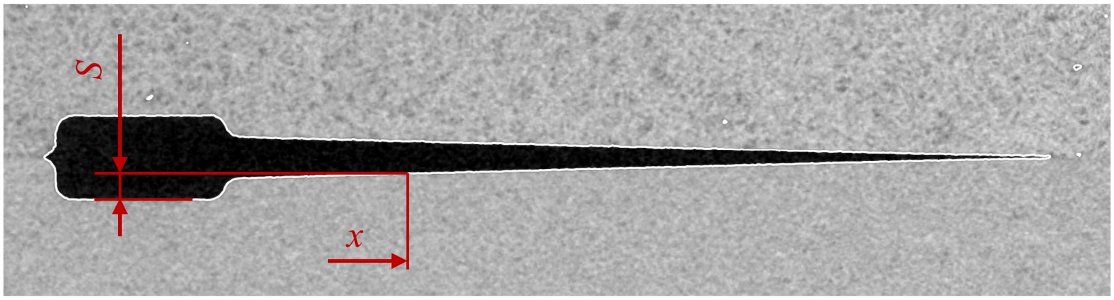

Figure 89. Diagram of unidirectional mono-material measurements of the height difference between the reference step and the tempered plane at certain *x* coordinate *S*.

The measurements were performed on all 10 individual components; however, the results obtained on both halves of mono-material assemblies (including the Al/SiC sample) were similar. Therefore, in Figure 90, results obtained only on one half of mono-material assemblies, and the

SiC part of the Al/SiC sample are plotted, whereas the results obtained on both halves of the Ti/Al sample are included in the charts.

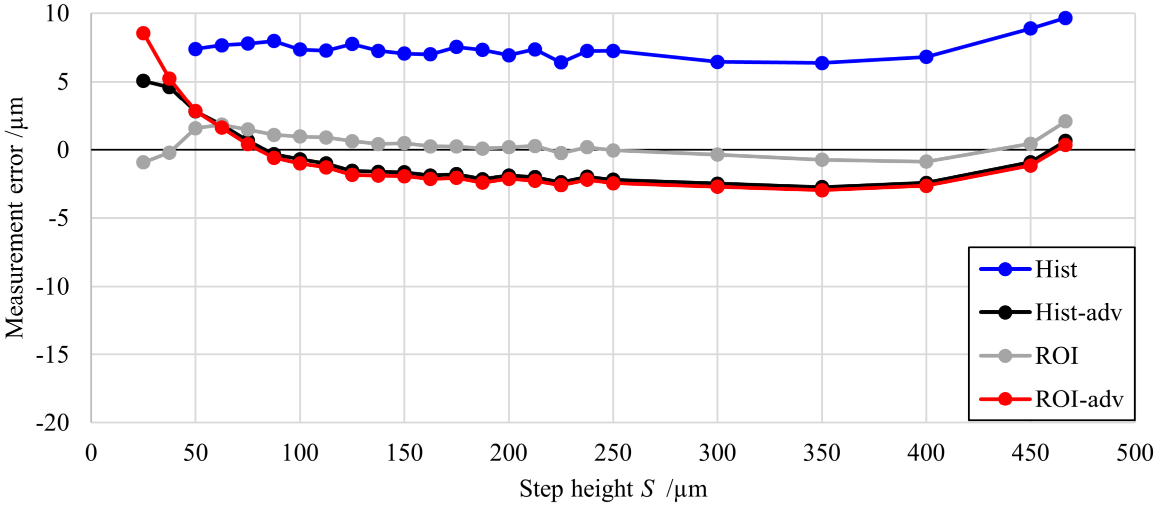
a) Lower part of the Ti/Ti sample

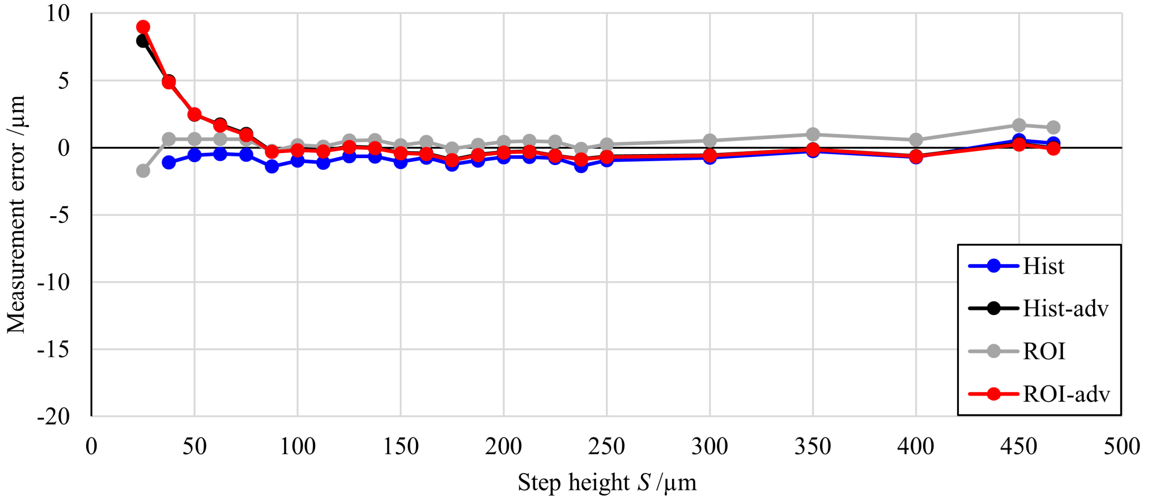
b) Lower part of the Al/Al sample

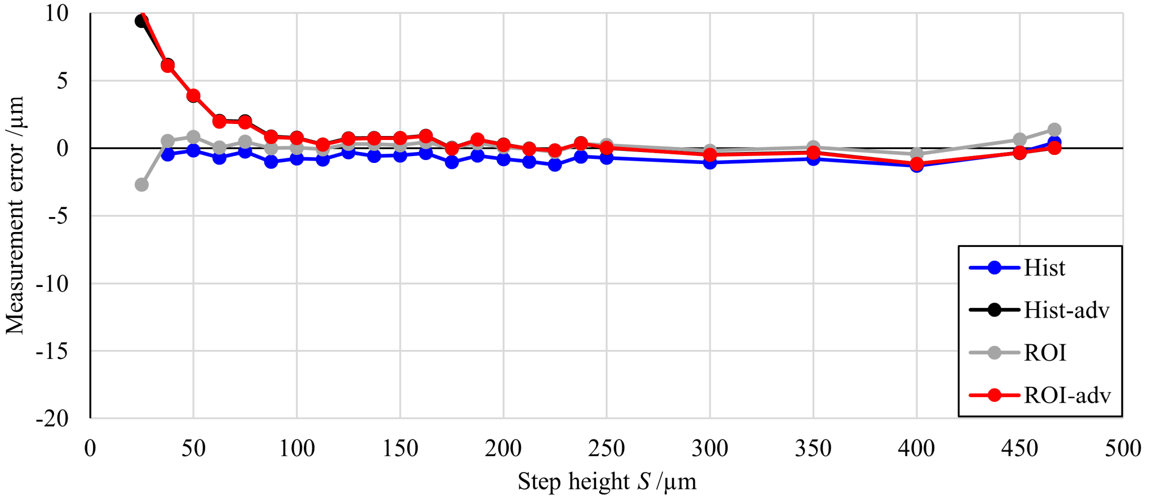
c) Lower part of the SiC/SiC sample

d) SiC part of the Al/SiC sample

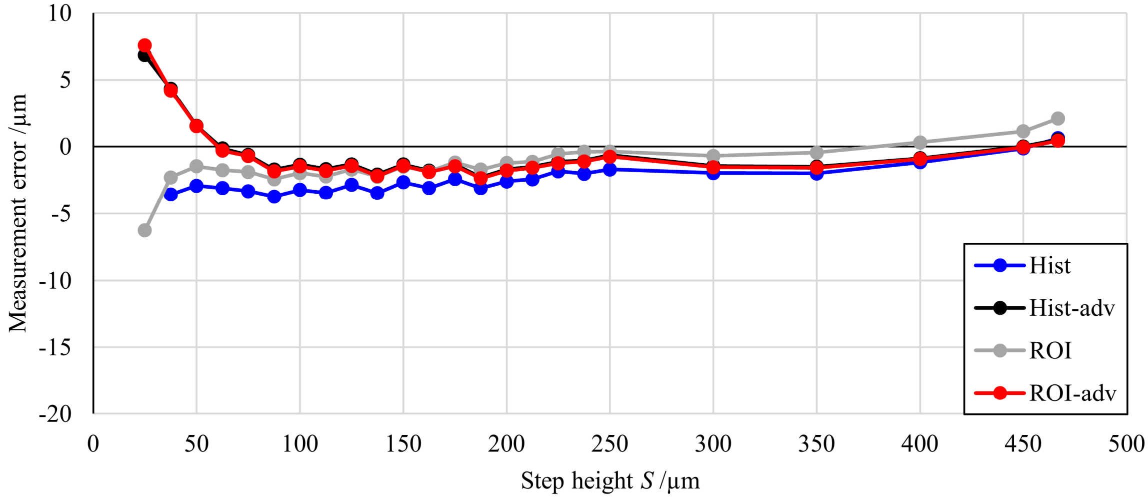

e) Ti part of the Ti/Al sample

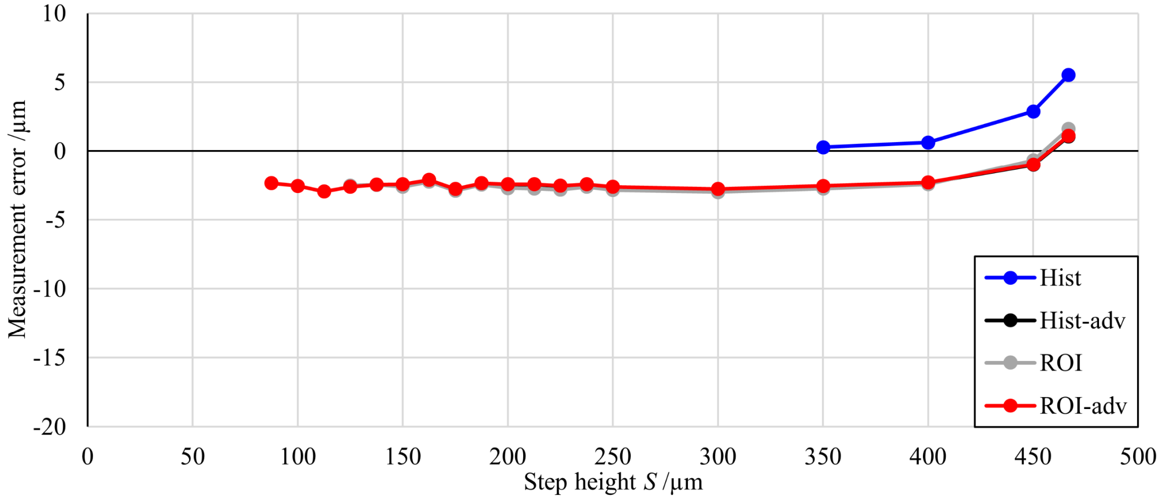

f) Al part of the Ti/Al sample

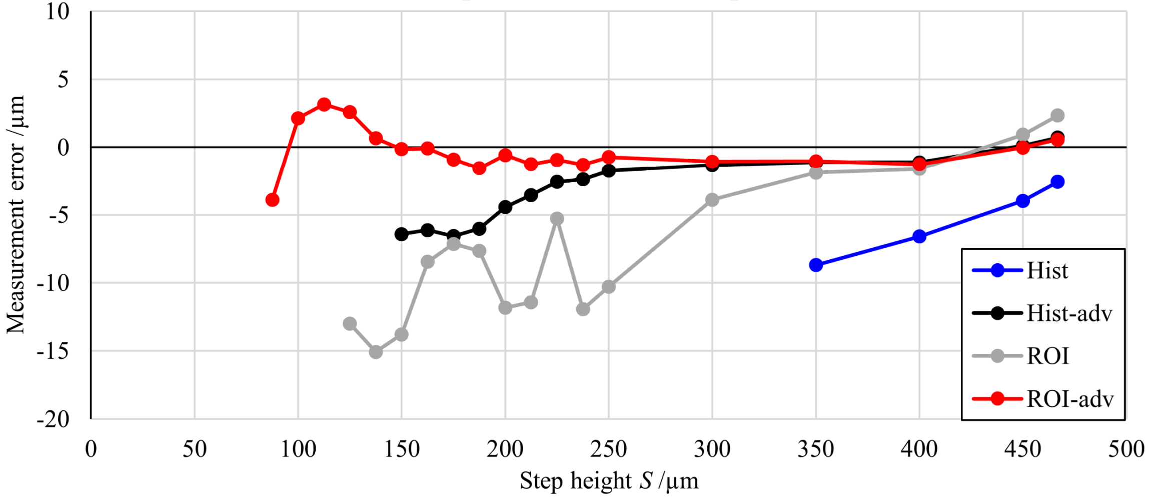

Figure 90. Measurements of the height difference between the reference step and the tempered plane at certain *x* coordinates *S* using different surface determination procedures on different samples.

It can be clearly seen from the results in Figure 90 that the measurement results obtained on the sample composed of the materials with the highest difference in attenuation coefficients (Ti/Al) are affected by multi-material effects. In particular, the measurement errors plotted in Figure 90-f (Al part of the Ti/Al sample) are significantly higher with respect to all other samples. Higher errors on the Ti/Al sample can be also observed in Figure 90-e (Ti part of the Ti/Al sample) when using the *Hist* surface determination procedure. This confirms the trends observed on the gap measurements shown earlier in this section; i.e. that measurements on samples consisting of materials with high difference in attenuation coefficients are more problematic.

Furthermore, when using the *Hist* surface determination procedure, the errors on the mono-material sample composed of Ti (i.e. of a high-attenuating material) are also higher with respect to other mono-material samples (including the Al/SiC one). This confirms the observations made earlier in this section, where higher errors on the Ti/Ti sample were measured as well.

6.5 Dual-energy CT scanning

Clear multi-material effects on measurement results were observed in Section 6.4.3. These effects were most significant in the case where materials with a large difference in attenuation coefficients were combined, i.e. the Ti/Al sample. Larger measurement errors on this assembly are related to difficulties in determining correctly the surface on the low-absorbing material, which can be mainly attributed to beam hardening effects. This phenomenon arises from the fact that typical industrial CT systems use polychromatic X-ray sources [3,11]. Furthermore, when optimizing the settings of a CT scan, one has to compromise between overexposing low-attenuating materials and penetrating sufficiently those with high attenuation coefficient [152]. However, this approach often results in poor contrast between different materials as observed in the experimental study presented in Section 6.4. Dual-energy CT scanning (DECT) is a promising technique for improving the contrast in CT data when scanning multi-material components. The work in this section was carried out in collaboration with Anton Jansson and Prof. Lars Pejryd from Örebro University. In particular, the DECT method used in this experimental study was developed at Örebro University. Therefore, a brief explanation of the method is given here; further details can be found in [152,153].

6.5.1 DECT method

The main principle behind DECT in general is combining CT data acquired using two different energies. The idea is to use high-quality data from each energy level and eliminate the data with low quality, so that one high-quality dataset is achieved. Several DECT approaches exist and are discussed e.g. in [153]. The method used in this study is based on the sequential acquisition approach and the pre-reconstruction data processing method. In sequential acquisition, the workpiece (i.e. the gap standard in the present case) is scanned twice, each time with a different energy. The goal is to achieve one set of overexposed and one set of underexposed projections. The two sets of projections are subsequently fused before the reconstruction [153].

The computational step is performed in a dedicated software Oxct (Örebro University, Sweden) [152]. In the first step, the overexposed projections are used as templates to select values from the over-and underexposed projections during the fusion. The template is then used as a weight to fuse the two original projections in the second step. The process is schematically explained in Figure

91. In the third step, the datasets are reconstructed using FDK algorithms in a commercial software. Further details on the method can be found in [152,153].

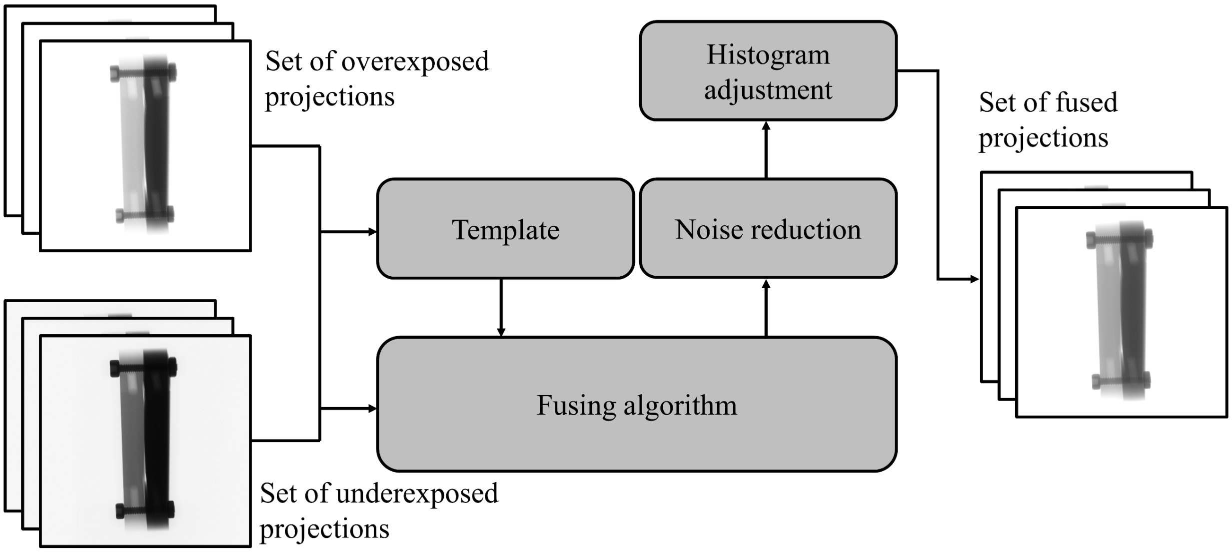

Figure 91. Schematic explanation of the DECT principle. Adapted from [153].

6.5.2 Experimental set-up and evaluation

Since the aim of this study is to improve the results obtained on multi-material samples, only Al/SiC and Ti/Al samples were scanned. The scans were acquired using the same CT system as in Section 6.4. Furthermore, the same position of the sample as shown in Figure 83-a and CT scanning parameters listed in Table 37 (except for voltage and current) were used for scanning. The tube voltage and current settings for low- and high-energy scans are presented in Table 39.

Table 39. Tube voltage and current for low- and high-energy scans of the two multi-material samples.

	Low-energy scan		**High-energy scan**	
Sample	**Voltage/kV**	**Current/µA**	**Voltage/kV**	**Current/µA**
Ti/Al	113	97	220	50
Al/SiC	110	100	220	50

Three scans at both energy levels were acquired (i.e. six scans per sample in total) in an alternating sequence (i.e. changing the energy levels after each scan). This sequence was chosen in order to reduce possible movement of the sample between the scan pair used for the data fusion, and to reduce the effect of the focal spot drift. The stability of the sample is critical for proper fusion of the image sets since any movement contributes to blurring of the image that can subsequently affect the measurement accuracy.

The fused data sets were reconstructed at Örebro University using VGStudio MAX 2.2, as well as at the University of Padova using CTPro (Nikon Metrology X-Tek, UK) to investigate the influence of the reconstruction software. The individual reconstructed volumes were subsequently evaluated following the same procedures and using the same surface determination methods as presented in Section 6.4.2. Finally, the results obtained from the three corresponding reconstructed volumes were averaged and compared to results obtained on single energy scans (i.e. the conventional technique used in Section 6.4).

6.5.3 Results

The two samples were analyzed according to the procedure explained in Section 6.4.2. In order to evaluate the performance of DECT, results obtained on datasets acquired using conventional single-energy scanning are plotted as a reference together with DECT values in charts shown in Figure 92 – Figure 94. Furthermore, in order to analyze the influence of reconstruction software, results obtained from CT volumes reconstructed by VGStudio MAX and CTPro were compared. Separate charts were constructed for the Ti/Al and Al/SiC sample, and individual surface determination techniques to isolate single influence factors. For the same reason as in the previous experiments, the number of plotted points is not consistent over all diagrams, and only results obtained on the tempered planes are shown.

It should be noted that due to the excessive noise on the surface determined by the *Hist* method, it was not possible to fit measurement features; thus, the *Hist* results are missing in the following results.

a) His-adv

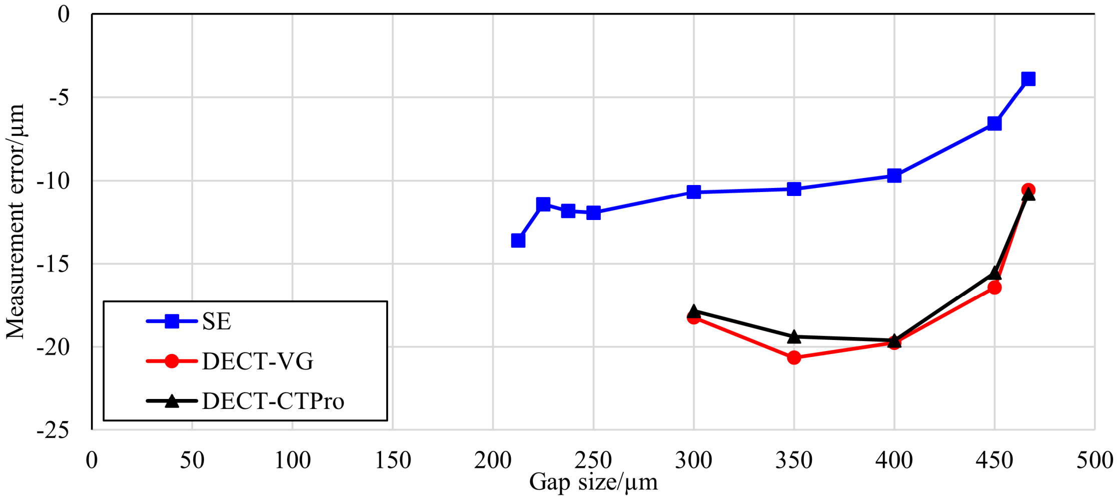

b) ROI

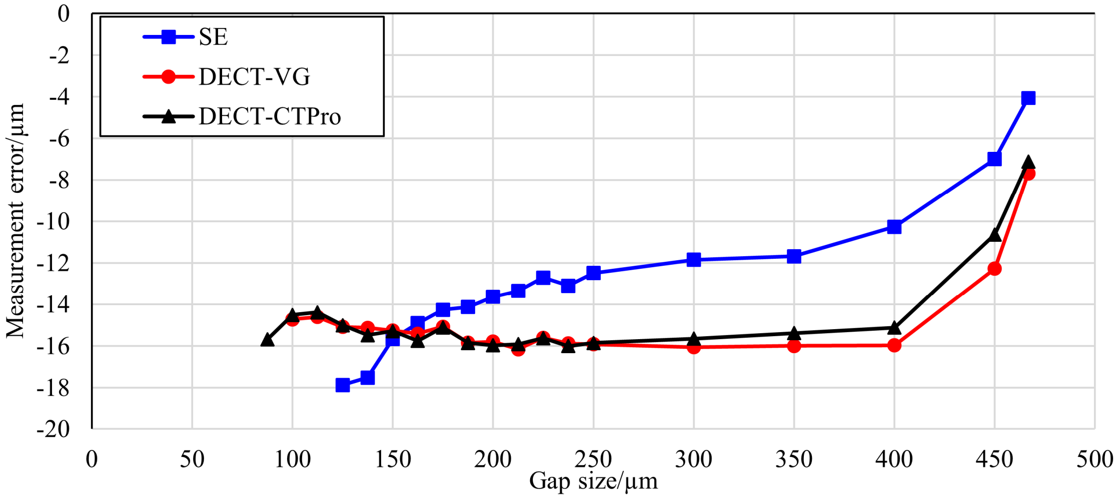

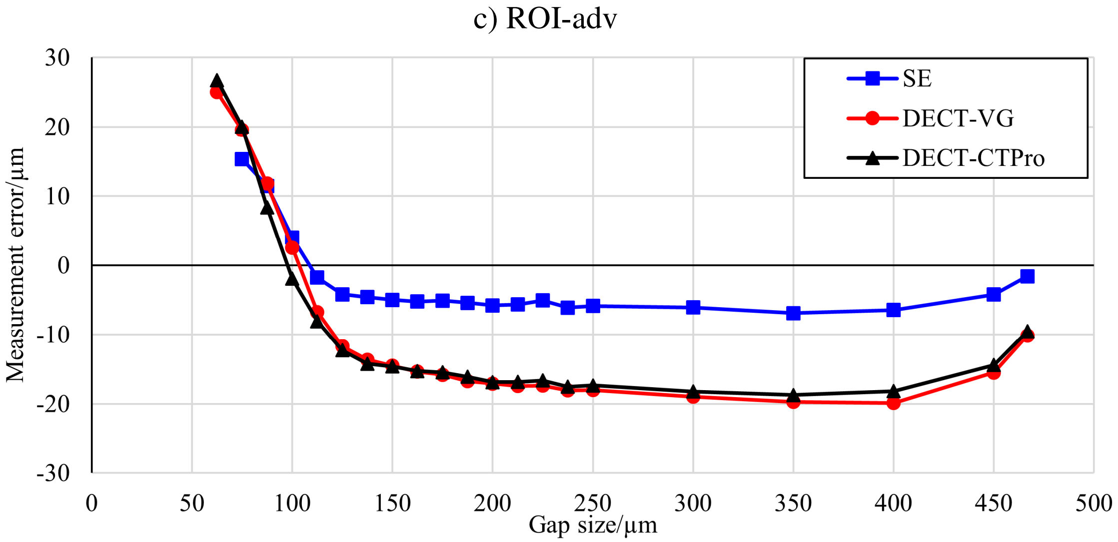

Figure 92. Results of DECT scanning for Ti/Al sample and different surface determination methods. Single-energy (conventional) scanning is denoted as "SE", DECT data reconstructed by VGStudio MAX as "DECT-VG", and DECT data reconstructed by CTPro as "DECT-CTPro".

Results obtained on the Ti/Al sample are shown in Figure 92. In general, measurement errors are higher using the DECT approach. This can be explained by the fact that the fusion procedure (i.e. the fusion of the two sets of projections) is very sensitive to any kind of movement of the sample or the focal spot. If the object (or the focal spot) moves between the low- and the high-energy scan, the projection of the sample is not at the exactly same position on two corresponding radiographs. As a result, when fusing a pair of projections, a certain amount of blur is introduced to the fused radiograph, depending on the difference of the projected object position between the related radiographs. In the present case, the position changed by roughly one pixel, which resulted in larger measurement errors with respect to single-energy scans. The only exception are measurements performed on surfaces defined by ROI and ROI-adv procedures, where the enhanced contrast achieved by dual-energy scanning allowed measurements of smaller gaps. As a result, measurement errors near to the smallest measurable gap by SE are equal to those acquired by DECT and with decreasing gap are even higher.

The benefits of DECT can be seen in Figure 93 where smallest measurable gaps for different surface determination methods are plotted. Furthermore, smallest measurable gaps for both multi-material samples are summarized in Table 40.

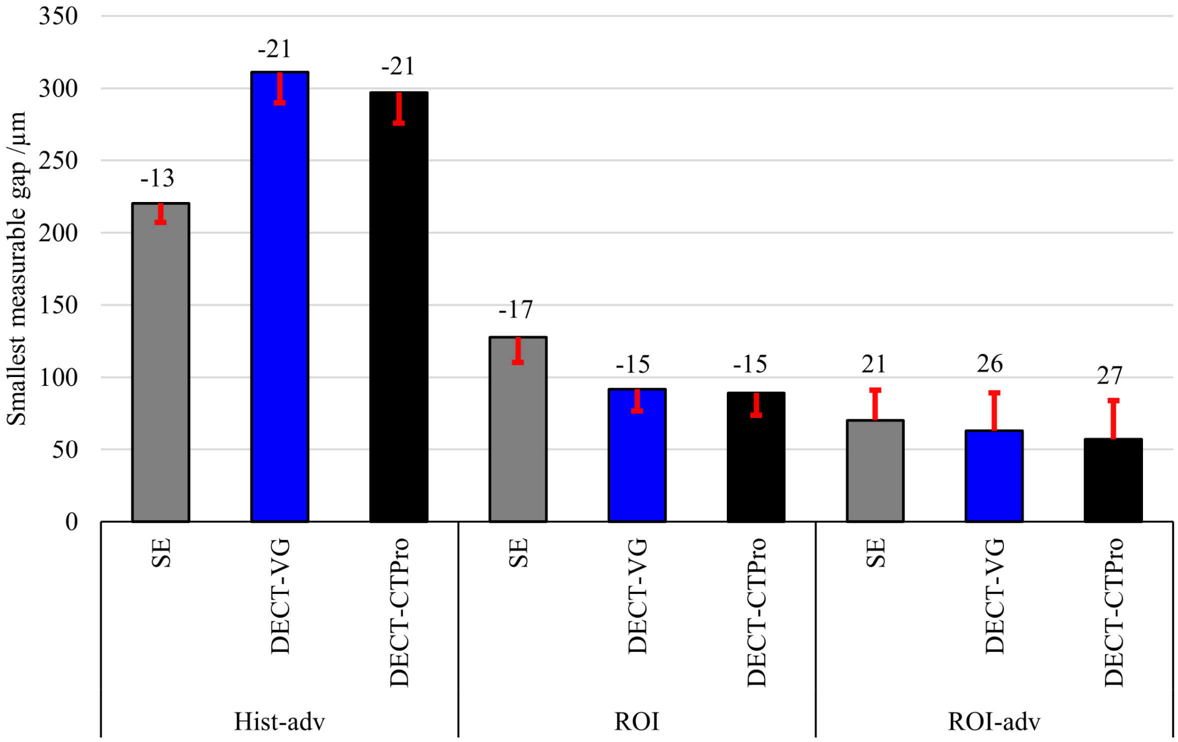

Figure 93. Smallest measurable gap measured on the Ti/Al sample using different scanning methods and surface determination procedures.

It can be clearly seen from Figure 93 that, except for *Hist-adv* where the surface was too noisy, systematically smaller gaps could be measured using DECT approach with measurement errors of magnitude similar to SE scanning. This proves that DECT has potential to improve measurement results obtained from multi-material workpieces. Further evidence of the improvement is shown in Table 41 where CNRs calculated according to Equation 6.1 are presented. The CNR of the Al part of the Ti/Al sample calculated on both DECT datasets is higher than the CNR of the same component calculated on the SE dataset. Finally, no significant difference between VG and CTPro reconstructions was observed.

Results obtained on the second multi-material sample, i.e. Al/SiC, are shown in Figure 94.

a) Hist-adv

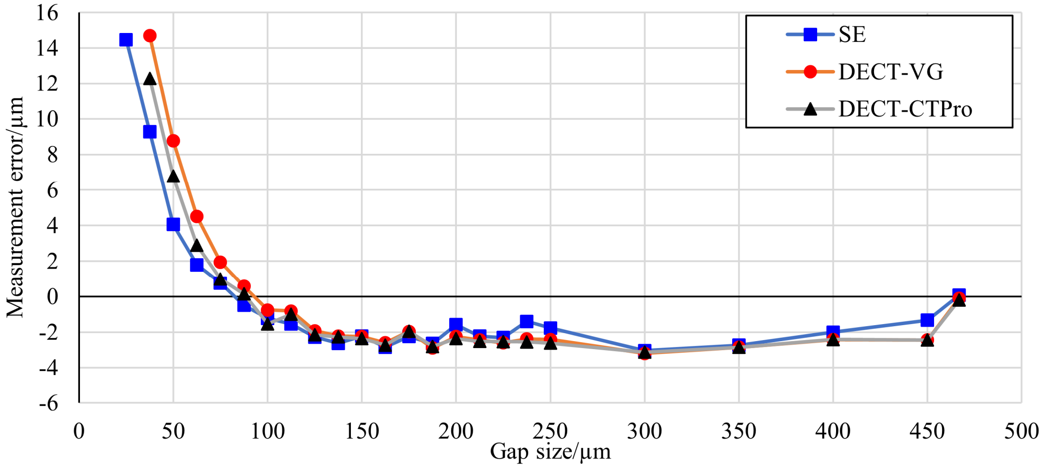

b) ROI

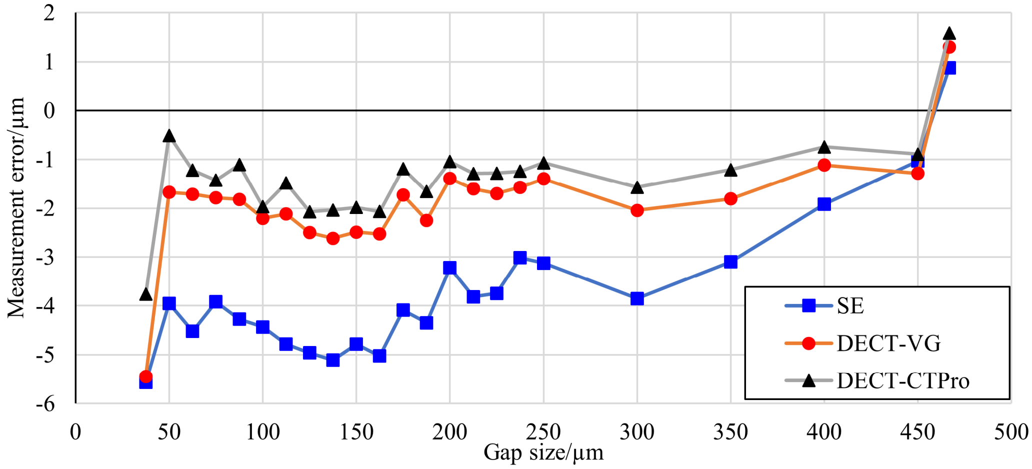

c) ROI-adv

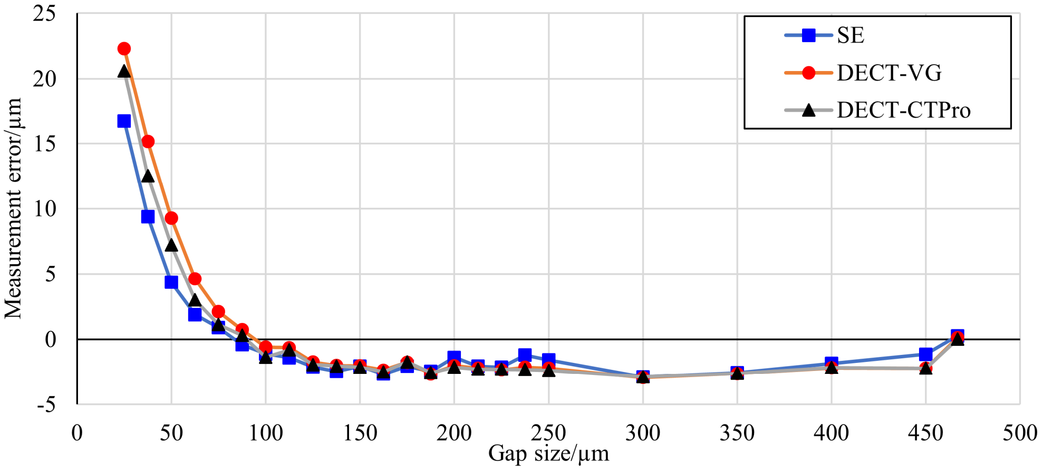

Figure 94. Results of DECT scanning for Al/SiC sample and different surface determination methods. Single-energy (conventional) scanning is denoted as "SE", DECT data reconstructed by VGStudio MAX as "DECT-VG", and DECT data reconstructed by CTPro as "DECT-CTPro".

It can be seen from the results in Figure 94 that there is no significant difference between SE scanning and DECT. This is due to the fact that although the Al/SiC sample is technically multi-material, the attenuation coefficients are very similar. This was also proved in Section 6.4, where this sample was considered mono-material. Similarly to the first experimental study, lower errors were obtained and smaller gaps could be measured on the Al/SiC sample with respect to the Ti/Al assembly. This trend is confirmed also by the results shown in Figure 95, where the smallest measurable gaps for different scanning approaches and surface determination methods are plotted.

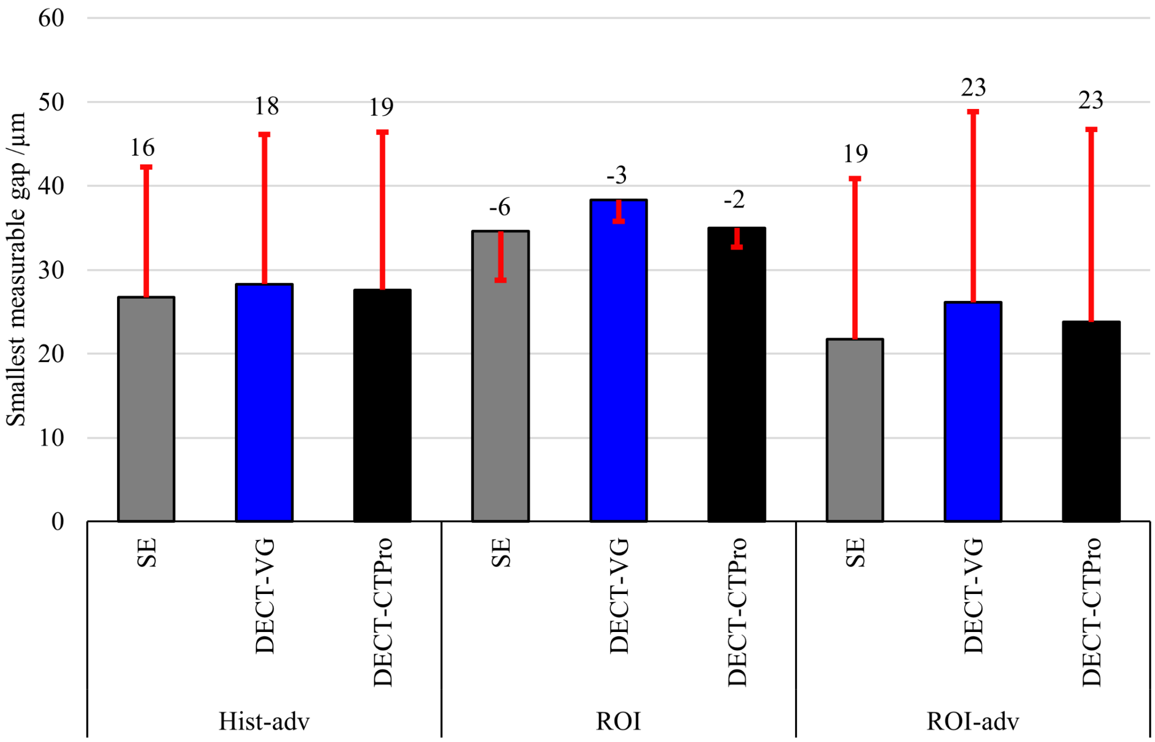

Figure 95. Smallest measurable gaps measured on the Al/SiC sample using different scanning methods and surface determination procedures.

The smallest measurable gap as well as the measurement errors are similar for all the scanning methods and surface determination procedures as shown in Figure 95. Slightly smaller gap was measured only on the SE reconstructed volume in the case of ROI-adv surface determination.

A summary of smallest measurable gaps measured on both samples is shown in Table 40.

Table 40. Smallest measurable gaps measured on both samples.

		Ti/Al		**Al/SiC**	
Surface determination	**Scanning method**	**Smallest gap/µm**	**Measurement error/µm**	**Smallest gap/µm**	**Measurement error/µm**
Hist-adv	**SE**	220.4	-13.3	26.7	15.5
	DECT-VG	311.1	-21.0	28.3	17.9
	DECT-CTPro	297.1	-21.0	27.6	18.8
ROI	**SE**	127.7	-17.4	34.6	-5.8
	DECT-VG	91.8	-15.0	38.3	-2.6
	DECT-CTPro	89.2	-15.4	35.0	-2.3
ROI-adv	**SE**	70.4	20.8	21.7	19.1
	DECT-VG	63.1	26.3	26.1	22.8
	DECT-CTPro	57.2	26.8	23.8	23.0

The values of CNR for both multi-material samples scanned with both the SE scanning and the DECT are shown in Table 41. It can be seen that while the CNR on the Ti part of the Ti/Al sample is similar for both scanning methods, the CNR measured on the Al part, which is the most critical, was increased by roughly 20 %. This proves that better quality of data can be obtained by using DECT when scanning multi-material workpieces. However, in order to implement the proposed method for dimensional metrology, the problem with the instability of the sample/focal spot and its effect on measurement results must be addressed.

Table 41. The values of CNR for both samples scanned with different methods.

	CNR			
	Ti/Al sample		Al/SiC sample	
Scanning method	**Al**	**Ti**	**Al**	**SiC**
SE	**2.49**	11.25	14.46	14.03
DECT-VG	**2.90**	11.18	13.23	12.69
DECT-CTPro	**2.97**	11.44	13.81	13.24

6.6 Conclusions

A series of mono- and multi-material reference standards was designed and manufactured for investigating the multi-material effects on measurements of gaps by CT. The samples were made of aluminum, titanium and carbon-reinforced silicon carbide (SiC). The gaps are formed by two identical opposing surfaces featuring discrete steps and tempered surfaces. The gap sizes range from theoretically 0 µm to 1000 µm. The reference standards were calibrated using a high-precision tactile micro-CMM.

An experimental study was performed in order to evaluate the capabilities of the reference standards and to investigate the performance of CT in multi-material gap measurements. A set of CT scans was acquired and evaluated by different methods using global and local thresholding and further data post-processing. The CT measured gaps were compared to the reference values from the tactile micro-CMM and measurement errors were evaluated with respect to the method used for data processing.

In general, by using local adaptive thresholding, lower measurement errors were achieved. Furthermore, the multi-material effect was significantly decreased by using local adaptive algorithms, i.e. the offset between measurement errors for mono- and multi-material samples was equalized by using local adaptive thresholding. Nonetheless, the sample made of materials with the highest difference between attenuation coefficients (Ti/Al) demonstrated the highest errors even using local adaptive thresholding. Furthermore, the trends of measurement errors on this sample were different compared to other assemblies. The increase of measurement errors was most significant for the smallest gaps. It was also observed that measurements on mono-material samples made of materials with high attenuation coefficients are more problematic; the errors measured on the Ti/Ti sample were systematically higher than on other mono-material samples. The smallest measurable gap in terms of existing surfaces for constructing measurement features was affected by the multi-material effects as well; the smallest gap measured on the Ti/Al, comparing results from all surface determination procedures, was four times larger than the smallest gap measured on other samples.

A complementary study was performed using the series of reference standards to investigate the multi-material influence on mono-material unidirectional measurements. Results obtained in this study confirmed the above-mentioned observations; i.e. that the measurement results obtained on the Ti/Al sample (i.e. the sample with high difference in attenuation coefficients) suffer from multi-material effects. Errors obtained on the critical Al part were significantly higher with respect to other samples.

Since the two experimental studies proved that dimensional measurements performed on multi-material samples suffer from additional multi-material effects, an alternative dual-energy CT (DECT) approach was used to improve the scan quality, and subsequently also the measurement results. In this study, only multi-material samples (Ti/Al and Al/SiC) were analyzed following the same evaluation procedures as in the first experimental study. The results showed that, especially on the Ti/Al sample, measurement errors obtained from DECT scans are higher. This was caused by the fact that the sample/focal spot was not stable during the scanning; as a result, additional blur was introduced during the fusion of low- and high- energy scans. However, the enhanced contrast (by 20% on the critical Al part) achieved by dual-energy scanning resulted in the possibility to measure smaller gaps with respect to conventional, single-energy scanning. This proves that by using DECT, an improvement in measurement results on multi-material workpieces can be achieved. While significant improvements with respect to the smallest measurable gap were achieved on the Ti/Al sample, results obtained on the Al/SiC sample were similar for both scanning methods. In order to implement the proposed method for dimensional metrology, further steps must be performed to eliminate the error caused by the instability of the sample/focal spot during scanning.

This chapter gives an insight into the complex problem of multi-material gap measurements. Further research shall be directed towards applying further techniques for surface determination and data (material) separation. Additional experiments with the Ti/SiC sample shall be performed in order to confirm the trends observed on the Ti/Al standard that has similar material properties. Moreover, further experiments and CT scans with different CT settings and sample orientations need to be performed in order to isolate the multi-material effects and gain a comprehensive overview of the problem. Another aspect that shall be addressed in future research is the multi-material effect on structural resolution, since the configuration of the reference standard allows measurements on a continuous feature with gaps ranging from 500 µm to theoretically zero. Finally, in order to gain robust measurement results, the evaluation of the test uncertainty shall be performed in subsequent works.

7 GOOD PRACTICE GUIDE FOR DEVELOPING REFERENCE STANDARDS FOR CT DIMENSIONAL METROLOGY

The purpose of this chapter is to summarize observations and experience obtained during the Ph.D. project related to developing new reference standards for CT dimensional metrology. The findings are organized in such a way that form a “good practice” guide for CT users and researchers through all the stages of new reference standards development. These individual steps towards creating and using new reference standards are defined in the following sections: (i) material choice, (ii) design, (iii) manufacturing and (iv) calibration. This guide should help the reader to make good choices when developing new reference standards for CT dimensional metrology.

7.1 Material choice

A thorough review of existing reference standards for CT dimensional metrology is given in Section 3.4. It can be observed that several materials are applied repeatedly in various standards. In particular, the combination of a **carbon fiber** (CTE=0.2×10^{-6} K^{-1}) support with **ruby spheres** (CTE=5.4×10^{-6} K^{-1}) is used in many standards for performance verification and correction of scale errors. Examples of such objects can be found in Figure 14, namely 27-sphere gauge [49], CT ball plate [22], CT tree [22], tetrahedron [7], mini probe [50], CT crown [52], and CT tube [53]. Carbon fiber and ruby are often selected for several reasons: both the materials are thermally and dimensionally stable, stiff, relatively cheap and when mounted together they provide good contrast in acquired X-ray projections. The latter characteristic is given by the fact that the two materials have significantly different attenuation coefficients; in particular, carbon fiber is almost transparent to X-rays, and, in combination with its other characteristics, is ideal for creating frameworks for various arrangement of precision spheres. Advantage of using ruby spheres pertains mainly to their commercial availability in several precision grades with form errors going down to hundredths of µm (as they are produced for applications e.g. in CMM probing systems). Therefore, they can be easily calibrated with relatively low measurement uncertainty.

Another typical material often used for manufacturing reference standards is **aluminum** (CTE=21-24×10^{-6} K^{-1}). This material offers relatively low CTE and attenuation coefficient, good metrological and long-term stability (stability can be improved by suitable material treatment methods), and since aluminum is widely used in industry, the costs are reasonable. Another advantage of aluminum is its rather good machinability; this allows, compared to ruby or carbon fiber that are difficult to machine, more freedom in designing various features, including sculptured surfaces and complex structures. Furthermore, aluminum can be manufactured with conventional manufacturing processes, such as turning or milling, as well as used by novel technologies, such as die casting, metal injection molding and additive manufacturing (AM). CT metrological reference standards made of aluminum are shown in Figure 15 (hole plate [55]), Figure 16 (“cactus” step gauge [58], prismatic standards with internal features [2]), Figure 18 (step cylinder without a central hole [50], step cylinder with a central hole [62], step wedge [22], hollow cylinders [50]), Figure 20 (aluminum step gauge enclosed in a glass tube [65]), Figure 21 (an assembly of multi-material step gauges [60], multi-material hole cube (MM-HC) [68]), Figure 23 (line pair gauges [36,74], Figure 30 (miniaturized cylinder head [96]). Aluminum was also used for the construction of two standards developed in this Ph.D. project presented in Chapter 4 and Chapter 6.

Titanium (CTE=8.5-9×10^{-6} K^{-1}) offers similar characteristics as aluminum in terms of stability, and CTE. However, the attenuation coefficient is higher, it is more expensive, and manufacturing of titanium by conventional technologies is more challenging. On the other hand, this material is widely used in additive manufacturing [154]. Examples of reference standards made of titanium are shown in Figure 15 (calotte cube [56,57]), and Figure 21 (multi-material hole cube (MM-HC) [68]). Titanium was also used in Chapter 6 for the construction of the proposed reference standard.

Glass materials, such as **zerodur®** (i.e. a glass-ceramic material, CTE=0.1×10^{-6} K^{-1}) or **borosilicate glass** (CTE=3-5×10^{-6} K^{-1}) are used for their metrological stability, low CTE and relatively low attenuation coefficient. However, these materials are brittle and difficult to machine. Therefore, simple geometries, such as (hollow) cylinders and plates with simple features, are typically selected for reference standards made of these materials. Glass-like materials were used for constructing objects e.g. in Figure 17 (pan flute gauge [7], fiber gauge [61]), Figure 20 (aluminum step gauge enclosed in a glass tube [65]), Figure 22 (hourglass standard [70]), Figure 23 (line pair gauges [36,74]).

Similar characteristics as in glass materials can be found in **ceramics**. Typically, ceramic precision spheres (CTE=8×10^{-6} K^{-1}) are used for various applications; examples of such objects are in Figure 14 (tetrahedral reference standard [51]), Figure 21 (multi-material sphere [67]). A ceramic material (SiC/Cesic®, CTE=2.09×10^{-6} K^{-1}) was also used for the construction of the reference standard presented in Chapter 6.

Another group of materials sometimes used for the construction of reference standards are different kinds of **polymers**. These materials offer a wide range of attenuation coefficients suitable for CT scanning, and typically good machinability. Furthermore, polymer objects can be manufactured by various technologies, including AM, injection molding etc. However, for certain polymers, the CTE is rather high (see the range of CTE in Figure 96-d), and, more importantly common polymers are not dimensionally stable from the long-term point of view. This is mainly due to the fact that these materials are sensitive to the environment (e.g. water absorption, etc.). Objects made of polymers can be found in e.g. Figure 21 (multi-material step gauges made of polyetheretherketone (**PEEK**) and polyphenylene sulphide (**PPS**) [60]).

The above-mentioned materials can be characterized as CT scanning-appropriate as their attenuation coefficients are rather low and, therefore, relatively thick materials can be penetrated by typical industrial CT systems. **Steel** (CTE=10-17×10^{-6} K^{-1}), on the contrary, common material used for the construction of reference standards for conventional tactile and optical CMSs is typically less suitable for CT scanning because of its higher attenuation coefficient. It can be, however, used for applications where the contrast is the most important characteristic. More specifically, in cases where only radiographs are analyzed, full penetration of the material is often not even necessary. Examples of such objects can be found in Section 3.4.3 where reference standards for the calibration of CT instrument geometry are introduced, e.g. in Figure 26 (an object composed of plastic square and four slices of high-density material [87]), Figure 27 (an object composed of a plastic plate and two steel balls [88], number of spheres aligned vertically off the rotation axis [89]), Figure 28 (an object composed of steel spheres arranged in two circular patterns or in a helical trajectory mounted on a plastic cylinder, and the candy cane standard). Steel balls were used also in the object proposed in Chapter 5.

It can be seen from the list of different materials used for various reference standards that the choice of the proper material is strongly dependent on the final use of the reference standard. Therefore, the use of the object should be considered in the first place when selecting materials for a specific reference standard.

In order to provide complete information of the most important attribute related to CT scanning, attenuation coefficients of the most typical materials for the construction of CT reference standards are shown in Table 42.

Table 42. Attenuation coefficients for the most typical materials for the construction of CT reference standards [139].

Material	**Attenuation coefficient μ for photon energy in range* 20-200 kV/cm^{-1}**
C	0.98-0.27
Ruby	8.54-0.49
Al	8.85-0.34
Ti	69.42-0.60
Fe	195.11-1.17
SiC	9.98-0.41
Zerodur	6.16-0.32
Borosilicate glass	5.43-0.28
Si_3N_4	9.61-0.44
PEEK	0.66-0.17
PPS	2.95-0.17

* 20-200 kV is a typical range of energy spectrum for common industrial CT systems

The penetrability of a material by X-rays depends on its density and atomic number *Z*. In practice, however, density is typically considered sufficient for assessing material X-ray attenuation properties. Therefore, it must be considered when choosing a proper material. However, as explained in the previous text, defining general range of acceptable densities is not possible; typical materials used in reference standards reviewed in Section 3.4 consist of materials with density ρ ranging from 1000-5000 kg/m^3, and this range is also used for the Ashby charts in Figure 96 for simplicity. However, in cases where full penetration is not required, materials with higher densities, such as steel or lead, can be used.

While required material characteristics, such as machinability, stiffness, yield strength, density, etc., depend on design, final use of the object and other factors, metrological stability is necessary for any material of which an object designed for metrological use is constructed. The most critical characteristic that defines the thermal stability of material is the coefficient of thermal expansion

(CTE). In general, materials with the lowest CTE possible should be selected; the Ashby charts in Figure 96 show materials with CTE up to 30×10^{-6} K^{-1}, which corresponds to a linear expansion by 0.3 µm on a 10 mm length and 1 K temperature difference. However, this value should be considered the upper limit, and materials with lower CTE (around 10×10^{-6} K^{-1} and lower) should be preferred.

a) Overview of material groups within CTE < 30×10^{-6} K^{-1} and ρ < 5000 kg/m^3

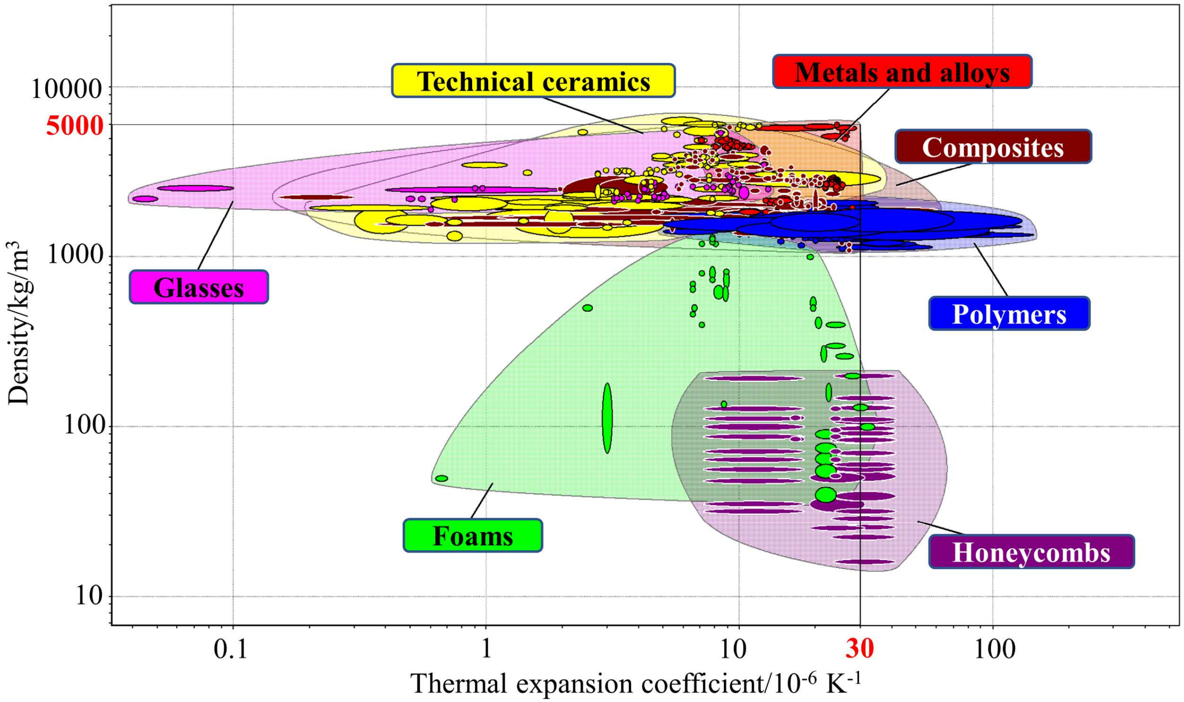

b) Overview of **metals and alloys** within CTE < 30×10^{-6} K^{-1} and ρ < 5000 kg/m^3

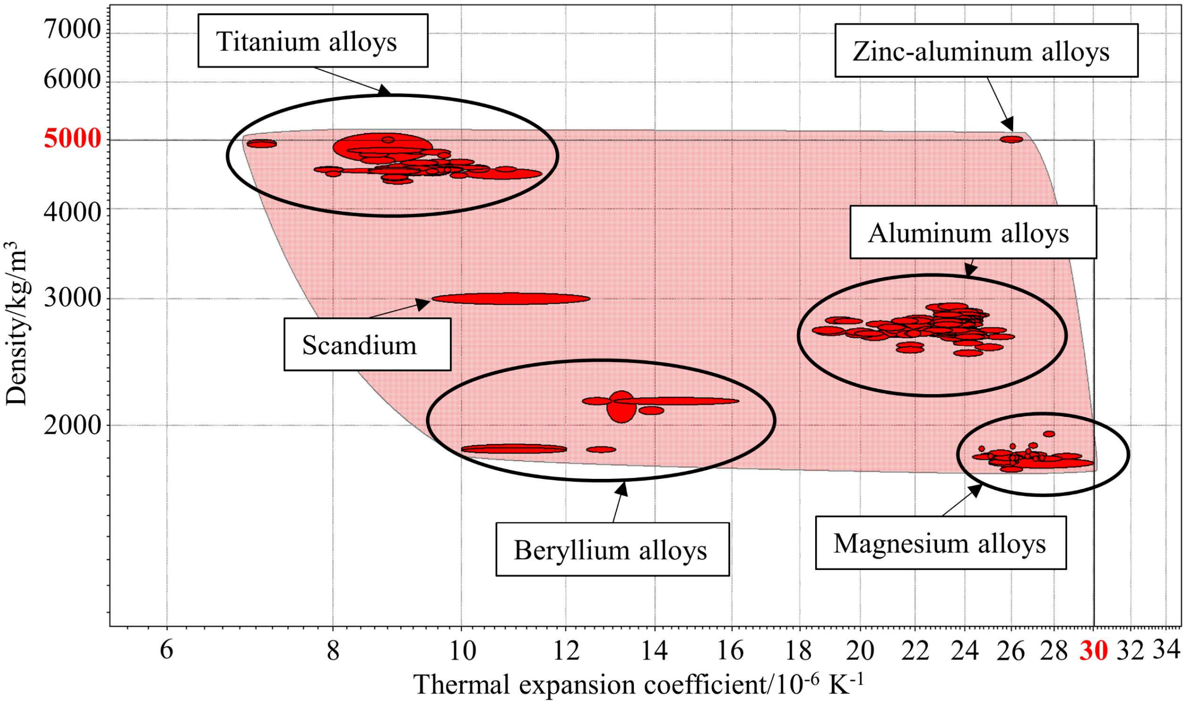

c) Overview of **glasses and technical ceramics** within CTE < 30×10^{-6} K^{-1} and ρ < 5000 kg/m^3

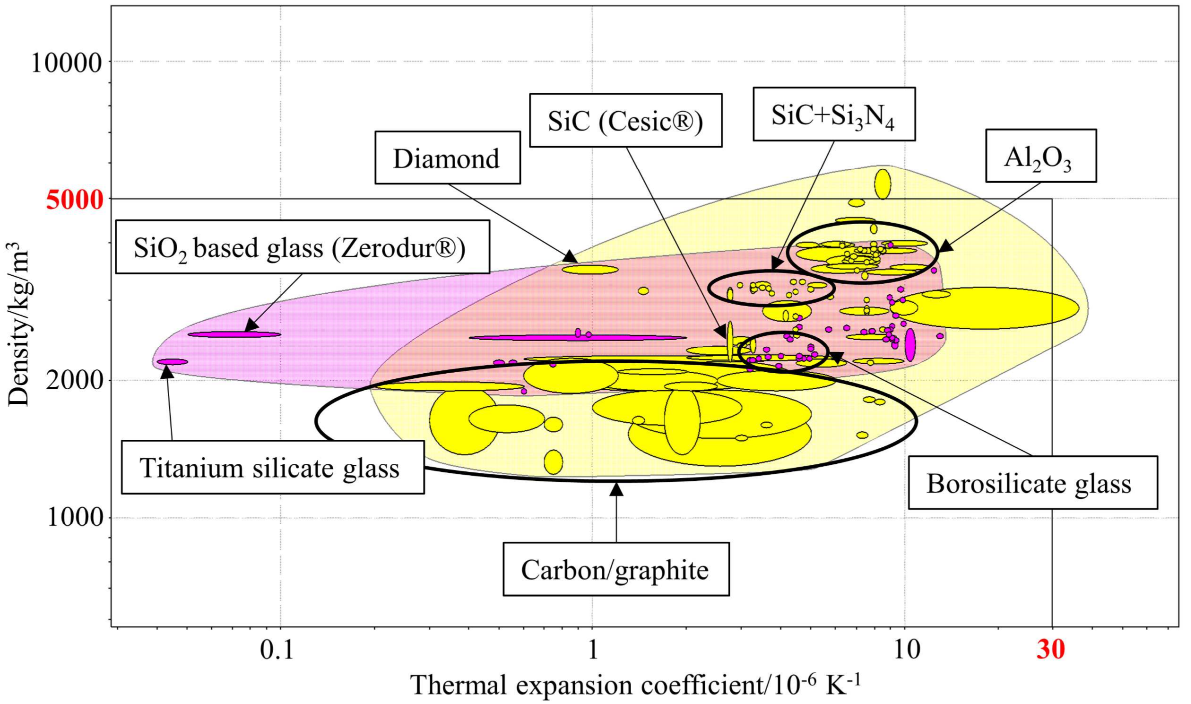

d) Overview of **polymers** within CTE < 30×10^{-6} K^{-1} and ρ < 5000 kg/m^3

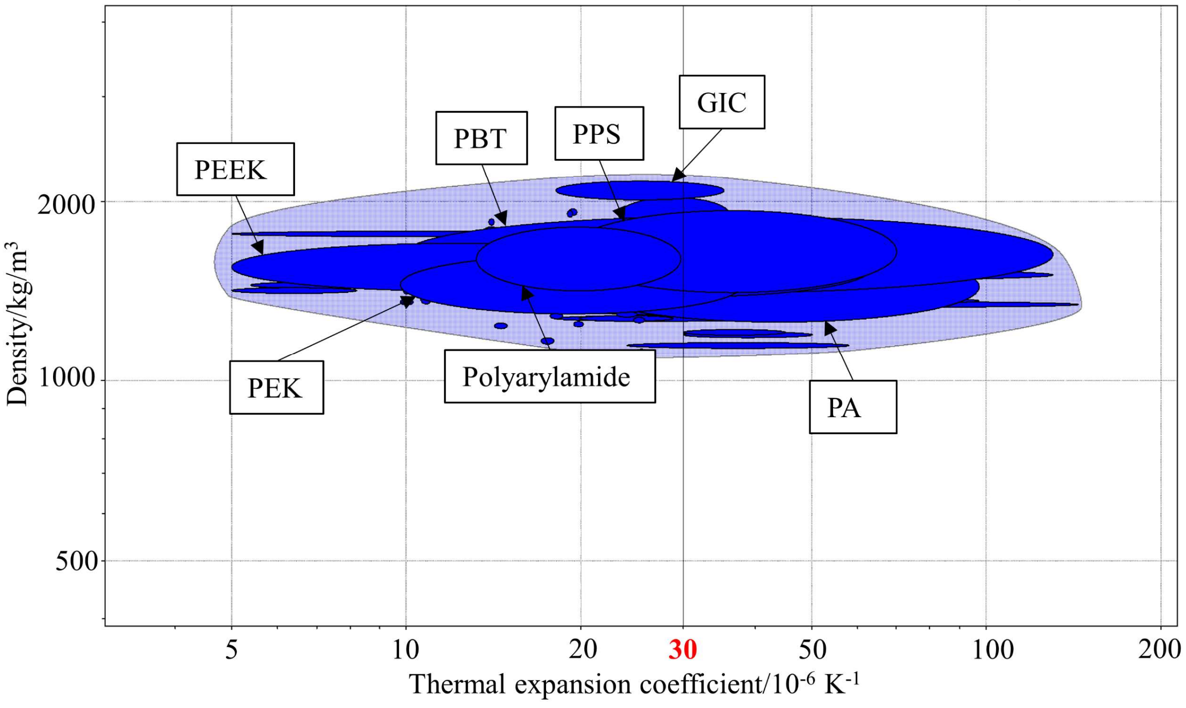

e) Overview of **composites** within CTE < 30×10^{-6} K^{-1} and $\rho < 5000$ kg/m^3

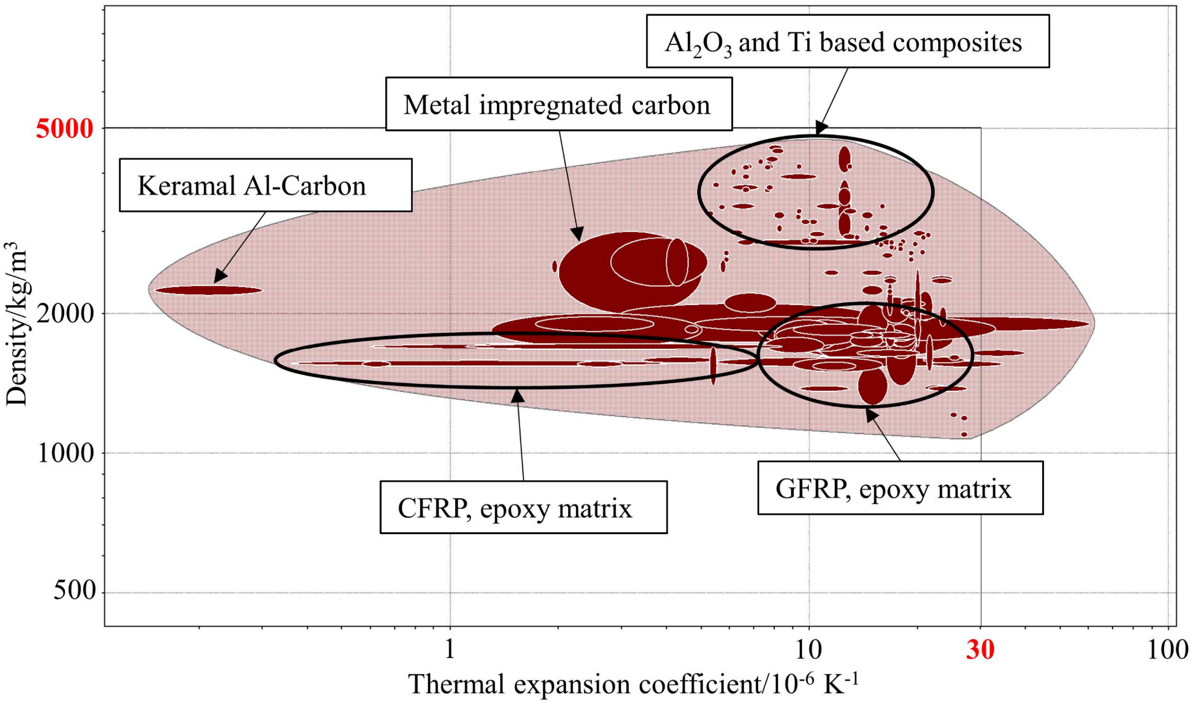

Figure 96. Ashby charts of typical materials suitable for constructing reference standards for CT dimensional metrology. Data were obtained from CES EduPack 2014 [155].

Charts in Figure 96 can be used as a first-step guideline when selecting suitable materials/material groups for a specific object. However, choosing an appropriate material for a reference standard for dimensional metrology in general is not a trivial task. In the case of CT, the problem becomes even more complex as numerous aspects, sometimes contradictory, must be considered. Following factors should be taken in account when choosing the material(s):

1) Intended use of the reference standard.
2) Metrological, thermal and long-term stability of the material.
3) Attenuation coefficient.
4) Possible manufacturing technologies and machinability.
5) Costs.
6) Homogeneity.
7) In case the final object is an assembly, practical consideration regarding connecting individual materials should be taken into account.

Use of the object is at the first place since not only material choice, but also further development phases strongly depend on the way the metrological artifact will be used. In terms of material choice, typical applications of reference standards in CT dimensional metrology can be divided into: (i) radiographic use (i.e. analysis of radiographic projections of the object), (ii) tomographic use (i.e. analysis of the CT reconstructed volume). In the first case, full penetration is not typically required – the aim is to have as much contrast as possible so that fitting of standard features (e.g. lines to edges in the case of objects with plane-parallel features or ellipses/circles to spherical features) is facilitated. Therefore, even materials that are typically not suitable for CT scanning (i.e. materials with high attenuation coefficients) can be used here. Examples of objects composed of high-attenuating materials can be found in Section 3.4.3 (reference standards for the calibration of CT instrument geometry), as many CT instrument geometry estimation techniques are based on analyzing radiographs. This approach is applied also in the method proposed in Chapter 5, where the reference standard is among other materials composed of steel (high-attenuating material) spheres. On the other hand, objects that are used for the evaluation of reconstructed volume should be constructed of materials that ensure good contrast between measurement features and framework, and at the same time sufficient penetrability to ensure low-noise volume with smooth surfaces. For this reason, typically carbon fibers (low-attenuating) are used as a support for other features made from higher-attenuating materials.

Special attention should be dedicated to connecting materials when designing mono- or multi-material assemblies. The connection can be established either as a removable or permanent joint; both solutions have their advantages and shortfalls. Removable joints are typically represented by various screws made of metals or polymers. The advantage of connecting two parts by screws is relative simplicity and reliability. Furthermore, this connection is not permanent, and the object can be dismounted and mounted again, which can be necessary in some cases (see Chapter 4 as an example). However, screws can cause unintentional bending of material, and, in case of screws with small diameters or made of light materials, the screw material can relax and cause instability of the whole assembly. Different CTE of screws and remaining parts can also cause different expansion within the workpiece. Further problems can arise during scanning; if the screw is made of a material with higher attenuation coefficient than the other components, severe image artifacts can appear in projections depending on the difference of attenuation coefficients.

Permanent joints are typically represented by various glues, two-part epoxy adhesives, tapes, etc. In this case, there are usually no problems related to scanning as these materials are typically low-attenuating. However, glues and other adhesives have typically higher CTE (even higher than 100×10^{-6} K^{-1} in some cases). Therefore, even if the other parts of an assembly are made of low-CTE materials, significant instabilities can be introduced by the connecting material. Therefore, the thickness of the connecting material shall be reduced to a minimum in these cases. Further considerations must be also made regarding the choice of proper glue/epoxy; each type is appropriate for connecting different materials; and connecting some materials, such as stainless steel with low surface roughness, is a challenging task. Another point that must be considered is the stiffness of these materials, which is with respect to screws significantly lower.

Since some materials are not suitable for all measuring techniques, the calibration method and measuring instruments should be defined already when selecting the material. For example, soft materials are not suitable for contact-probing (tactile) CMSs, whereas parts with reflective surface or transparent materials should not be measured by some optical CMSs. Furthermore, when using a tactile CMS, chemical reactions or adhesion between the material of the touch probe and the workpiece can occur; e.g. adhesion between aluminum and ruby sphere of a touch probe, when the touch probe gets contaminated by the aluminum pulled-out from the base material.

7.2 Design

Similarly to material choice, the intended use of the reference standard is the most critical aspect when designing a novel metrological artifact. The difference between designs can be clearly seen in the review in Section 3.4, where the reference standards are divided into four groups according to their main use: (i) metrological performance verification and scale correction, (ii) application specific standards, (iii) calibration, and (iv) uncertainty evaluation.

It can be observed that reference standards belonging to the first three groups typically consist of simple features, such as spheres, planes, cylinders etc. There are several reasons for selecting these geometries:

1) Components with these standard shapes (e.g. precision spheres) are available on the market in different materials, with a large range of sizes, various precision grades, surface finish etc., and are relatively cheap.
2) Fitting of geometrical primitives, such as spheres, planes and cylinders, on CT data facilitates the evaluation of results. These elements are well-defined in commercially available software, and their implementation is simple. Furthermore, several modes for fitting the primitives can by typically selected, such as least-squares, Chebyshev, etc.
3) Most of procedures defined in available standards and guidelines related not only to CT dimensional metrology, but dimensional metrology in general, are based on the evaluation of these simple geometries; e.g. ISO/CD 10360-11 [30] suggests variety of reference standards to be used for the metrological performance verification of CT systems, such as multi-sphere objects, hole plates, etc. (i.e. objects composed of simple measurement features).
4) Manufacturing of standard shapes is well defined and established, and usually results in low form errors and good surface quality.
5) Simple geometries also facilitate calibration, since typical procedures used for the evaluation of measurement uncertainty (i.e. methods described in ISO 15530-3 [28] and VDI/VDE 2630-2.1 [29]), a necessary step for any calibration, are based on the use of calibrated workpieces. These standards [28,29] require that a calibrated workpiece, similar to the workpiece to be measured in its dimensions, shape and other characteristics, be used for the establishment of measurement traceability. Calibrated spheres, rings (i.e. cylinders), or prismatic parts (i.e. planes) are available on the market in different materials, sizes, precision grades, and surface quality, and are suitable for transferring the traceability to measurements of simple geometries. On the contrary, calibration of complex and free form shapes is challenging and demands elaborate and often multi-step procedures resulting in higher measurement uncertainties.

The uncertainty of CT measurements is typically evaluated according to standards and guidelines based on the use of calibrated workpieces, i.e. ISO 15530-3 [28] and VDI/VDE 2630-2.1 [29]. The evaluation through determining each source of error and propagating its quantity to uncertainty in the measurement result according to GUM [26] is not possible due to numerous and complex CT influence factors. As required in [28,29], the calibrated workpiece should be similar to the workpiece to be measured including its dimensions, shape, surface finish, wall thickness, material, etc. Therefore, it is not always possible to construct the reference object only from simple geometries. Thus, the fourth group of reference standards presented in Section 3.4.4 (i.e. reference standards for the evaluation of CT measurement uncertainty) includes also objects with complex and internal features, sculptured surfaces, and various surface quality and roughness depending on the quality of the measured workpiece. An example of a reference standard that includes low-quality surface inherent to the production method by which the sample was manufactured, i.e. casting, is shown in Figure 30-d [96] (a miniaturized cylinder head).

Free form surfaces can be also included in objects that are directly dedicated to investigating CT metrological performances in measuring sculptured geometries. Examples of these objects are shown in Figure 97.

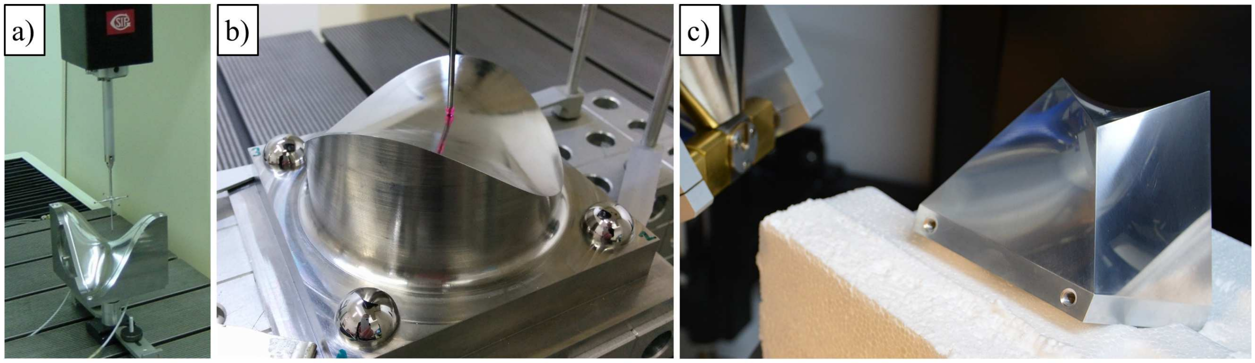

Figure 97. Free form reference standards: a) double-sine PTB standard [156], b) Hyperbolic Paraboloid free form standard (HP) [157], c) Spatial Hyperbolic Paraboloid (SHP) (courtesy of Czech Metrology Institute CMI)

It should be noted that all three artifacts in Figure 97 are composed of geometries that can be mathematically described, which facilitates the calibration and determination of measurement uncertainty.

An interesting approach is introduced in [25,158], where objects with artificial roughness are used for the evaluation of surface roughness influence on CT dimensional measurements. These objects were produced by different manufacturing technologies (turning and Fused Deposition Modelling (FDM)) to achieve different roughness profiles. Schematic representation of these objects is shown in Figure 98.

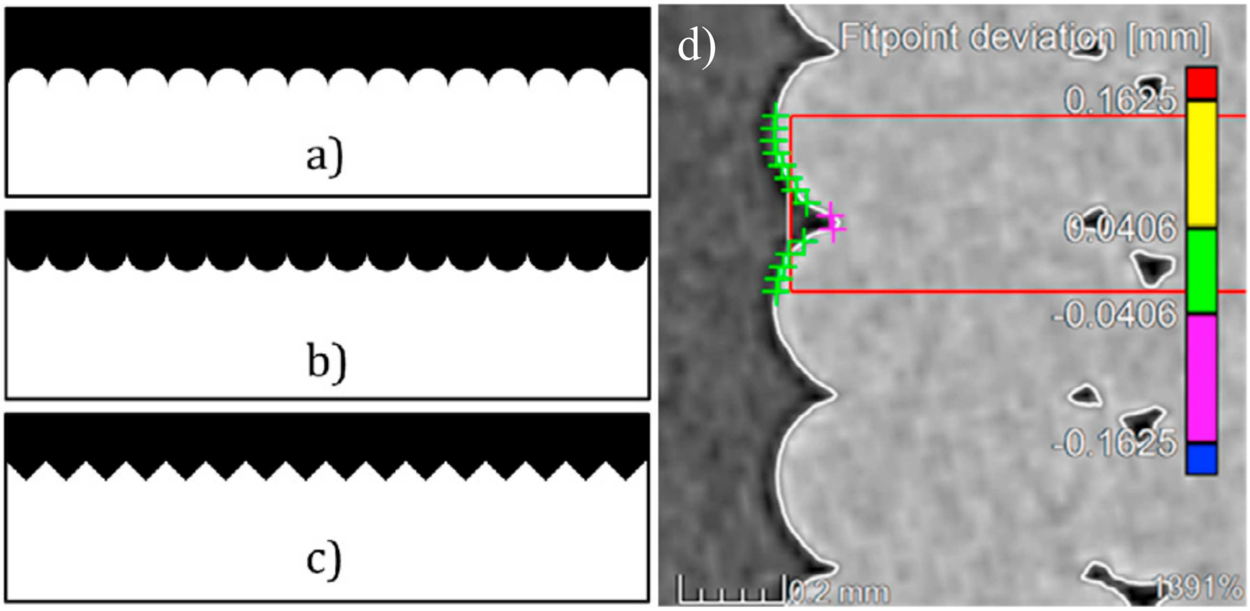

Figure 98. Schematic representation of reference standards with artificial roughness: a) section of FDM produced profile [25], b) section of turned profile [25], c) section of a triangular profile – this profile was not manufactured; it was modelled in a software instead [25], d) example of the evaluation of CT data on the FDM manufactured sample [158].

In many cases, the object does not remain at the developing institution for the lifetime; e.g. the reference standard for CT instrument geometry calibration introduced in Chapter 5 that was used for experiments at a collaborating institution, or inter-laboratory comparisons [7,64,65], where the reference standards were sent to participants. Therefore, the object should be also designed with respect to possible transportation and packaging. Most importantly, the object must be designed in a way that it is possible to protect it from any unintentional damage, and ideally also from vibrations and collisions. Typically, a standard or custom protective shielding is used. Examples of reference standards packaging can be found in Figure 99.

Figure 99. Examples of packaging of reference standards: a) tetrahedron in a sealed box [7], b) pan flute in a sealed box [7], c) calotte cube in a sealed box [7], d) tetrahedron in a membrane box [7], e) open suitcase with reference standards used for CT Audit [7], f) closed and secured CT Audit suitcase [7], g) multi-material assembly of a step gauge sealed in a glass tube used in [65], h) protective box for the step gauge for INTERAQCT comparison on assemblies [65], i) protected reference standard for CT instrument geometry calibration proposed in this Ph.D. thesis.

The objects in Figure 99-a-c were protected from damage and contamination by sealing them in a thin plastic box that was covering the objects even during the scanning [7]. Furthermore, in order to increase the safety, these objects were protected by a membrane box as shown in Figure 99-d, and these boxes were carried in a foam-filled secured suitcase (Figure 99-e, f) [7]. The membrane box shown in Figure 99-d is commercially available and can be used as a simple solution for certain reference standards. During the INTERAQCT comparison on assemblies, step gauges sealed in a glass tube (Figure 99-g) were sent to participants. The objects were protected by a foam-filled box as shown in Figure 99-h [65]. The CT^2 standard presented in Chapter 5 was protected from being damaged by a Plexiglas cylindrical box mounted on the table support. The lid of the box was covered by soft-foam, pushed against the CT^2 and secured by screws. This configuration ensures that the object remains stable during transporting and the spheres are protected from being damaged or detached.

Practical considerations when designing a new reference standard for CT dimensional metrology can be summarized into following steps:

1) The use of the object is critical in the designing phase similarly to the material choice; therefore, the final application of the artifact should be clear before starting designing activities. The measurands of the designed object should reflect the measurands used in the final application.
2) "Smart" geometries, i.e. geometries that combine simplicity and efficiency should be designed; e.g. when defining measurands, continuous measurement features should be preferred instead of discrete ones. An example of benefits when measuring on continuous features is shown in Figure 100, where these two approaches are compared; the object used in the comparison is the gap standard introduced in Chapter 6.

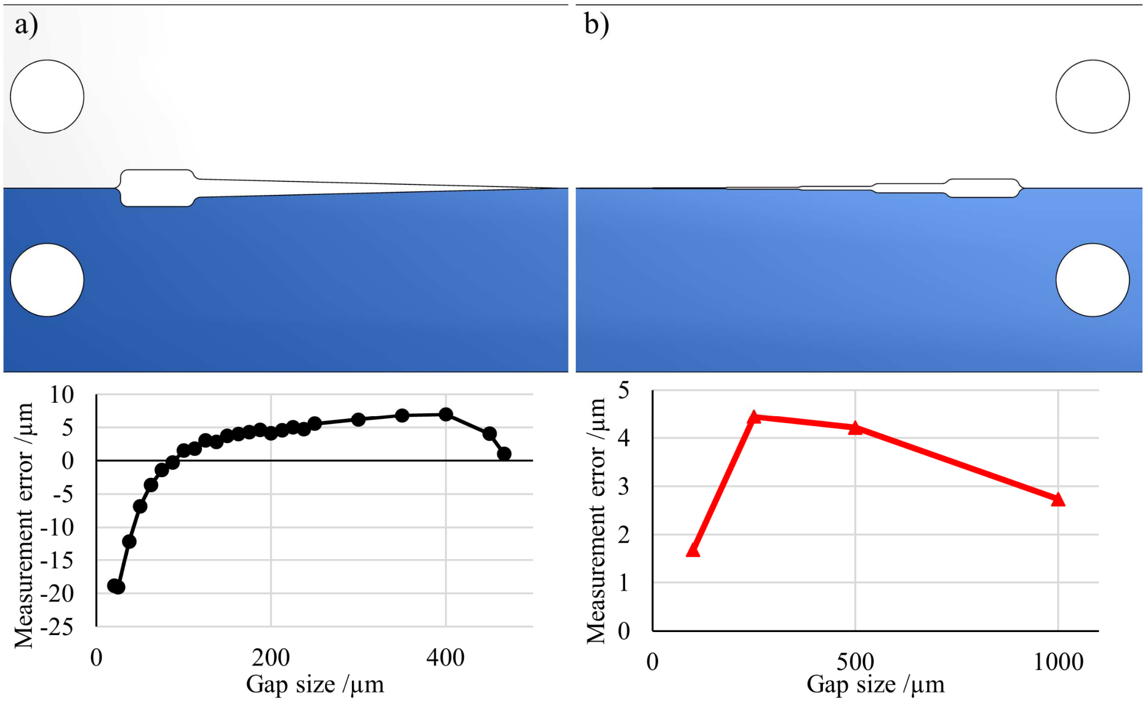

Figure 100. Comparison of measurements measurement results obtained on continuous (a) and discrete (b) features demonstrated on the gap standard developed in this Ph.D. thesis.

It can be seen from the charts at the bottom of Figure 100-a, b that significantly more information can be extracted from the continuous geometries. Furthermore, the limit, i.e. the smallest measurable gap in this case, can be evaluated when using continuous features, whereas the discrete configuration in Figure 100-b limits the resolution of the used method.

3) Standard features, such as spheres, planes and cylinders should be preferred instead of free form surfaces unless the aim is to investigate the free form specific effects. The benefits of

using simple geometries were explained earlier in this section. In special cases, where free form surfaces or high surface roughness is necessary, several factors should be considered:

- In the case of sculptured surfaces, it should be possible to describe these shapes mathematically as explained in the above-text. Alternatively, a breakdown of the complex shape to geometrical primitives should be possible as described in [159] to facilitate the calibration.
- In the case of surfaces with high roughness, it should be possible to characterize their profile according to international standards, e.g. ISO 4287 [122]. An example of such objects is shown in Figure 98 [25,158].

4) Manufacturing should be considered when developing a new design so that the production complexity and costs are reduced; e.g. too tight tolerances should be avoided on features that are not critical for the function of the object, and the features should be distributed in a way that the object can be machined in the lowest number of mountings possible to eliminate possible inaccuracies introduced by re-mounting the workpiece. Furthermore, miniature, high-aspect ratio and internal features require advanced technologies, such as AM, μ-injection molding and μ-machining that can introduce additional aspects, with respect to conventional techniques (e.g. turning, milling, etc.), influencing the manufacturing accuracy.
5) The form error of measurement features should be low and the surface quality should be high with low roughness. An exemption are specific cases where the effects of these characteristics are analyzed; cf. [25,158] where the roughness study is discussed.
6) Dimensions of the object should allow scanning by the available CT system. The size of the object should also be suitable for the intended analyzes; e.g. the highest accuracy can be expected in the central beam (i.e. the plane perpendicular to the rotary axis and intersecting the focal spot) and its vicinity. All other slices are affected by beam artifacts, which are pronounced towards the borders of the detector. However, depending on the aim of the object use and subsequent evaluation, the highest accuracy might or might not be necessary. In specific cases, e.g. extremes of the detector can be the analyzed regions, and the reference standard should be designed considering this requirement. In the case of CT instrument geometry calibration (see Section 3.4.3 for the overview of these reference standards), the aim is typically to cover as large portion of the detector as possible to take into account all possible effects. This applies also to the reference standard presented in Chapter 5, where the object was designed to cover the whole detector. Finally, since the X-ray beam is divergent, the reconstructed model of the object is magnified; the magnification is defined by the distance of the object from the X-ray source and the distance of the X-ray source to the detector. Therefore, the magnification at which the object will be scanned should be also considered. Ideally, the object should be designed in a way that it can be scanned in different magnifications so that also the behavior of CT dimensional measurements in different VS is mapped.
7) The CT scanning is performed by rotating the object and acquiring radiographic projections. Therefore, the scanning volume is cylindrical. Thus, by designing standards with a cylindrical shape, individual projections of the object acquired as a function of the rotary stage angular position cover consistent portion of the detector. Hence, cylindrical shapes should be preferred in order to eliminate the effects of different detector coverage during the rotation.

8) Given the assumptions made in reconstruction algorithms (see Section 2.3 for more details), and the fact that the X-ray beam is polychromatic, beam hardening effects are present in reconstructed volumes. These effects are intensified in case the scanned workpiece is composed of different materials and large differences in wall thickness are present in the object. Therefore, to achieve high-quality CT reconstructed volumes, multi-material assemblies and large differences in wall thickness should be avoided, unless the beam hardening effects (see [22,50,58,59,62]) or multi-material effects (see e.g. Chapter 6 or [60,65,67,68]) are the subject of the study. It should be noted that low-absorbing materials (e.g. carbon fibers) that are typically used for the construction of the framework for various features usually do not cause beam hardening effects.
9) The configuration of the object should be adapted for calibration by other means, typically tactile or optical CMSs. The accessibility of features that should be probed by a tactile CMS should be ensured, as well as the visibility of features that are intended to be measured by an optical CMS. In the case of internal features, the configuration should be dismountable so that the measurement features can be accessed. Examples can be found in Chapter 4 and 6, where a complete dismountable configuration, and a two-step calibration procedure (before and after the assembly) were used. An interesting approach were applied in [96], where a miniaturized cylinder head was cut into four pieces and reference features were mounted and machined on individual parts for defining a datum system (see Figure 30-d).
10) If the object is composed of several components, the connection should be stable; various methods for connecting components were discussed previously in this section.
11) In the case of symmetrical designs, it is critical to break the symmetry by a reference feature that ensures the unambiguous identification of single components. An example is shown in Chapter 5, where the steel balls are arranged in a completely symmetrical arrangement. One additional sphere was used to facilitate the identification of individual spheres.
12) In order to ensure that all components of an assembly are in their correct position, simple features, such as centering pins, can be used for guiding individual parts and keeping them stable until the connection is fixed e.g. by screw or a glue. This approach was used in Chapter 6 for positioning the parts of the multi-material gap standard and also in [68] for assembling the multi-material hole cube shown in Figure 21.
13) The design of a reference standard should be also adapted for safe packaging and transporting as discussed earlier in this section.

7.3 Manufacturing

Whole range of techniques can be used for manufacturing reference standards, namely turning, milling, AM, (micro) injection molding, casting, grinding, electrical discharge machining (EDM), etc. The selection of proper technology depends on the design of the object, the material(s) of which the reference standard is composed and the number of parts to be produced; e.g. turning is suitable for rotational shapes, milling for flat ones, AM for manufacturing internal features, injection molding for multiple and complex geometries, and micro-technologies for micro parts or macro parts with micro features. The accuracy, as well as the surface quality depend not only on the selected technology, but also on the processing parameters. The purpose of this section, however, is not to give a complete overview of available technologies. Instead, the aim of this section is to provide practical considerations related to manufacturing processes and quality requirements.

Typically, reference standards for dimensional metrology are manufactured with high precision, low form errors and high surface quality. This is usually required to minimize the contribution of form errors, surface roughness and other factors to systematic errors and measurement uncertainty. Furthermore, the fact that the calibration of a reference standard is typically performed by other means than CT brings additional effects [29]; i.e. depending on the used sensor (CT, tactile, optical), different physical interaction between the measured surface and the sensor occur resulting in significantly different acquired points. In particular, the filtering of surface roughness differs drastically (as shown also in [25,158]). Therefore, by minimizing surface roughness, its effect on measurement results is minimized as well. For this reason, common reference standards consist of high precision features, such as:

- High precision spheres available on the market in different materials, sufficient size range and different grades. The grades for e.g. steel balls range according to ISO 3290-1 [140] from 3 – 200 with permissible deviation of diameter and form error ranging from 0.08-5 µm, and with surface roughness *Ra* ranging from 0.010-0.150 µm. High precision steel balls were also used for the reference standard developed in Chapter 5
- Cylindrical holes and calottes with low form error and roughness. These features are typically machined by (micro) milling or EDM. Micro milling was used for machining artificial internal defects in the reference standard presented in Chapter 4 and shown in Figure 31. EDM technology was applied to machining calottes in e.g. calotte cube [56,57] shown in Figure 15, and to machining cylindrical holes in the hole plate [55] shown in Figure 15.
- Low-roughness and low-form error planes. Planar geometries can be produced by various technologies, most common of which are milling and EDM. The latter technology was used for manufacturing the multi-material gap standards presented in Chapter 6 and shown in Figure 81-b.

EDM and µ-EDM are used for precision machining (as an alternative to conventional machining technologies, such as turning and milling) since this technique is relatively accurate and good surface quality can be achieved by using this technology. However, this technique requires that the machined material be conductive. Finishing technologies, such as grinding, polishing, lapping, etc., are often used for achieving high quality surfaces.

Designers tend to require tight tolerances on major part of geometries, sometimes just to get rid of the responsibility for proper tolerancing. However, each unnecessary tolerance increases the costs of manufacturing and subsequently of the reference standard. This is especially relevant for the advanced technologies that are typically expensive. Therefore, each manufacturing step should be already discussed with respect to design in order to avoid needless costs. Ideally, the manufacturer (technologist) and designer should collaborate already during the designing phase in order to optimize the design with respect to manufacturing. The collaboration from initial phases of development can save significant amount of expenses and processing time.

It is not always necessary to manufacture perfect features with low roughness and form errors. Depending on the final use, a certain level of form error or surface roughness can be even required in case the reference standard is intended to be used for the evaluation of measurement uncertainty according to VDI/VDE 2630-2.1 [29] and ISO 15530-3 [28]. In these publications, similarity of the calibrated and the measured workpieces is required; therefore, if the sample to be measured contains features with high form errors or surface roughness, these characteristics should feature also the calibrated object. An example of such object is shown in Figure 30-d where a miniaturized cylinder head [96] was produced by casting and consists of low-precision surfaces, as well as surfaces with high roughness.

High-quality manufacturing is also sometimes not necessary for all components of an assembly; e.g. in the case of multi-sphere standards (e.g. shown in Figure 14) where the framework is constructed of carbon fibers, the surface quality of this structure is not relevant with respect to the measurement accuracy, and can be neglected. The same case is the object developed in Chapter 5 (Figure 58), where the surface quality of the carbon fiber tube is low as it is not relevant for the use of the object.

7.4 Calibration

VIM [6] defines calibration as "operation that, under specified conditions, in a first step, establishes a relation between the quantity values with measurement uncertainties provided by measurement standards and corresponding indications with associated measurement uncertainties and, in a second step, uses this information to establish a relation for obtaining a measurement result from an indication". Therefore, in order to carry out a proper calibration, a valid statement of measurement uncertainty must be provided. The method for the evaluation of measurement uncertainty described in GUM [26] requires that each source of error be determined and its quantity propagated to uncertainty in the measurement result.

However, identification and quantification of each error source can be challenging, and in the case of complex features and calibration tasks can become even extremely difficult or impossible. Therefore, alternative procedures based on the use of a calibrated workpiece that is utilized as a means to transfer the measurement traceability are commonly applied. These methods are described in ISO 15530-3 [28] and VDI/VDE 2630-2.1 [29] and were discussed in detail in Section 3.2.2. Procedures described in [28,29] were also used for the calibration of reference standards developed in this Ph.D. thesis, and can be found in Sections 4.3, and 6.3.2. Further examples can be found in various publications, e.g. in [22,95,96], where also so-called "hybrid" approach (i.e. combination of different methods for the evaluation of measurement uncertainty) is applied.

Typically, high-precision conventional tactile and optical (micro) CMSs are used for performing calibration tasks. There are several reasons for using these measurement techniques:

- Tactile and optical CMSs are well-established in industry and dimensional metrology.
- The MPE of high-precision tactile (micro) CMSs, and optical CMSs can go below 1 µm, ensuring low systematic errors.
- The standardization platform is well-defined with respect to CT. Therefore, conventional CMSs are considered more reliable.
- Easier calculation of measurement uncertainty due to the lower number of influence factors.

The calibration procedure should ensure minimization of systematic errors and measurement uncertainty. For this reason, specific methods, such as the method for calibration of ball and hole plates described by German Calibration Service (DKD) [141] and applied e.g. in [142] are used. The procedure described in [141] uses so-called "reversal" methods [54] and is applied for the compensation of systematic measurement errors. The reversal methods are based on multiple measurements changing the relative orientation of the workpiece, which results in different measurement errors in each object position (ideally with opposite signs). This allows calculating the systematic errors and eliminating them from measurement results [54]. The reversal approach was applied in the calibration of the CT^2 standard introduced in Section 5.3. The use of a dedicated calibration procedure introduced in this section allowed calibration of sphere center positions with measurement uncertainty below the MPE of the used tactile CMM. Similar calibration procedures were also used e.g. in [22]. Low calibration uncertainty is critical since the uncertainty of calibration then propagates to the final (CT) measurement results.

Choice of a proper measurement technique is crucial for achieving accurate results and low measurement uncertainty. Certain combinations of shapes and materials, and measurement techniques can result in significant measurement errors; e.g. not all materials are suitable for measurements by all CMSs. Soft materials, for example, should not be measured by tactile CMSs, since the physical probing can cause bending and deflection of the material. Therefore, non-contact techniques should be preferred for this kind of standards. Furthermore, the material of touch probe should be chosen carefully with respect to possible chemical reaction or adhesion with the object material; e.g. ruby touch probes are not suitable for aluminum parts since the ruby can get contaminated by aluminum due to adhesion (i.e. aluminum gets pulled-out from the part by the touch probe). In the case of aluminum, e.g. diamond probes should be used. On the other hand, optical sensors should not be used for measuring reflective surfaces or transparent materials.

Measurement equipment and probing strategies should also be chosen carefully; e.g. when using styli with small diameter, bending and deflection effects can occur when applying too high probing forces. Furthermore, the selection of the proper probe diameter is critical e.g. for morphological filtering of the probed surface as described e.g. in [24,29]. A series of guidelines related to dimensional measurements by CMSs can be found e.g. in [160–163].

Advanced technologies, such as fiber probe sensors can be an interesting solution for measurements of micro features. Fiber probes (Figure 101) are typically mounted on multi-sensor CMSs, and in combination with other sensors represent promising solution for complex geometries.

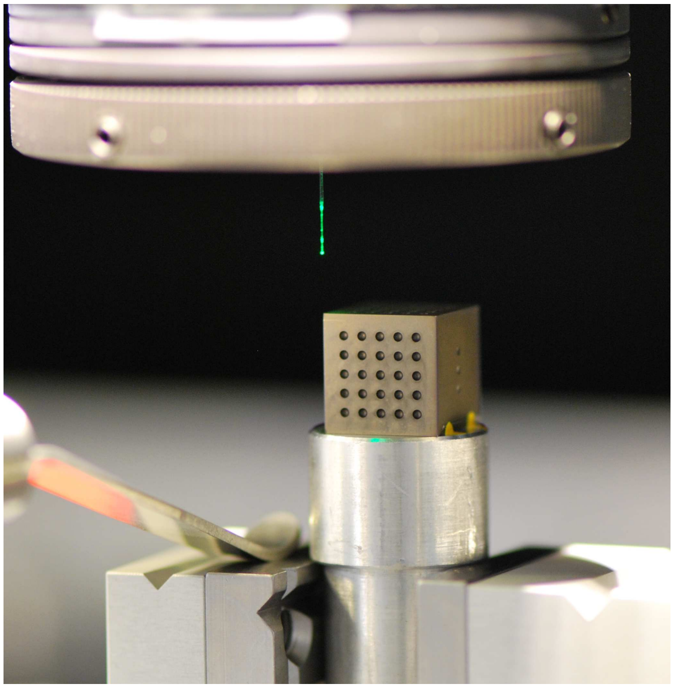

Figure 101. Measurements with fiber probe. Courtesy of PTB.

In some special cases, however, calibration is not even necessary. More specifically, reference standards must be calibrated when they are used for metrological traceability establishment [164]. Methods, so-called "self-calibration" techniques, do not require calibration as described e.g. in [165]. Two simple examples are shown in Figure 102: (i) in Figure 102-a, a closure is used to square the table of a disk sander, (ii) in Figure 102-b, the tilt of the vertical axis of the rotary stage is evaluated by analyzing two projections of an object with plane-parallel features rotated by 180°.

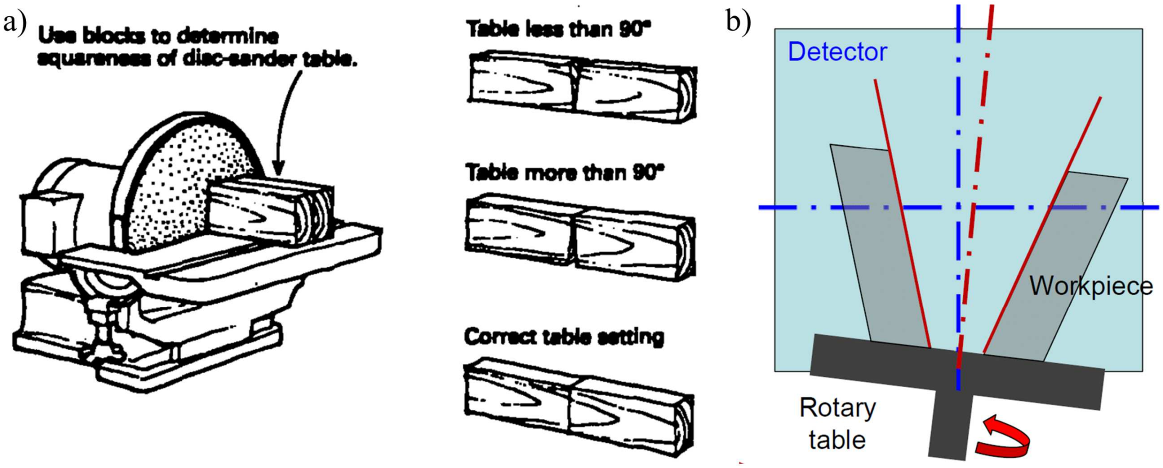

Figure 102. Self-calibration techniques: a) schematic explanation of squaring up the table of a disk sander [165], b) evaluation of the rotary axis tilt [164].

7.5 Conclusions

The main findings and experience related to the development of reference standards for CT dimensional metrology obtained during the Ph.D. project were summarized and organized in this chapter. The structure of the chapter reflects the typical procedure for developing new reference standards, i.e. starting with material choice and following with design, manufacturing, and calibration. Several considerations are suggested in each development step so that the content forms a good practice guide for developing reference standards for CT dimensional metrology.

The development procedure should start with a thorough assessment of the assumed application of the object, whether the object is intended to be used for radiographic or tomographic analyses, and what kind of results are expected to be obtained by using the object. When selecting proper material(s) for constructing the object, its metrological, thermal, and long-term stability should be ensured. Further material characteristics, such as the attenuation coefficient, possible manufacturing technologies, machinability, costs, homogeneity, and possible connection materials, should be also considered. Once careful analysis of the above-mentioned considerations has been carried out, appropriate material(s) for the construction of the reference standard can be selected

Design of the reference standard should be, similarly to the material, selected based on the intended use of the metrological artifact. “Smart” geometries, i.e. geometries that are simple and efficient at the same time should be preferred (e.g. using continuous instead of discrete features). Furthermore, it is recommended to use simple geometries, such as spheres, planes and cylinders to facilitate the fitting of measurement features, and evaluation of results. In cases where sculptured or rough surfaces are used, it should be possible to mathematically describe or characterize them according to international standards, respectively. Manufacturing technologies should be already taken into consideration during the designing phase, and unnecessarily tight tolerances should be avoided. Furthermore, the distribution of features should be optimized with respect to the chosen manufacturing technology and to minimizing re-mounting operations. Dimensions of the object should fit the measurement volume and should be suitable for the intended analyses with respect to the position within the measurement volume and its coverage. Furthermore, dimensions and the overall design should allow scanning in different magnifications to map possible effects related to the voxel size. The shape of the designed object should be ideally cylindrical in order to reflect the form of the CT measurement volume. In order to avoid beam hardening effects, the object should be constructed of one material (or materials with similar attenuation coefficients), and large differences in wall thickness should be avoided. The design should be also optimized with respect to the calibration, i.e. the measurement features should be accessible externally; thus, in the case of internal geometries, the object should be dismountable. Moreover, the stability of assemblies should be ensured, and in case of symmetrical standards, the symmetricity should be eliminated to ensure unambiguous identification of individual features (e.g. by introducing an additional non-symmetrical feature). Finally, the design of the reference object should allow sufficient protection from unintentional damages.

Precision manufacturing is typically required for reference standards applied in dimensional metrology in general. High accuracy and high-quality surfaces can be achieved both by conventional and advanced technologies, such as AM, micro injection molding, EDM, grinding, polishing, etc. Typically, reference standards consist of simple features, such as precision spheres, cylinders and calottes, and planes. Manufacturing technologies, such as milling or (micro) EDM, are usually used for machining the simple geometries. AM is commonly used for objects with internal features, whereas (micro) injection molding is applied for manufacturing parts with complex or micro features. Low form errors and good surface quality are not necessarily required e.g. for objects that are used as calibrated workpieces for the evaluation of measurement uncertainty according to procedures defined by international standards and guidelines. These methods demand calibrated workpieces similar to the parts to be measured; i.e. in case the part under investigation has significant form errors and surface roughness, the calibrated workpiece should have similar characteristics.

Calibration of CT reference standards is usually performed according to methods described in ISO 15530-3 and VDI/VDE 2630-2.1. Since the features and calibration tasks are usually complex, the application of GUM approach, that requires complete knowledge of all influence factors, is challenging and often not possible. For the calibration of reference standards, high-accuracy CMSs with low MPE should be used. Furthermore, advanced measurement techniques, such as reversal methods, should be applied in order to minimize systematic errors and calibration uncertainty. Typically, high-precision tactile and optical (micro) CMSs are used for calibration.

It should be noted, however, that any of the suggestions presented here is not absolutely general; the use of the reference standard is always critical when taking decisions in any phase of the development procedure.

8 CONCLUSIONS

The general conclusions of the Ph.D. work are summarized in this chapter. The Ph.D. thesis can be divided into three parts. In the first part (Chapters 1-3), X-ray computed tomography (CT) as a promising tool for NDT and dimensional metrology was introduced, the basic principles of the technology were explained, as well as the individual steps of CT dimensional measurement chain. Then, the aspects of measurement traceability were discussed and issues pertaining to CT were defined. The observations were supplemented by a summary of existing international standards and guidelines related to CT in general with focus on dimensional metrology, and identification of CT influence factors. Finally, a thorough overview of available reference standards, identified as tools for testing CT systems, evaluating CT specific effects and enhancing CT dimensional measurement traceability, was provided. Based on the overview, several areas where reference standards are missing were identified. In the second part (Chapters 4-6), three reference standards that reflect the lack of metrological artifacts discussed in the first part were developed. All development phases, i.e. material choice, designing, manufacturing and calibration, were described in detail. Furthermore, the novel standards were experimentally applied, and the observations were discussed. In the third part of the thesis (Chapter 7), the experience and findings related to the development of metrological artifacts were summarized to form a good practice guideline for developing reference standards for CT dimensional metrology.

In order to accept CT as a reliable instrument for dimensional metrology, measurement results must be traceable to the SI unit. However, this is still challenging task, due to the lack of international standards, numerous and complex CT influence factors, and the fact that CT is relatively new measurement technique. For the purpose of this project, the process of the metrological traceability establishment was divided into four mainstays: (i) metrological performance verification according to international standards, (ii) metrological performance verification of CT specific applications (a step added in order to cover the versatility of CT technology), (ii) calibration, and (iv) evaluation of measurement uncertainty.
Significant research efforts have been directed towards developing international standards related to CT dimensional metrology. A committee draft of standard from ISO 10360 series related to the acceptance and reverification tests for coordinate measuring systems focused on CT systems is under development. It applies similar principles that are present in tests related to conventional optical and tactile CMSs. However, the standard has not been finalized and published yet.
Several approaches for evaluating the uncertainty of CT dimensional measurements (necessary for achieving the metrological traceability) have been tested. The method proposed by GUM requires that each source of error be determined and its quantity propagated to uncertainty in the measurement result. Given the complex nature and amount of CT influence factors, this method is typically not applicable. Therefore, alternative empirical approaches based on the use of a calibrated workpiece similar to the investigated part are used. The methods are explained in ISO 15530-3 and in VDI/VDE 2630-2.1. Further procedures, such as computer simulation according

to the Supplement 1 of GUM, or uncertainty budget as per ISO/IEC GUIDE 98-3 can be also applied, although their use is not so common.

The possibility to achieve the traceability of CT measurements, and to study CT specific effects through dedicated reference standards, similarly to other CMSs, was discussed in Section 3.4. The objects were divided into four groups corresponding to the previous division of steps towards the traceability of CT measurements: (i) metrological performance verification and scale correction, (ii) metrological performance verification of CT specific applications, (iii) calibration, and (iv) uncertainty evaluation.

Since CT is a multi-purpose device, and several analyses can be performed on a CT data set simultaneously, the metrological performance of individual inspection tools should be verified. One of important CT applications is the detection and evaluation of internal porosity; a reference standard that was developed in this Ph.D. thesis for studying this CT application, and experimental results are presented in Chapter 4.

Calibration of CT instrument for any task is not possible due to numerous and complex errors sources. An important contribution to measurement uncertainty comes from geometrical misalignments. While several standards for estimating geometrical parameters exist, calibration of these parameters, i.e. the measurement by comparison to a traceable reference, has not yet been achieved. Therefore, a reference standard for the calibration of CT instrument geometry was developed and presented, together with a calibration method and experimental results, in Chapter 5.

It was observed that major part of standards for metrological performance verification is focused on mono-material measurements; however, multi-material effects are critical for CT dimensional metrology, and should be further investigated. Hence, a multi-material reference standard was developed and the specific multi-material effects were discussed in Chapter 6.

The reference standard developed for the establishment of CT porosity measurements traceability and for evaluating their accuracy was presented in Chapter 4. The standard is made of aluminum and consists of a cylindrical body and four removable pins. Hemispherical calottes are milled on the faces of pins so that they form artificial internal porosity at the interface of the pin faces and the bottom of the hole drilled in the body when mounted together. A method to establish the traceability of CT internal porosity measurements was presented here. The method is based on the novel reference standard calibrated following a dedicated multiple-step procedure, and on an approach adapted from international standards and guidelines (ISO 15530-3 and VDI/VDE 2630-2.1). Measuring instruments based on different measuring principles (tactile, optical, CT) were used to calibrate the object to minimize the calibration uncertainty, and thus also the uncertainty of subsequent measurements; the values of expanded calibration uncertainties evaluated with a confidence level of 95 % for diameter D, depth Z and volume V of a defect are 2.1 µm, 1.4 µm and 1.6 % of the measured volume, respectively.

The reference standard was then used for a thorough evaluation of the accuracy of CT porosity measurements (Section 4.4) and the observations were summarized as follows:

- CT scanning parameters can significantly influence CT porosity measurement errors particularly when measuring small defects; the variation caused by scanning with a given range of tube voltage and current was up to 4 µm and 3 % for defect diameter and depth, and volume, respectively. In general, by using higher voltage and current, lower errors were obtained; therefore, higher values of these parameters should be preferred. However, it should be noted that higher tube power can result in larger focal spot size, and thus in lower resolution. The two main reasons for the improvement in measurements with higher tube voltage and current are: (i) the image noise decreases with increasing the tube current; (ii) the generation of X-rays increases with the square of the tube voltage, i.e. by increasing voltage, lower noise and better contrast can be achieved in the acquired projections.

- The results obtained on 12 repeated scans showed that measurements of smaller defects are more problematic; more specifically, mean errors obtained on smaller defects were up to 5 µm and 10 % for diameter and depth, and volume measurements, respectively, whereas they were below 2 µm and 5 % for larger defects. The standard deviations calculated on the set of 12 scans followed the same trend, i.e. up to 11 µm and 6 % for smaller and around 2 µm and 2 % for larger defects.
- The results were validated by a simulation study, which resulted in similar trends. The magnitude of errors, however, was lower with respect to experiments as the simulations did not cover the whole range of influence factors present in real CT scanning.
- Performances of three different software tools in evaluating the internal porosity on CT data were compared; the lowest measurement errors were obtained by using VGStudio MAX.
- CT systematically evaluated the volume of individual defects with a positive deviation; i.e. it measured larger volumes compared to the calibrated values. This effect is caused by averaging, lower sharpness of CT data and decrease of information content with decreasing magnification.

The possibility to reduce systematic errors of CT porosity measurements by optimizing the threshold value was also discussed (Section 4.4.6). While ISO-50% threshold value (the average gray value between the material and the background peak) is used by default, the lowest measurement errors were achieved using ISO-35%, which was subsequently suggested as the optimized value for the specific configuration and workpiece material – aluminum.

The reference object with artificial porosity was also used for improving the accuracy of CT porosity measurements obtained from an industrial part (Section 4.5). The procedure is based on initial information of total void content calculated on the reference standard and its comparison with the calibrated value. Based on the deviation, the threshold value is iteratively modified until the error converges to a defined limit. The optimal value is then used for the evaluation of porosity inside the sample under investigation. Results evaluated on the experimental data (Section 4.5.4) showed that significantly different defect volumes can be obtained when using threshold values calculated considering the whole dataset and the region containing only the analyzed sample. The total void content evaluated using the two different threshold values resulted in deviations equal to -12 % and +6 % from the optimized value evaluated according to the proposed procedure.

A method to use the optimization procedure in industry was proposed (Section 4.5.3). A set of reference standards covering the material range in production should be manufactured and calibrated. These standards should be scanned either before the scan of the investigated part or, more preferably, together with the part. The threshold value can be optimized following the proposed iterative procedure, thereby reducing the systematic errors of CT porosity evaluation. Furthermore, by comparing the measured values obtained from the reference standard to the calibrated ones, and by evaluating the measurement uncertainty according to procedures defined in ISO 15530-3 and VDI/VDE 2630-2.1, the traceability of CT porosity measurements obtained from the investigated (industrial) part can be achieved.

The outputs presented in Chapter 4 prove the high capability of CT in evaluating internal voids and porosity. Furthermore, a method to achieve the traceability of CT porosity measurements was developed and a procedure to facilitate its application in industry was proposed.

The standard designed for the calibration of CT instrument geometry, so-called CT Calibration Tube (CT^2) was developed in Chapter 5. The object is composed of 49 steel balls attached on a carbon fiber cylinder. The spheres are arranged in a dedicated spatial pattern ensuring optimized distribution of projected markers on radiographic images, and reducing overlapping sphere projections at the same time. The standard is adapted for both static (i.e. projections are acquired in one angular position of the object) and dynamic (i.e. projections are acquired in multiple angular position of the object) use. The CT^2 standard was calibrated (Section 5.3.3) by a tactile CMM using so-called reversal methods to minimize systematic errors and calibration uncertainty.

The estimation of CT geometrical parameters was carried out by minimizing reprojection errors (Section 5.4), which is based on comparing modelled and observed projection data of the reference standard. The performance of the CT^2 standard was compared to a state-of-the-art equivalent through a simulation study (Section 5.5). The outputs of the study show not only strong agreement between simulated and minimized geometrical parameters, but also that the CT^2 standard outperformed the equivalent standard in six out of seven parameters in terms of deviation from the nominal value. To satisfy the requirements given by the definition of the term “calibration”, a Monte Carlo approach was implemented to assess uncertainty in the measured geometrical parameters (Section 5.6).

The method for calibrating CT system geometry was validated by experiments performed on a custom CT system (Section 5.7). Several detector misalignments were applied to the CT system detector and the CT system geometry was solved by minimization in each step. In the final phase, the system was aligned to its nearly ideal geometry following an iterative procedure (Section 5.7.1), where in each iterative step the residual misalignments were evaluated and corrected in the subsequent step. The ability to align the CT system was demonstrated by evaluating the errors of sphere center to center distance (SD) measurements obtained from reconstructed data sets of the CT^2 standard. Several observations were made based on the results:

- typical commercial reconstruction software can correct the horizontal detector offset and the detector in-plane rotation error, and fails in other geometrical misalignments. Furthermore, the commercial correction method was proven unstable; the method proposed here is stable, and can solve the complete CT instrument geometry.
- It was possible to align the CT system to its nearly ideal geometry, which was validated by significantly reducing SD measurement errors.
- The ability to modify the alignment of the CT system in a controlled way was proved by comparing misalignments introduced to the detector physically and misalignments calculated by the minimization; the largest deviation between introduced and minimized detector rotation was lower than 0.025°.

Furthermore, so-called FlexCT algorithm was used for the software-based correction of reconstructions (Section 5.7.2). Individual datasets representing different detector misalignments were reconstructed taking into consideration the CT system geometrical parameters evaluated by the minimization procedure, and SD measurement errors were evaluated. The errors obtained from FlexCT reconstructions were reduced with respect to those reconstructed by VG independently from the misaligned angle and the magnitude of the applied rotation; the errors were below ± 5 µm which confirms excellent performance of the minimization procedure in combination with the FlexCT reconstruction.

The outputs obtained on the CT^2 standard showed a great potential of the proposed method in calibrating CT system geometry. Furthermore, the comparison between physical and software alignment showed that the software one results in slightly lower SD measurement errors. Given this fact, a holistic CT system geometry alignment procedure – using the complete set of tools presented in Chapter 5 (i.e. the CT^2 standard, the minimization procedure and FlexCT) – was proposed: an iterative physical "rough" alignment is made in the first step, and the FlexCT algorithm along with residual misalignments calculated by minimization can be used for the "fine" correction of the reconstructed volume.

Multi-material measurements were addressed in Chapter 6; more specifically, after a thorough analysis of possible multi-material measurement scenarios, and after considering the research already being performed in this field, the multi-material gap measurements were selected. For this purpose, a series of mono- and multi-material reference standards was designed and manufactured. The samples were made of aluminum, titanium and carbon-reinforced silicon carbide (SiC). The gaps are formed by two identical opposing surfaces featuring discrete steps and tempered surfaces. The gap sizes range from theoretically 0 µm to 1000 µm. The reference standards were calibrated using a high-precision tactile micro-CMS (Section 6.3.2).

Experiments were performed to evaluate the performance of CT in multi-material gap measurements (Section 6.4). Furthermore, different surface determination techniques were applied in order to investigate their influence on measurement results. Individual methods and multi-material effects were evaluated by comparing the measured values to the reference ones, and by measuring the smallest measurable gap. Several observations were made based on the results (Section 6.4.3):

- In general, local adaptive thresholding resulted in lower measurement errors.
- Multi-material effects were reduced by using local adaptive thresholding as well. However, the sample made of materials with the highest difference between attenuation coefficients (Ti/Al) demonstrated the highest errors even using local adaptive thresholding. Furthermore, the trends of measurement errors on this sample were different compared to other assemblies. The increase of measurement errors was most significant for the smallest gaps.
- Measurements on mono-material samples made of materials with high attenuation coefficients (Ti/Ti) resulted in systematically higher errors than on other mono-material samples; this behavior confirms that also mono-material effects influence measurement errors.
- The smallest measurable gap was also influenced by the multi-material effects; more specifically, the smallest gap measured on the Ti/Al sample, irrespectively of the surface determination procedure, was four times larger than the smallest gap measured on other samples.

A complementary study performed on the series of reference standards to investigate the multi-material influence on mono-material unidirectional measurements was performed (Section 6.4.3). Results from this study confirmed the above-mentioned observations; i.e. that the measurement results obtained on the Ti/Al sample (i.e. the sample with high difference in attenuation coefficients) suffer from multi-material effects. Errors obtained on the critical Al part were significantly higher with respect to other samples.

Since the existence of multi-material influence on measurement results was proven, an alternative dual-energy CT (DECT) approach was used to improve the scan quality, and subsequently also the measurement results (Section 6.5). Only multi-material samples (Ti/Al and Al/SiC) were included in this study. The results (Section 6.5.3) obtained especially on the Ti/Al sample showed that the image quality can be improved by DECT; the contrast on the critical Al part was increased by 20 %. As a result, it was possible to measure smaller gaps with respect to the conventional scanning. This proved that by using DECT, an improvement in measurement results on multi-material workpieces can be achieved. However, due to the nature of the DECT fusing algorithm, the image quality is sensitive to the stability of the focal spot/sample during scanning. Given the fact that there was a non-negligible instabilty of the sample projection between low- and high-energy scans, higher errors were measured on DECT data sets. While significant improvement with respect to the smallest measurable gap was achieved on the Ti/Al sample, results obtained on the Al/SiC sample were similar for both scanning methods.

The study performed on the multi-material gap standards in Chapter 6 confirmed the existence of additional multi-material effects that influence the measurement results. A DECT approach showed potential to reduce these effects; however, in order to implement the proposed methods for dimensional metrology, further steps must be performed to eliminate the error caused by the instability of the focal spot/sample during scanning.

In Chapter 7, four main steps in developing new reference standards for CT dimensional metrology were described. Suggestions related to material choice, design, manufacturing, and calibration of reference standards were summarized so that users and/or researchers interested in developing new metrological artifacts should be able to make good choices with respect to individual development steps.

8.1 Outlook

Further research in terms of reference standards should be oriented towards multi-purpose artifacts that integrate features suitable for performing different types of CT system testing and characterizing CT specific aspects. By integrating different tasks into one object, the establishment of measurement traceability can be significantly simplified.

Furthermore, effects of various influence factors described in Section 3.3 have not been investigated sufficiently or at all. These effects should be quantified in order to understand their influence on measurement results as required in GUM. In order to understand these factors, new reference standards should be developed to study them.

CT specific applications were discussed in Section 3.4.2, and a reference standard for testing the performance of CT porosity measurements was developed in Chapter 4. However, reference standards for verifying CT metrological performances in e.g. fiber analysis, wall thickness analysis and other CT-related analyses are missing and should be developed. Furthermore, accuracy of these applications should be evaluated and measurement traceability should be established using, for example, the same way as described in Chapter 4.

Complete calibration of CT system for any measurement task is not possible due to the numerous and complex CT influence factors (described in Section 3.3). One of these factors, calibration of CT instrument geometry was studied in Chapter 5. However, even if effects of various factors have been investigated, calibration as per the definition of the term (i.e. measurement by comparison to a traceable reference) has not yet been demonstrated for the major part of them. Therefore, reference standards that ensure “complete” calibration of individual influence factors should be developed.

A thorough study of multi-material effects on gap measurements was performed in Chapter 6. Further research should be directed towards applying different techniques for surface determination and data (material) separation. Additional experiments with the Ti/SiC sample should be performed in order to confirm the trends observed on the Ti/Al object that has similar material properties. Moreover, further experiments and CT scans with different CT settings and sample orientations need to be performed in order to isolate the multi-material effects and gain a comprehensive overview of the problem. Another aspect that should be addressed in future research is the multi-material effect on structural resolution, since the configuration of the reference standard allows measurements on a continuous feature with gaps ranging from 500 μm to theoretically zero. Finally, in order to gain robust measurement results, the evaluation of the test uncertainty should be performed in subsequent works.

REFERENCES

[1] VDI/VDE 2630-1.1 Computed tomography in dimensional measurement - Basics and definitions. VDI/VDE Society for Metrology and Automation Engineering, 2009.

[2] Kruth J-P, Bartscher M, Carmignato S, Schmitt R, De Chiffre L, Weckenmann A. Computed tomography for dimensional metrology. CIRP Annals - Manufacturing Technology 2011;60:821–42. doi:10.1016/j.cirp.2011.05.006.

[3] Hsieh J. Computed Tomography - Principles, Design, Artifacts, and Recent Advances. Second. Bellingham: SPIE; 2009.

[4] De Chiffre L, Carmignato S, Kruth J-P, Schmitt R, Weckenmann A. Industrial applications of computed tomography. CIRP Annals - Manufacturing Technology 2014;63:655–77. doi:10.1016/j.cirp.2014.05.011.

[5] European Commission's 7th Framework Programme FP7-PEOPLE - Grant agreement No 607817. INTERAQCT 2013. https://www.interaqct.eu/ (accessed October 21, 2017).

[6] BIPM, IEC, IFCC, ILAC, ISO, IUPAC, et al. JCGM 200 International vocabulary of metrology — Basic and general concepts and associated terms (VIM). International Organization for Standardization, 2008. doi:10.1016/0263-2241(85)90006-5.

[7] Carmignato S. Accuracy of industrial computed tomography measurements: Experimental results from an international comparison. CIRP Annals - Manufacturing Technology 2012;61:491–4. doi:10.1016/j.cirp.2012.03.021.

[8] Bartscher M, Hilpert U, Goebbels J, Weidemann G. Enhancement and Proof of Accuracy of Industrial Computed Tomography (CT) Measurements. CIRP Annals - Manufacturing Technology 2007;56:495–8. doi:10.1016/j.cirp.2007.05.118.

[9] Schmitt R, Niggemann C. Improving the Production using X- Ray Computed Tomography - Potentials and Challenges. National Conference on CT Scanning - Application of CT Scanning in Industry 2011.

[10] Christoph R, Neumann HJ. X-ray Tomography in Industrial Metrology 2011. http://www.werth.de (accessed October 21, 2017).

[11] Buzug TM. Computed Tomography - From Photon Statistics to Modern Cone-Beam CT. Berlin: Springer; 2008. doi:10.1007/978-3-540-39408-2.

[12] Tan Y. Scanning and Post-Processing Parameter Optimization for CT Dimensional Metrology. KU Leuven, 2015.

[13] Bioclinica. The Evolution of CT Scan Clinical Trials 2011. http://www.bioclinica.com/ (accessed June 26, 2017).

[14] Tesla Memorial Society of New York 1979. http://www.teslasociety.com/pbust.htm (accessed June 26, 2017).

[15] Carmignato S, Dewulf W, Leach R. Industrial X-Ray Computed Tomography. Springer; 2017. doi:10.1007/978-3-319-59573-3.

[16] Poludniovski G, Evans P, DeBlois F, Landry G, Verhaegen F. SpekCalc 2009. http://spekcalc.weebly.com/ (accessed June 27, 2017).

[17] Ciernak R. Technical Concepts of X-ray Computed Tomography Scanners. 2011. doi:10.1007/978-0-85729-027-4.

[18] Stock SR. MicroComputed Tomography: Methodology and Applications. 2008. doi:doi:10.1201/9781420058772.fmatt.

[19] Ferrucci M, Leach RK, Giusca CL, Carmignato S, Dewulf W. Towards geometrical calibration of X-ray computed tomography systems - A review. Measurement Science and Technology 2015;26. doi:10.1088/0957-0233/26/9/092003.

[20] Feldkamp LA. Practical cone-beam algorithm. Optical Society of America 1984;1:612–9.

[21] Radon J. On the determination of functions from their integral values along certain manifolds. IEEE Transactions on Medical Imaging 1986;5:170–6. doi:10.1109/TMI.1986.4307775.

[22] Müller P. Coordinate metrology by traceable computed tomography. Technical University of Denmark, 2012.

[23] VDI/VDE 2630-1.2 Computed tomography in dimensional measurement - Influencing variables on measurement results and recommendations for computed-tomography dimensional measurements. VDI/VDE Society for Metrology and Automation Engineering, 2010.

[24] Carmignato S, Savio E. Traceable volume measurements using coordinate measuring systems. CIRP Annals - Manufacturing Technology 2011;60:519–22. doi:10.1016/j.cirp.2011.03.061.

[25] Carmignato S, Aloisi V, Medeossi F, Zanini F, Savio E. Influence of surface roughness on computed tomography dimensional measurements. CIRP Annals - Manufacturing Technology 2017. doi:http://dx.doi.org/10.1016/j.cirp.2017.04.067.

[26] BIPM, IEC, IFCC, ILAC, ISO, IUPAC, et al. JCGM 100 Evaluation of Measurement Data—Guide to the Expression of Uncertainty in Measurement. International Organization for Standardization, 2008.

[27] VDI/VDE 2630-1.3 Computed tomography in dimensional measurement - Guideline for the application of DIN EN ISO 10360 for coordinate measuring machines with CT sensors. VDI/VDE Society for Metrology and Automation Engineering, 2011.

[28] ISO 15530-3 Geometrical product specifications (GPS) - Coordinate measuring machines (CMM): Technique for determining the uncertainty of measurement - Use of calibrated workpieces or measurement standards. International Organization for Standardization, 2011.

[29] VDI/VDE 2630-2.1 Computed tomography in dimensional measurement - Determination of the uncertainty of measurement and test process suitability of coordinate measurements systems with CT sensors. VDI/VDE Society for Metrology and Automation Engineering, 2015.

[30] ISO/CD 10360-11 Geometrical Product Specifications (GPS) - Acceptance and

reverification tests for coordinate measuring systems (CMS): CMMs using the principle of computed tomography (CT). International Organisation for Standardization, 2017.

[31] VDI/VDE 2630-1.4 Computed tomography in dimensional metrology - Measurement procedure and comparability. VDI/VDE Society for Metrology and Automation Engineering, 2010.

[32] ISO 15708-1 Non-destructive testing — Radiation methods — Computed tomography - Principles. International Organisation for Standardization, 2002.

[33] ISO 15708-2 Non-destructive testing — Radiation methods — Computed tomography — Examination practices. International Organisation for Standardization, 2002.

[34] EN 16016-1 - Non Destructive Testing - Radiation method - Computed tomography - Terminology. European Committee for Standardization, 2011.

[35] EN 16016-2 - Non Destructive Testing - Radiation method - Computed tomography - Principle, equipment and samples. European Committee for Standardization, 2011.

[36] EN 16016-3 - Non Destructive Testing - Radiation method - Computed tomography - Operation and interpretation. European Committee for Standardization, 2011.

[37] EN 16016-4 - Non Destructive Testing - Radiation method - Computed tomography - Qualification. European Committee for Standardization, 2011.

[38] ASTM E 1441 Standard Guide for Computed Tomography (CT) Imaging. ASTM International, 2011.

[39] ASTM E 1695 Standard Test Method for Measurement of Computed Tomography (CT) System Performance. ASTM International, 1995.

[40] ASTM E 1570 Standard Practice for Computed Tomographic (CT) Examination. ASTM International, 2011.

[41] ASTM E 1672 Standard Guide for Computed Tomography (CT) System Selection. ASTM International, 2012.

[42] ISO 10360-2 Geometrical Product Specifications (GPS) — Acceptance and reverification tests for coordinate measuring machines (CMM) — CMMs used for measuring size. International Organisation for Standardization, 2001.

[43] Illemann J, Bartscher M, Jusko O, Härtig F, Neuschaefer-Rube U, Wendt K. Procedure and reference standard to determine the structural resolution in coordinate metrology. Measurement Science and Technology 2014;25. doi:10.1088/0957-0233/25/6/064015.

[44] Zanini F, Carmignato S. Two-spheres method for evaluating the metrological structural resolution in dimensional computed tomography. Measurement Science and Technology 2017;28. doi:https://doi.org/10.1088/1361-6501/aa85b7.

[45] ISO 10360-8 Geometrical product specifications (GPS) — Acceptance and reAcceptance and reverification tests for coordinate measuring systems (CMS) — CMMs with optical distance sensors. International Organisation for Standardization, 2013.

[46] ISO 14253-1 Geometrical Product Specifications (GPS) - Inspection by measurement of workpieces and measuring equipment - Decision rules for proving conformance or non-conformance with specifications. International Organisation for Standardization, 1998.

[47] BIPM, IEC, IFCC, ILAC, ISO, IUPAC, et al. JCGM 101 Evaluation of measurement data — Supplement 1 to the " Guide to the expression of uncertainty in measurement " — Propagation of distributions using a Monte Carlo method. International Organisation for Standardization, 2008.

[48] ISO/IEC GUIDE 98-3 Uncertainty of measurement. Guide to the expression of uncertainty in measurement. International Organisation for Standardization, 2008.

[49] Lettenbauer H, Georgi B, Weiß D. Means to verify the accuracy of CT systems for metrology applications (in the absence of established international standards). International Symposium on Digital Industrial Radiology and Computed Tomography, Lyon, France: 2007.

[50] Neuschaefer-Rube U, Bartscher M, Neukamm M, Härtig F, Ehrig K, Staude A, et al. Dimensional Measurements with Micro-CT - Test Procedures and Applications. "Microparts" Interest Group Workshop 2009.

[51] Léonard F, Brown SB, Withers PJ, Mummery PM, McCarthy MB. A new method of performance verification for x-ray computed tomography measurements. Measurement Science and Technology 2014;25. doi:10.1088/0957-0233/25/6/065401.

[52] Stolfi A, De Chiffre L. CT crown for on-machine scale calibration in computed tomography. euspen's 16th International Conference & Exhibition, Nottingham, UK: 2016.

[53] Stolfi A, De Chiffre L. 3D artefact for concurrent scale calibration in Computed Tomography. CIRP Annals - Manufacturing Technology 2016;65:499–502. doi:10.1016/j.cirp.2016.04.069.

[54] Trapet E, Savio E, De Chiffre L. New advances in traceability of CMMs for almost the entire range of industrial dimensional metrology needs. CIRP Annals - Manufacturing Technology 2004;53:433–8. doi:10.1016/S0007-8506(07)60733-1.

[55] Bartscher M, Sato O, Härtig F, Neuschaefer-Rube U. Current state of standardization in the field of dimensional computed tomography. Measurement Science and Technology 2014;25. doi:10.1088/0957-0233/25/6/064013.

[56] Neuschaefer-Rube U, Neugebauer M, Ehrig W, Bartscher M, Hilpert U. Tactile and Optical Microsensors - Test Procedures and Standards. Measurement Science and Technology 2008;19. doi:10.1088/0957-0233/19/8/084010.

[57] Bartscher M, Sato O, Illemann J, Neuschaefer-Rube U. Coordinate metrology using computed tomography systems — an overview of PTB's activities with a focus to standardization. Industrial CT Scanning German-Austrian-Danish Workshop, Munich, Germany: 2013.

[58] Kiekens K, Welkenhuyzen F, Tan Y, Bleys P, Voet A, Kruth J-P, et al. A test object with parallel grooves for calibration and accuracy assessment of industrial computed tomography (CT) metrology. Measurement Science and Technology 2011;22. doi:10.1088/0957-0233/22/11/115502.

[59] De Chiffre L, Carmignato S, Cantatore A, Jensen JD. Replica calibration artefacts for optical 3D scanning of micro parts. euspen International Conference, San Sebastian, Spain: 2009.

[60] Borges de Oliveira F, Stolfi A, Bartscher M, De Chiffre L, Neuschaefer-Rube U. Experimental investigation of surface determination process on multi-material components for dimensional computed tomography. Case Studies in Nondestructive Testing and Evaluation 2016;1:1–11. doi:10.1016/j.csndt.2016.04.003.

[61] Carmignato S, Dreossi D, Mancini L, Marinello F, Tromba G, Savio E. Testing of x-ray microtomography systems using a traceable geometrical standard. Measurement Science and Technology 2009;20. doi:10.1088/0957-0233/20/8/084021.

[62] Heinzl C, Kastner J, Georgi B, Lettenbauer H. Comparison of surface detection methods to evaluate cone beam computed tomography data for three dimensional metrology. International Symposium on Digital industrial Radiology and Computed Tomography, Lyon, France: 2007.

[63] Sun W, Brown S, Leach RK. An overview of industrial X-ray computed tomography. NPL REPORT ENG 32 2012.

[64] Angel J, De Chiffre L. CIA-CT comparison - Inter laboratory comparison on Industrial Computed Tomography - Final report. Kgs. Lyngby, Denmark: 2013.

[65] Stolfi A, De Chiffre L. InteraqCT Comparison on Assemblies - Final report. Kgs. Lyngby, Denmark: 2016.

[66] Hermanek P, Borges De Oliveira F, Carmignato S, Bartscher M. Experimental investigation of new multi-material gap reference standard for testing computed tomography systems. 7th Conference on Industrial Computed Tomography, Leuven, Belgium: 2017.

[67] Borges De Oliveira F, Stolfi A, Bartscher M, Neugebauer M. Creating a Multi-material Probing Error Test for the Acceptance Testing of Dimensional Computed Tomography Systems. 7th Conference on Industrial Computed Tomography, Leuven, Belgium: 2017.

[68] Borges De Oliveira F, Bartscher M, Neuschaefer-Rube U, Tutsch R, Hiller J. Creating a Multi-Material Length Measurement Error Test for the Acceptance Testing of Dimensional Computed Tomography Systems. 7th Conference on Industrial Computed Tomography, Leuven, Belgium: 2017.

[69] Hermanek P, Borges De Oliveira F, Carmignato S, Bartscher M, Savio E. Experimental investigation on multi-material gap measurements by computed tomography using a dedicated reference standard. euspen's 17th International Conference & Exhibition, Hannover: 2017.

[70] Carmignato S, Pierobon A, Rampazzo P, Parisatto M, Savio E. CT for Industrial Metrology – Accuracy and Structural Resolution of CT Dimensional Measurements. Conference on Industrial Computed Tomography (ICT), Wels, Austria: 2012.

[71] Arenhart FA, Nardelli VC, Donatelli GD. Characterization of the Metrological Structural Resolution of CT Systems Using a Multi-Wave Standard. XXI IMEKO World Congress "Measurement in Research and Industry," Prague, Czech Republic: 2015.

[72] Fleßner M, Vujaklija N, Helmecke E, Hausotte T. Determination of metrological structural resolution of a CT system using the frequency response on surface structures. MacroScale 2014:1–10. doi:10.7795/810.20150223B.

[73] Japan Inspection Instruments Manufacturers' Association (JIMA) 2016.

http://www.jima.jp/english/index.html (accessed July 7, 2017).

[74] Staude A, Goebbels J. Determining the Spatial Resolution in Computed Tomography – Comparison of MTF and Line-Pair Structures. International Symposium on Digital Industrial Radiology and Computed Tomography, Berlin, Germany: 2011.

[75] Weiß D, Shi Q, Kuhn C. Measuring the 3D resolution of a micro-focus X-ray CT setup. 4th Conference on Industrial Computed Tomography (iCT), Wels, Austria: 2012.

[76] Van de Casteele E. Model-based approach for Beam Hardening Correction and Resolution Measurements in Microtomography. Universiteit Antwerpen, 2004.

[77] EN 60336 Methods for determining the characteristics of focal spots in diagnostic X-ray tube assemblies for medical use. International Organisation for Standardization, 1995.

[78] Rong XJ, Krugh KT, Shepard SJ, Geiser WR. Measurement of focal spot size with slit camera using computed radiography and flat-panel based digital detectors. Medical Physics 2003;30. doi:10.1118/1.1579583.

[79] Russo P, Mettivier G. Method for measuring the focal spot size of an x-ray tube using a coded aperture mask and a digital detector. Medical Physics 2011;38. doi:10.1118/1.3567503.

[80] Flay N, Sun W, Brown S, Leach RK, Blumensath T. Investigation of the Focal Spot Drift in Industrial Cone-beam X-ray Computed Tomography. Digital Industrial Radiology and Computed Tomography, Ghent, Belgium: 2015.

[81] Hiller J, Maisl M, Reindl LM. Physical characterization and performance evaluation of an x-ray micro-computed tomography system for dimensional metrology applications. Measurement Science and Technology 2012;23. doi:10.1088/0957-0233/23/8/085404.

[82] Weiss D, Deffner A, Kuhn C, Zeiss C, Messtechnik I. Einfluß der Quellbewegung auf Reproduzierbarkeit und Antastab- weichung im Röntgen-Computertomographen. 3rd Industrielle Computertomografie Tagung, Wels, Austria: 2010.

[83] Vogeler F, Verheecke W, Voet A, Kruth J-P. Positional Stability of 2D X-ray Images for Computer Tomography. International Symposium on Digital Industrial Radiology and Computed Tomography, Berlin, Germany: 2011.

[84] Uhlman N, Salamon M, Burtzlaff S. Components and Methods for Highest Resolution Computed Tomography. International Symposium on NDT in Aerospace December, Furth, Germany: 2008.

[85] Neuschaefer-Rube U, Bartscher M, Hilpert U. Application of multisensor measurements and sensor data fusion in coordinate metrology. NCSL International Workshop and Symposium, Orlando, FL, USA: 2008.

[86] Konopczyński T, Rathore J, Kröger T, Zheng L, Garbe CS. Reference Setup for Quantitative Comparison of Segmentation Techniques for Short Glass Fiber CT Data. 7th Conference on Industrial Computed Tomography, Leuven, Belgium: 2017.

[87] Sun Y, Hou Y, Zhao F, Hu J. A calibration method for misaligned scanner geometry in cone-beam computed tomography. NDT and E International 2006;39:499–513. doi:10.1016/j.ndteint.2006.03.002.

[88] Noo F, Clackdoyle R, Mennessier C, White T a, Roney TJ. Analytic method based on identification of ellipse parameters for scanner calibration in cone-beam tomography. Physics in Medicine and Biology 2000;45:3489–508. doi:10.1088/0031-9155/45/11/327.

[89] Gross D, Heil U, Schulze R, Schoemer E, Schwanecke U. Auto calibration of a cone-beam-CT. Medical Physics 2012;39:5959–70. doi:10.1118/1.4739247.

[90] Cho Y, Moseley DJ, Siewerdsen JH, Jaffray DA. Accurate technique for complete geometric calibration of cone-beam computed tomography systems. Medical Physics 2005;32:968–83. doi:10.1118/1.1869652.

[91] Rougee A, Picard CL, Trousset YL, Ponchut C. Geometrical calibration for 3D x-ray imaging. Medical Imaging 1993: Image Capture, Formatting, and Display 1993. doi:10.1117/12.146963.

[92] Claus BEH. Geometry calibration phantom design for 3D imaging. Physics of Medical Imaging, vol. 6142, San Diego, CA, USA: 2006. doi:10.1117/12.652342.

[93] Probst G, Ametova E, Kruth J, Dewulf W. Radiograph based SDD and SRD calculations. 7th Conference on Industrial Computed Tomography, Leuven, Belgium: 2017.

[94] Illemann J, Bartscher M, Neuschaefer-Rube U. An efficient procedure for traceable dimensional measurements and the characterization of industrial CT systems. Digital Industrial Radiology and Computed Tomography, Ghent, Belgium: 2015.

[95] Müller P, Hiller J, Dai Y, Andreasen JL, Hansen HN, De Chiffre L. Estimation of measurement uncertainties in X-ray computed tomography metrology using the substitution method. CIRP Journal of Manufacturing Science and Technology 2014;7:222–32. doi:10.1016/j.cirpj.2014.04.002.

[96] Bartscher M, Neukamm M, Koch M, Neuschaefer-rube U, Staude A, Goebbels J, et al. Performance assessment of geometry measurements with micro-CT using a dismountable work-piece-near reference standard. 10th European Conference on Non-Destructive testing, Moscow, Russia: 2010.

[97] Staude A, Goebbels J, Ehrig K, Bartscher M, Koch M, Neuschaefer-Rube U. A new test piece for geometry and defect measurements with micro-CT. 10th European Conference on Non-Destructive testing, Moscow, Russia: 2010.

[98] Kruth J-P, Levy G, Klocke F, Childs THC. Consolidation phenomena in laser and powder-bed based layered manufacturing. CIRP Annals - Manufacturing Technology 2007;56:730–59. doi:10.1016/j.cirp.2007.10.004.

[99] Wits WW, Carmignato S, Zanini F, Vaneker THJ. Porosity testing methods for the quality assessment of selective laser melted parts. CIRP Annals - Manufacturing Technology 2016;65:201–4. doi:10.1016/j.cirp.2016.04.054.

[100] Nicoletto G, Anzelotti G, Konečná R. X-ray computed tomography vs. metallography for pore sizing and fatigue of cast Al-alloys. Procedia Engineering 2010;2:547–54. doi:10.1016/j.proeng.2010.03.059.

[101] Nikishkov Y, Guillaume S, Makeev A. Structural analysis of composites with porosity defects based on X-Ray Computed Tomography. Journal of Composite Materials 2013. doi:10.1177/0021998313494917.

[102] Tang M, Pistorius PC. Oxides, porosity and fatigue performance of AlSi10Mg parts produced by selective laser melting. International Journal of Fatigue 2017;94:192–201. doi:10.1016/j.ijfatigue.2016.06.002.

[103] Yadollahi A, Shamsaei N. Additive Manufacturing of Fatigue Resistant Materials: Challenges and Opportunities. International Journal of Fatigue 2017;98:Under review. doi:10.1016/j.ijfatigue.2017.01.001.

[104] Bauereiß A, Scharowsky T, Körner C. Defect generation and propagation mechanism during additive manufacturing by selective beam melting. Journal of Materials Processing Technology 2014;214:2497–504. doi:10.1016/j.jmatprotec.2014.05.002.

[105] Kempen K, Yasa E, Thijs L, Kruth J-P, Van Humbeeck J. Microstructure and mechanical properties of selective laser melted 18Ni-300 steel. Physics Procedia 2011;12:255–63. doi:10.1016/j.phpro.2011.03.033.

[106] Tapia G, Elwany AH, Sang H. Prediction of porosity in metal-based additive manufacturing using spatial Gaussian process models. Additive Manufacturing 2016;12:282–90. doi:10.1016/j.addma.2016.05.009.

[107] Aboulkhair NT, Maskery I, Tuck C, Ashcroft I, Everitt NM. The microstructure and mechanical properties of selectively laser melted AlSi10Mg: The effect of a conventional T6-like heat treatment. Materials Science and Engineering A 2016;667:139–46. doi:10.1016/j.msea.2016.04.092.

[108] Dewulf W, Pavan M, Craeghs T, Kruth J-P. Using X-ray computed tomography to improve the porosity level of polyamide-12 laser sintered parts. CIRP Annals - Manufacturing Technology 2016;65:205–8. doi:10.1016/j.cirp.2016.04.056.

[109] Zhu H, Wu B, Li D, Zhang D, Chen Y. Influence of Voids on the Tensile Performance of Carbon/epoxy Fabric Laminates. Journal of Materials Science and Technology 2011;27:69–73. doi:10.1016/S1005-0302(11)60028-5.

[110] Yi JZ, Gao YX, Lee PD, Flower HM, Lindley TC. Scatter in fatigue life due to effects of porosity in cast A356-T6 aluminum-silicon alloys. Metallurgical and Materials Transactions A 2003;34:1879–90. doi:10.1007/s11661-003-0153-6.

[111] Müller De Almeida SF, Neto ZDSN. Effect of void content on the strength of composite laminates. Composite Structures 1994;28:139–48. doi:10.1016/0263-8223(94)90044-2.

[112] Lambert J, Chambers AR, Sinclair I, Spearing SM. 3D damage characterisation and the role of voids in the fatigue of wind turbine blade materials. Composites Science and Technology 2012;72:337–43. doi:10.1016/j.compscitech.2011.11.023.

[113] VDG P 201 Volume Deficits of Non-Ferrous Metal Castings. Verein Deutscher Gießereifachleute, 2002.

[114] VDG P 202 Volume Deficits of Castings Made from Aluminium , Magnesium , and Zinc Casting Alloys BDG-Reference Sheet. Verein Deutscher Gießereifachleute, 2010.

[115] Slotwinski JA, Garboczi EJ, Hebenstreit KM. Porosity Measurements and Analysis for Metal Additive Manufacturing Process Control. Journal of Research of the National Institute of Standards and Technology 2014;119:494–528. doi:10.6028/jres.119.019.

[116] Khademzadeh S, Carmignato S, Parvin N, Zanini F, Bariani PF. Micro porosity analysis in additive manufactured NiTi parts using micro computed tomography and electron microscopy. Materials and Design 2016;90:745–52. doi:10.1016/j.matdes.2015.10.161.

[117] Kastner J, Plank B, Salaberger D, Sekelja J. Defect and Porosity Determination of Fibre Reinforced Polymers by X-ray Computed Tomography. NDT in Aerospace 2010 - We1A2 2010.

[118] Birt EA, Smith RA. A review of NDE methods for porosity measurement in fibre-reinforced polymer composites. Insight - Non-Destructive Testing and Condition Monitoring 2004;46:681–6.

[119] Suhot MA, Chambers AR. The effect of voids on the flexural fatigue properties of carbon/epoxy composites. 16th International Conference on Composite Materials, Kyoto, Japan: 2010.

[120] Nikishkov Y, Airoldi L, Makeev A. Measurement of voids in composites by X-ray Computed Tomography. Composites Science and Technology 2013;89:89–97. doi:10.1016/j.compscitech.2013.09.019.

[121] Jansson A, Zekavat AR, Pejryd L. Measurement of Internal Features in Additive Manufactured Components by the use of Computed Tomography. Digital Industrial Radiology and Computed Tomography (DIR 2015), Ghent, Belgium: 2015.

[122] ISO 4287 Geometrical product specifications (GPS) - Surface texture: Profile method - Terms, definitions and surface texture parameters. International Organization for Standardization, 1997.

[123] EA-4/02 M Evaluation of the Uncertainty of Measurement In Calibration. EA Laboratory Committee, 2013.

[124] Dabankah EM, Hermanek P, Carmignato S, Kasperl S. Assessment of CT simulated data based on POD Numerical Model Approach. Digital Industrial Radiology and Computed Tomography (DIR 2015), Ghent, Belgium: 2015.

[125] Hermanek P, Carmignato S. Reference object for evaluating the accuracy of porosity measurements by X-ray computed tomography. Case Studies in Nondestructive Testing and Evaluation 2016;1:1–6. doi:10.1016/j.csndt.2016.05.003.

[126] Stoessel R, Kiefel D, Oster R, Diewel B, Llopard Prieto L. µ-Computed Tomography for 3D Porosity Evaluation in Carbon Fibre Reinforced Plastics (CFRP). International Symposium on Digital Radiology and Computed Tomography, Berlin, Germany: 2011.

[127] D. Kiefel, Stoessel R, Plank B, Heinzl C, Kastner J. CFRP Porosity Characterisation Using µ-Computed Tomography with Optimized Test Parameters Supported by XCT-simulation. 5th Conference on Industrial Computed Tomography, Wels, Austria: 2014.

[128] Gondrom-Linke S, Günther T. Physical and Technical Boundary Conditions for an Automated Industrial 3D-CT Inspection Dealing with Typical Production Cycle Times. 19th World Conference on Non-Destructive Testing 2016, Munich, Germany: 2016.

[129] Dillencourt MB, Samet H, Tamminen M. A general approach to connected-component labeling for arbitrary image representations. Journal of the ACM 1992;39:253–80. doi:10.1145/128749.128750.

[130] Tan Y, Kiekens K, Kruth J-P, Voet A, Dewulf W. Material Dependent Thresholding for Dimensional X-ray Computed Tomography. International Symposium on Digital Industrial Radiology and Computed Tomography, Berlin, Germany: 2011.

[131] Kiekens K, Tan Y, Kruth J, Voet A, Dewulf W. Parameter Dependent Thresholding for Dimensional X-ray Computed Tomography. International Symposium on Digital Industrial Radiology and Computed Tomography, Berlin, Germany: 2011.

[132] Hermanek P, Carmignato S. Establishment of metrological traceability in porosity measurements by X-ray computed tomography. SPIE Optical Engineering + Applications, San Diego, CA, USA: 2017.

[133] Von Smekal L, Kachelriess M, Stepina E, Kalender WA. Geometric misalignment and calibration in cone-beam tomography. Medical Physics 2004;31:3242–66. doi:10.1118/1.1803792.

[134] Ford JC, Zheng D, Williamson JF. Estimation of CT cone-beam geometry using a novel method insensitive to phantom fabrication inaccuracy: implications for isocenter localization accuracy. Medical Physics 2011;38:2829–40. doi:10.1118/1.3589130.

[135] Xu J, Tsui BMW. An analytical geometric calibration method for circular cone-beam geometry. IEEE Transactions on Medical Imaging 2013;32:1731–44. doi:10.1109/TMI.2013.2266638.

[136] Ferrucci M, Ametova E, Carmignato S, Dewulf W. Evaluating the effects of detector angular misalignments on simulated computed tomography data. Precision Engineering 2016;45:230–41. doi:10.1016/j.precisioneng.2016.03.001.

[137] Parzen E. On Estimation of a Probability Density Function and Mode. The Annals of Mathematical Statistics 1962;33:1065–76. doi:10.1214/aoms/1177704472.

[138] Murray Rosenblatt. Remarks on Some Nonparametric Estimates of a Density Function. The Annals of Mathematical Statistics 1956;Volume 27:832–7. doi:10.1214/aoms/1177728190.

[139] Chantler CT, Olsen K, Dragoset RA, Chang J, Kishore AR, Kotochigova SA, et al. X-Ray Form Factor, Attenuation and Scattering Tables (version 2.1) 2005. http://physics.nist.gov/ffast (accessed October 21, 2017).

[140] ISO 3290-1 Rolling bearings - Balls - Steel balls. International Organization for Standardization, 2014.

[141] Hüser D, Trapet E, Wäldele F, Wiegand U. Kalibrierung von Kugel- und Lochplatten als Normale für Koordinatenmeßgeräte. Anleitung für DKD-laboratorien 1993.

[142] Kunzmann HI, Trapet E, Waldele F. Results of the International Comparison of Ball Plate Measurements in ClRP and WECC. CIRP Annals - Manufacturing Technology 1995;44:479–82. doi:10.1016/S0007-8506(07)62367-1.

[143] Ferrucci M, Hermanek P, Ametova E, Chilingaryan S, Carmignato S, Dewulf W. Measurement of the X-ray computed tomography system geometry—part 2: minimization of reprojection errors. Submitted to Precision Engineering 2017.

[144] Fila T, Vavrik D. A multi-axial apparatus for carrying out x-ray measurements, particularly computed tomography. European patent EP2835631, 2016.

[145] Fila T, Krumpova I, Jandejsek I, Kloiber M, Turecek D, Vavrik D. Utilization of dual-source X-ray tomography for reduction of scanning time of wooden samples. 16th International Workshop on Radiation Imaging Detectors, Trieste, Italy: 2014. doi:10.1088/1748-0221/10/05/C05008.

[146] Bartscher M, Illemann J, Neuschaefer-Rube U. ISO test survey on material influence in dimensional computed tomography. Case Studies in Nondestructive Testing and Evaluation 2016;1. doi:10.1016/j.csndt.2016.04.001.

[147] Kiekens K, Tan Y, Kruth J-P, Voet A, Dewulf W. Parameter dependent thresholding for dimensional X-ray computed tomography. International Symposium on Digital Industrial Radiology and Computed Tomography, Berlin, Germany: 2011.

[148] Ontiveros S, Yagüe JA, Jiménez R, Brosed F. Computer tomography 3D edge detection comparative for metrology applications. Procedia Engineering 2013;63:710–9. doi:10.1016/j.proeng.2013.08.263.

[149] Heinzl C, Kastner J, Groeller E. Surface extraction from multi-material components for metrology using dual energy CT. IEEE Transactions on Visualization and Computer Graphics 2007;13:1520–7. doi:10.1109/TVCG.2007.70598.

[150] Haitham Shammaa M, Ohtake Y, Suzuki H. Segmentation of multi-material CT data of mechanical parts for extracting boundary surfaces. CAD Computer Aided Design 2010;42:118–28. doi:10.1016/j.cad.2009.08.003.

[151] ISO 14253-5 Geometrical product specifications (GPS) - Inspection by measurement of workpieces and measuring equipment: Uncertainty in verification testing of indicating measuring instruments. International Organisation for Standardization, 2015.

[152] Jansson A, Ekengren J, Zekavat A-R, Pejryd L. Effects of X-ray Penetration Depth on Multi Material Computed Tomography Measurements. 6th Conference on Industrial Computed Tomography, Wels, Austria: 2016.

[153] Jansson A, Pejryd L. A dual-energy approach for improvement of the measurement consistency in computed tomography. Measurement Science and Technology 2016;27. doi:10.1088/0957-0233/27/11/115013.

[154] Herderick E. Additive manufacturing of metals: A review. Materials Science and Technology Conference and Exhibition, Ohio, USA: 2011.

[155] Granta Design. CES EduPack 2014 2014.

[156] Zelený V, Linkeová I, Skalník P, Hynek J. Use of on-board metrology systems for area-scanning on machine tools. Czech Metrology Institute, 2016.

[157] Zelený V, Linkeová I, Skalník P. Calibration of freeform standard. euspen's 15th International Conference & Exhibition, Leuven, Belgium: 2015.

[158] Aloisi V, Carmignato S. Influence of surface roughness on X-ray computed tomography dimensional measurements of additive manufactured parts. Case Studies in Nondestructive Testing and Evaluation 2016;6:104–10. doi:10.1016/j.csndt.2016.05.005.

[159] Savio E, De Chiffre L. An artefact for traceable freeform measurements on coordinate measuring machines. Precision Engineering 2002;26:58–68. doi:10.1016/S0141-

6359(01)00098-8.

[160] Flack D. Good Practice Guide No. 130 Co-ordinate measuring machine task-specific measurement uncertainties. National Physical Laboratory, 2013.

[161] Flack D. Good Practice Guide No. 41 CMM Measurement Strategies. National Physical Laboratory, 2011.

[162] Flack D. Good Practice Guide No. 42 CMM Verification. National Physical Laboratory, 2011.

[163] Flack D. Good Practice Guide No. 43 CMM Probing. National Physical Laboratory, 2014.

[164] Carmignato S. Reference objects for Computed Tomography. 5thCIA-CT Conference and InteraqCT event ”Industrial Applications of Computed Tomography”, Lyngby, Denmark: 2015.

[165] Evans CJ, Hocken RJ, Estler WT. Self-Calibration: Reversal, Redundancy, Error Separation, and “Absolute Testing.” CIRP Annals - Manufacturing Technology 1996;45:617–34. doi:10.1016/S0007-8506(07)60515-0.